

**Measurement of the High Mass Drell-Yan Differential Cross
Section in the electron-positron channel with the ATLAS
Experiment at $\sqrt{s} = 7$ TeV**

THÈSE

présentée à la Faculté des sciences de l'Université de Genève
pour obtenir le grade de Docteur des sciences, mention physique

par

Katalin Nikolics

Autriche

Thèse N° 4541



**UNIVERSITÉ
DE GENÈVE**

FACULTÉ DES SCIENCES

**Doctorat ès sciences
Mention physique**

Thèse de *Madame Katalin NIKOLICS*

intitulée :

**" Measurement of the High Mass Drell-Yan Differential Cross
Section in the Electron-positron Channel with the ATLAS
Experiment at $\sqrt{s} = 7 \text{ TeV}$ "**

La Faculté des sciences, sur le préavis de Messieurs M. NESSI, suppléant professeur titulaire et directeur de thèse (Département de Physique nucléaire et corpusculaire), G. IACOBUCCI, professeur ordinaire et codirecteur de thèse (Département de physique nucléaire et corpusculaire) et A. NISATI, professeur (Département de physique, Université de Rome La Sapienza, Italie), autorise l'impression de la présente thèse, sans exprimer d'opinion sur les propositions qui y sont énoncées.

Genève, le 19 mars 2013

Thèse - 4541 -


Le Doyen, Jean-Marc TRISCONE

N.B. - La thèse doit porter la déclaration précédente et remplir les conditions énumérées dans les "Informations relatives aux thèses de doctorat à l'Université de Genève".

Abstract

This thesis reports the study of the stability of the beam pipe within the ATLAS experiment and of the high mass Drell-Yan $Z/\gamma^* \rightarrow e^+e^-$ differential cross section measurement using 4.92 fb^{-1} of ATLAS data recorded in 2011 at a centre-of-mass energy of 7 TeV.

The beam pipe studies used reconstructed secondary hadronic interaction vertex distributions in the 2010-2012 data. The results indicate a very good stability and will be used for the insertion of the new beam pipe. A simulation study for the design of the new beam pipe has been conducted in addition to estimate the influence of a change of material and the difference between three options for the position of a new vacuum flange in the beam pipe inside the electromagnetic calorimeter end-caps. A gain of 27 % in radiation length was found when replacing the stainless steel beam pipe with aluminium but no significant difference between the three flange positions could be observed. These results have been used by the ATLAS engineering for the design of the new beam pipe that will be installed during the 2013/14 LHC shutdown.

In order to perform the Drell-Yan cross section measurement the identification efficiency of electrons has been evaluated up to a transverse energy of 500 GeV. The results are presented separately in bins of pseudorapidity η and transverse energy E_T and compared to previous measurements for $E_T < 50\text{ GeV}$. Good agreement is found. At high E_T the data agrees well with the Monte Carlo simulations.

The Drell-Yan differential cross-section is reported as a function of the electron-positron invariant mass, m_{ee} , for events with $116 < m_{ee} < 1500\text{ GeV}$ in a fiducial region with e^\pm pseudorapidity of $|\eta| < 2.5$, and transverse energy $E_T > 25\text{ GeV}$. The precision of the measurement at high m_{ee} is dominated by the statistical uncertainty on the data. The results of the differential cross section measurement are compared to the predictions of perturbative next-to-next-to leading order QCD calculations and various event generators. The data are largely consistent with the theoretical predictions.

Resumé

Cette thèse rapporte une étude de la stabilité du tube de faisceau à l'intérieur de l'expérience ATLAS et une mesure de la section efficace différentielle du processus Drell-Yan $Z/\gamma^* \rightarrow e^+e^-$ à partir des 4.92 fb^{-1} de données d'ATLAS qui ont été enregistrées en 2011 à une énergie de centre de masse de 7 TeV. L'étude de la stabilité du tube de faisceau utilise les distributions des vertex secondaires des interactions hadroniques de la période 2010-2012 pour estimer une déviation du plan horizontal. Ces résultats indiquent une excellente stabilité et déterminent certains paramètres pour le changement de la structure des supports d'un nouveau tube. Une étude avec des simulations permet quant à elle d'estimer l'influence d'un changement de matériau pour la partie du tube de faisceau dans les calorimètres bouchons d'ATLAS ainsi que la différence entre trois options pour la position d'une nouvelle bride à vide. Une réduction en terme de longueur de radiation de l'ordre de 27% a été estimée avec le choix de l'aluminium comme matériel. Quant à la position de la bride, aucune différence significative a été observée entre les trois cas étudiés. Cette information a été utilisée par l'ingénierie d'ATLAS pour le design du prochain tube de faisceau qui sera installé pendant le shutdown du LHC en 2013/14.

Pour la mesure de la section efficace du processus Drell-Yan, l'efficacité d'identification des électrons à haut E_T jusqu'à 500 GeV a été mesurée par une méthode "Tag-and-Probe" qui utilise l'isolation calorimétrique des électrons pour la discrimination contre les jets hadroniques. Les résultats sont présentés séparément dans des intervalles de la pseudorapidité η et de l'énergie transverse E_T pour deux niveaux d'identification. Les valeurs obtenues sont en très bon accord avec les mesures antérieures restreintes à $E_T < 50 \text{ GeV}$. À haut E_T les données sont en accord avec les prédictions de la simulation Monte Carlo.

Les résultats de la section efficace sont présentés en fonction de la masse invariante pour des événements avec $116 < m_{ee} < 1500 \text{ GeV}$ dans une région de pseudorapidité η inférieure à 2.5 et impulsion transverse $E_T > 25 \text{ GeV}$. Ces mesures, limitées en précision par l'incertitude systématique à basse masse invariante et par l'incertitude statistique à haute masse invariante, sont comparées aux prédictions de QCD perturbative et cinq générateurs d'événements.

Contents

1	Introduction	3
2	Theoretical Introduction	6
2.1	The Standard Model of Particle Physics	6
2.2	Electroweak Theory	8
2.3	Quantum Chromodynamics	11
2.3.1	The Parton Model and the Drell-Yan Process	12
2.4	Monte-Carlo Generators	18
3	The ATLAS Experiment at the Large Hadron Collider	20
3.1	The Large Hardon Collider at CERN	20
3.1.1	Collision Rate and Luminosity	23
3.2	The ATLAS Experiment	25
3.2.1	The Detector Subsystems	27
3.2.2	Trigger and Data Acquisition	31
3.3	Electrons in ATLAS	35
3.3.1	Reconstruction	35
3.3.2	Identification	37
3.4	The LHC Beam Pipe within the ATLAS Experiment	43
3.4.1	Stability Studies of the Current Configuration	43
3.4.2	ATLAS Beam Pipe Upgrade	54
3.4.3	Summary	65
4	High Mass Drell-Yan Differential Cross Section Measurement	67
4.1	Fiducial differential cross section	68
4.2	Data and Simulated Monte Carlo Samples	68
4.2.1	Data	68
4.2.2	Monte Carlo	69
4.3	Candidate Event Selection	74

4.4	Background Estimation	75
4.4.1	Data-driven Background Component	75
4.4.2	Simulated Background Component	76
4.4.3	Data - Monte Carlo Comparison	78
4.5	Electron Identification Efficiency Measurement	82
4.5.1	Methodology	82
4.5.2	Data and Monte Carlo Samples, Trigger and Event Selection	85
4.5.3	Background Estimation	88
4.5.4	Statistical and Systematic Uncertainties	97
4.5.5	Efficiencies from Monte Carlo Simulation	98
4.5.6	Results and Comparison to Previous Measurements	99
4.5.7	B-Layer Hit Efficiency Measurement	113
4.5.8	Summary	113
4.6	Efficiency and Migration Corrections	121
4.7	Systematic Uncertainties	125
4.7.1	Background estimation	125
4.7.2	Uncertainties on Corrections	125
4.8	Results and Comparison to Theory	129
4.9	Summary	133
5	Summary and Conclusion	134
A	Electron Identification Efficiency	136
A.1	Data Taking Periods	136
A.2	ATLAS Monte Carlo Production for 2011	136
A.3	Electron Isolation Distributions	138
A.3.1	Bins of Transverse Energy	138
A.3.2	Bins of Pseudorapidity	150
A.4	Efficiency Measurement for $m_{ee} > 76$ GeV	160
B	Acknowledgments	163
	Bibliography	164

Chapter 1

Introduction

While in ancient times the naked eye would suffice to make significant observations, today complicated machineries are necessary to see what happens at both ends of the physical spectrum: the macro- as well as the microcosm. To explore the latter, the Large Hadron Collider (LHC) together with its huge and intricate detector systems such as the ATLAS experiment have been built in order to discover new physics and test the predictions of the Standard Model (SM) of Particle Physics, the present theory of elementary particles and the forces that act between them.

The SM has been very successful in correctly predicting the observed phenomena at colliders, yet it has shortcomings. For instance, it does not include gravity, while on an observational level it fails to explain the nature of the dark matter observed in the universe. Despite the open theoretical questions, the SM has made remarkable predictions that have later been experimentally confirmed, among the most prominent being the discovery of the W and Z bosons at the Super Proton Synchrotron (SPS) at CERN in 1983. These big discoveries from three decades ago are nowadays produced in huge quantities in the pp collisions at the LHC and are used as “standard candles” for detector calibration.

Dilepton production via the Drell-Yan process $q\bar{q} \rightarrow \gamma^*/Z \rightarrow \ell^+\ell^-$ can test the predictions of perturbative Quantum Chromodynamics (pQCD), the theory that describes the strong interaction of the quarks that constitute the proton, the neutron and the other hadrons. Precise knowledge of the Drell-Yan cross section can also give insight into the parton distribution functions (PDF's) of the proton. This thesis reports a measurement of the Drell-Yan cross section in the electron-positron final state for invariant masses above the Z boson peak ($m_{ee} = 116\text{--}1500\text{ GeV}$). The full 2011 data set recorded by the ATLAS experiment was used, corresponding to an integrated luminosity of $\mathcal{L} = 4.92\text{ fb}^{-1}$ at a pp centre-of-mass energy of $\sqrt{s} = 7\text{ TeV}$.

An accurate knowledge of particle identification efficiencies is required in order to perform a cross sections measurement. As the identification efficiency depends on the transverse energy (E_T) of a given particle, it is necessary to know the efficiency throughout the entire E_T spectrum considered in

the analysis. As the high E_T range is becoming more accessible, it is important to understand well the particle identification performance of the detector in this region. Identification efficiencies for electrons were measured only up to an E_T of 50 GeV in a data-driven way. As part of this work the measurement was extended up to $E_T = 500$ GeV, to support the high-mass Drell-Yan cross section measurement up to an invariant mass of the electron-positron pair of 1500 GeV.

Owing to the LHC, new realms of physics have become accessible and with that come certain technical challenges that need to be addressed: high interaction rates and radiation doses, large particle multiplicities and energies, as well as the requirements for precision measurements have set new standards for the design of particle detectors. To ensure a stable detector performance, it is necessary to monitor the actual geometrical stability of the detector and the beam pipe to account for possible mis-alignment. To estimate the position stability of the beam pipe, a qualitative study has been conducted in this work using a mapping of secondary vertices reconstructed from hadronic interactions with the material of the beam pipe in the ATLAS detector. These data (taken in 2010 - 2012) were then compared to those recorded by a hydrostatic levelling sensor system installed in the cavern of the ATLAS experiment.

The technical stop of the LHC starting in 2013 will be used to tune the accelerator to full nominal performance and this will also grant the experiments an opportunity for detector maintenance and upgrade. The exposure to hard radiation from the collisions can induce radioactivity in the surrounding material that can then lead to damage of detector modules or interfere with the trigger performance. Studies have shown that the main source of radiation through radio-activation will be the beam pipe and thus a change of material is envisaged. Within the scope of this work, a simulation study was performed to estimate the reduction in radiation length for the traversing particles due to the new material of the beam pipe as well as to evaluate the differences between several positioning options of a new vacuum flange to support the ATLAS engineering for the design of the new beam pipe.

The entirely personal contributions of the author to the work presented in this thesis include in particular:

- **Beam pipe studies:** Creating the XML model of the new beam pipe, the GEANT4 simulation and the extraction of the data. Preparation of data for the secondary hadronic interaction study, the data processing and analysis.
- **Drell-Yan Differential Cross Section Measurement:** Cut flow for the event selection of the cross section measurement as well as the measurement of the electron identification efficiencies in data and Monte Carlo. This work includes a Tag-and-Probe efficiency measurement which was used to provide scale factors for the Monte Carlo derived efficiencies on two different identification levels.

Chapter 2

Theoretical Introduction

2.1 The Standard Model of Particle Physics

In the early decades of the 20th century, only a small number of “elementary particles”, thought to be the basic building blocks of matter, were known: the proton, the neutron, the electron and the photon. All these particles are stable¹. This picture had changed profoundly by the 1960’s. Today the standard reference *Review of Particle Properties* [1] displays a long list of particles. As accelerator energies and luminosities increase, this number is still growing.

Matter is made of atoms which themselves consist of the positively charged protons and the electrically neutral neutrons in the nucleus which is surrounded by negatively charged electrons. Through deep inelastic scattering experiments it was shown that protons and neutrons themselves are not elementary particles but a bound state of quarks. Quarks are fermions with spin- $\frac{1}{2}$ and non-integer charge (in units of electron charge) which however do not exist as free particles in nature but always appear in bound states of two (mesons) or three (baryons) quarks [2]. There are six flavours of quarks (in increasing order of mass): up, down, strange, charm, bottom/beauty and top, forming three generations. Leptons such as the electron also come in three generations: the charged electron (e), muon (μ) and tau (τ) - as well as their associated neutral partners, the neutrinos. For each particle, quark or lepton, there is also an antiparticle. Quarks and leptons communicate through spin-1 force-mediating particles, gauge bosons: the gluons in case of the strong interaction between quarks, the photon in the case of electromagnetic interaction of electrically charged particles, and the Z^0 and W^\pm bosons in case of the weak interaction. Quarks interact with all bosons, leptons do not interact with gluons (g) and are thus not sensitive to the strong interaction. Neutrinos in particular do not interact with photons either and are hence not affected by the electromagnetic interaction that acts on charged particles. Gluons, the W^\pm and the Higgs boson, the boson of the Higgs field which gives mass to the weak gauge bosons and to fermions through the Yukawa coupling, interact

¹The neutron is only stable in nuclear matter, the free neutron decays via beta decay: $n \rightarrow p + e^- + \bar{\nu}$

also with themselves.

This classification of particles with its underlying Quantum Field Theory (Quantum Chromodynamics - QCD - the theory of strong interaction, and Electroweak Theory) constitutes the Standard Model (SM) of Particle Physics (Table 2.1) [3]. The Standard Model describes our universe very accurately, its most recent success being the discovery of a scalar boson compatible with the properties of the SM Higgs boson by the ATLAS [4] and CMS [5] collaborations. However, the SM has its limits and is to our current knowledge incomplete as it does not accommodate gravity, for example, nor does it explain neutrino oscillations, a mixing effect only possible if neutrinos have a non-zero mass.

	1 st generation	2 nd generation	3 rd generation	force carriers	
mass →	2.4 MeV/c ²	1.27 GeV/c ²	171.2 GeV/c ²	0	
charge →	2/3	2/3	2/3	0	
spin →	1/2	1/2	1/2	1	
	u up	c charm	t top	γ photon	
	4.8 MeV/c ²	104 MeV/c ²	4.2 GeV/c ²	0	
	-1/3	-1/3	-1/3	0	
	1/2	1/2	1/2	1	
	d down	s strange	b bottom	g gluon	
	< 2.2 eV/c ²	< 0.17 eV/c ²	< 15.5 eV/c ²	91.2 GeV/c ²	
	0	0	0	0	
	1/2	1/2	1/2	1	
	ν_e e neutrino	ν_μ μ neutrino	ν_τ τ neutrino	Z ⁰ Z boson	
	0.511 MeV/c ²	105.7 MeV/c ²	1.777 GeV/c ²	80.4 GeV/c ²	~ 125 GeV/c ²
	-1	-1	-1	± 1	0
	1/2	1/2	1/2	1	0
	e electron	μ muon	τ tau	W ^{\pm} W boson	H Higgs

Table 2.1: *The ingredients of the Standard Model (SM) of Particle Physics: all elementary particles of matter, force-carrying gauge bosons, as well as the Higgs boson. A scalar boson compatible with a SM Higgs boson was recently discovered [4, 5]. There are antiparticles to all fermions: quarks - $(\bar{u}), (\bar{c}), (\bar{t}), (\bar{d}), (\bar{s}), (\bar{b})$ - and leptons, $(\bar{\nu}_e), (\bar{\nu}_\mu), (\bar{\nu}_\tau)$ [6].*

The Standard Model (SM) of Particle Physics is a Quantum Field Theory, more precisely a gauge theory, based on the gauge group $SU(3)_C \otimes SU(2)_L \otimes U(1)_Y$. The $SU(3)$ gauge group corresponds to the strong interaction (QCD), $SU(2)_L \otimes U(1)_Y$ is associated with the electroweak theory. C represents the colour charge of the strong interaction, L refers to left-handed chirality and Y to weak hyper charge which are conserved quantities of the respective symmetry group. Colour charge is a quantity carried by quarks and gluons that cannot be directly observed: hadrons come in colour-singlet states and thus appear colourless to the observer. Colour was proven to exist when baryons (Λ^{++}) were found that seemed to possess three up quarks with parallel spins and vanishing orbital angular momentum, and therefore could not have an antisymmetric wavefunction unless there was

a hidden quantum number [3].

Chirality indicates whether a particle transforms in a left- or right-handed representation of the Poincaré group. For Dirac fermions, chirality is defined by the operator γ^5 with eigenvalues ± 1 and thus a Dirac field can be split into left- and right-handed components. For massless particles chirality equals helicity, defined as the projection of the particle's spin onto its momentum. While helicity is not an intrinsic property of a particle, its chirality is. While one particle can appear in different helicity states, particles with different chiralities really are two different particles [7].

The weak hypercharge (Y) is related to the third component of the weak isospin (T_3) and the electric charge through the analogous of the Gell-Mann - Nishijima formula:

$$Q = T_3 + Y/2 \quad (2.1)$$

Left-handed fermions with $T = \frac{1}{2}$ and can be arranged into doublets with $T_3 = \pm \frac{1}{2}$ behaving the same way under weak interaction. For instance, left-handed up-type quarks (u, c, t) with $T_3 = +\frac{1}{2}$ always transform into left-handed down-type quarks (d, s, b) with $T_3 = -\frac{1}{2}$ and vice versa. A quark decay however always changes the quark's T_3 . A parallel doublet representation exists for left-handed charged leptons (e^-, μ^-, τ^-) with $T_3 = -\frac{1}{2}$, and neutrinos (ν_e, ν_μ, ν_τ) with $T_3 = +\frac{1}{2}$. Right-handed fermions with $T = 0$ form singlets that do not interact weakly. As a consequence, the W^\pm boson interacts only with left-handed fermions [8].

2.2 Electroweak Theory

The Electroweak (EW) interaction is the unified description of electromagnetism and the weak interaction. Very different in nature at low energies, these two forces are manifestations of the same force (the electroweak force) above the unification energy of the order 100 GeV.

For contributions to the unification of the weak and electromagnetic interaction between elementary particles, Abdus Salam [9], Sheldon Glashow [10, 11] and Steven Weinberg [12] were awarded the Nobel Prize in Physics in 1979. The existence of the electroweak interaction was experimentally established in two stages, the first being the discovery of neutral currents in neutrino scattering by the Gargamelle collaboration at CERN [13] in 1973, and the second in 1983 by the UA1 [14] and the UA2 [15] collaborations that involved the discovery of the W and Z gauge bosons in proton-antiproton collisions at the converted Super Proton Synchrotron (SPS/CERN).

Historically there were already several attempts to construct a gauge theory for the (electro)weak interaction, such as by Schwinger in 1957 [16] who suggested a model based on the group $O(3)$. Further attempts followed by Bludman [17] and Leite Lopes [18] in 1958, already suggesting an $SU(2)$ gauge group, incorporating neutral currents. Finally, Glashow suggested a theory based on the gauge group $SU(2) \otimes U(1)$.

An essential ingredient of the model is “spontaneous symmetry breaking” which generally means

that a system possesses a certain symmetry under which the ground state (identified with the vacuum in field theories) is yet not invariant. Or in other words: the ground state is degenerate. The symmetry breaking process can be sketched by starting off with the Lagrangian of a complex ϕ^4 theory

$$\mathcal{L} = (\partial_\mu \phi)(\partial^\mu \phi^\dagger) - \mu^2 \phi^\dagger \phi - \lambda(\phi^\dagger \phi)^2 = (\partial_\mu \phi)(\partial^\mu \phi^\dagger) - V(\phi, \phi^\dagger) \quad (2.2)$$

where λ denotes self interaction and μ^2 is a parameter (in usual scalar field theory μ^2 is identified with the mass of the field quanta). The ground state is then obtained by minimizing the potential V :

$$\frac{\partial V}{\partial \phi} = \mu^2 \phi^\dagger + 2\lambda \phi(\phi^\dagger \phi) \quad (2.3)$$

Now when $\mu^2 > 0$, the minimum occurs at $\phi^\dagger = \phi = 0$. If however, $\mu^2 < 0$, there is a local maximum at $\phi = 0$, and a minimum at

$$|\phi|^2 = -\mu^2/2\lambda = v^2, \quad (2.4)$$

as depicted in Fig. 2.1. When ϕ is treated as an operator, this condition refers to the vacuum

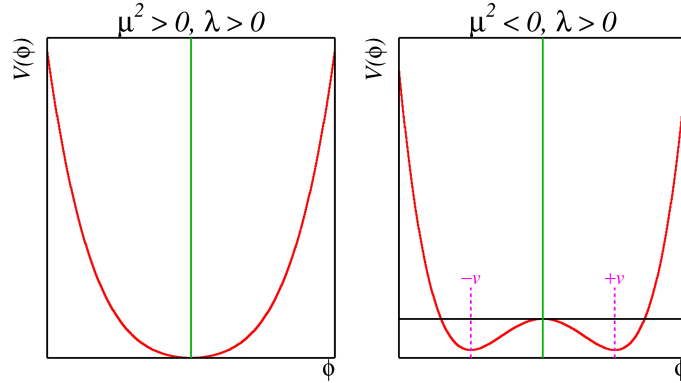


Figure 2.1: *Symmetry breaking through the Higgs mechanism. By adding a scalar field to the potential, the ground state (identified with the vacuum in a field theory) is no longer at $\phi = 0$ but becomes degenerate, it acquires a non-zero expectation value and breaks the original symmetry of the Lagrangian.*

expectation value of ϕ

$$|\langle 0|\phi|0\rangle| = v \quad (2.5)$$

Now choosing a particular vacuum leads to a particular choice for the values of the field as well which then results in what is known as the Goldstone Theorem [19]: as a result of a non-vanishing vacuum expectation value, what would have been two massive fields (the real parts of ϕ) become

one massive and one massless, the latter called the Goldstone boson, for whose existence we have no evidence in nature. The Higgs Mechanism named after P. Higgs [20]² implies that the Lagrangian that exhibits the spontaneous symmetry breakdown is also invariant under local, rather than global, gauge transformations. This property eliminates the massless Goldstone boson and gives mass to the gauge boson(s).

In the Salam-Weinberg Model of electroweak interaction, symmetry breaking via the Higgs Mechanism is used to generate the weak vector-boson masses while the photon remains massless. Moreover, fermion masses are generated through Yukawa-couplings to the Higgs doublet. The $SU(2)$ gauge field then has a triplet as gauge bosons, (W^1, W^2, W^3) with coupling g , and the $U(1)$ the neutral field B (coupling g'). The charged weak bosons appear as a linear combination of W^1 and W^2 , while the photon and the neutral weak boson Z are both given by a mixture of W^3 and B .

The matter fields - leptons and quarks - are organized in families, with the left-handed (chirality $-1/2$) fermions belonging to weak isodoublets while the right-handed (chirality $+1/2$) components transform as weak isosinglets. To break the symmetry, a complex scalar potential (Higgs field) is added to the Lagrangian:

$$\Phi = \begin{pmatrix} \phi^+ \\ \phi^0 \end{pmatrix} \quad (2.6)$$

with a vacuum expectation value $\langle \Phi \rangle_0 = \begin{pmatrix} 0 \\ v/\sqrt{2} \end{pmatrix}$ where v was measured to be $v \approx 246.2 \text{ GeV}$ [23]. From the symmetry breaking, one neutral Higgs scalar, H , remains in the physical particle spectrum³. The boson masses in the EW sector are then given (at tree level, i.e., to lowest order in perturbation theory) by [26],

$$M_H = \lambda v \quad (2.7)$$

$$M_W = \frac{1}{2}gv = \frac{ev}{2\sin\theta_W} \sim 80 \text{ GeV}/c^2 \quad (2.8)$$

$$M_Z = \frac{1}{2}\sqrt{g^2 + g'^2}v = \frac{ev}{2\sin\theta_W \cos\theta_W} = \frac{M_W}{\cos\theta_W} \sim 90 \text{ GeV}/c^2 \quad (2.9)$$

$$M_\gamma = 0 \quad (2.10)$$

where $\theta_W \equiv \arctan(g'/g)$ is the weak Weinberg angle and $e \equiv g\sin\theta_W$ is the electric charge of the positron. The measured values for the W and Z masses are in excellent agreement with the predictions [27, 26]:

$$M_W = 80.385 \pm 0.015 \text{ GeV}/c^2 \quad (2.11)$$

$$M_Z = 91.1876 \pm 0.0021 \text{ GeV}/c^2 \quad (2.12)$$

²Independently also proposed by Guralnik et al. [21] and Englert & Brout [22].

³This is the case for the so-called minimal model, in non-minimal models such as minimal supersymmetric extensions of the Standard Model (MSSM), there are additional charged and neutral scalar Higgs particles [24, 25]

2.3 Quantum Chromodynamics

With the growing spectrum of hadrons (strongly interacting particles) observed, it became unsatisfactory from the principles of simplicity to regard all the observed particles as elementary in the late 1960's. When looking at the new particles as a function of conserved quantum numbers such as isospin or strangeness, it appeared natural to classify them in analogy to the energy levels of a hydrogen atom. Thus the hadron spectrum can be interpreted as evidence that those particles are indeed composed of more fundamental particles. Hence the observed hadron resonances are excitations of a few ground states. Eventually, this idea led to the quark model: hadrons are formed by smaller constituents, quarks, antiquarks and gluons, collectively known as partons. However, due to the so-called colour confinement, quarks and gluons do not appear as free particles: a quark of specific flavour comes in three colours; gluons come in eight colours; hadrons are colour-singlet combinations of quarks, anti-quarks, and gluons. Evidence of the internal structure of hadrons has come from deep inelastic scattering experiments [28]. Quantum Chromodynamics is the gauge field theory that describes the strong interactions of coloured quarks and gluons. The symmetry group is $SU(3)_C$ and the Lagrangian (up to a gauge fixing term) is written as

$$\begin{aligned}\mathcal{L}_{QCD} = & -\frac{1}{4}G_{\mu\nu}^{(a)}G^{(a)\mu\nu} + i\sum_q \bar{\psi}_q^i \gamma^\mu (D_\mu)_{ij} \psi_q^j \\ & - \sum_q m_q \bar{\psi}_q^i \psi_{qi},\end{aligned}\tag{2.13}$$

$$G_{\mu\nu}^{(a)} = \partial_\mu A_\nu^a - \partial_\nu A_\mu^a - g_s f_{abc} A_\mu^b A_\nu^c,\tag{2.14}$$

$$(D_\mu)_{ij} = \delta_{ij}\partial_\mu + ig_s \sum_a \frac{\lambda_{i,j}^a}{2} A_\mu^a,\tag{2.15}$$

where g_s is the QCD coupling constant, and the f_{abc} are the structure constants of the $SU(3)$ algebra (λ are the Gell-Man matrices [2]). The ψ_q^i are the 4-component Dirac spinors associated with each quark field of colour $i = 1, 2, 3$ and flavour q , and the $A_\mu^a(x)$ with $a = 1\dots 8$ are the Yang-Mills (gluon) fields.

The effective QCD coupling constant α_s is then given by $\alpha_s = g_s^2/4\pi$. α_s is not a fixed term but depends on the energy scale μ , this effect is called the “running” of the coupling constant. So α_s is a function of the energy scale μ and its scale dependence is controlled by the β -function:

$$\begin{aligned}\mu \frac{\partial \alpha_s}{\partial \mu} &= 2\beta(\alpha_s) = -\frac{\beta_0}{2\pi}\alpha_s^2 - \frac{\beta_1}{4\pi^2}\alpha_s^3 - \dots, \\ \beta_0 &= 11 - \frac{2}{3}n_f, \\ \beta_1 &= 51 - \frac{19}{3}n_f\end{aligned}\tag{2.16}$$

where n_f is the number of quarks with mass less than the energy scale μ . In solving this differential equation for α_s , a constant of integration is introduced. This constant is the fundamental constant of QCD that must be determined from experiment (in addition to the quark masses). The most sensible choice for this constant is the value of α_s at a fixed-reference scale μ_0 , for example with the usual choice $\mu_0 = M_Z$ (Fig. 2.2). The third (non-Abelian) term in Eq. 2.14 in which QCD differs from QED, gives rise to triplet and quartic gluon self-interactions and ultimately to *asymptotic freedom* [29], the fact that quarks and gluons can be regarded as quasi-free in collisions with high momentum transfer Q (“hard processes”). Or in other words: $\alpha_s \rightarrow 0$ as $Q \rightarrow \infty$. In this domain, perturbative QCD (pQCD) is the standard tool to perform calculations and thus make predictions. Let us consider a “typical” QCD cross section calculated perturbatively:

$$\sigma = \sum_{i=0} A_i \alpha_s^i \quad (2.17)$$

The coefficients A_i come from calculating the appropriate Feynman diagrams. In performing such calculations, various divergences arise, and these must be regulated in a consistent way. This requires a particular renormalization scheme (RS), the most commonly used one is the modified minimal subtraction \overline{MS} [30]. Physical quantities, such as a cross section calculated to all orders in perturbation theory, do not depend on the RS. On the other hand, truncated series do exhibit RS dependence. In practice, QCD cross sections are known to leading order (LO), or to next-to-leading order (NLO), or in some cases, to next-to-next-to-leading order (NNLO); and it is only the latter two cases, which have reduced RS dependence, that are useful for precision tests.

2.3.1 The Parton Model and the Drell-Yan Process

The parton model pictures hadrons as a collection of point-like quasi-free particles. It describes the cross section for high-energy scattering of hadrons with another particle as an incoherent sum of the cross sections of the point-like partons in the hadron with those the other hadron. The hadronic factors in the cross sections are parametrized by so-called structure functions, which are expressed in terms of *parton distribution functions* (PDFs), the momentum distribution functions of the partons within the hadron. The PDFs represent the probability densities to find a parton carrying a momentum fraction x at a squared energy scale Q^2 .

The “prototype” process for the parton model is lepton-nucleon scattering, i.e. $\ell N \rightarrow \ell' X$, where ℓ and ℓ' are the incident and scattered leptons, N is the target nucleon, and X is the set of final state hadrons (Fig. 2.3). The particles in the final state X are not measured, so the cross section is for the sum over all hadronic final states, an *inclusive* cross section. This contrasts with an *exclusive* cross section in which the final states are restricted to a specific subset. In the prototype process, $\ell N \rightarrow \ell' X$, the kinematics of the inclusive scattering depends on the momentum transfer $q = k - k'$ from the lepton to the hadrons and the invariant mass, W , of the hadronic final state,

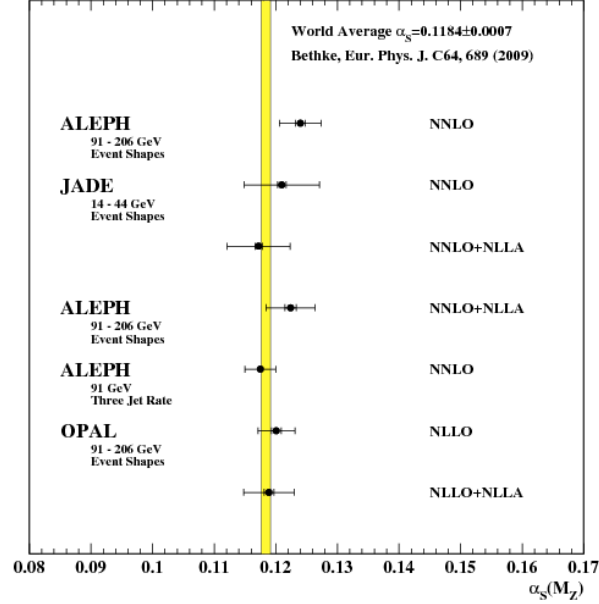


Figure 2.2: Summary of the measured value of $\alpha_s(M_Z)$ determined from event shapes. Hadronic event shape distributions were compared to theoretical predictions based on next-to-next-to-leading-calculations (NNLO) and NNLO combined with resummed next-to-leading-logarithm calculations (NLLA). The values shown indicate the measured value of α_s by the respective experiment, the yellow band indicates the world average of the strong coupling [31].

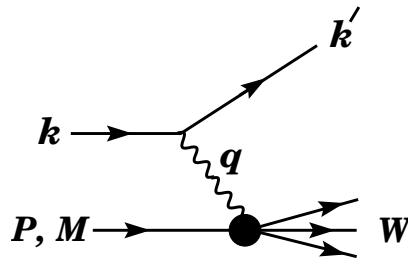


Figure 2.3: Kinematic quantities for the description of deep inelastic scattering. The quantities k and k' are the four-momenta of the incoming and outgoing leptons, P is the four-momentum of a nucleon with mass M , and W is the mass of the recoiling hadronic system X . The exchanged particle is a γ , W^\pm or Z ; it transfers four-momentum $q = k - k'$ to the nucleon. [26]

where $W = (P + q)^2 = M^2 + 2M\nu + q^2$, and M is the mass of the target nucleon or other hadron [32]. k and k' are the energy-momentum 4-vectors of the incident and scattered electron, P is the energy-momentum 4-vector of the target hadron, and $\nu = E - E' = q \cdot P/M$ is the energy transfer to the target hadron in its rest frame or in other words, the energy loss of the scattered lepton.

Bjorken [33, 34] predicted that the hadronic factor in the cross section would depend only on the ratio $x = (-q^2)/(2p \cdot Q) = (-q^2)/(2M\nu)$, rather than on ν and q separately:

$$\frac{d^2\sigma}{dx dQ^2} = \sum_i f_i(x) Q_i^2 \cdot \frac{2\pi\alpha^2}{Q^2} \left[1 + \left(1 - \frac{Q^2}{xs} \right) \right] \quad (2.18)$$

where α is the electromagnetic coupling constant and $Q^2 = -q^2$, and xs is the square of the lepton-nucleon centre of mass energy in terms of the longitudinal fraction of the proton's momentum carried by the parton.

This property, called *scaling*, was expected to hold in the *deep inelastic* limit in which the energy transfer and momentum transfer are much larger than the target hadron mass. Feynman then interpreted scaling in terms of constituents of the nucleon that he called *partons* and the Bjorken x can be identified with the fraction of the longitudinal hadron momentum carried by a given parton. Bjorken scaling implies that during a rapid scattering process, interactions among the constituents of the proton can be ignored. Experimental data on deep inelastic scattering showed that the carriers of electric charge have spin 1/2 and can be identified with quarks. However, sum rules together with data show that the charged partons carry only about 1/2 of the energy-momentum of the nucleon, the other half is carried by gluons:

$$\int_0^1 dx [f_u(x) + f_d(x) + f_{\bar{u}}(x) + f_{\bar{d}}(x) + f_s(x) + f_{\bar{s}}(x) + f_g(x)] x = 1 \quad (2.19)$$

where $f_i(x)$, $i = u, d, \bar{u}, \bar{d}, g$ are the distribution functions for the quarks, antiquarks and gluons in the hadron; contributions of partons heavier than the strange quark are discarded in the above equation. The distribution functions for quarks and antiquarks can be separated into distributions of valence as well as sea quarks (see Fig. 2.4). The *valence quarks* contribute to the quantum numbers of the hadron. Along with the valence quarks, hadrons contain also virtual quark-antiquark pairs ($q\bar{q}$) referred to as *sea quarks*. Sea quarks form when a gluon of the hadron's colour field splits. This process also works in reverse in that the annihilation of two sea quarks produces a gluon. Sea quarks are not stable like their valence counterparts, and they typically annihilate each other within the interior of the hadron. Despite this, sea quarks can hadronize, for instance in high-energy collisions.

Structure functions cannot be calculated in perturbative QCD. In the parton model, structure functions are expressed directly in terms of non-perturbative (quark or gluon) PDFs (Fig. 2.4). The

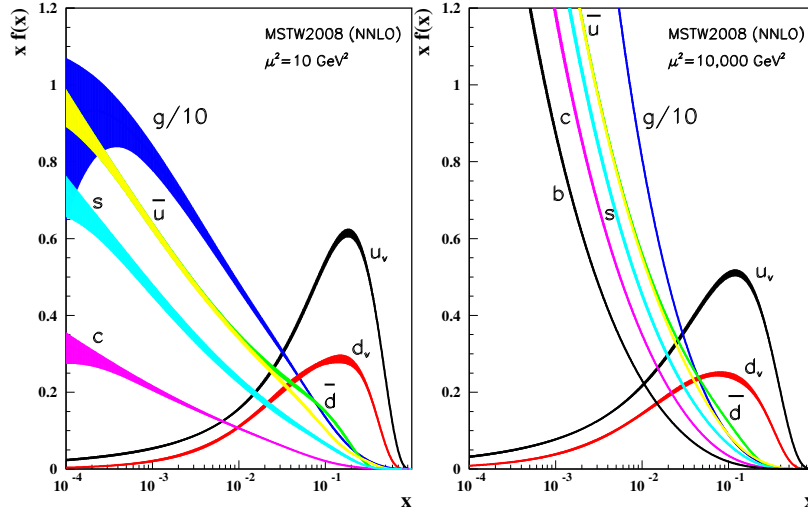


Figure 2.4: Distributions of x times the unpolarized parton distributions $f(x)$ (where $f = u_v, d_v, \bar{u}, \bar{d}, s, c, b, g$) and their associated uncertainties using the NNLO MSTW2008 parameterization [35] at a scale $\mu_2 = 10 \text{ GeV}^2$ and $\mu_2 = 10,000 \text{ GeV}^2$. The valence quarks denoted by a v subscript are more likely to carry a large fraction of the proton's momentum. The gluon distribution (g) is scaled down by a factor 10.

evolution of these PDFs as a function of the energy scale μ is described by the Dokshitzer-Gribov-Lipatov-Altarelli-Parisi (DGLAP) equation [36, 37, 38]. It has the schematic form

$$\frac{\partial f}{\partial \ln \mu^2} = \frac{\alpha_S(\mu^2)}{2\pi} \sum_b (P_{ab} \otimes f_b) \quad (2.20)$$

where f is the PDF and P_{ab} , which describes the parton splitting $b \rightarrow a$, is given as a power series in α_S . Although perturbative QCD can predict the evolution of the parton distribution functions from a particular scale, μ_0 , these DGLAP equations cannot predict them a priori at any particular μ_0 . Thus they must be measured at a starting point μ_0 before the predictions of QCD can be compared to the data at other scales, μ . In general, all observables involving a hard hadronic interaction can be expressed as a convolution of calculable, process-dependent coefficient functions and these universal parton distributions.

The parton model was extended by S. Drell and T.-M. Yan to hadron-hadron scattering, in the form of the Drell-Yan mechanism [39] for the production of lepton pairs. The Drell-Yan process occurs in high energy hadron-hadron scattering when a quark and an antiquark of the participating hadrons annihilate form a virtual photon or Z boson which then decays into a $\ell\bar{\ell}$ pair (Fig. 2.5). Experimentally, it was first observed in 1970 by Christenson et al. [40] at the Alternating Gradient

Synchrotron of the Brookhaven National Laboratory in proton - uranium collisions:

$$p + U \rightarrow \mu^+ \mu^- + X \quad (2.21)$$

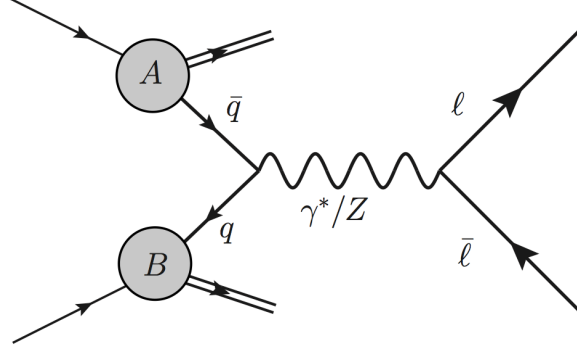


Figure 2.5: *Feynman diagram of the Drell-Yan process at tree-level: a quark and antiquark of hadrons A and B annihilate to form a virtual Z/γ , which then decays into two opposite-charge leptons.*

The cross-section is currently described by perturbative QCD (pQCD) at up to next-to-next-to-leading order (NNLO, including higher-order corrections to tree-level Feynman diagrams) precision with NLO electroweak corrections. With a simple signature suffering from relatively small background contamination, experimental measurements of the cross section therefore provide an excellent testing ground for the predictions of pQCD within the Standard Model. A list of Drell-Yan subprocesses up to $\mathcal{O}(\alpha_S^2)$ can be found in Table 2.2, some of the corresponding Feynman diagrams are shown in Figs. 2.6, 2.7 and 2.8, more diagrams can be found in Ref. [41].

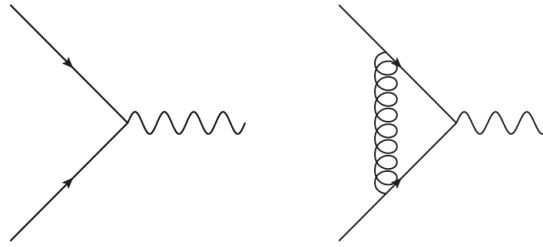


Figure 2.6: *Born contribution and one-loop correction to the subprocess $q + \bar{q} \rightarrow V$ [41].*

Order	Drell-Yan subprocess	
α_S^0	$q + \bar{q} \rightarrow$	V
α_S^1	$q + \bar{q} \rightarrow$	V (one-loop correction)
	$q + \bar{q} \rightarrow$	$V + g$
α_S^2	$(q)\bar{q} + g \rightarrow$	$V + q(\bar{q})$
	$q + \bar{q} \rightarrow$	V (two-loop correction)
	$q + \bar{q} \rightarrow$	$V + g$ (one-loop correction)
	$q + \bar{q} \rightarrow$	$V + g + g$
	$(q)\bar{q} + g \rightarrow$	$V + q(\bar{q})$ (one-loop correction)
	$(q)\bar{q} + g \rightarrow$	$V + q(\bar{q}) + g$
	$q + \bar{q} \rightarrow$	$V + q + \bar{q}$
	$(q)\bar{q} + (q)\bar{q} \rightarrow$	$V + (q)\bar{q} + (q)\bar{q}$
	$g + g \rightarrow$	$V + q + \bar{q}$

Table 2.2: List of Drell-Yan parton subprocesses up to $\mathcal{O}(\alpha_S^2)$, where V is the virtual Z or γ boson [41].

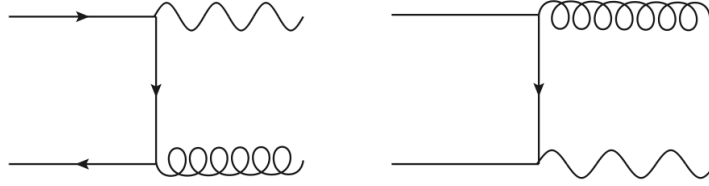


Figure 2.7: Diagrams contributing to the subprocess $q + \bar{q} \rightarrow V + g$. The graphs corresponding to the subprocess $q(\bar{q}) + g \rightarrow V + q(\bar{q})$ can be obtained from those presented in this figure via crossing [41].

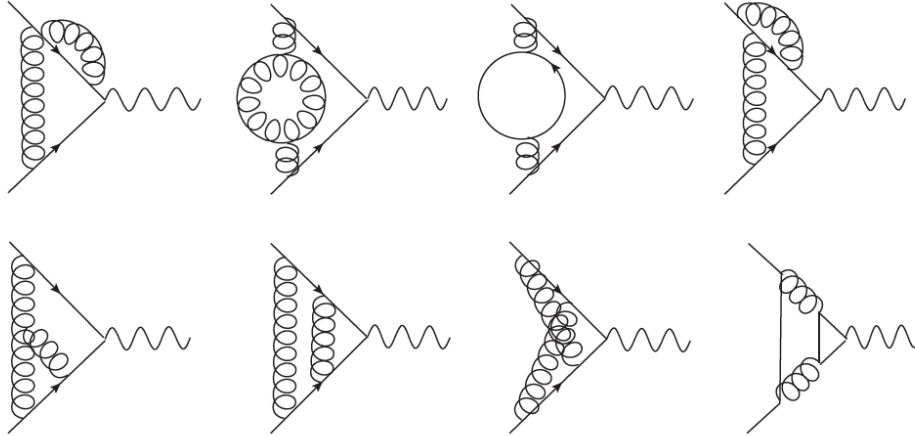


Figure 2.8: Two-loop correction to the subprocess $q + \bar{q} \rightarrow V$ [41].

2.4 Monte-Carlo Generators

General-purpose Monte-Carlo (MC) event generators provide modelling of high-energy collisions. In particular, they play an essential role in modelling QCD processes (especially for aspects beyond fixed-order perturbative QCD). In data analysis they are used together with detector simulation to provide a realistic estimate of the detector response to collision events.

Simulated data can be used to study complex multi-particle physics final states: predict signal event rates and topologies, estimate backgrounds and study detector performance. Event generators are built from several components, that describe the physics starting from very short distance scales, up to the typical scale of hadron formation and decay. MC event generators must thus describe well all ingredients of elementary particle processes: the structure of hadrons, hard scattering (only hard subprocess, no additional partons), parton showers, hadronization (the process by which a set of coloured partons (after showering) is transformed into a set of colour-singlet hadrons, which may then subsequently decay further) as well as multiple parton-parton interactions and beam remnants.

The MC generation of an event involves several stages: it starts with the generation of the kinematics and partonic interactions of the hard scattering process at some high scale Q . This is followed by a parton shower, usually based on the successive random generation of gluon emissions and $g \rightarrow q\bar{q}$ splittings. Each emission is generated at a scale lower than the previous emission, following a (soft and collinear re-summed) perturbative QCD distribution that depends on the momenta of all previous emissions. Common choices of scale for the ordering of emissions are virtuality, transverse momentum or angle. Parton showering stops at a scale of order 1 GeV, at which point a hadronization model is used to convert the resulting partons into hadrons. One widely-used model implemented in the PYTHIA [42] involves stretching a colour “string” across quarks and gluons, and breaking it up into hadrons [43, 44]. Another model breaks each gluon into a $q\bar{q}$ pair and then groups quarks and anti-quarks into colourless “clusters”, which then give the hadrons [45]. For pp processes, modelling is also needed to treat the collision between the two hadron remnants, which generates the so-called *underlying event*, usually implemented via additional $2 \rightarrow 2$ scatterings (*multiple parton interactions*) at a scale of a few GeV.

The parton shower approach (Fig. 2.9) for a collision event reads as: $2 \rightarrow n = (2 \rightarrow 2) \oplus \text{initial state radiation (ISR)} \oplus \text{final state radiation (FSR)}$. $(2 \rightarrow 2)$ indicates the hard scattering part [46], although some event generators include matrix-elements for higher-order hard subprocesses $2 \rightarrow n$. As the parton shower approach underestimates the radiation of hard jets, schemes have been developed for matching with matrix elements for a realistic description of multi-jet backgrounds [47].

Since QCD is weakly interacting at short distances (below a femtometer), the components of the MC generator dealing with short-distance physics are based upon perturbation theory. At larger distances, all soft hadronic phenomena, like hadronization and the formation of the underlying event, cannot be computed from first principles, and one must rely upon QCD-inspired models [26].

Various MC event generator programs use different approximations for the different steps in the

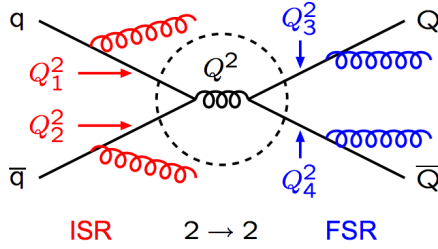


Figure 2.9: The parton shower approach is illustrated: space-like ($Q^2 \sim -m^2 > 0$) parton showers from the incoming quarks are called initial state radiation ISR (red), time-like ($Q^2 \sim m^2 > 0$) parton showers are called final state radiation FSR (blue) from the outgoing hadrons [46]. The parton shower approach indicates collinear and/or soft partons.

calculations and hence the uncertainty on the theoretical predictions rely to some extent on the choice of MC generator. Not all generators provide all steps and some of them must therefore be interfaced with generators that provide the remaining processes for a full MC simulation.

The generators used in this work are as follows:

- **PYTHIA** is a general purpose event generator with emphasis on multi-particle production in collisions between elementary particles, in particular hard interactions in e^-e^+ , pp and ep colliders. Hard scattering processes are calculated in LO approximation, higher order corrections are approximated with a parton shower approach which has limited accuracy for predicting events with higher jet multiplicity. **PYTHIA** can be interfaced with **PHOTOS** [48] for QED final state radiation. [42]
- **HERWIG** is a general purpose event generator similar to **PYTHIA** but with a different modelling for parton showers and the hadronization process. [49]
- **ALPGEN** is a LO event generator with exact matrix element calculation for multi-partonic final states via $2 \rightarrow n$ processes. It is interfaced with **HERWIG** for hadronization simulation and **JIMMY** [50] for the modelling of the underlying event. [51]
- **MC@NLO** is an event generator that includes full NLO calculations of rates for QCD processes during hard scattering. It is useful for precision measurements where LO precision is not sufficient. It is interfaced with **HERWIG** and **JIMMY** which add higher order approximations of the parton shower and the hadronization simulation. [52]
- **SHERPA** is a general purpose event generator for high-energy collision events. It contains a tree-level matrix-element generator for the calculation of hard scattering processes. QCD parton emission off the initial and final states is described through a parton-shower model. The fragmentation of partons into primary hadrons is described using a phenomenological cluster-hadronization model. A simple model of multiple interactions is used to account for the underlying event. [53]

Chapter 3

The ATLAS Experiment at the Large Hadron Collider

3.1 The Large Hardon Collider at CERN

The superconducting Large Hadron Collider (LHC) is currently the highest energy collider and with a circumference of ~ 26.7 km also the biggest particle accelerator in the world. It is situated at CERN (Conseil Européen pour la Recherche Nucléaire) in Switzerland and France and is home to 7 experiments: the two general purpose experiments ATLAS and CMS, ALICE studying heavy ion collisions, LHCb which is dedicated to B physics, LHCf focusing on forward production of neutral particles, MoEDAL, the monopole and exotics physics search detector at the LHC and finally, TOTEM which measures total and diffraction pp cross sections.

The LHC collides bunches of protons and Lead (Pb) ions at a nominal energy of 7 TeV for protons and 2.76 TeV for Pb ions, as well as 7 TeV protons with 2.76 TeV Pb ions. Proton-proton collisions were conducted with 3.5 TeV proton beams in 2010 and 2011 and 4 TeV beams in 2012. The bunches are circulated in two separate beam pipes until they are brought to collision at four interaction points. The beam lines cross at an angle of $300 \mu\text{rad}$ at the centre of the detectors. Nominal and delivered machine performance parameters are given in Table 3.1.

The maximum energy obtainable is a function of the radius of the bending sections of the machine and the strength of the dipole magnetic field that keeps particles on their orbits. The LHC uses some of the most powerful dipoles and radio-frequency (RF) cavities in existence. The size of the tunnel, magnets, cavities and other essential elements of the machine, represent the main constraints that determine the design energy of 7 TeV per proton. The RF cavities generate a longitudinal oscillating voltage, whose frequency is set such that it gives particles an accelerating force as they pass through. Fig. 3.1 shows a schematic of the LHC ring with four interaction points at the large experiments.

	delivered	nominal
Circumference (km)	26.659	
Maximum beam energy (TeV)	4	7
Luminosity ($10^{30} \text{ cm}^{-2} \text{ s}^{-1}$)	5×10^3	1.0×10^4
Time between collisions (ns)	49.90	24.95
Bunch length (cm)	9	7.5
Particles per bunch (units 10^{10})	15	11.5
β^* , amplitude function at interaction point (m)	0.6	0.55

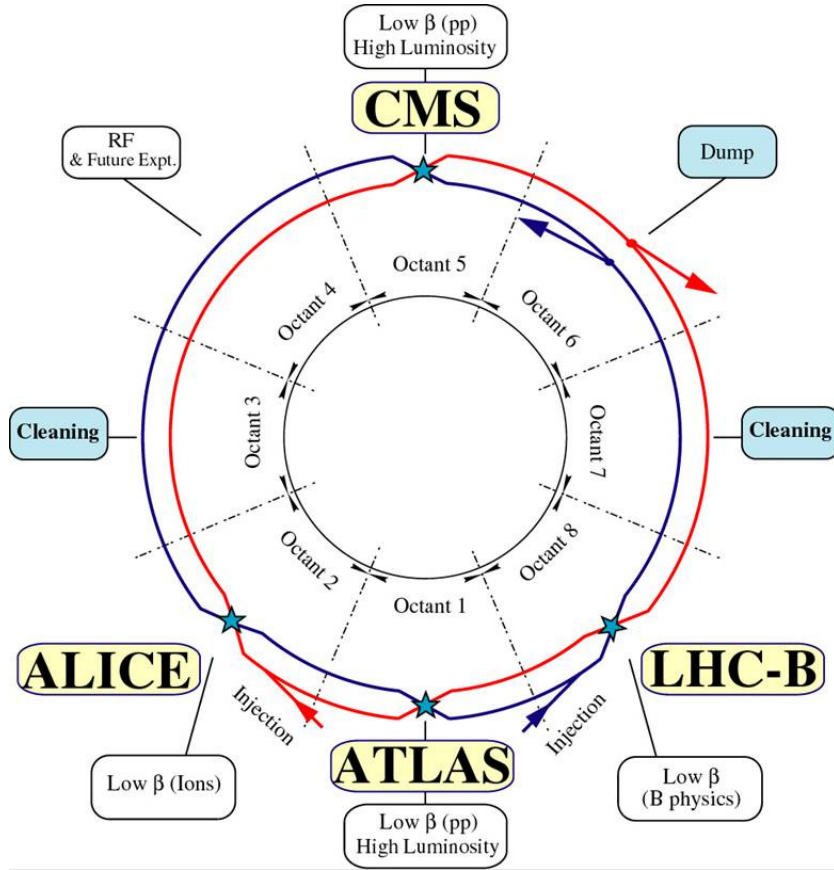
Table 3.1: Delivered performance of the LHC in 2012 and nominal values for pp collisions.

Figure 3.1: Schematic of the LHC ring and the 4 large experiments (ATLAS, CMS - multi-purpose, ALICE - heavy ion physics, LHCb - B physics), beam injection points, beam halo cleaning and beam dump.

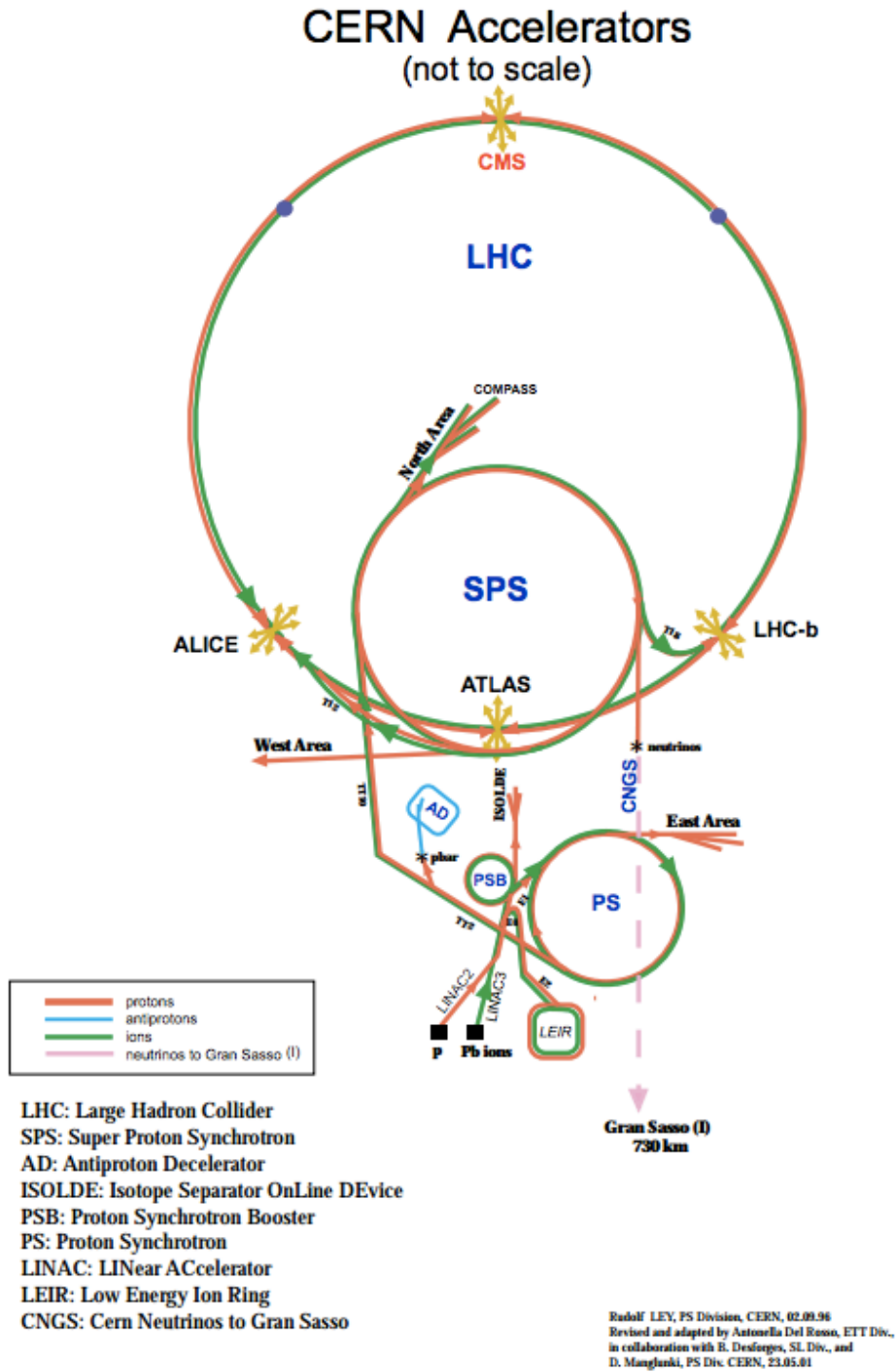


Figure 3.2: The proton lifecycle: the protons are produced and pre-accelerated before injection into the LHC and then collided at the centre of the experiments. [54]

There are two synchrotrons feeding the LHC with particles: the Proton Synchrotron (PS) and the Super Proton Synchrotron (SPS) - Fig. 3.2. In fact, the PS is responsible to ensure the bunch spacing of 25 ns that is eventually circulated in the LHC. Protons are obtained by stripping electrons from hydrogen atoms. Protons are injected into the PS Booster (PSB) at an energy of 50 MeV from Linac2. The Booster accelerates them to 1.4 GeV and the beam is then fed to the Proton Synchrotron (PS) where it is accelerated to 25 GeV. Protons are then sent to the Super Proton Synchrotron (SPS) where they are accelerated to 450 GeV and finally transferred to the LHC (both in a clockwise and an anticlockwise direction, the filling time is 4 min. 20 s per LHC ring) where they are accelerated for 20 minutes to their nominal energy of 7 TeV. Beams circulate for many hours inside the LHC beam pipes under normal operating conditions.

Protons arrive at the LHC in bunches, which are prepared in the PS. Between each consecutive bunch there are 7,5 m. With a circumference of ~ 26.7 km there should be: 26659 divided by 7,5 ~ 3550 bunches, but, to allow a correct sequence of bunches injected into the ring, and to be able to insert new bunches when non-useful ones are extracted, it is necessary to allow additional space. So the number of bunches circulated in the LHC is actually 2808.

3.1.1 Collision Rate and Luminosity

The number of events expected in a collider experiment, N , is the product of the total cross section σ_{exp} times the instantaneous luminosity integrated over time:

$$N = \sigma_{exp} \cdot \int \mathcal{L}(t) dt \quad (3.1)$$

For colliders that employ particle bunches (containing n_1 and n_2 particles colliding with a head-on frequency f) such as the LHC, the expression for the luminosity reads as

$$\mathcal{L} = f \frac{n_1 n_2}{\sigma_x \sigma_y} \quad (3.2)$$

where σ_x and σ_y characterize the root-mean-squared transverse beam sizes in the horizontal and vertical directions. In this simplified formula it is assumed that the bunches are identical in transverse profile, that the profiles are Gaussian and independent of position along the bunch, and the particle distributions are not altered during bunch crossing.

Instantaneous luminosity is usually given in units of $\text{cm}^{-2} \text{s}^{-1}$ while integrated luminosity is rather quoted as the inverse of the standard measures of cross section such as picobarns or femtobarns, where 1 barn corresponds to 10^{-24}cm^2 . The integrated luminosity delivered by the LHC and recorded by the ATLAS experiment is shown in Fig. 3.3(a).

The beam size can be expressed in terms of two quantities: emittance ϵ , and the amplitude function β . Emittance can be regarded as the smallest opening through which the beam can pass

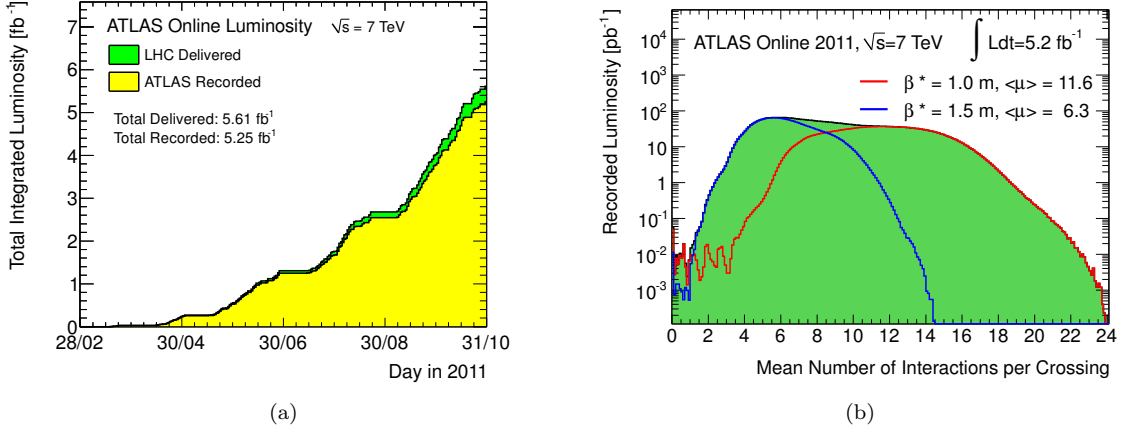


Figure 3.3: (a) Cumulative luminosity versus day delivered to (green), and recorded by ATLAS (yellow) during stable beams and for pp collisions at 7 TeV centre-of-mass energy in 2011 (b) Luminosity-weighted distribution of the mean number of interactions per crossing for 2011 [55].

and can also be considered as a measurement of the parallelism of a beam. In a colliding beam accelerator, keeping the emittance small means that the likelihood of particle interactions will be greater resulting in higher luminosity. The emittance is given in units of length. The amplitude function is then determined by the accelerator magnet configuration and powering. When expressed in terms of the cross-sectional size of the bunch and the transverse emittance, the amplitude function β becomes

$$\beta = \frac{\pi \sigma_x \sigma_y}{\epsilon} \quad (3.3)$$

So, β is roughly the width of the beam squared divided by the emittance. If β is low, the beam is narrower, “squeezed”. If it is high, the beam is wide and straight. β is also expressed in units of length [56].

Then, equation 3.2 can also be rewritten in terms of emittances and amplitude functions as

$$\mathcal{L} = f \frac{n_1 n_2}{4 \sqrt{\epsilon_x \beta_x^* \epsilon_y \beta_y^*}} \quad (3.4)$$

where $\beta_i^* = \beta_i/4\pi$, $i = x, y$ denotes the amplitude function at the interaction point, assuming different values for the x and y plane. β^* is the distance to the IP where the beam cross section is twice the cross section at the IP [54]. A schematic of the beam cross section before and then “squeezed” at the IP is shown in Fig. 3.4.

Even though the bunches get strongly squeezed at the interaction points, the proton “density” in the bunch is still very small and thus the probability for collisions is too. However, due to the huge quantity of protons/bunch, collisions do occur. From simple geometrical considerations, the probability for a pp collision can be estimated as given by the proton size (d_{proton}^2 with $d_{\text{proton}} \sim 1$ fm)

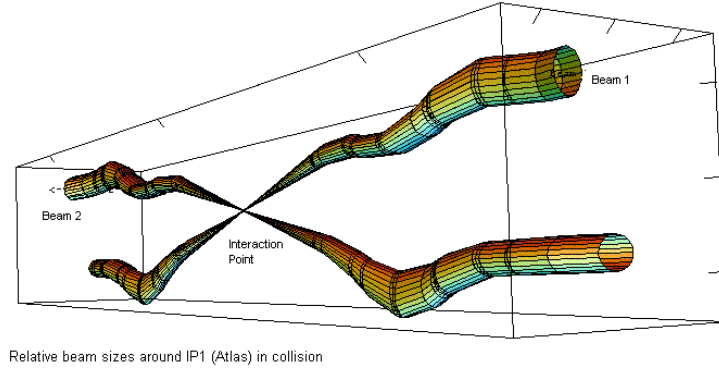


Figure 3.4: *Schematic of the relative beam cross sections close to the interaction point of ATLAS.*

and the cross-sectional size of the bunch (σ^2 , with $\sigma = 16 \mu\text{m}$) at the interaction point:

$$P(\text{collision}) \approx d_{\text{proton}}^2 \cdot \sigma^2 = 10^{-21} \quad (3.5)$$

Now with $\sim 10^{11}$ protons/bunch, the approximate number of collisions is then $P(\text{collision}) \times$ the (number of protons/bunch) 2 : $4 \cdot 10^{-21} \times (10^{11})^2 = 40$ collisions/bunch crossing. In reality, not all of those are inelastic scatterings that give rise to particles at sufficient high angles with respect to the beam axis (a “primary vertex” in the reconstructed event). The number of *effective* collisions per bunch crossing is roughly 20. This feature of multiple pp collisions in one event is referred to as “pile-up” (Fig. 3.3(b)).

3.2 The ATLAS Experiment

The ATLAS (**A** Toroidal **LHC** Apparatu**S**) Experiment is an “multi-purpose” detector, meaning it was designed and built for high-precision measurements of Standard Model processes as well as searches of new particles predicted by Beyond-Standard-Model theories. It has a cylindrical layout, measures 44 m in length, has a diameter of 25 m (Fig. 3.5) and weighs approximately 7000 t. It is placed in a cavern about 100 m underground at Point 1 of the LHC. The coordinate system is defined in the cavern as follows: The beam direction defines the z -axis and the $x-y$ plane is transverse to the beam direction. The positive x -axis is defined as pointing from the interaction point to the centre of the LHC ring and the positive y -axis points upwards. The side-A of the detector is defined as that with positive z and side-C is that with negative z . The azimuthal angle ϕ is measured around the beam axis from x to y , and the polar angle θ is the angle from the beam axis. The pseudorapidity is defined as $\eta = -\ln(\tan(\theta/2))$ and the transverse momentum and energy are defined as $p_T = p \sin \theta$ and $E_T = E \sin \theta$, respectively. The distance ΔR in the pseudorapidity-azimuthal angle space is

defined as $\Delta R = \sqrt{\Delta\eta^2 + \Delta\phi^2}$.

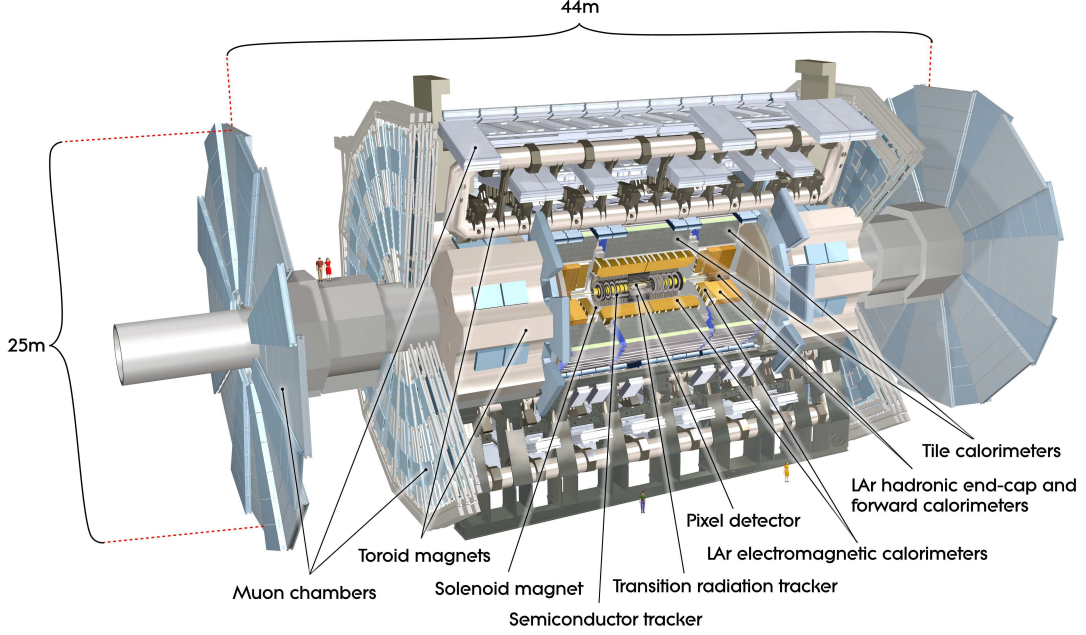


Figure 3.5: *The ATLAS Detector and its layered design consisting of several sub-detector systems.*

The basic guidelines of the detector design include the following [57]:

- Very good electromagnetic calorimetry for electron and photon identification and measurements, complemented by full-coverage hadronic calorimetry for accurate jet and the missing transverse energy E_T^{miss} measurement.
- High-precision muon momentum measurements, with the capability to guarantee accurate measurements at the highest luminosity using the external muon spectrometer alone.
- Efficient tracking at high luminosity for high- p_T lepton-momentum measurements, electron and photon identification, τ -lepton and heavy-flavour identification.
- Large acceptance in pseudorapidity (η) with almost full azimuthal angle (ϕ) coverage.
- Triggering and measurements of particles at low- p_T thresholds, providing high efficiencies for most physics processes of interest at LHC (such as Higgs boson searches).

3.2.1 The Detector Subsystems

The ATLAS Detector consists of several sub-detector systems, they are described below.

Inner Detector

The Inner Detector (Fig. 3.6) which serves the reconstruction of charged particle tracks within a pseudorapidity range of $|\eta| < 2.47$, is placed closest to the beam pipe and immersed in a 2 T magnetic field generated by a solenoid magnet. It is made of three sub-detectors: The pixel detector consisting of three layers is the closest to the beam pipe. It provides three precision measurements over the full coverage, and mostly determine the track impact parameter resolution and the ability to identify short-lived particles. The Pixel detector is followed by four layers of stereo pairs of silicon microstrips (Semiconductor Tracker SCT) which provide eight hits per track at intermediate radius, contributing to the measurement of momentum, impact parameter and vertex position, as well as providing good pattern recognition by the use of high granularity. The transition radiation tracker (TRT) is made of layers of gaseous straw tubes. Electron identification capability is added by employing Xenon gas to detect transition-radiation photons created in a radiator between the straws. This technique is intrinsically radiation hard, and allows a large number of measurements, typically 36, to be made on every track. However, the detector must cope with a large occupancy and high counting rates at the LHC design luminosity. [58].

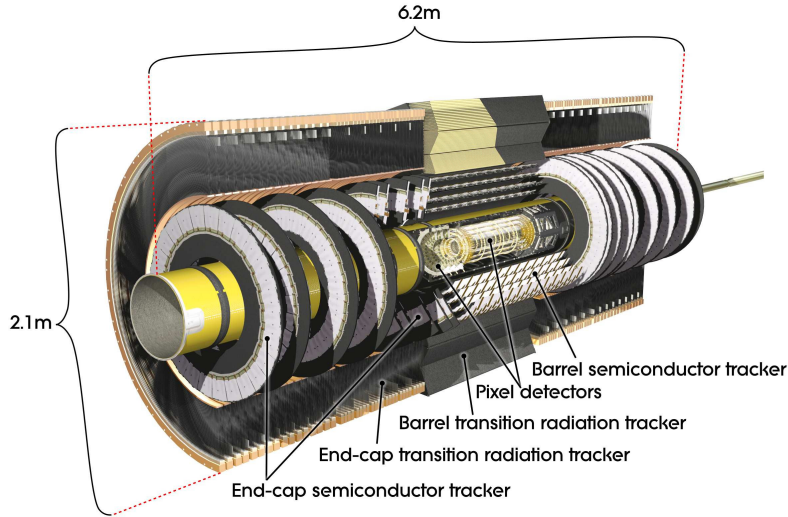


Figure 3.6: (a) The Inner Detector with its 3 sub-detectors: Pixel, Semiconductor Tracker (SCT) and Transition Radiation Tracker (TRT).

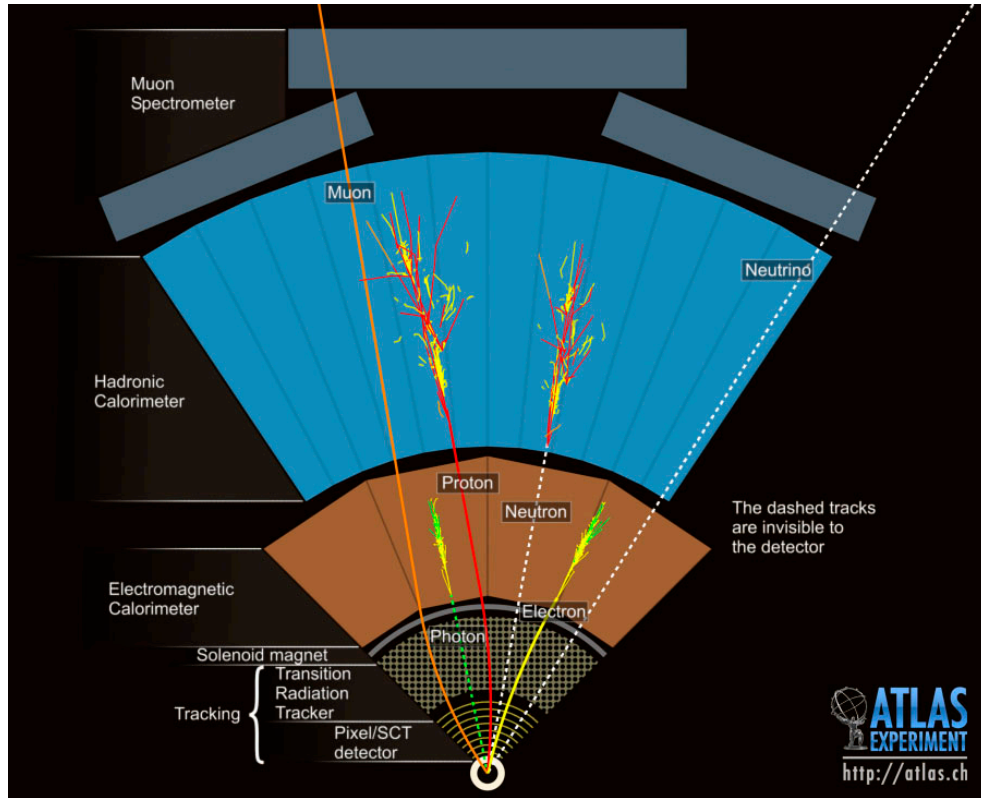


Figure 3.7: *Particle detection and identification in ATLAS: different types of particles passing through the layers of the detector and leaving a characteristic signal. Only neutrinos escape without being directly seen in the detector - they are indirectly detected as missing energy (E_T^{miss}).*

Electromagnetic Calorimeter

The electromagnetic (EM) calorimeter (Fig. 3.8, see also sections 3.3.1 and 3.3.2) is a liquid Argon (LAr) detector with accordion-shaped Kapton electrodes and lead absorber plates that provides a full ϕ coverage without any cracks. The lead thickness in the absorber plates has been optimised as a function of η in terms of EM calorimeter energy resolution. The EM calorimeter is divided into three layers: strip, middle and back. In the central region of $|\eta| < 2.47$ the first layer of the EM calorimeter consists of fine-grained strips in the η -direction (with a coarser granularity in ϕ), which offer excellent $\gamma - \pi^0$ discrimination. At high energy, most of the EM shower energy is collected in the second layer which has a lateral granularity of 0.025×0.025 in $\eta \times \phi$ space. In the range $|\eta| < 1.8$, these two layers are complemented by a presampler layer placed in front with coarse granularity to correct for energy lost in the material before the calorimeter. Finally, a back layer enables a correction to be made for the tail of very high energy EM showers.

Along η , the central part of the calorimeter is composed of two half-barrels, centered around the z axis and covering a pseudorapidity range of $|\eta| < 1.37$. The outer part of the EM calorimeter (end-caps) is made of two wheels on each side of the electromagnetic barrel. The inner and the outer end-cap wheels cover the ranges of $1.375 < |\eta| < 2.5$ and $2.5 < |\eta| < 3.2$, respectively. The transition region between the barrel and the end-cap calorimeters ($1.37 < |\eta| < 1.52$) has a larger amount of inactive material in front of the first active calorimeter layer, therefore it needs more attention to reach the design performance. The EM calorimeter is preceded by a presampler detector over the pseudorapidity range $|\eta| < 1.8$, installed immediately behind the cryostat cold wall, and used to correct for the energy lost in the material (ID, cryostats, coil) upstream of the calorimeter. A module of the EM calorimeter of the barrel region is shown in Fig. 3.9, where also the granularity of the three layers as well as the presampler and trigger towers are depicted.

Hadronic Calorimeter

The hadronic barrel calorimeter is a cylinder divided into three sections: the central barrel and two identical extended barrels. It is based on a sampling technique with plastic scintillator plates (tiles) embedded in an iron absorber. At larger pseudorapidities, where higher radiation resistance is needed, the intrinsically radiation-hard LAr technology is used for all the calorimeters: the hadronic end-cap calorimeter, a copper LAr detector with parallel-plate geometry, and the forward calorimeter, a dense LAr calorimeter with rod-shaped electrodes in a tungsten matrix. An important parameter in the design of the hadronic calorimeter is its thickness: it has to provide good containment for hadronic showers and reduce punch-through into the muon system to a minimum.

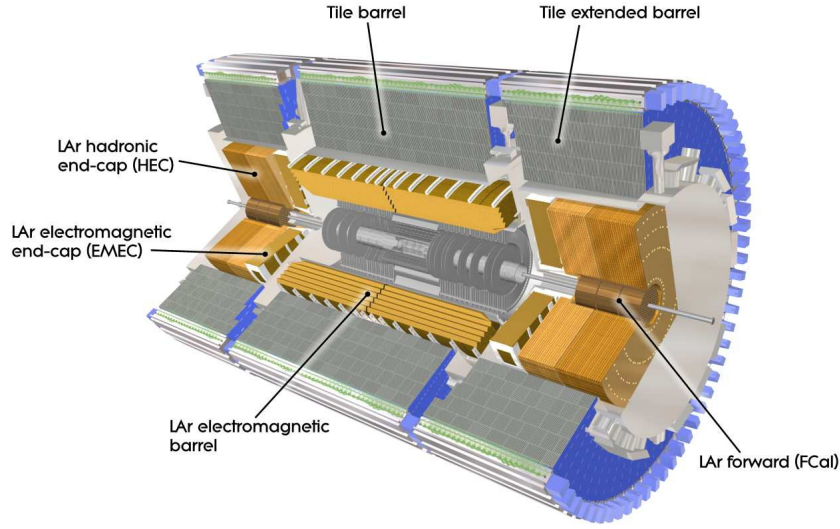


Figure 3.8: The ATLAS Calorimeter system consisting of the liquid Argon (LAr) electromagnetic calorimeter and the Tile hadronic calorimeter.

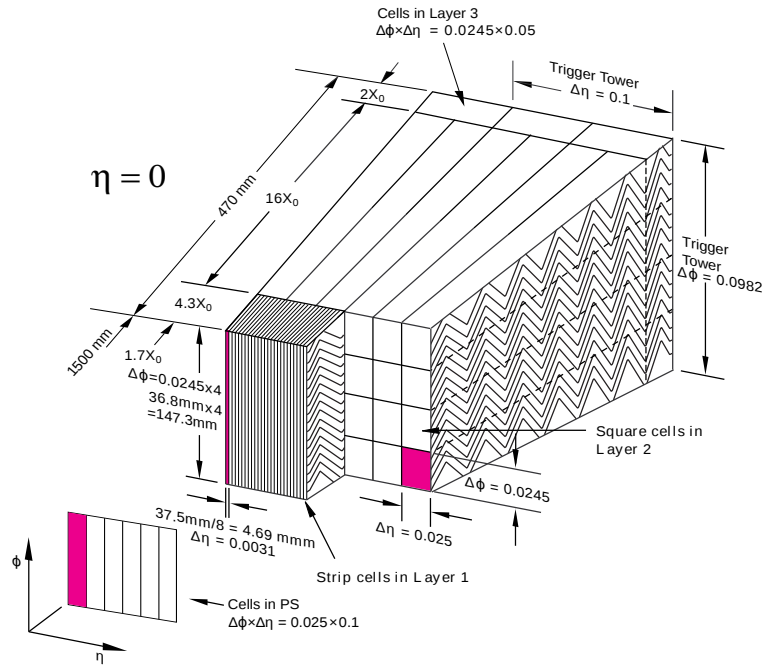


Figure 3.9: Sketch of a barrel module of the Electromagnetic Calorimeter in ATLAS. The accordion structure with the ganging of electrodes in ϕ is illustrated for the different layers. The granularity in η and ϕ of the cells of the three layers and the presampler, together with that of the trigger towers is also displayed.

Muon Spectrometer

The concept of the Muon Spectrometer is based on the magnetic deflection of muon tracks in the large superconducting air-core toroid magnets, instrumented with separate trigger and high-precision tracking chambers. Over most of the η -range, a precision measurement of the track coordinates in the principal bending direction of the magnetic field is provided by Monitored Drift Tubes (MDTs). At large pseudorapidities and close to the interaction point, Cathode Strip Chambers (CSCs) with higher granularity are used in the innermost plane over $2 < |\eta| < 2.7$, to withstand the more demanding rate and background conditions. Trigger and reconstruction algorithms have been optimised to cope with these difficult background conditions resulting from penetrating primary collision products and from radiation backgrounds, mostly neutrons and photons in the 1 MeV range, produced from secondary interactions in the calorimeters, shielding material, beam pipe and LHC machine elements. The muon trigger system covers the pseudorapidity range $|\eta| \leq 2.4$. Resistive Plate Chambers (RPCs) are used in the barrel and Thin Gap Chambers (TGCs) in the end-cap regions.

Magnet System

The ATLAS superconducting magnet system consists of a central solenoid (CS) providing the Inner Detector with magnetic field, surrounded by a system of three large air-core toroids generating the magnetic field for the muon spectrometer. The two end-cap toroids are inserted in the barrel toroid at each end and line up with the CS. The CS provides a central field of 2 T with a peak magnetic field of 2.6 T at the surface of the superconductor itself. The peak magnetic fields on the superconductors in the Barrel Toroid and End-Cap Toroid are 3.9 and 4.1 T, respectively. The barrel toroid provides 2 to 6 Tm and the end-cap toroid contributes with 4 to 8 Tm in the 0.0-1.3 and 1.6-2.7 pseudorapidity ranges respectively. The bending power is lower in the transition regions where the two magnets overlap ($1.3 < |\eta| < 1.6$). The position of the CS in front of the EM calorimeter demands a careful minimisation of the material in order to reach the desired calorimeter performance. A schematic of the material distribution in the detector in units of radiation length X_0 is shown in Fig. 3.10.

3.2.2 Trigger and Data Acquisition

The main challenges at the LHC that have an impact on the trigger system are an unprecedented interaction rate of $\sim 10^9$ interactions per second, the need to select rare physics processes with high efficiency while rejecting much higher-rate background processes, and large and complex detectors with huge numbers of channels $\mathcal{O}(10^7)$. Decisions must be taken every 50 ns (25 ns at nominal performance), at the bunch-crossing rate of 20 (40) MHz. Already in 2011, not yet at design luminosity, each bunch crossing contained many primary interactions (“pile-up”). At the end of the decision chain the event storage rate is limited to approximately 300-400 Hz, by practical limitations in the

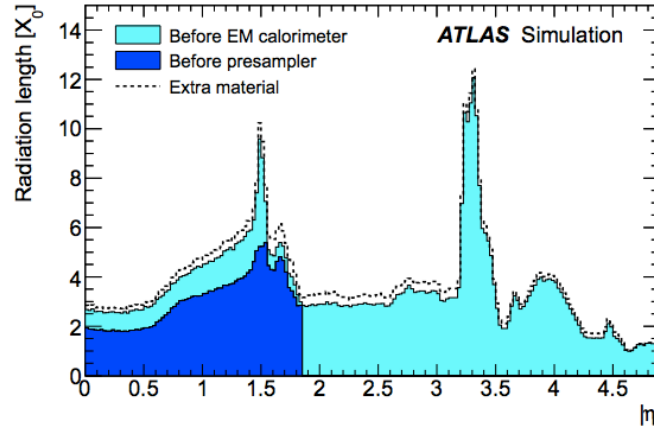


Figure 3.10: *Material distribution as a function of η in units of radiation length X_0 traversed by a particle before the EM calorimeter and the pre-sampler.*

offline computing power and storage capabilities. The average event size is of the order of 1.5 MB.

The ATLAS Trigger operates on three levels, where each level significantly reduces the number of accepted events: Level 1 (LVL1), Level 2 (LVL2) and Event Filter (EF) (Fig. 3.11). The LVL1 is a hardware trigger based on coarse calorimeter and muon information and has a latency of $2\mu\text{s}$. It is designed to receive data at the full LHC bunch-crossing rate of 40 MHz. The output rate is limited by the capabilities of the front-end systems to 75 - 100 kHz. LVL2 is a software trigger with a the latency to make the trigger decision of $\sim 40\text{ ms}$. At LVL1, the full event granularity is available within a Region of Interest (RoI). RoI's are identified by the η and ϕ directions of the LVL1 trigger objects as well as a the transverse momentum thresholds that have been passed. Only event data in regions around η and ϕ flagged by LVL1 as interesting regions with electromagnetic (electrons or photons), tau, jet or muon candidates is unpacked from the read-out buffer in the data preparation. The advantage of this concept is that only 1-4% of the data volume is unpacked and analyzed, saving time especially for the reconstruction algorithms. LVL2 provides a reduction of a factor of about 100 resulting in an input rate to the EF of the order of $\sim 1\text{ kHz}$. The Event Filter works in a similar way to LVL2, however, its latency is $\sim 4\text{ s}$ for making the trigger decision. At this level the offline reconstruction algorithms are used.

Combining LVL2 and the EF gives a reduction factor of order 10^3 and are together called the High Level Trigger [59]. The available trigger signatures are Minimum Bias, Jet, Tau, Missing ET, Muon, B Physics, Bjet and EGamma. Each signature contains several trigger chains which are configurations of the reconstructed trigger objects. So-called pre-scale factors can be applied to certain trigger chains to reduce the number of accepted events. Typical trigger stream rates and sizes are displayed in Figs. 3.12(a) and 3.12(b). For completeness, the performance of the detector and trigger subsystems in 2011 is given in Table 3.2.

The trigger streams used in this work are *EGamma* for the Drell-Yan cross section measurement (Section 4.5.2) and *Minimum Bias* for the beam pipe stability study (Section 3.4.1).

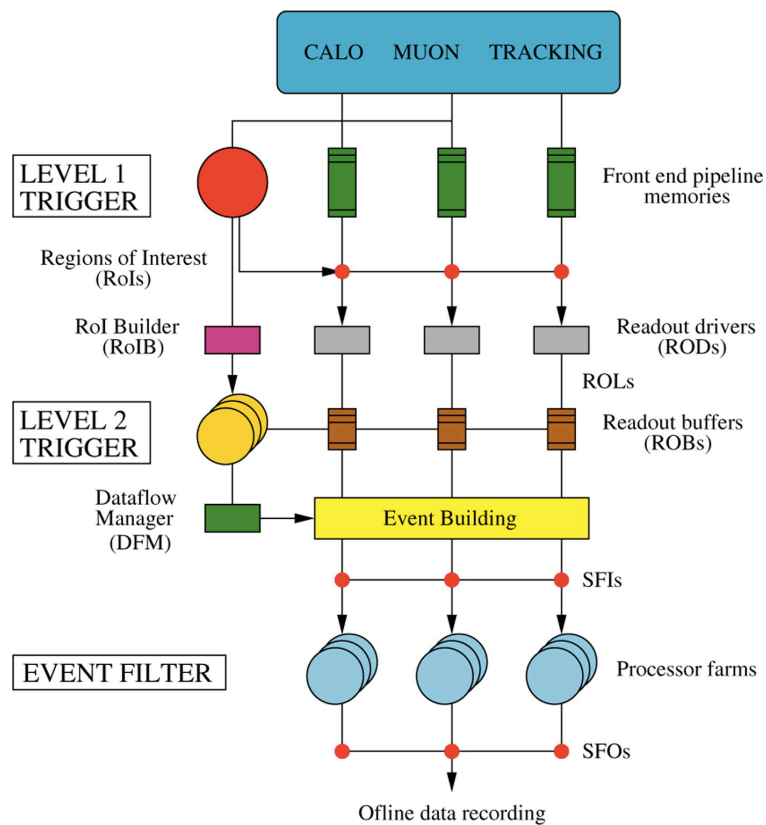


Figure 3.11: Schematic overview of the ATLAS Trigger and Data Acquisition (DAQ) system [60].

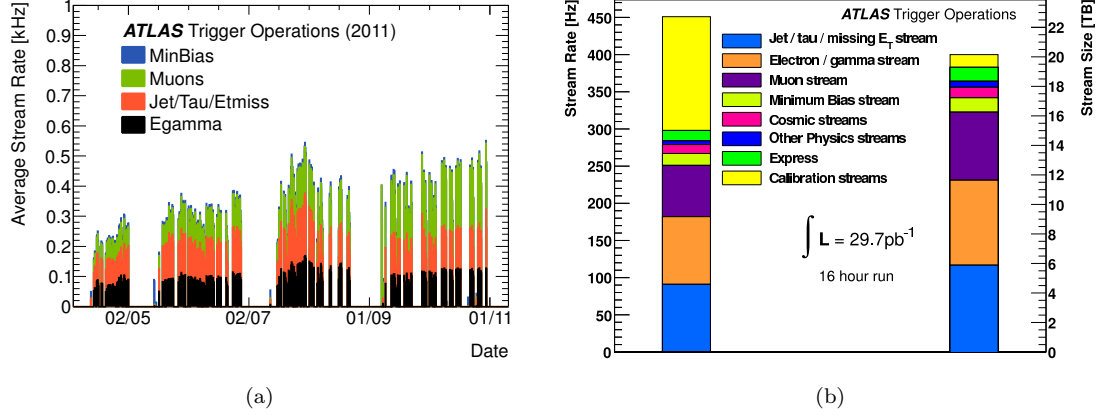


Figure 3.12: Trigger stream and rate sizes in 2011: 3.12(a) average stream rate per day over the full 2011 pp collision period. 3.12(b) shows the rate per stream and data volume per stream (stream size) for one run.

Subdetector	Number of Channels	Operational Fraction
Pixels	80 M	96.4%
SCT Silicon Strips	6.3 M	99.2%
Transition Radiation Tracker (TRT)	350 k	97.5%
LAr EM Calorimeter	170 k	99.8%
Tile Calorimeter	9800	96.2%
Hadronic End-Cap LAr Calorimeter	5600	99.6%
Forward End-Cap LAr Calorimeter	3500	99.8%
LVL1 Calo Trigger	7160	99.9%
LVL1 Muon RPC Trigger	370 k	99.0%
LVL1 Muon TGC Trigger	320 k	100%
Muon Drift Tubes (MDT)	350 k	99.7%
Cathode Strip Chambers (CSC)	31 k	97.7%
RPC Barrel Muon Chambers	370 k	97.0%
TGC End-Cap Muon Chambers	320 k	97.9%

Table 3.2: ATLAS Detector Status 2011 [61].

3.3 Electrons in ATLAS

Electrons are produced in many Standard Model and hypothetical exotic processes and thus a good knowledge of the performance including the efficiency of reconstructing and identifying an electron as such in the detector is necessary. In hadron colliders one has to deal with a large hadronic activity produced in the collision event. Hadronic jets can fake the signal of an electron in the detector and thus constitute an important background for electron final states.

The electron reconstruction and identification algorithms used in ATLAS are designed to achieve both a large background rejection and a high and uniform efficiency over the full acceptance of the detector. Isolated electrons (electrons having little track and calorimeter activity nearby) need to be separated from hadrons in jets, from background electrons (originating mostly from photon conversions in the tracker material), and from non-isolated electrons from heavy flavour decays using identification and isolation cuts.

A detailed description of the electron performance of the ATLAS detector, can be found in Ref. [62, 63].

3.3.1 Reconstruction

The ATLAS electromagnetic (EM) calorimeter has a fine segmentation in both the lateral ($\eta \times \phi$ space) and the longitudinal directions of the particle shower (Fig. 3.9). As a brief reminder, pseudorapidity η is defined as $\eta = -\ln [\tan(\theta/2)]$, where the polar angle θ is measured with respect to the LHC beamline. The azimuthal angle ϕ is measured with respect to the x-axis, which points towards the center of the LHC. The z-axis is parallel to the anti-clockwise beam viewed from above.

The standard electron reconstruction procedure is based on clusters reconstructed in the EM calorimeter, which then are associated to tracks of charged particles reconstructed in the Inner Detector. Information from both detectors is used to allow electrons to be identified with the lowest possible amount of background, keeping in mind that the optimum between the identification efficiency and background rejection depends on the analysis.

Electron reconstruction begins with the creation of a preliminary set of seed clusters. Seed clusters with energies above 2.5 GeV are formed by a sliding window algorithm, where the seed cluster size is $\Delta\eta \times \Delta\phi = 3 \times 5$ in middle layer cell units (0.025×0.025). After an energy comparison, duplicate clusters are removed from nearby seed clusters. An electron is defined by the existence of one or more reconstructed tracks matched to the seed cluster. The track-to-cluster matching thus forms the central part of the electron reconstruction. Reconstructed tracks are matched to seed clusters by extrapolating them from their last measurement point to the second layer of the calorimeter. The impact point η and ϕ coordinates of the extrapolated track are then compared to the corresponding seed cluster η and ϕ in that layer. If their difference is below a certain threshold (0.2 in η , 0.1 in ϕ) then the track is considered matched to the cluster. Special care is taken in order

to account for Bremsstrahlung losses: the $\Delta\phi$ window is larger on the side where the extrapolated track bends as it traverses the tracker magnetic field. In the case of tracks that do not contain silicon hits, the matching is restricted to the ϕ coordinate, due to the fact that the accuracy on the η coordinate, as measured by the TRT, is limited. It can happen that more than one track matches the same seed cluster. In this case all the tracks are retained and ordered according to the quality of their match. The track with the smallest difference $\Delta R = \sqrt{\Delta\eta^2 + \Delta\phi^2}$ between its impact point on the second calorimeter layer and the seed cluster position is considered as the best match. Tracks with silicon hits have priority over tracks without silicon hits, since the latter are more likely to be attributed to photon conversions. The information related to the track-to-cluster matching is retained for all the tracks assigned to the reconstructed electron object and the best matched track is used during the particle identification described in Section 3.3.2.

Electromagnetic showers characterized by tracks matched to the seed cluster are considered as electron candidates. The electromagnetic cluster is then recomputed using a $\Delta\eta \times \Delta\phi = 3 \times 7$ (5×5) sliding window in middle layer cell units in the barrel (end-caps). A 3×5 seed cluster size is explicitly chosen to be a subset of the final electromagnetic cluster sizes. Several corrections to the reconstructed cluster energy are then applied. Finally, the electron four-momentum is computed using also the track information from the best track matched to the original seed cluster. The energy is taken as the cluster energy. The ϕ and η directions are taken from the corresponding track parameters unless the track contains no silicon hits, in which case η is provided by the cluster η .

There is an inherent ambiguity between a prompt electron and a converted photon, since both objects are characterized by the existence of tracks pointing to an electromagnetic cluster. In the current reconstruction strategy, objects that have tracks matched to seed clusters will subsequently be treated as electrons. As a result, almost all converted photons will be handled as electrons during this stage of the reconstruction and end up in the electron container. This results in a significant contamination of the electron sample by converted photons but ensures on the other hand a high electron reconstruction efficiency. The particle identification criteria, described later in Section 3.3.2, select prompt electrons from the original electron candidate sample.

The quality of the reconstructed energy of an electron object relies on the conditions of the EM calorimeter. Three types of problems may arise during data taking that needed to be accounted for at the analysis level [62]:

- Failures of electronic front-end boards (FEBs). A few percent of the cells are not read out because they are connected to non-functioning FEBs (see Tables A.1 and A.2 in the appendix). As this can have an important impact on the energy reconstruction in the EM calorimeter, the electron is rejected if part of the cluster falls into a dead FEB region in the EM calorimeter strip or middle layer. If the dead region is in the back layer or in the presampler detector, which in general contain only a small fraction of the energy of the shower, the object is considered good and an energy correction is provided at the reconstruction level.

- High voltage (HV) problems. Sometimes the HV sectors are operated under non-nominal high voltage, or have a zero voltage on one side of the readout electrode. In the very rare case when a part of the cluster falls into a dead high-voltage region, the cluster is rejected. Non-nominal voltage conditions increase the equivalent noise in energy but do not require special treatment for the energy reconstruction.
- Isolated cells producing a high noise signal or no signal at all. These cells are masked at the reconstruction level, so that their energy is set to the average of the neighbouring cells. Nonetheless an electron is rejected, if any of the cells in its core, defined as the 3×3 cells in the middle layer, is masked.

These requirements are also applied to the MC samples when performing comparisons with data.

Electron Energy Scale

The EM calorimeter energy scale was derived from test-beam measurements. The energy scale of the electron was subsequently evaluated in-situ by constraining the di-electron invariant mass to the well-known Z peak lineshape [64, 65].

The correction factors α_i are defined as

$$E_{\text{rescale}} = \frac{E}{1 + \alpha_i} \quad (3.6)$$

where E is the measured energy, E_{rescale} is the true energy. α_i are then the residual miscalibration for a given bin i determined by a log-likelihood fit [62]. The results for 2011 are given in Fig. 3.13. The variation of the energy scale correction within a given calorimeter component is due to several effects related to electronic calibration, high voltage correction, additional material in front of the calorimeter, differences in the calorimeter and pre-sampler energy scales, and differences in lateral leakage between data and Monte-Carlo.

The fractional energy resolution in the EM calorimeter is determined by

$$\frac{\sigma_E}{E} = \frac{a}{\sqrt{E}} \oplus \frac{b}{E} \oplus c \quad (3.7)$$

where a is the sampling term, b is the noise term and c is the constant term [58, 66]. Since Monte-Carlo does not reproduce the energy resolution perfectly, a smearing of the Z distribution to match the data is applied to account for this discrepancy.

3.3.2 Identification

An excellent particle identification capability is essential at the LHC. Especially final states with small branching ratios and high backgrounds need powerful and efficient electron identification to

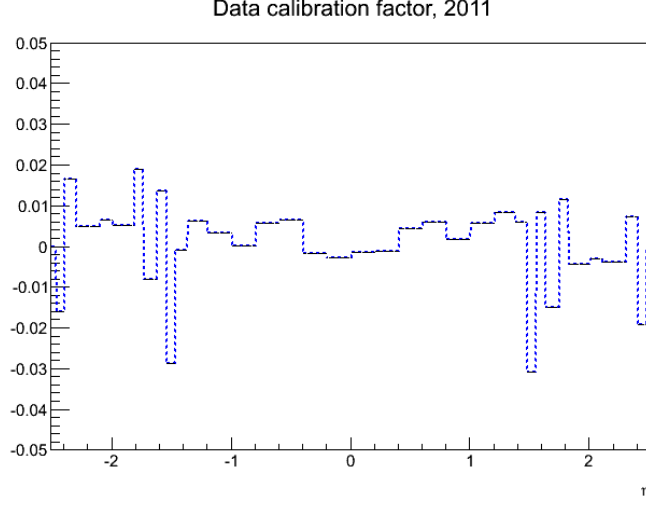


Figure 3.13: *Energy scale correction factors in 2011 as a function of pseudorapidity η .*

observe a signal. Electron identification in ATLAS relies on cuts using variables that provide good separation between isolated electrons and jets (faking electrons) and variables to discriminate against photon conversions. These include calorimeter, tracker and combined calorimeter/tracker information.

Calorimeter cluster-based identification uses variables from the first (strip) and middle layer of the EM calorimeter where electromagnetic showers deposit most of their energy.

Variables from the strip layer are:

- E_{ratio} is the ratio of the energy difference between the largest and second largest energy deposits in the cluster over the sum of these energies and discriminates against jets with π^0 decays ($\pi^0 \rightarrow \gamma\gamma$) that give two maxima in the EM calorimeter.
- w_{tot} is the total shower width determined in a window corresponding to the cluster size (a maximum of $\Delta\eta \times \Delta\phi = 0.0625 \times \sim 0.2$, corresponding typically to 40 strips in η).
- f_{side} is the shower shape in the shower core: $[E(\pm 3) - E(\pm 1)]/E(\pm 1)$, where $E(\pm n)$ is the energy in $\pm n$ strips around the strip with highest energy (Fig. 3.14(a)). This variable allows discrimination between electrons and hadronic jets at a value of ~ 0.55 , as used in Section 4.5.3.

Variables from the middle layer of the EM Calorimeter are:

- R_η is the lateral shower shape defined as the ratio of the uncalibrated energy (sum of cell energies) in a window of size $\Delta\eta \times \Delta\phi = 3 \times 7$ cells over the energy in a window of 7×7 .
- R_ϕ is the ratio between the uncalibrated energy (sum of cells) in a window of size $\Delta\eta \times \Delta\phi = 3 \times 3$ and the uncalibrated energy in a window of size 3×7 . R_ϕ has potential to discriminate

against hadronic background at a value of 0.9, see Fig. 3.14(c).

- $w_{\eta 2}$ is the lateral width of the shower in the second EM Calorimeter layer.

In addition, except in the region $0.8 < |\eta| < 1.37$, the two calorimeter variables hadronic leakage R_{had} and R_{had1} are defined as the ratio of the energy deposit in a certain part of the hadronic calorimeter divided by the energy deposit in the EM calorimeter:

- R_{had1} is the cluster E_T in the first layer of the hadronic calorimeter divided by the cluster E_T in the EM calorimeter
- R_{had} is the cluster E_T in the hadronic calorimeter divided by the cluster E_T in the EM calorimeter

Cuts on the EM cluster variables greatly reduce background from charged hadrons. The remaining background is dominated by photon conversion and low multiplicity jets containing high- p_T π^0 's. This is further reduced by track quality cuts as well as cuts on track matching variables and the energy-momentum ratio. Track-based identification variables are:

- $n_{\text{Pixel}}, n_{\text{Si}}$ are number of hits in the Pixel and SCT.
- d_0 is the track transverse impact parameter.
- $\Delta\eta, \Delta\phi$ are angular variables for best calorimeter cluster-track match to measure the track-cluster distance in ΔR .
- E/p : ratio of calorimeter cluster energy over track momentum measured in the Inner Detector (as in the case of electrons - unlike other particles- this ratio is close to 1).
- n_{TRT} is the number of total hits in the TRT.
- f_{HT} is the fraction of high threshold hits to the total number of hits in the TRT to discriminate against hadrons (Fig. 3.14(d)).
- n_{BL} is the number of hits in the innermost Pixel layer, called the B-Layer. It discriminates against electrons originating from photon conversions.

A full summary of the variables used for the different ID levels is presented in Table 3.3.

Definitions of *Loose*, *Medium* and *Tight* Electron Identification Levels

In 2011, three reference sets of cuts to be used in data analyses were defined with an expected jet rejection of about 500, 5000 and 50000, respectively: *Loose*, *Medium* and *Tight*. The work reported in Section 4.5 focuses on the measurement of the identification efficiency for *Medium* selection for the Drell-Yan cross section measurement.

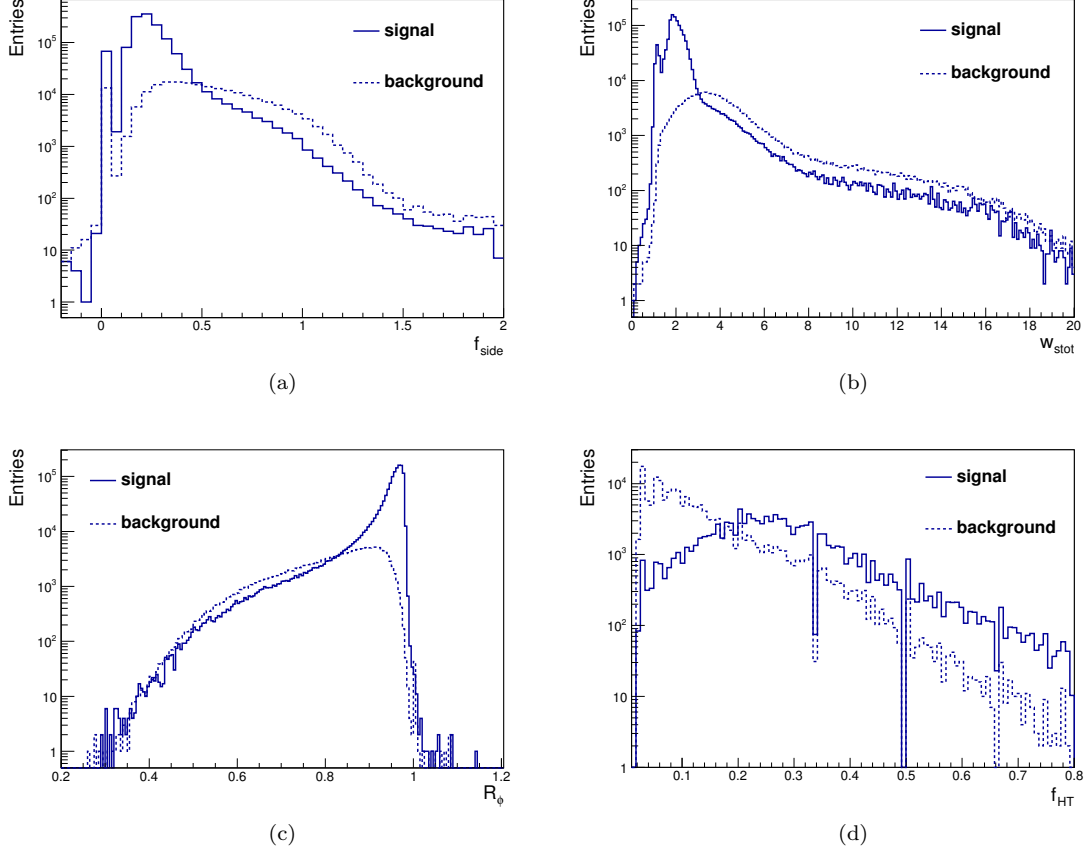


Figure 3.14: *Discrimination potential of EM calorimeter cluster and TRT hit variables: Distributions of discriminating variables for electrons from $Z \rightarrow ee$ decays (solid line) compared to those from jets from W +jets (dotted line). For the background, the tag is the truth matched electron from the W , the probe is then a jet faking an electron. (a) f_{side} , the shower shape in the shower core in the strip layer. (b) The total shower width in the first (strip) EM Calorimeter compartment, w_{stot} . (c) R_ϕ , the ratio of calibrated energy in a window of $\Delta\eta \times \Delta\phi = 3 \times 3$ to uncalibrated energy in $\Delta\eta \times \Delta\phi = 3 \times 7$. (d) f_{HT} , ratio of High Threshold Hits in the TRT to all hits.*

Shower shape variables of the middle EM calorimeter layer and hadronic leakage variables are used in the *Loose* selection. First EM layer calorimeter cuts, track quality requirements and track-cluster matching are added at the level of the *Medium* selection. The *Tight* selection adds E/p , B-Layer hit requirements and the particle identification potential of the TRT. [65]. An electron identified at a given level is also identified as such on any lower level. Also, converted photons which are ambiguous with reconstructed electrons are specifically labelled and removed by the application of the *Tight* set of cuts. The shower variables used in the *Loose* and *Medium* selection are performed on a cut optimisation in 10 bins of cluster η (defined by calorimeter geometry, detector acceptances and regions of increasing material in the inner detector) and 11 bins of cluster E_T (from 5 to above 80 GeV).

For the measurement of the identification efficiency in Section 4.5, cuts on the following variables play an important role for the discrimination of real electrons from background: R_ϕ , f_{side} and the calorimeter isolation. The calorimeter isolation is used to discriminate between isolated and non-isolated electrons, the latter often being faked by hadronic jets. This variable represents the transverse isolation energy in a cone with half-opening angle $R_0 = 0.15, 0.20, 0.25, 0.3, 0.35$ or 0.4 . It is defined as the E_T sum of the energy deposited in calorimeter cells in a cone ($E_T^{cone}(R_0)$), centered around the electron candidate, where a core of $\Delta\eta \times \Delta\phi = 5 \times 7$ cells is subtracted from the total cone energy:

$$E_T^{cone}(R_0) = \left(\sum_{\Delta R < R_0}^{cells} E_T \right) - E_T^{5 \times 7} \quad (3.8)$$

For isolated electrons, the distribution is expected to peak at values close to zero, with a width determined by the combination of electronic noise, shower leakage, underlying event and pile-up contributions. For the background from jets, a much wider distribution is expected reaching values well beyond unity.

However, in its “raw” form, the value of this variable may be modified by two effects: A photon or electron will leak some of its energy outside of the central core, and will cause the isolation energy to grow as a function of electron (photon) E_T . Alternatively, soft energy deposits from interactions different from the hard scattering generating the electron (photon) will contribute to the isolation energy depending on the amount of activity in the current event (both from “underlying events” and “in-time pileup”) as well as previous events (“out-of-time pileup”). Applying corrections for these two effects shifts the peak of the isolation distribution as it subtracts energy from the isolation value.

Such a correction is applied in the work in Chapter 4 to make the isolation variable more robust against pile-up and less dependent of the transverse energy of the electron.

Type	Description	Name
Loose selection		
Acceptance	$ \eta < 2.47$	
Hadronic leakage	Ratio of E_T in the first layer of the hadronic calorimeter to E_T of the EM cluster (used over the range $ \eta < 0.8$ and $ \eta > 1.37$)	R_{had1}
	Ratio of E_T in the hadronic calorimeter to E_T of the EM cluster (used over the range $ \eta > 0.8$ and $ \eta < 1.37$)	R_{had}
Middle layer of EM calorimeter	Ratio of the energy in 3×7 cells over the energy in 7×7 cells centred at the electron cluster position	R_η
	Lateral width of the shower	$w_{\eta 2}$
Medium selection (includes loose)		
Strip layer of EM calorimeter	Total shower width	w_{stot}
	Ratio of the energy difference between the largest and second largest energy deposits in the cluster over the sum of these energies	E_{ratio}
Track quality	Number of hits in the pixel detector (≥ 1)	n_{pixel}
	Number of total hits in the pixel and SCT detectors (≥ 7)	n_{Si}
	Transverse impact parameter ($ d_0 < 5$ mm)	d_0
Track-cluster matching	$\Delta\eta$ between the cluster position in the strip layer and the extrapolated track ($ \Delta\eta < 0.01$)	$\Delta\eta$
Tight selection (includes medium)		
Track-cluster matching	$\Delta\phi$ between the cluster position in the middle layer and the extrapolated track ($ \Delta\phi < 0.02$)	$\Delta\phi$
	Ratio of the cluster energy to the track momentum	E/p
	Tighter $\Delta\eta$ requirement ($ \Delta\eta < 0.005$)	$\Delta\eta$
Track quality	Tighter transverse impact parameter requirement ($ d_0 < 1$ mm)	d_0
TRT	Total number of hits in the TRT	n_{TRT}
	Ratio of the number of high-threshold hits to the total number of hits in the TRT	f_{HT}
Conversions	Number of hits in the b-layer (≥ 1)	n_{BL}
	Veto electron candidates matched to reconstructed photon conversions	

Table 3.3: Definition of variables used for *Loose*, *Medium* and *Tight* electron identification cuts for the central region of the detector with $|\eta| < 2.47$.

3.4 The LHC Beam Pipe within the ATLAS Experiment

In the scope of the Insertable B-Layer project [67] the current beam pipe of the ATLAS experiment will be replaced by a new version with a smaller diameter during the technical stop of the LHC starting in 2013. This will allow for other changes as well such as alterations to the supporting infrastructure in case of insufficient position stability of the beam pipe and choosing a different material with a lower activation potential as it is currently the case.

Two studies were conducted in this work to assess parameters for a precise positioning of the beam pipe and the choice of material of the new beam pipe. The first study focuses on evaluating the precise knowledge of the position of the current beam pipe as well as the stability over time. This determines the parameters for the installation of the new beam pipe with respect to positioning and a possible need for changes to the supporting infrastructure to guarantee a stable beam pipe. The second study estimates the influence of the material choice for the new ATLAS beam pipe as well as a possible difference between three options for the position of a new vacuum flange in terms of interaction probability for traversing particles.

The 38 m long beam-pipe section in the ATLAS experimental area consists of seven parts with increasing diameter and pipe thickness as one moves away from the interaction point (IP). They are bolted together with flanges to form a fully in-situ bakeable ultra-high vacuum system. The part closest to the IP with a length of ~ 7 m is made of beryllium with 10 cm aluminium flanges on both ends, a diameter of 58 mm and a thickness of 0.8 mm. The remaining six chambers are made of stainless steel with a thickness of 1 mm and are installed symmetrically on both sides of the IP. They are supported by the end-cap LAr cryostats, the end-cap toroids and the forward shielding, respectively.

Despite the thin envelope, particles emerging from the collision point do interact with the material of the pipe which induces secondary vertices. On a longer time scale, these interactions can lead to an activation of the the beam pipe (and detector) material. As ATLAS plans to replace all pipes during the technical stop, moving from stainless steel to a material with a smaller activation potential was envisaged at the same time.

3.4.1 Stability Studies of the Current Configuration

To monitor the stability of the position of the ATLAS beam pipe around the interaction point of the proton beam, two methods were chosen that can reveal movements of the ATLAS beam pipe: the results of the hydrostatic levelling sensor (HLS) system and the analysis of secondary hadronic interactions, particles coming from the primary collision vertex and interacting with the material of the beam pipe and the detector.

Cavern movement survey results

ATLAS is supported by nine pairs of feet standing on 20 m long big stainless steel rails - the bedplates - fixed to the 5 m thick concrete floor of the cavern. According to the civil engineering simulations a long term 1 mm per year heave of the floor is predicted for several years after the excavation phase due to hydrostatic pressure. In addition a short term settlement of 4-6 mm due to the weight of the experiment is expected [68, 69]. The aim of the floor stability monitoring via hydrostatic levelling sensors is to confirm and refine these predictions in order to guarantee for a good and stable alignment of the detector and the beam pipe with the beam line during data taking.

A series of HLS have been placed in the ATLAS cavern to monitor the movements of the floor and as a consequence, of the detector itself. These sensors form an H-shaped hydraulic network which consists of a total of 6 sensors in the bedplates plus 2 sensors in the A and C side of the trenches. The absolute position of the sensors was determined at the beginning of the measurement with a precision of 2 mm in x and y , and 1 mm in z (the coordinate system in the cavern is depicted in Fig. 3.15).

The layout of the sensors in the cavern is shown in Fig. 3.16(a). Data recorded from 1st of January until 8th of December 2010 was used for this study. This includes the measurement of the relative position of the sensors yielding an average value per day. A detailed report about the HLS survey results can be found in Refs. [70, 68, 69].

The HLS sensors provide vertical distances with respect to the equipotential water surface of the hydraulic network, which is the reference height. This system works according to the principle of the communicating vessels, as depicted in Fig. 3.16. The sensor measures the distance to the water surface through capacitive technology and the difference in water level between two such sensors indicates the height difference between them.

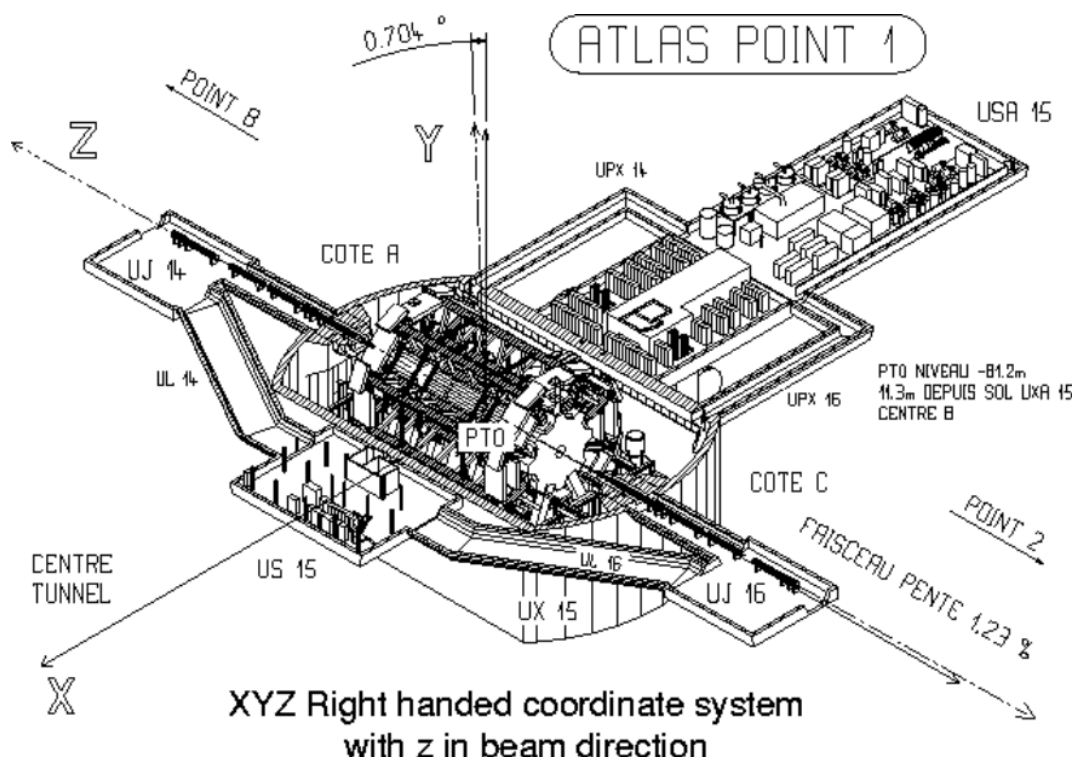


Figure 3.15: *Coordinate system of the ATLAS cavern [70].*

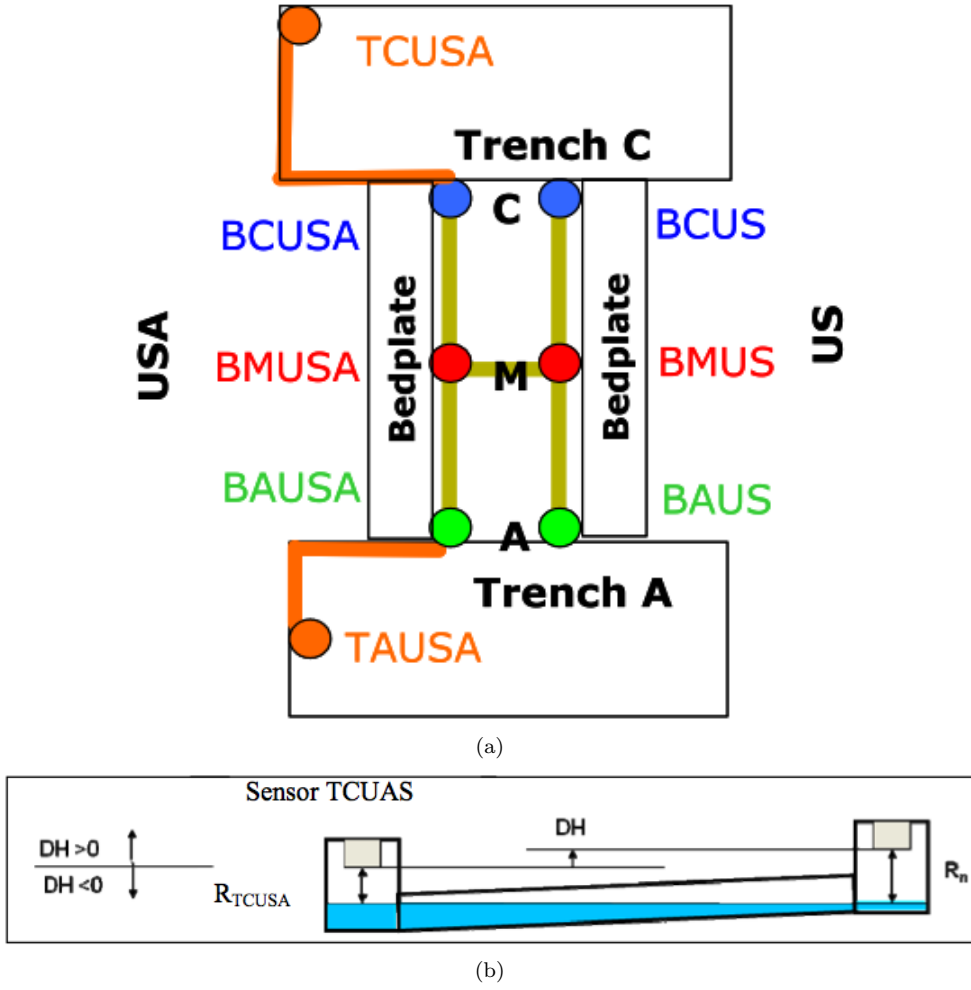


Figure 3.16: (a) Schematic of the layout of the HLS as positioned in the ATLAS cavern [70]. (b) Working concept of a hydrostatic sensor based on the principle of communicating vessels and used for the monitoring of the cavern floor movement.

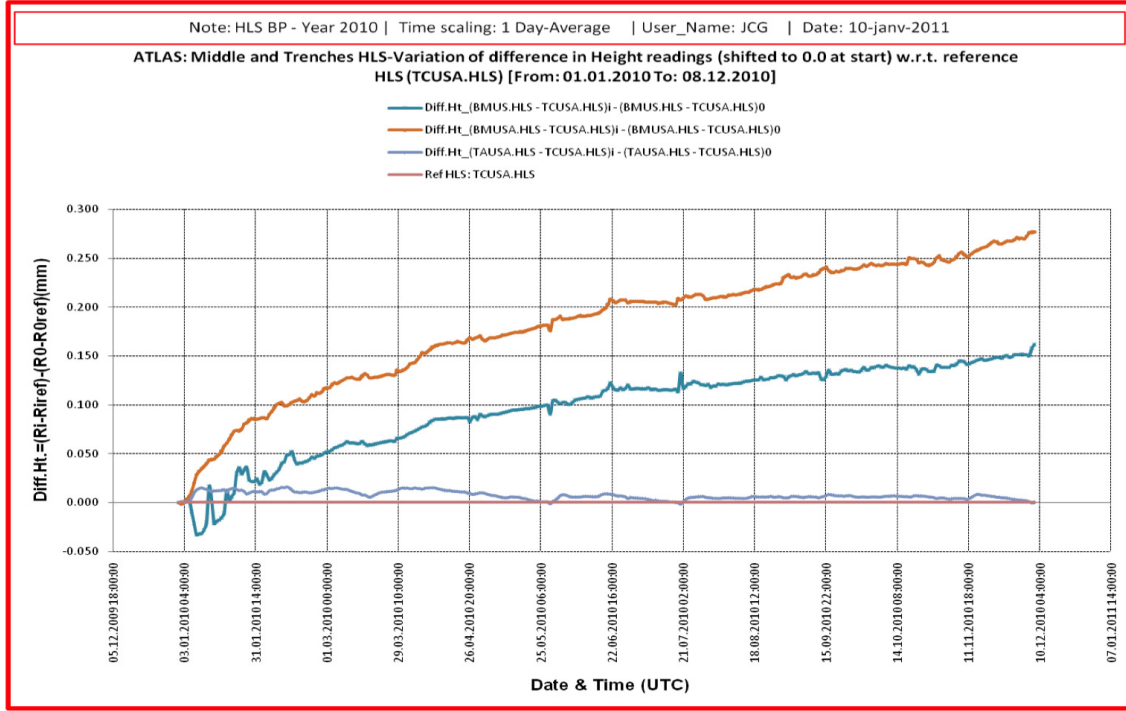
The values shown in the plots are the differences of the height measurements:

$$DH(t) = R_n(t) - R_{TCUSA}(t) \quad (3.9)$$

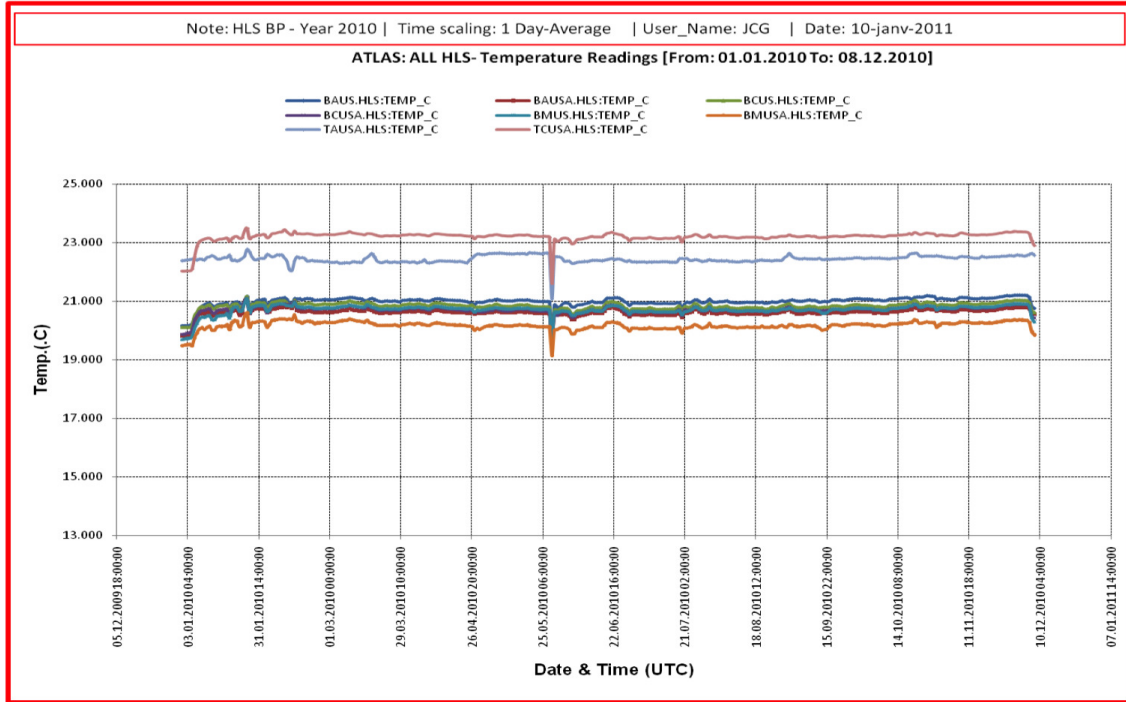
Where $R_n(t)$ is the average of the distances to the water surface measured during a given period at time (t) . The precision of the differences in height to the reference sensor TCUSA is estimated to be $30 \mu\text{m}$ at 1σ level. Furthermore, the data are normalized to the starting point value as follows:

$$DH_{\text{variation}} = DH(t) - DH(t_0) \quad (3.10)$$

The readout of the sensors positioned in the centre and in the corner of the cavern is plotted as



(a)



(b)

Figure 3.17: (a) Difference between centre and trenches readout values BMUS-TCUSA (blue) and BMUSA-TCUSA (orange) as well as the difference between those two values, TAUSA-TCUSA. (b) Temperature in the ATLAS cavern as a function of time. The data was recorded from January - December 2010.

a function of time in Fig. 3.17(a). From the sensor readout results an increasing tendency of the measured values can be observed for both BMUS-TCUSA (blue) and BMUSA-TCUSA (orange), which indicate the difference between the sensors in the center and in the corner of the cavern on both US and USA side, as shown in Fig. 3.17(a). The increase of these two values can be interpreted as an uplift or heave of the floor in the cavern centre, which confirms the predictions of the LHC civil engineering simulations. However, the significant value concerning a possible movement of the beam pipe is TAUSA-TCUSA, the purple data in Fig. 3.17(a). It indicates the overall horizontal tilt of the beam pipe, as it shows the difference in height of the two corners of the cavern with respect to each other. Any deviation from a flat curve could thus be interpreted as one corner of the cavern having moved more than the other. Or, in other words, this would indicate a tilt in the horizontal plane of the detector and, as a consequence, also of the beam pipe. However, the TAUSA-TCUSA data do not follow the uplifting trend of the middle part of the cavern as can be seen in Fig. 3.17(a). Consequently, no tilt in the horizontal plane of the beam pipe can be observed, the position of the beam pipe can be regarded as stable.

For completeness, the cavern temperature is plotted in Fig. 3.17(b) as a function of time. Also the temperature in the cavern is stable in the respective data taking period and no movement of the beam pipe results from changes of the cavern temperature.

Secondary Hadronic Interactions - Data Selection, Methodology and Results

Hadrons created in the primary interaction of the proton beams in the ATLAS detector will interact with the surrounding material as they pass through various layers, e.g. the beam pipe, Pixel and SCT layers, support structures etc. and sometimes produce more than two outgoing particles. Using these secondary vertices, one can create a mapping of the interior of the detector around the interaction point. The data used for this analysis come from the *Minimum Bias* trigger stream from all of 2011 until end of June 2012.

The *Minimum Bias* trigger selects all types of inelastic interactions with minimal bias, across the full acceptance of the ATLAS detector. It collects single-, double- and non-diffractive events, with the majority belonging to the last category. The term *Minimum Bias* originates from the experimental requirement of a minimal number of tracks (or hits) in a given instrumented region. The diffractive part of pp interactions can be classified as:

- single diffractive dissociation: $p + p \rightarrow p + X$ with X denoting anything that is not the original beam particle
- double diffractive dissociation: $p + p \rightarrow X$

In the experimental setting, diffraction is defined by an observable gap, of some minimal size in rapidity. However, some differences exist between theoretical and experimental terminology [71].

An event in ATLAS may have several interaction vertices with an unknown a-priori multiplicity, photon conversions, K_S , Λ decays, etc. Thus a clean detection of material interactions requires reconstruction and elimination of all other secondary vertices. This is achieved with a universal vertex finding algorithm designed to find all vertices in an event. For a full description and comprehensive study of the algorithm, see Ref. [72].

In order to find particles originating from the primary vertex, stringent limits are put on the allowed values of transverse and longitudinal impact parameters. As a result, the reconstruction efficiency for secondary track candidates strongly depends on both radial (r -) and longitudinal (z -) coordinates of the vertex they originate from. The algorithm starts by finding all possible intersections of pairs of selected tracks. It assumes that these two secondary tracks are coming from a single point and determines the vertex position and modifies track parameters to satisfy this assumption. Differences between the measured track parameters and the recalculated ones define the vertex χ^2 . The reconstructed two-track vertices define the full vertex structure in the track set because any N -track vertex is simply a union of corresponding two-track sub-vertices.

The track selection cuts were optimized for reconstruction efficiency, they are as follows:

- Track $p_T \geq 300$ MeV
- More than 1 hit in the SCT detector system
- Track Fit $\chi^2/dof < 5$
- Transverse impact parameter $d_0 > 5$ mm

The impact parameter requirements removes approx. 99% of primary tracks, as well as many secondaries produced in K_S decays and γ conversions. In general, particles produced in secondary hadronic interactions have much larger impact parameters, especially in comparison to γ conversions, which tend to point back to the primary vertex. The reconstructed secondary vertices have spatial resolutions ranging from $\sim 200 \mu\text{m}$ to 1 mm. Monte Carlo simulation studies indicated that vertices inside the beam pipe (see Fig. 3.19(a)) and almost all of the vertices in the gaps between material surfaces are due to combinatorial background, with a very small fraction of the latter due to interactions with the gases in these gaps (the density of silicon is about 1000 (1500) times the density of CO_2 (N_2)). Some vertices come also from heavy flavour decays. The beam pipe envelope, consisting of a beryllium cylinder, followed by layers of aerogel, kapton tape and coatings, extends from a radius of 28 mm to 36 mm.

The positions of the secondary hadronic vertices coming from material interaction yield a mapping of the material distribution in the detector as sketched also in Fig. 3.18. Figs. 3.19(a) and 3.19(b) show the vertex distribution with the beam pipe and the structure of the Inner Detector

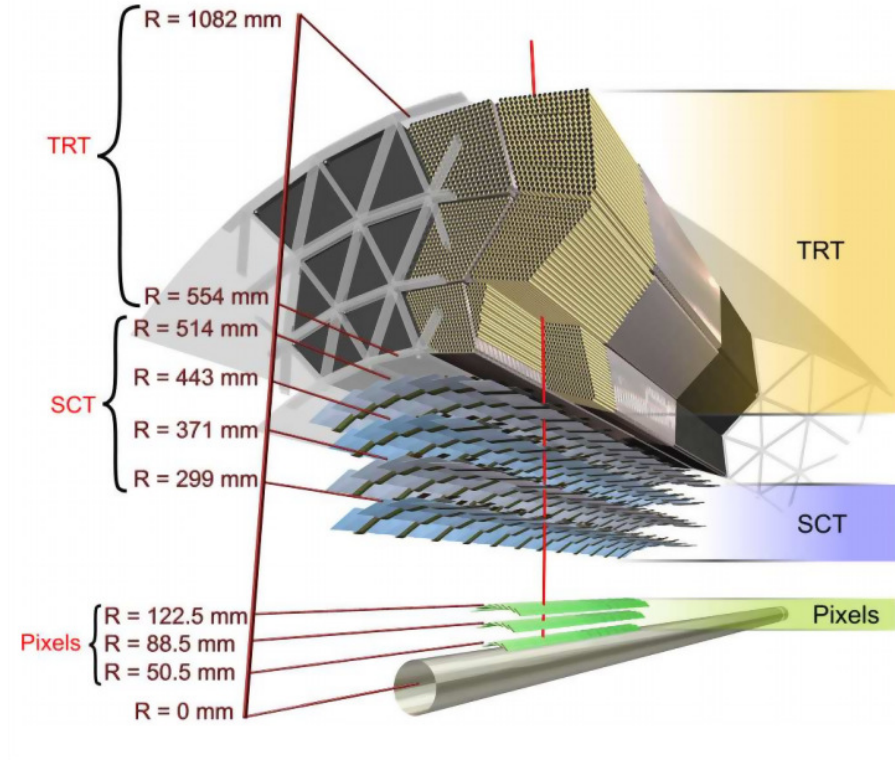


Figure 3.18: *Sensors and structural elements traversed by a charged track of $10 \text{ GeV } p_T$ in the barrel inner detector ($\eta = 0.3$). The track traverses successively the Be beam-pipe, the three cylindrical silicon-pixel layers with individual sensor elements, the four cylindrical double layers of barrel silicon-microstrip sensors (SCT), and approximately 36 axial straws of 4 mm diameter contained in the barrel transition-radiation tracker modules within their support structure [73].*

clearly visible. The ϕ coordinate of the vertices as a function of the radius is plotted in Fig. 3.19(b). The sinusoidal shape visible at a radius of ~ 29 mm indicates a shift of the nominal origin of the beam pipe in x and y . The non-centrality of the beam spot with respect to the nominal origin is also visible in the “crosshair” view in Fig. 3.19(a). The evolution of the beam spot position with time (for 2011) is given in Fig. 3.20.

Computing the position of the beam pipe (in x, y, z) for several points in time yields an estimate for the stability of the beam pipe over time. The data used for this analysis was collected by the Minimum Bias trigger stream with ~ 10 M events per data point which corresponds to a period of several days or weeks. For 2010, datasets from adjacent runs were combined over a period of not more than four days. For 2011 and 2012, datasets were combined from longer periods of time for sufficient statistics: July - November 2011, April, May, June 2012. The 2011 data and each month of 2012 represent one data point.

A fit of the radius and the ϕ coordinate distribution of the secondary vertices was performed to obtain the position of the beam pipe and thus to give an estimate for a possible shift of the centre of the beam pipe with respect to the nominal origin:

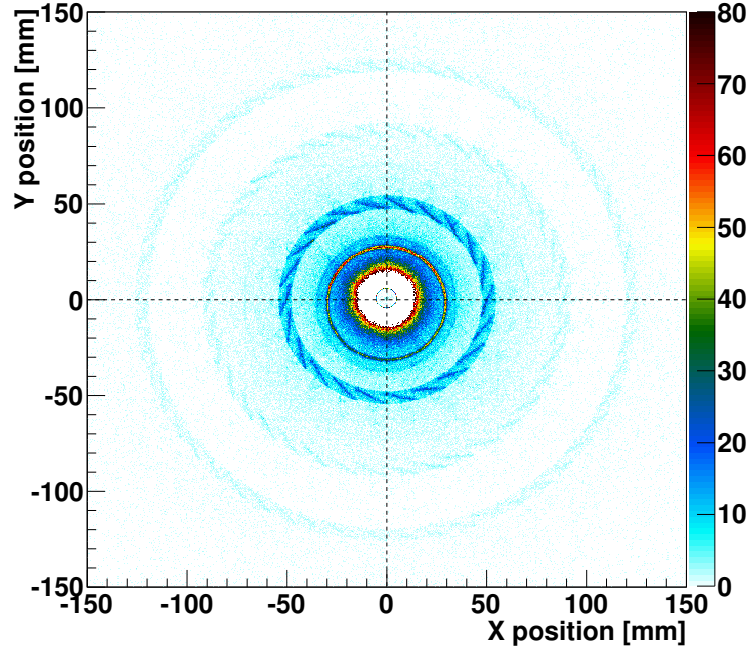
$$r(\phi) = p_0 + p_1 \cdot \sin(p_2 + \phi) \quad (3.11)$$

where p_0 , p_1 and p_2 are the fit parameters, as shown in Fig. 3.21). The position of the centre of the beam pipe in x and y follows then from the fit parameters.

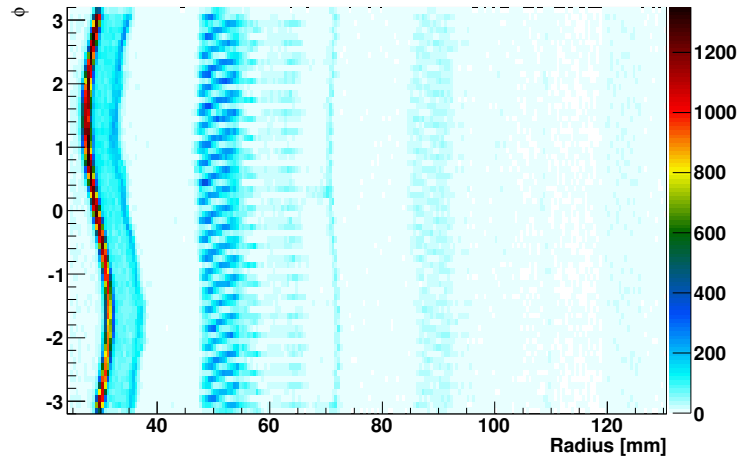
A similar procedure can be performed in the direction of the z axis to give an estimate of a possible tilt of the pipe along the beam line. This is assumed to show in a deviation from the horizontal plane assumed resulting from a movement of the beam pipe supports. No effects such as sagging of the pipe under its own weight or construction imperfection that could result in a deviation from a straight pipe are taken into account.

The estimation of this possible tilt (vertical displacement along the y -axis ΔY) was performed by fitting the profile of the $x - z$ projection of the secondary vertex distribution (Fig. 3.22(a)) with a linear function in the range ± 300 mm from the interaction point, as sketched in Fig. 3.22(b). This range was chosen for the fit according to the high efficiency range for the reconstruction of the secondary, as given in Ref. [72]. The inclination of the beam pipe is then defined as the deviation from the horizontal plane: $\Delta Y(z) = p_1 \cdot z$, computed from the linear fit, the uncertainty is taken from the fit as well. As the slope of the fit function is expected to be very small within the fit range, the deviation from the horizontal plane due to that slope is computed at a distance of 3.7 m from the IP to give a more substantial measure of a possible tilt of the beam pipe. The distance of 3.7 m from the IP was chosen as it is the edge of the innermost part of the ATLAS beam pipe. The position precision of the beam pipe survey results of Ref. [74] at that point is given as 1.5 mm at one σ level.

The results are plotted in Fig. 3.23 for the position in x , in Fig. 3.24 in y and the deviation from the horizontal plane extrapolated to a position of 3.7 m from the IP in z in Fig. 3.25. All values

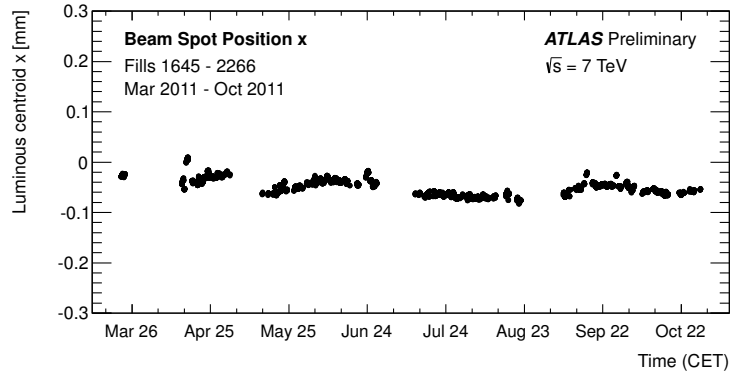


(a) slice plane in xy

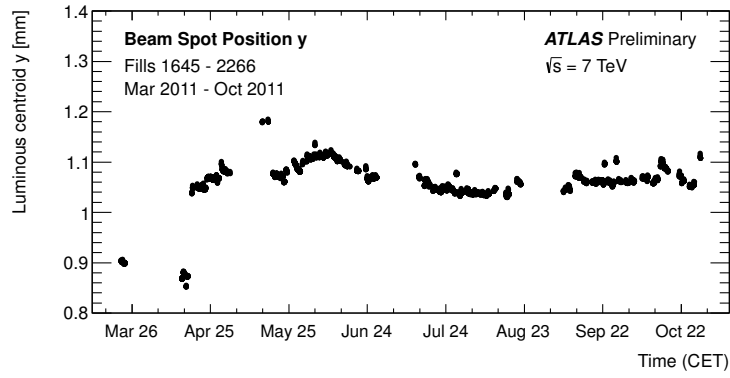


(b) projection along z axis

Figure 3.19: (a) Distribution of secondary vertices in the xy -plane for data from July 2011 - June 2012. Note that for the sake of a better contrast, bins with content > 100 were omitted from the plot. (b) Secondary vertex distribution in ϕ as a function of the radius, for data from 2010.



(a)



(b)

Figure 3.20: Position of the beam spot in x and y [mm] as a function of time throughout 2011.

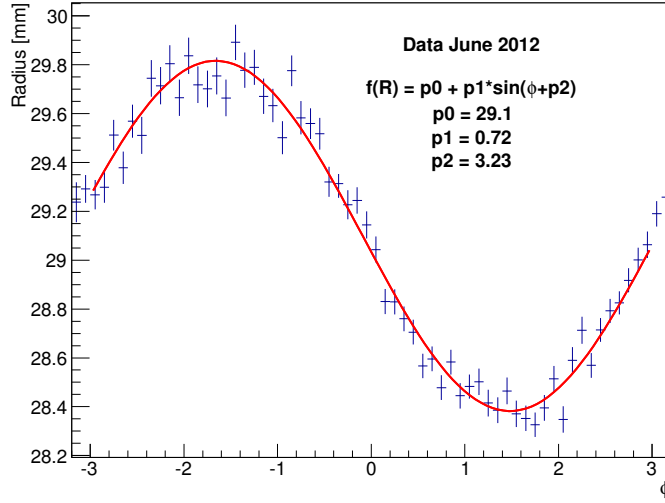


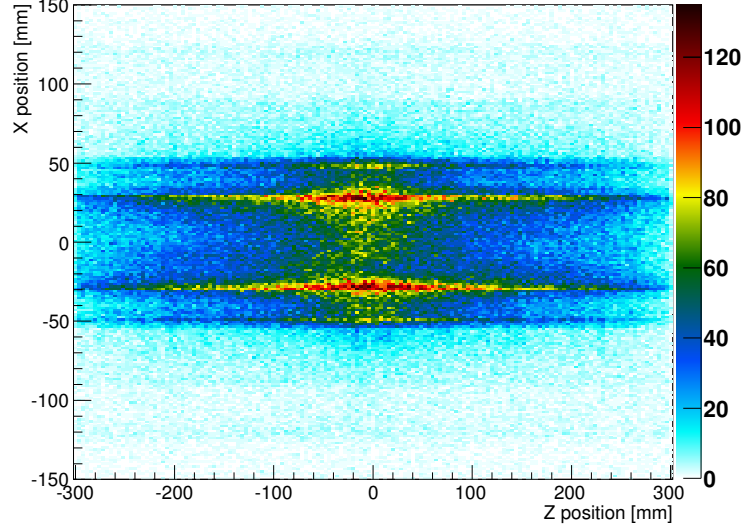
Figure 3.21: The radius of the beam pipe as a function of the azimuthal angle ϕ and the fitted function $r(\phi) = p_0 + p_1 \cdot \sin(p_2 + \phi)$. The errors are only statistical.

from the fits for the position in x and y and z are also listed in Tables 3.4 and 3.5.

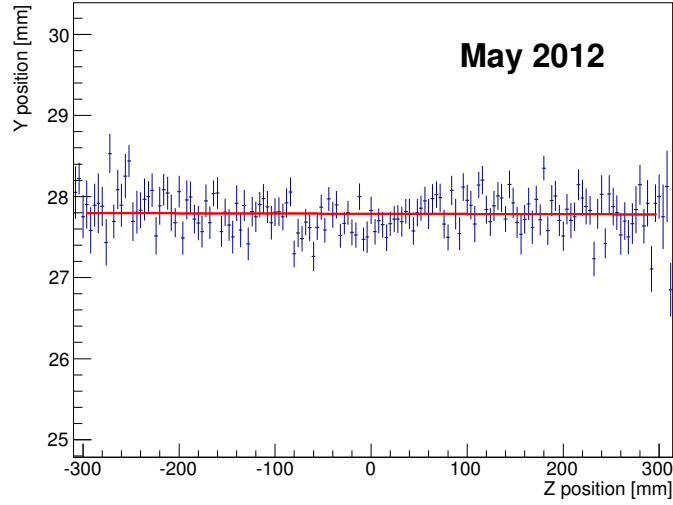
The aim of this analysis was a qualitative evaluation of a possible movement of the beam pipe over time, hence no detailed assessment of the systematic uncertainties was performed. A crude attempt was made to quantify the systematic uncertainty arising from the selection of bins used for the profile plot of the secondary vertex distributions which is linked to the finite thickness of the beam pipe of 0.2 mm and the spatial resolution of the reconstructed secondary vertices. For the vertical displacement, an additional source of uncertainty is the fit range along z . By varying the fit range for the z -axis projection fit as well as the bin selection used for the profile plot, the average systematic uncertainty was estimated to be at most 1.0 mm. This estimate for the total uncertainty is comparable the precision of the beam pipe position of 1.5 mm as quoted by the beam pipe survey. Hence the support structure of the ATLAS beam pipe was proved to yield sufficient stability during data taking periods.

3.4.2 ATLAS Beam Pipe Upgrade

After three years of operation with stable proton beams, the LHC and thus the experiments including ATLAS went offline in a technical stop at the end of 2012. Until then, the material of the ATLAS detector as well as the beam pipe have been exposed to hard radiation which can lead not only to eventual material fatigue but also to induced radioactivity of the surrounding material. A comprehensive study was conducted in the past to assess the expected activation in different regions and for different data-taking scenarios. The full study explaining methods and assumptions used in



(a)



(b)

Figure 3.22: (a) The $x - z$ projection of the distribution of all secondary vertices. Vertices with a radius smaller than 27mm have been removed from the plot. (b) The profile (for the x coordinate) of the beam pipe along the z -axis and a linear fit whose fit parameter (slope) is used to extrapolate the vertical displacement in y of the beam pipe from the horizontal plane at 3.7m from the IP.

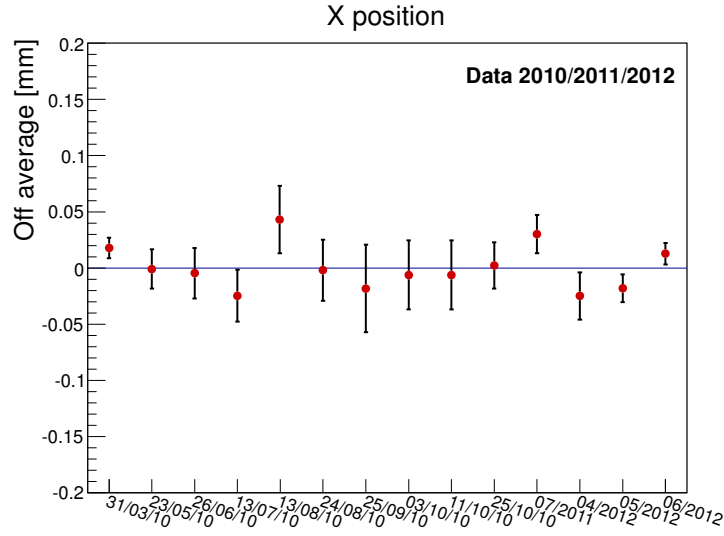


Figure 3.23: The difference between the beam pipe position in x and the average in the respective time period (in mm). Due to a shift of the average value between 2010 and 2011/12, the respective average for that time interval was taken to compute the variation. The quoted uncertainties are taken from the fit.

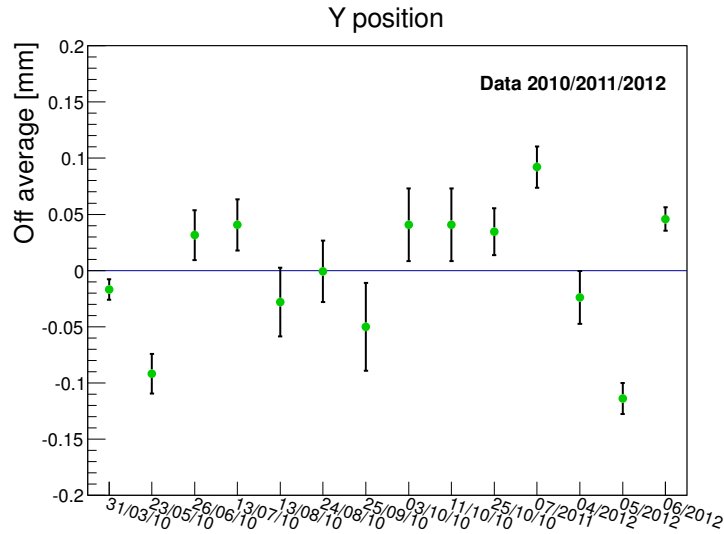


Figure 3.24: The difference between the beam pipe position in y and the average in the respective time period (in mm). Due to a shift of the average value between 2010 and 2011/12, the respective average for that time interval was taken to compute the variation. The quoted uncertainties are taken from the fit.

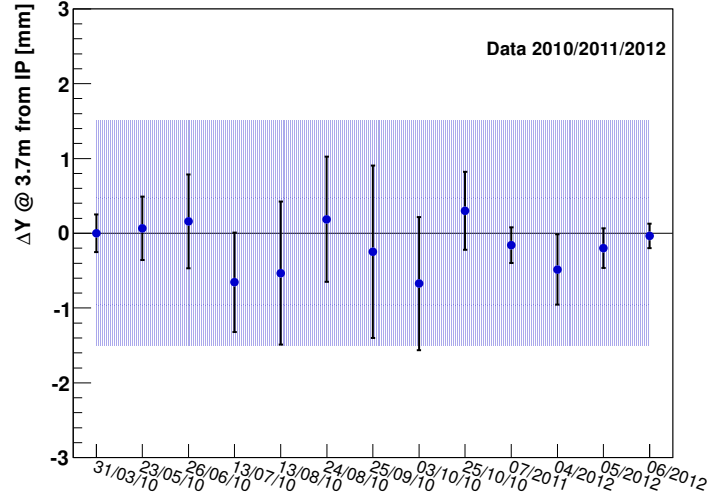


Figure 3.25: *Extrapolated (from the linear fit) vertical displacement (ΔY) of the beam pipe at a distance of 3.7m from the IP inside the detector. The blue dots represent the data points, the blue shaded band illustrates the precision of the position of the beam pipe from the survey measurement. No trend indicating a tilt of the horizontal plane over time can be observed. The quoted uncertainties on the data are taken from the fit.*

	X position (mm)		Y position (mm)	
31/03/10	-0.21	± 0.01	-1.85	± 0.01
23/05/10	-0.23	± 0.02	-1.92	± 0.02
26/06/10	-0.23	± 0.02	-1.80	± 0.02
13/07/10	-0.25	± 0.02	-1.79	± 0.02
13/08/10	-0.18	± 0.03	-1.86	± 0.03
24/08/10	-0.23	± 0.03	-1.83	± 0.03
25/09/10	-0.25	± 0.04	-1.88	± 0.04
03/10/10	-0.23	± 0.03	-1.79	± 0.03
11/10/10	-0.23	± 0.03	-1.79	± 0.03
25/10/10	-0.23	± 0.02	-1.80	± 0.02
07/2011	-0.06	± 0.02	-0.72	± 0.02
04/2012	-0.12	± 0.02	-0.84	± 0.02
05/2012	-0.11	± 0.01	-0.93	± 0.01
06/2012	-0.08	± 0.01	-0.77	± 0.01

Table 3.4: *Fitted values of the position in x and y of the centre of the ATLAS beam pipe in 2010-2012. The quoted uncertainties come from the fit.*

	ΔY (mm) @ 3.7 m from the IP	
31/03/10	0.00	± 0.25
23/05/10	0.07	± 0.42
26/06/10	0.16	± 0.63
13/07/10	-0.65	± 0.66
13/08/10	-0.53	± 0.96
24/08/10	0.18	± 0.84
25/09/10	-0.25	± 1.15
03/10/10	-0.67	± 0.89
25/10/10	0.30	± 0.52
07/2011	-0.16	± 0.24
04/2012	-0.49	± 0.47
05/2012	-0.20	± 0.27
06/2012	-0.04	± 0.16

Table 3.5: *Extrapolated values of the shift in y position from a linear fit of the ATLAS beam pipe in 2010-2012. The quoted uncertainties come from the fit.*

the calculation of the induced activity can be found in Ref. [75]. Induced radioactivity can increase the level of background radiation effects significantly and the main conclusion of the before mentioned studies is that the beam-pipe will be the major source of induced radioactivity in ATLAS. These background radiation effects include:

- Increased detector occupancy: in tracking detectors this can lead to inefficiencies, decreased resolution and fake tracks. In calorimeters, the increased pile-up fluctuations degrade energy resolution.
- For penetrating tracks, the rates of spurious triggers can increase. Increased occupancies can also increase the rates of random triggers.
- Radiation damage of silicon detectors and electronics.
- Deposits of local radiation can disrupt electronic signals or destroy components.
- Wire detectors can experience “aging” due to polymerized deposits on the wires caused by radiation interacting with organic additives in the detector gas. This can reduce the detector efficiency.
- Nuclear interactions in dense materials lead to the creation of residual radionuclides. The resulting dose rates from such material activation can lead to radiological hazards that impact access and maintenance scenarios.

At high-energy electrons lose energy mostly by bremsstrahlung when interacting with matter, while photons convert to e^+e^- pairs. The characteristic quantity for such interactions is called the radiation length X_0 , usually measured in $\text{g} \cdot \text{cm}^{-2}$ or, when divided by the material density, it is given in units of length. It is the distance over which a high-energy electron loses all but $1/e$ of its energy by bremsstrahlung, or, for the photon case, $7/9$ of the mean free path for electron-positron pair production [76]. It has been calculated and tabulated by Y.S. Tsai [77] and is defined as [78]:

$$X_0 = \frac{716.408 \cdot A}{Z(Z+1) \ln \frac{287}{\sqrt{Z}}} \quad (3.12)$$

For composites, the radiation length can be approximated by the sum over the radiation lengths of the components multiplied by their fractional weight:

$$\frac{1}{X_0} = \sum_i \frac{w_i}{X_i} \quad (3.13)$$

As the entire ATLAS beam pipe will be exchanged during the technical stop starting in 2013, it will be possible to choose a new material for certain parts in order to minimize the activation of the beam pipe and thus to keep the above mentioned radiation effects as low as possible. As the radiation length is inversely proportional to the probability of a traversing particle interacting with the material, choosing a new material with a large intrinsic radiation length is preferable. To estimate the gain in units of radiation length when moving away from the current set-up to a material with a larger radiation length for the part of the beam pipe inside the LAr calorimeter end-cap, a simulation study was performed in this work.

The beam pipe within the ATLAS detector consists of four pieces: VI (vacuum Inner Detector), VA (vacuum LAr end-cap), VT (vacuum toroid end-cap), VJ (vacuum forward shielding) - symmetric with respect to the interaction point. The material of the VI pipe is beryllium ($X_0 = 35.28 \text{ g/cm}^2$), the other pipe parts are made of stainless steel ($X_0 \approx 1.76 \text{ g/cm}^2$) with diameters increasing progressively from 58 mm to 80 mm and finally to 120 mm, as depicted in Fig. 3.26. Chambers inside different detectors are mechanically decoupled by vacuum bellows, which also serve to absorb thermal expansion during bake-out. At the end of the VA closer to the interaction point, there is a vacuum ion pump. Behind this pump, the insertion of a new vacuum flange is foreseen, for which three different positions were considered. A possible difference on the radiation length for traversing particles comparing the three options was also evaluated in this simulation.

The simulation was done in GEANT4 using a model created with the *Persint* software package [79] as input for the detector geometry. The model was created in agreement with the CAD design sheets available for all parts of the beam pipe and all the parts described above (VI, VA, VT, VJ) were included in the model. An effort was made to model details of the pipe and the vacuum pump in terms of mechanics (iron shell, titanium interior parts) as well insulation (Kapton, silica aerogel). Fig. 3.28 shows some details of the vacuum pump in the VA part of the beam pipe as in

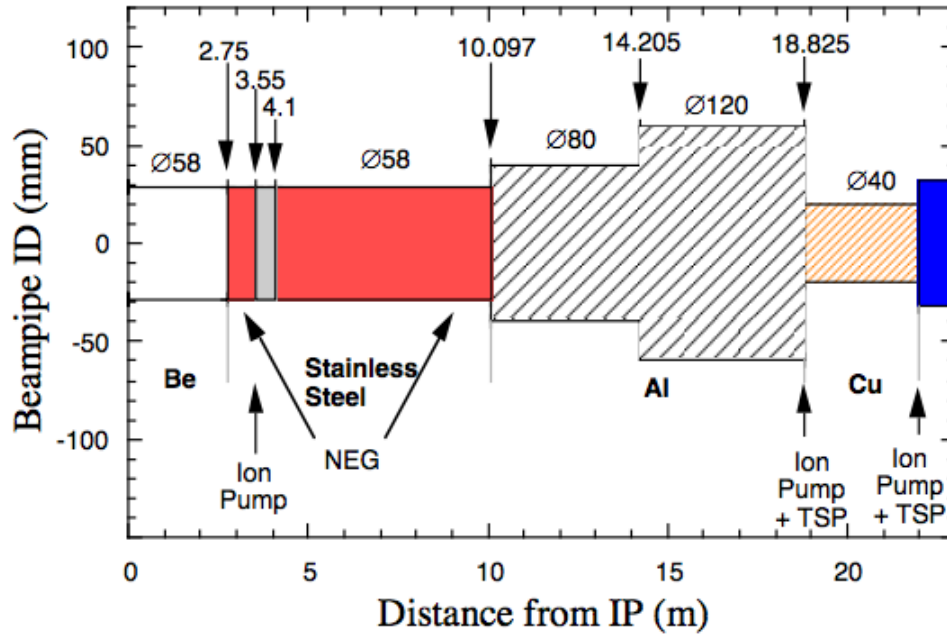


Figure 3.26: Shape of the ATLAS beam pipe showing the beam pipe inner diameter as a function of the distance from the IP.

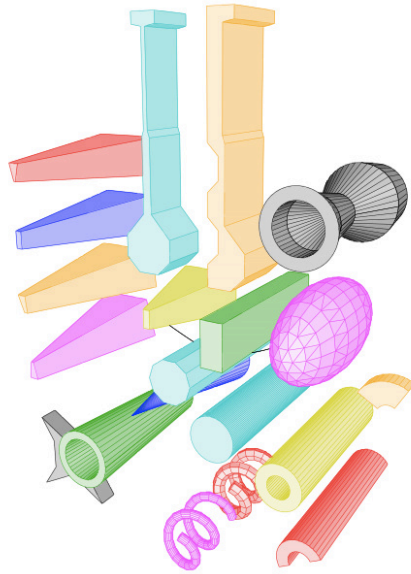


Figure 3.27: Basic geometric shapes available in the Persint software package to construct a composite object of any desired form.

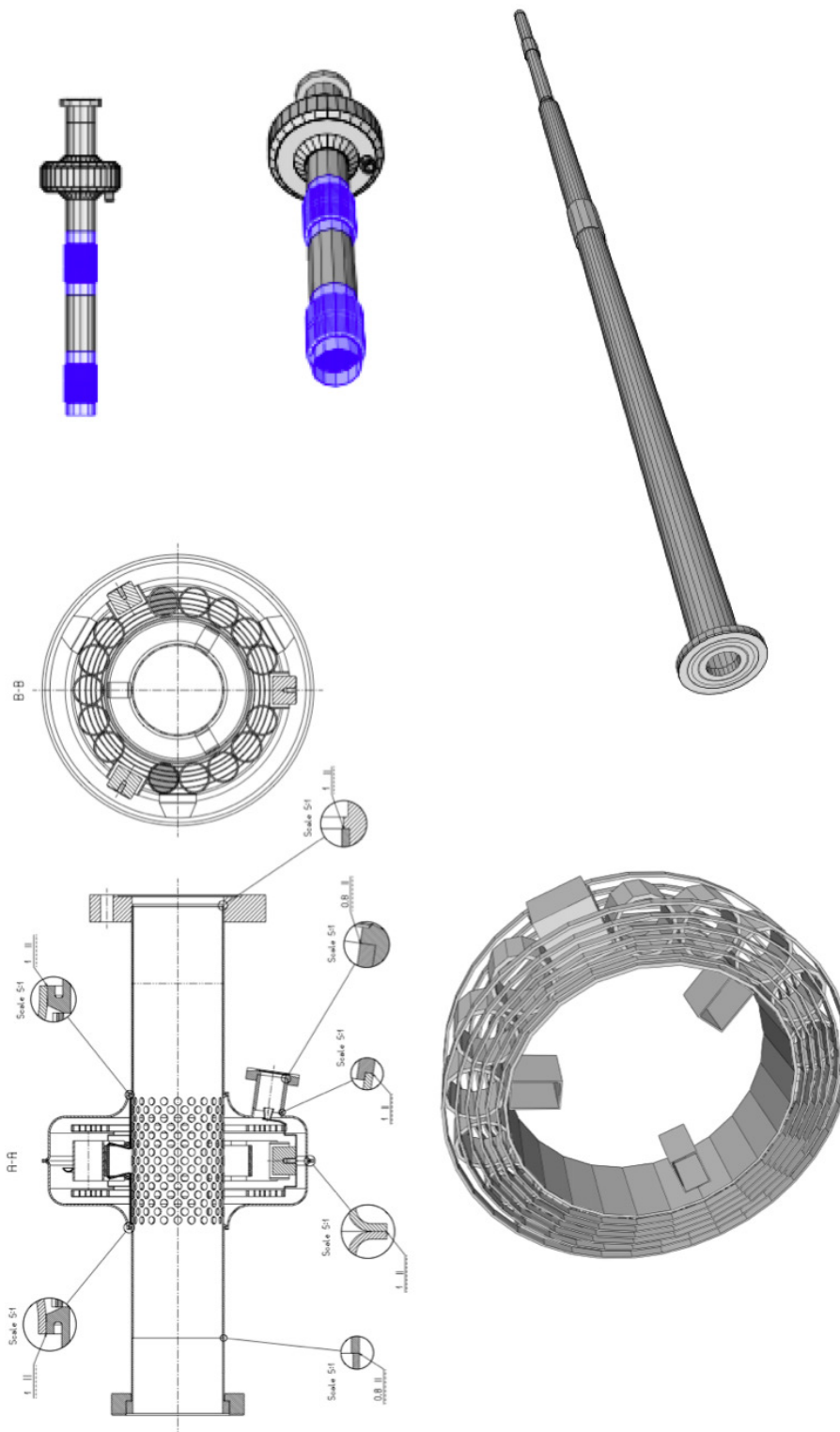


Figure 3.28: CAD design sheet of the vacuum ion pump of the VA part of the beam pipe and details of the pump as implemented in the beam pipe model for the simulation. Different colours in the model illustrate different materials: pipe in black - stainless steel, bellows in blue - aluminium.

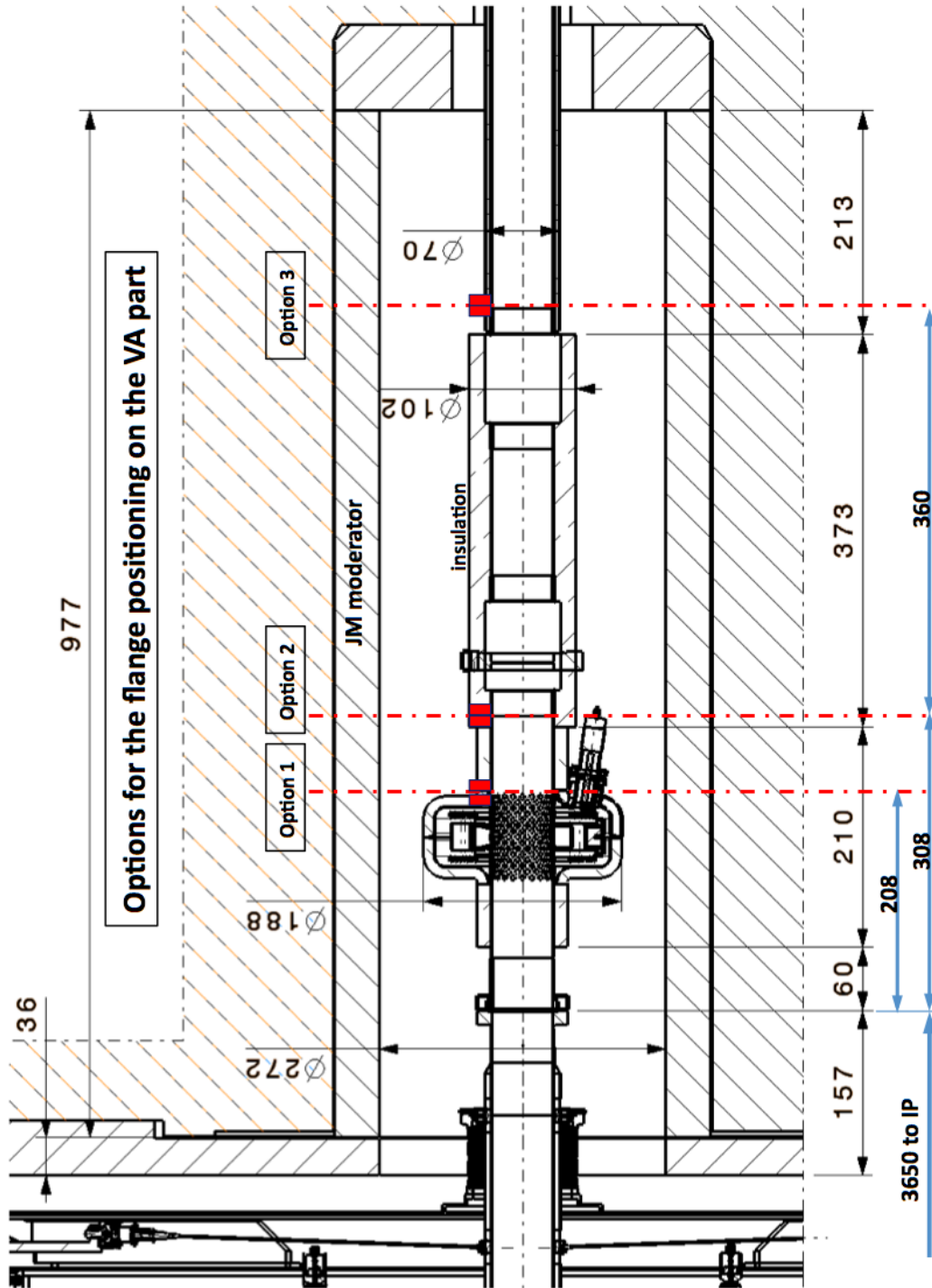


Figure 3.29: The three options for the position of the new vacuum flange behind the vacuum ion pump in the upgrade are shown as used in the simulation.

the CAD design drawing and the same part of the model used in the simulation, as well as the VT part of the model.

Particles with zero mass and charge and with a transverse momentum of 20 GeV were used for the simulation to measure tracking and material dependent parameters such as radiation length without further interaction with the material. The geometrical phase space of interest was in the forward region at a pseudorapidity covering the length of the VA beam pipe part ($3.0 < |\eta| < 6.5$). The material of the new VA part after the flange was set to aluminium with a radiation length of $X_0 = 8.9 \text{ g/cm}^2$, the three configurations considered for the position of the flange after the vacuum ion pump are shown in Fig. 3.29. The vacuum ion pump and the part of the VA supporting it will remain unchanged. The decrease in diameter for the VI part of the new beam pipe was not taken into account in this simulation.

The result of the simulation is shown in Fig. 3.30 for the pseudorapidity range affected by the changes. Plotted are the amount of material traversed by the particles in units of radiation length X_0 (a) and for completeness directly in units of material thickness (b). A difference with respect to the current set-up becomes visible at an η of ~ 5.2 . At smaller η values, Option 3 is favourable over Option 1 and 2, at higher η , it is less favourable than the two other options. The “gain” or reduction in units of % radiation length that particles emerging from the IP see with respect to the current configuration, is defined as

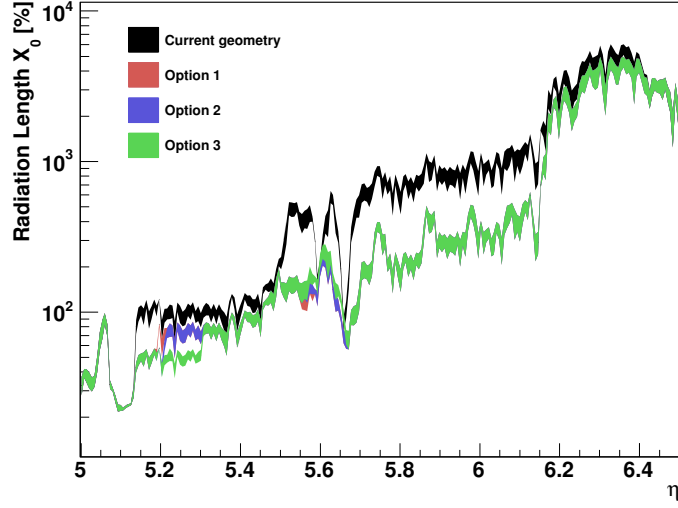
$$\text{gain} := 1 - \frac{\int X_0^i}{\int X_0^{\text{current}}} \quad (3.14)$$

The total gain or reduction in radiation length is 27.1%, coming from the change of material from stainless steel to aluminium. Overall, the position of the new flange has no significant impact on the result as the difference between the possible configurations is negligible ($\leq 0.1\%$). The exact values for the gain with respect to the current configuration for the three considered flange options is given below in Table 3.6.

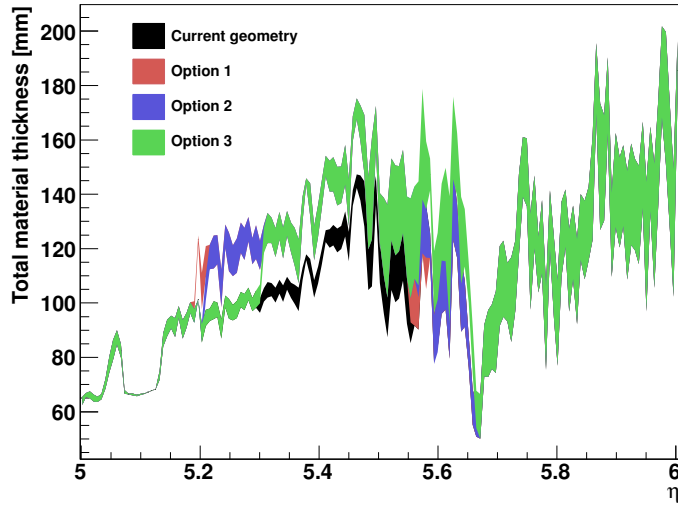
new flange position	gain in X_0 [%]
Option 1	27,101
Option 2	27,100
Option 3	27,091

Table 3.6: *Gain in % radiation length X_0 with respect to the current set-up for the three flange positions in Fig. 3.29. No significant difference can be observed.*

Thus none of the options for the flange position can be regarded as inherently more favourable than the others for the design of the new beam pipe in terms of minimal material interaction. Other (engineering) aspects had to be taken into account to choose a position for the new vacuum flange.



(a)



(b)

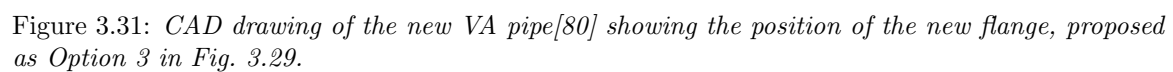
Figure 3.30: (a) The total material in units of relative radiation length (in %) traversed by the particles in the forward region, along the VA chamber of the beam pipe inside the LAr end-cap calorimeter. (b) The total amount of material traversed by the particles in the forward region. After $\eta \approx 5.65$ the beam pipe is the same for all configurations thus all curves are overlaid. The gain with respect to the current set up of the VA part is 27.1 % due to the change in material from stainless steel to aluminium. The position of the new flange has a negligible influence on the radiation length ($\leq 0.1\%$).

Finally, the results of this study were taken into account by the ATLAS engineering team for the design of the new beam pipe: the aluminium alloy AA2219 (Al 93 %, Cu 6.3 %, Mn 0.3 % and other metals) was chosen as the new material for the VA as well as the VT chambers of the beam pipe. For the new flange, a position corresponding to Option 3 was chosen, a CAD design drawing for the VA part of the ATLAS new beam pipe is shown in Fig. 3.31 [80].

3.4.3 Summary

The position stability of the ATLAS beam pipe has been measured using fits to secondary hadronic interaction vertices in data from 2010-2012. The results for 2010 were compared to the data recorded by a hydrostatic levelling sensor system installed in the ATLAS cavern. The sensor data as well as the values obtained from the secondary vertex fits show no movement of the horizontal plane of the beam pipe which can thus be regarded as stable.

A simulation study to assess the gain in radiation length for traversing particles showed a reduction of 27.1 %s for aluminium with respect to the current set-up made of stainless steel. No significant difference for the three different options under consideration for the position of a new flange in the VA (in the LAr calorimeter end-cap) part of the ATLAS beam pipe could be observed.



Chapter 4

High Mass Drell-Yan Differential Cross Section Measurement

The precise measurement of the Drell-Yan (DY) cross section allows a test of the predictions of perturbative QCD (pQCD) calculations. Moreover, the production of DY dilepton pairs represents a source of irreducible background for other SM measurements and to many new physics searches such as heavy gauge bosons (Z' , Z^* - e.g. [81]), techni-mesons [82], as well as spin-2 Randall-Sundrum gravitons [83] (G^* - excited Kaluza-Klein modes of the graviton [84, 85]).

Total and differential cross sections as a function of the dilepton mass ($m_{\ell\ell}$) in the Z -boson mass window ($66 < m_{\ell\ell} < 116$ GeV) have been reported previously by the ATLAS [86], CMS [87], CDF [88] and D0 [89] collaborations. The differential cross section as a function of $m_{\ell\ell}$ up to 600 GeV was measured by the CMS collaboration [90]. In addition, searches for new physics in the high mass tail of the $m_{\ell\ell}$ distribution have been performed [91, 92, 93, 94] and no deviations from the SM expectation observed. This analysis reports an extension of these analyses by providing a measurement of the DY cross section as a function of the electron-positron (for simplicity referred to as “dielectron”) invariant mass in the high mass region $116 < m_{ee} < 1500$ GeV.

The outline of the analysis is as follows: electron candidates are selected by cut-based identification and isolation requirements described in Sections 4.2 and 4.3. The jet background is estimated using a fake factor method and cross-checked with three other partially data-driven methods, as described in Section 4.4. The identification efficiency for electrons at high transverse energy is evaluated separately in bins of transverse energy and pseudorapidity, the measurement being described in Sections 4.5 and 4.5.7, with further efficiency and migration corrections detailed in Section 4.6. The evaluation of the systematic uncertainties is described in Section 4.7. The cross section is reported within a phase space close to the fiducial acceptance of the two electrons. The results are compared to predictions of pQCD calculations at next-to-next-to-leading order (NNLO) using

5 different parton distribution functions (PDFs) and to three Monte Carlo (MC) event generators: PYTHIA, MC@NLO and SHERPA in Section 4.8.

4.1 Fiducial differential cross section

The Drell-Yan differential cross section, $d\sigma/dm_{ee}$, is measured in 13 bins of m_{ee} from 116 to 1500 GeV in a fiducial region defined by the kinematic requirements of both electrons having a transverse momentum of $E_T > 25$ GeV and lying within $|\eta| < 2.5$,

$$\frac{d\sigma_{\text{fid}}}{dm_{ee}} = \frac{N_{\text{sig}}}{C_{\text{DY}} \cdot \mathcal{L}_{\text{int}}} \frac{1}{\Gamma_{\text{bin}}}, \quad (4.1)$$

where N_{sig} is the number of candidate events observed in a given bin of m_{ee} (of width Γ_{bin}) where the total background in that bin has been subtracted, \mathcal{L}_{int} is the integrated luminosity and C_{DY} is a bin-by-bin correction for efficiency and migration effects. It is defined as the ratio between the number of generated events that pass the signal selection in a reconstructed bin of m_{ee} and the total number of generated events within the fiducial region in the corresponding bin of true m_{ee} . It is obtained from MC and corrected for differences in reconstruction, identification and trigger efficiencies between data and MC. The correction factor C_{DY} includes the extrapolation over the small regions $1.37 < |\eta| < 1.52$ and $2.47 < |\eta| < 2.5$ not considered in the measurement. The extension of the fiducial volume has little dependence on m_{ee} and varies from about 10 to 13%. The purity, defined as the fraction of simulated events reconstructed in a particular m_{ee} bin that have true m_{ee} in the same bin, ranges from 70 to 90 %.

The cross sections are determined with respect to two conventions regarding QED final state radiation (FSR) corrections. For the Born level result, the true m_{ee} and electron kinematics are defined by the electrons coming from the Z/γ^* decay before FSR, corresponding to a full correction for FSR effects. At the “dressed” level, true final state electrons after FSR are recombined with radiated photons within a cone of $\Delta R = 0.1$, correcting only for collinear emissions.

4.2 Data and Simulated Monte Carlo Samples

4.2.1 Data

The analysis is based on a data sample collected at $\sqrt{s} = 7$ TeV during 2011. The data were recorded by a diphoton trigger requiring two electromagnetic objects passing the *Loose* identification criteria [95] with a transverse energy greater than 20 GeV (“2g20_loose”). Only events in which the EM calorimetry and the Inner Detector tracker recorded data with high quality and the solenoidal field was at its nominal value were used. These requirements yield an integrated luminosity of $\mathcal{L} = 4.92 \pm 0.09 \text{ fb}^{-1}$, see Fig. 3.3(a).

All electron candidates in the data have a correction applied to their cluster energy based on the results of an in-situ calibration performed during 2011. The event selection as described in Section 4.3 was done after this energy scale correction.

4.2.2 Monte Carlo

A summary of the complete set of MC samples used to model the signal and background processes are given in Tables 4.1 and 4.2, respectively. **PYTHIA 6.425** [42] and **MC@NLO 4.01** [52] were used to model the Drell-Yan signal. A combination of an inclusive sample and eight samples binned in mass of the dielectron pair was used. A cut on the true dielectron invariant mass was applied to the inclusive sample at 120 GeV to avoid double counting in the overlapping mass region with the m_{ee} -binned samples. **SHERPA 1.3.1** [53] was also used to generate signal samples with up to three additional partons. All **PYTHIA** and **HERWIG** [49] samples (DY signal process, di-boson backgrounds) use the **LO**** parton distribution functions, also known as MRSTMCa1 [96]. The **ALPGEN** [51] (W +jets background) and **MC@NLO** samples (DY signal process, $t\bar{t}$ background) used **HERWIG** to model parton showers and fragmentation processes and **JIMMY** for underlying event simulation. The **ALPGEN** samples used **CTEQ6L1** [97] PDFs and the **MC@NLO** samples **CT10** [98]. For the **ALPGEN** W +jets and **HERWIG** diboson samples, the calculated cross section is obtained by multiplying the generated cross section by a K -factor obtained by the ratio of the calculated over generated cross section of the inclusive production. All event generators are interfaced to **PHOTOS 3.0** [48] to simulate QED final state radiation, except for **SHERPA** which uses the method of Ref. [99].

All MC events have been generated at $\sqrt{s} = 7$ TeV and include the full ATLAS GEANT4 detector simulation. The simulation conditions are given in Table A.2 in the appendix. Settings of MC parameters that describe properties of minimum bias events and the underlying event are chosen based on results of previous ATLAS measurements [100]. All plots, tables and results shown are inclusive of all corrections unless otherwise stated:

- In the **PYTHIA** DY signal samples a discrepancy is observed in the transverse momentum (p_T) distribution of the Z boson when compared to data. A reweighting [101] of the **PYTHIA** MC to the 2010 **PYTHIA** simulation is therefore performed which yields good agreement with the 2010 ATLAS data, see Fig. 4.1. The Z boson p_T reweighting is performed as a function of m_{ee} . No attempt is made to do the same reweighting for **MC@NLO** in order to better match the data, as the difference between **MC@NLO** and data is similar to the difference observed between the reweighted **PYTHIA** and data.
- With the increasing instantaneous luminosity of the LHC beams in 2011, the effects of multiple interactions per bunch crossing (Fig. 3.3(b)) must be modelled. For example several track as well as calorimeter variables are pile-up dependent. There are two types of pile-up: pile-up from events from previous bunch crossings (as the time between two consecutive bunch crossings

Sample name	m_{ee} range (GeV)	Dataset No.	σB (pb)	Events (k)
PYTHIA 6.425 (MRSTMAL)				
$Z \rightarrow ee$	inclusive	106046	834.6	9 991
$Z \rightarrow ee$	120-250	105467	8.530	299
$Z \rightarrow ee$	250-400	105468	0.411	100
$Z \rightarrow ee$	400-600	105469	0.0665	100
$Z \rightarrow ee$	600-800	105470	0.0110	100
$Z \rightarrow ee$	800-1000	105471	0.00265	100
$Z \rightarrow ee$	1000-1250	105472	0.000893	100
$Z \rightarrow ee$	1250-1500	105473	0.000240	100
$Z \rightarrow ee$	1500-1750	105474	0.000073	100
MC@NLO 4.01 (CT10)				
$Z \rightarrow ee$	inclusive	106087	948.7	4 973
$Z \rightarrow ee$	120-250	126336	9.734	220
$Z \rightarrow ee$	250-400	126337	0.458	20
$Z \rightarrow ee$	400-600	126338	0.0734	20
$Z \rightarrow ee$	600-800	126339	0.0118	20
$Z \rightarrow ee$	800-1000	126340	0.00279	20
$Z \rightarrow ee$	1000-1250	126341	0.000916	20
$Z \rightarrow ee$	1250-1500	126342	0.000235	20
$Z \rightarrow ee$	1500-1750	126343	0.000068	20

Table 4.1: Summary of signal MC samples. The cross section times branching fraction σB is as reported by the generator. When combining the binned samples with the inclusive sample an upper cut on the true Z mass of 120 GeV is made on the events from the latter.

Sample name	Dataset No.	σB (pb) generated	σB (pb) calculated	Events (k)
W +jets background ALPGEN 2.13				
$W \rightarrow e\nu + 0$ partons	107680	6913.3	8296	3456.5
$W \rightarrow e\nu + 1$ parton	107681	1293.0	1551.6	632.5
$W \rightarrow e\nu + 2$ partons	107682	377.1	452.5	756
$W \rightarrow e\nu + 3$ partons	107683	100.9	121.1	202
$W \rightarrow e\nu + 4$ partons	107684	25.3	30.4	52
$W \rightarrow e\nu + 5$ partons	107685	6.9	8.3	14
$t\bar{t}$ background MC@NLO 4.01				
$t\bar{t} \rightarrow lX$	105200	2.7104	3.0240	20
WW, WZ and ZZ (diboson) backgrounds HERWIG 6.520				
WW	105985	11.49	17.46	2 489
WZ	105987	3.481	5.543	1 000
ZZ	105986	0.976	1.261	250

Table 4.2: Summary of MC background samples. The cross section times branching fraction σB includes the efficiency of any filtering at the MC generation level.

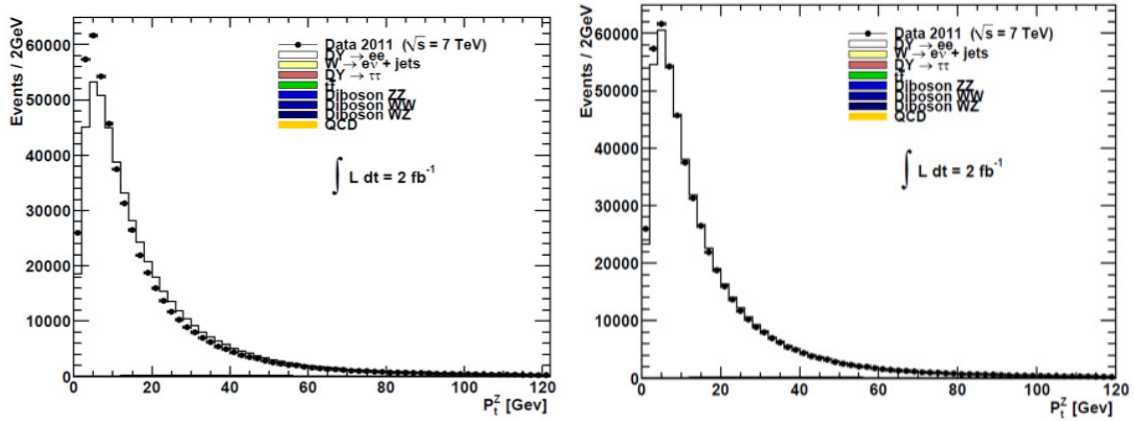


Figure 4.1: Comparison of data and Monte Carlo simulation before (left) and after (right) reweighting of the transverse momentum of the Z boson for the PYTHIA MC [102].

is shorter than the detector response time) and pile-up from multiple primary interactions in the same event (Fig. 4.2) that can result in several reconstructed primary vertices and overlapping tracks or calorimeter signals. In order to account for these pile-up effects, the events were reweighted according to the pile-up conditions in terms of the average number of primary vertices in the given data taking period. This reweighting proceeds as follows: the distribution of the average number of interactions per bunch crossing (μ) in the dataset is shown in Fig. 4.3(a). In all MC samples the simulated events are generated in four “channels” which correspond to data taking periods, each with a given μ distribution. The MC events from each channel are then reweighted in order to match the observed μ distribution. The required distribution of the weights needed to achieve the agreement in μ is shown in Fig. 4.3(b).

- The electron energy resolution in the MC has been corrected to match that measured in data during 2011 (more detail about this correction in Section 3.3.1).
- The PYTHIA and MC@NLO signal samples are reweighted to NNLO with m_{ee} -dependent K -factors using a modified version of `Phozpr` [103]. A detailed description as well as a table with the K -factor for PYTHIA with the MRSTMCa1 [96] PDF is given in the appendix C of Ref. [91]. The K -factor for MC@NLO with the CT10 PDF is calculated in the same way as the PYTHIA K -factor [104]. The K -factors for both PYTHIA and MC@NLO are plotted in Fig. 4.4. Due to the difference of LO \rightarrow NNLO (PYTHIA) and NLO \rightarrow NNLO (MC@NLO), the K -factors for the two event generators exhibit a different behaviour as a function of m_{ee} .
- In addition, the PYTHIA MC is reweighted by a mass-dependent electroweak K -factor calculated using `Horace` [105], taking into account missing contributions from initial state photon

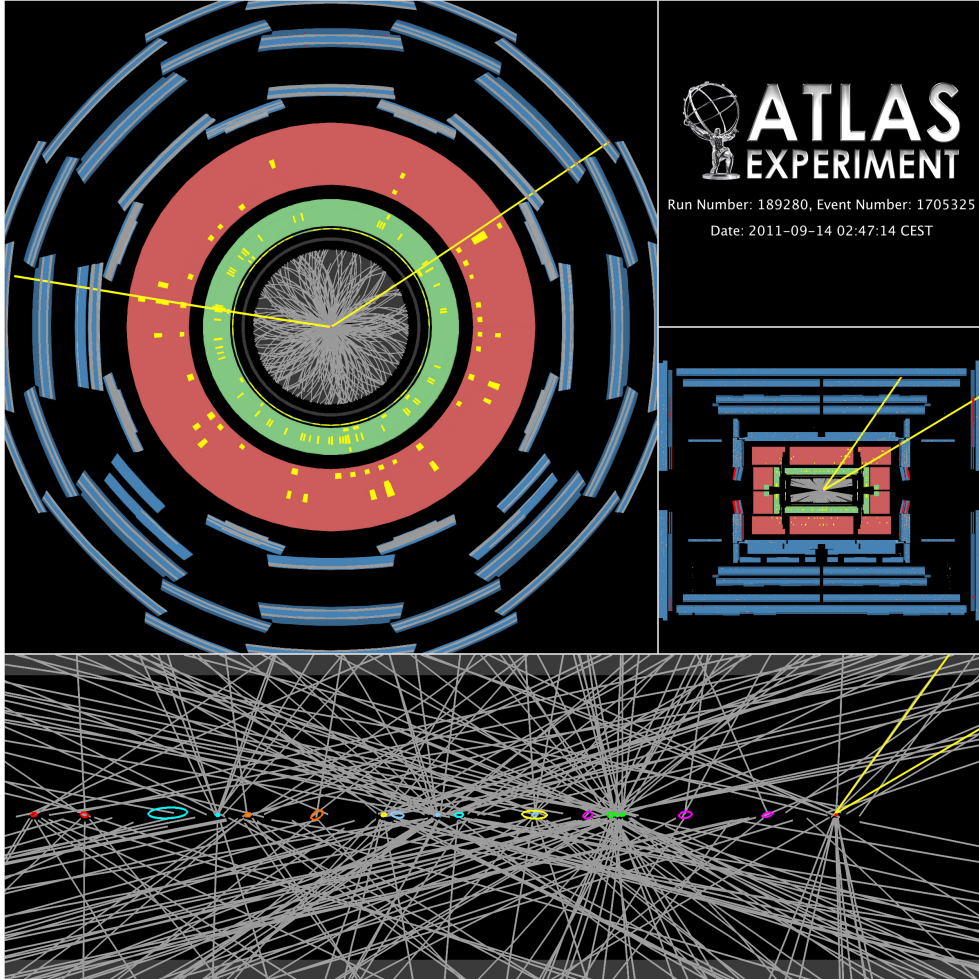


Figure 4.2: *Pile-up: Multiple (20) primary vertices in one event in September 2011. The effects of multiple interactions per bunch crossing (“pile-up”) must be modelled as several track and calorimeter variables and thus reconstruction and identification efficiencies are pile-up dependent. Corrections were applied in data to account for this effect.*

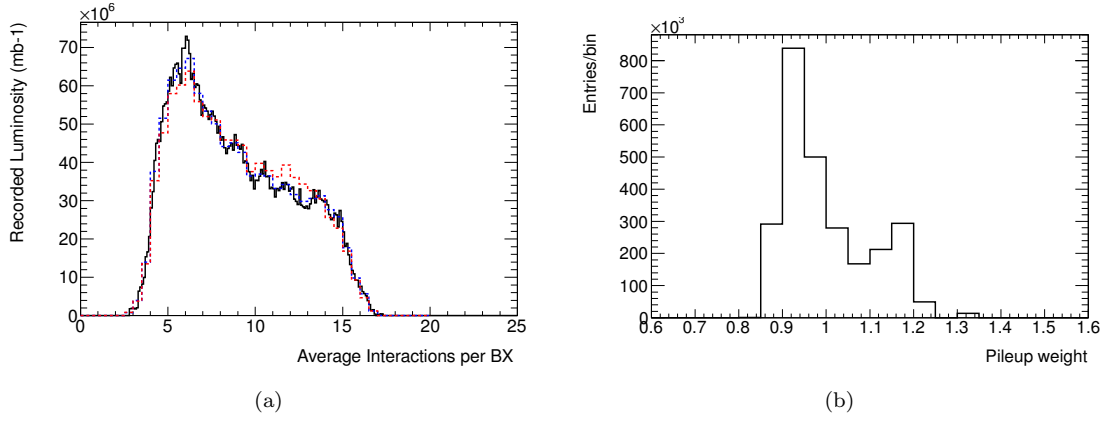


Figure 4.3: (a) Distribution of average number of interactions per bunch crossing (μ) in the data. Overlaid are the same distributions in PYTHIA DY signal MC before (dashed red line) and after (dashed blue line) applying the pile-up reweighting. The MC distributions are scaled to the data recorded integrated luminosity. (b) Distribution of pile-up event weights applied to MC events in order to better match the data distribution by the MC simulation.

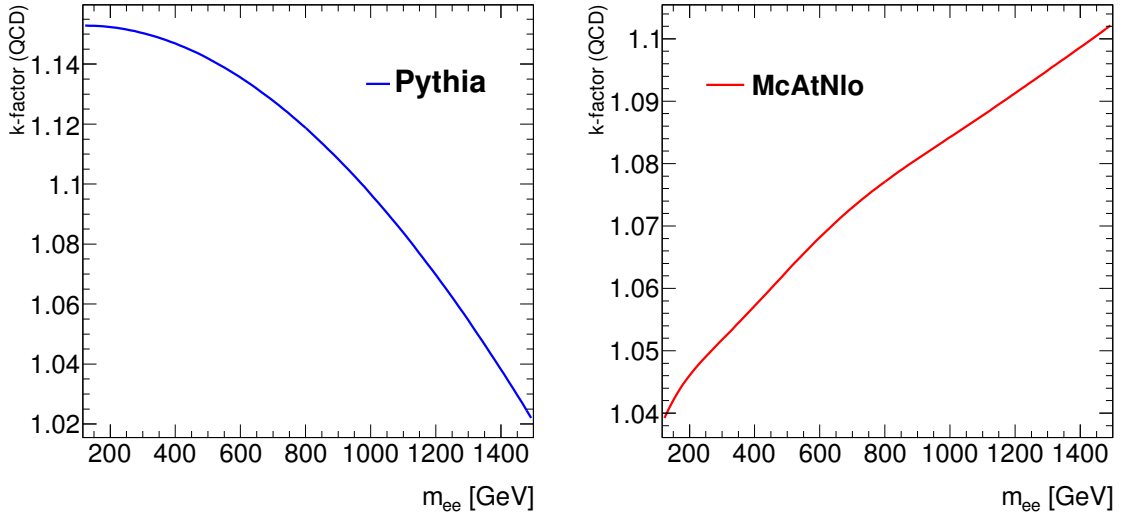


Figure 4.4: NNLO QCD K-factors for PYTHIA (left) and MC@NLO (right) [102].

radiation as well as electroweak loop corrections. The K -factor is shown in Fig. 4.5. For more details see Appendix D of Ref. [91].

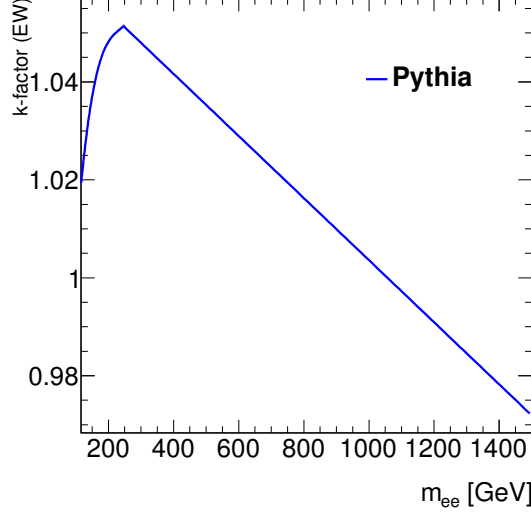


Figure 4.5: *Electroweak K-factors for PYTHIA.*

- *Scale factors* are applied to correct the trigger, reconstruction, identification and isolation efficiencies in MC to those measured in the data. These factors are described fully in Section 4.6.

4.3 Candidate Event Selection

On the event level, the good quality data are selected as recorded by the “2g20_loose” trigger. Events are required to have at least one vertex with more than two associated tracks. Events corresponding to possible noise bursts in the LAr calorimeter are also rejected. Events satisfying these criteria are then required to have at least two electrons satisfying the following selection:

- reconstructed by the standard algorithm where a cluster in the calorimeter is used as a seed and it is checked if a track in the Inner Detector matches the cluster;
- pseudorapidity $|\eta| < 2.47$ excluding the EM calorimeter transition region between calorimeter barrel and end-cap at $1.37 < |\eta| < 1.52$;
- transverse energy $E_T > 25$ GeV;
- Calorimeter Object Quality requirements (requirements satisfied, i.e., the calorimeter was working well in the respective region) and excluding possible liquid Argon noise bursts;
- pass *Medium* identification, as discussed in detail in Section 4.5;

- have a B-Layer hit if expected, i.e., if the innermost layer of the pixel detector was properly working in the region where the electron was passing through, the electron candidate is required to actually have at least one hit in this layer

For events with more than two electrons passing the above selection, the two highest E_T electrons are chosen, referred to as the leading and subleading electron. In order to help suppress the QCD and W +jets backgrounds, the leading electron is required to be *isolated*, by demanding $E_T^{\text{cone}}(0.2)$ (for the definition of the variable, see Section 3.3.2) to be less than 7 GeV.

This event selection follows the one used in exotic dielectron resonance searches. No requirement is made on the charge of the two electrons in order to avoid the related systematic uncertainties due to possible charge-misidentification, which at large transverse momenta are difficult to quantify and potentially significant due to the finite resolution of the Inner Detector.

4.4 Background Estimation

4.4.1 Data-driven Background Component

Significant backgrounds arise from multi-jet and W +jets processes where one or more jets¹ are misidentified as an electron, or, in other words, jets that “fake” electrons. Since precise MC modelling of the misidentification rate is difficult, the evaluation of this background component was done in a data-driven way. There are four methods:

- **Fakes Rate method (Jet stream):** This method is fully data driven and uses the probability of a jet faking an electrons (“fake rate”) derived from inclusive jet samples applied to loosely selected electron candidates in a normalization sample to estimate the total multi-jet and W +jets background.
- **Fakes Rate method (e/γ stream):** This method is similar to the above but uses fake rates obtained from the e/γ trigger stream
- **Isolation Fits method:** This method gives an estimate of the combined multi-jet and W +jets background by performing a template fit to the two-dimensional distribution of the isolation of each electron. The background template is obtained with reversed identification cuts and the signal template uses the DY MC.
- **Reverse Identification method:** In this method a template fit to m_{ee} is performed to determine the amount of multi-jet background, with the W +jets component being taken from MC. In the template fit, a background sample is obtained by reversing one of the electron identification cuts. This is fitted together with a MC template of signal plus other background components to the observed m_{ee} distribution.

¹An set of nearby particles associated to the hadronization of a parton from the collision, see [106] for a full description of the jet reconstruction algorithms used in ATLAS

Full details can be found in appendix A of Ref. [102]. Table 4.3 and Figs. 4.6 and 4.7 provide a comparison of the results of the four methods. Since the latter three estimate the sum of the multi-jet and W +jets components, the comparison is made by adding the W +jets prediction from MC to the multi-jet background estimated from the Reverse Identification method.

The Reverse ID method relies entirely on MC to predict the W +jets component for which the associated systematic uncertainties on the modelling of the jets “faking” the second electron are difficult to evaluate. It can be seen that its prediction for the total multi-jet plus W +jets background diverges from the other methods at high m_{ee} , where the W +jets contribution is dominant. The Isolation Fits method is also partially reliant on MC in order to form the signal templates for the Likelihood fit, and suffers from large statistical uncertainties at high m_{ee} . Note that the uncertainties have been symmetrised for simplicity, which in the highest invariant mass bins leads to uncertainties that do cover negative values.

The agreement between the two fake rate methods is very good and neither method is inherently more preferable than the other. For the central estimate the Fake Rate (Jet Stream) method is used, having a slightly smaller total uncertainty than the other methods which however serve as cross-checks. For this method, a systematic uncertainty is assigned from several sources. Firstly, the uncertainty on the fake rate is taken from the spread in the fake rates measured in the nine different jet (“fakes”) samples (collected under nine different inclusive jet trigger selections). Secondly, the uncertainty stemming from the contamination of the jet samples by real electrons is also considered. The statistical uncertainties on the fake samples also contribute to the systematic uncertainty of the fake rate. Overall, a conservative, flat 20% is assigned as the total systematic uncertainty of this background estimate, which is in addition to the statistical uncertainty on the normalization sample.

Note that the purely data driven W +jets estimates not only account for the direct production of a jet and a W boson decaying to electron plus neutrino, but also for W bosons first decaying to a τ lepton as well as for “indirect” W production from semi-leptonic $t\bar{t}$ events or even single top production.

4.4.2 Simulated Background Component

The $t\bar{t}$ and diboson (WW , WZ or ZZ) production backgrounds were taken from MC simulation. To avoid any possible double counting of events having one (or even two) fake electrons already estimated in the data driven techniques described above electrons are truth matched to ensure they originate from the W/Z boson or the t -quark decay.

It has been checked with MC that the contribution from the Drell-Yan process with two τ leptons in the final state and contribution from $W\gamma$ production process is negligible.

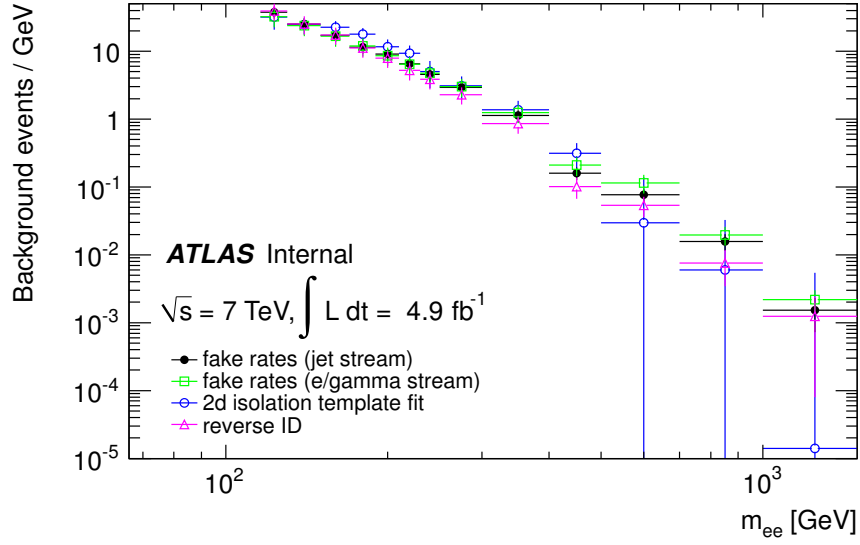


Figure 4.6: Total multi-jet and W +jets background per GeV in m_{ee} as predicted by four different methods.

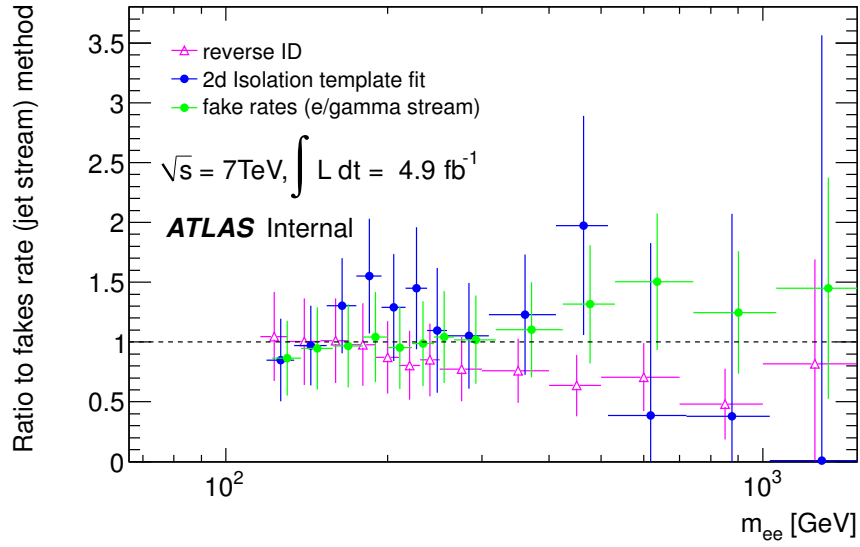


Figure 4.7: Ratio of the total multi-jet W +jets background from the Reverse ID, Fake Rates (e/ γ) and Isolation Fit methods to that predicted by the Fake Rates (Jet Stream) method.

4.4.3 Data - Monte Carlo Comparison

All relevant background contributions are shown in Table 4.4. They have been subtracted from the number of candidate data events to give the number of signal events N_{sig} in each bin of m_{ee} . The results are also plotted in fine binning Fig 4.8(a) and in the measurement bins in Fig. 4.8(b).

Method	m_{ee} [GeV]					
	116-130	130-150	150-170	170-190	190-210	210-230
Fake Rate (Jet)	530 ± 100	500 ± 100	345 ± 69	229 ± 46	182 ± 37	130 ± 26
Fake Rate (e/γ)	450 ± 140	480 ± 140	330 ± 100	239 ± 72	173 ± 52	128 ± 38
Reverse ID	550 ± 160	500 ± 150	350 ± 100	224 ± 65	158 ± 45	105 ± 31
Isolation fits	450 ± 160	490 ± 140	450 ± 100	356 ± 83	235 ± 65	188 ± 54

Method	m_{ee} [GeV]						
	230-250	250-300	300-400	400-500	500-700	700-1000	1000-1500
Fake Rate (Jet)	92 ± 19	147 ± 30	113 ± 23	32 ± 7	15 ± 4	4.7 ± 1.3	0.8 ± 0.4
Fake Rate (e/γ)	95 ± 29	150 ± 45	124 ± 37	42 ± 13	23 ± 7	5.9 ± 1.8	1.1 ± 0.4
Reverse ID	78 ± 23	114 ± 32	86 ± 25	20.3 ± 7.0	10.8 ± 3.6	2.28 ± 1.25	0.6 ± 0.6
Isolation fits	100 ± 43	155 ± 57	138 ± 48	63 ± 26	6 ± 22	21.8 ± 8.0	0.0 ± 3.0

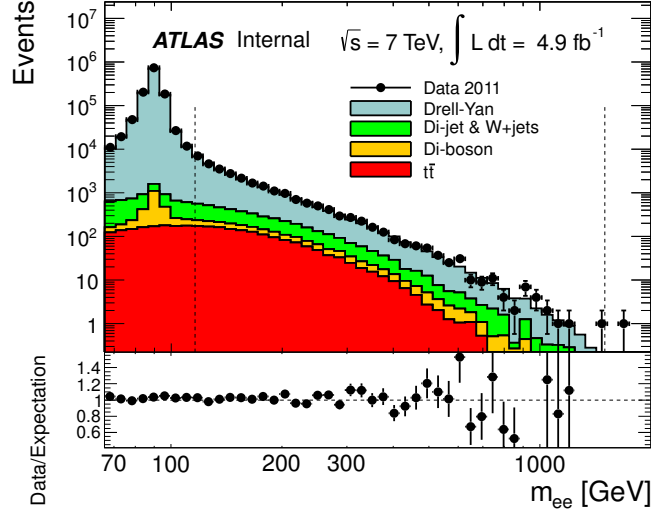
Table 4.3: Total QCD multi-jet and W +jets background expectation with statistical and systematic uncertainties from the four different methods. For the Reverse ID method the W +jets component is taken from Monte Carlo.

The number of events in the bins of m_{ee} used for the final measurement are shown in Table 4.4. Figure 4.9 compares the data with MC expectations for the distributions of p_T and η for the leading and subleading electrons in the m_{ee} region of the cross section measurement.

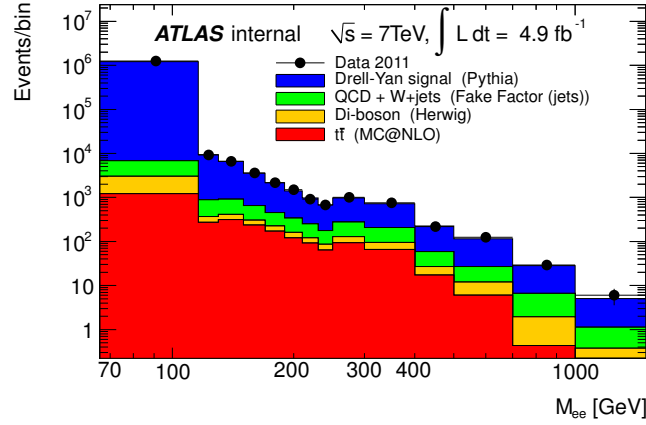
	m_{ee} [GeV]						
	66-116	116-130	130-150	150-170	170-190	190-210	210-230
Data	1253205	9214	6634	3609	2160	1489	918
multi-jet + W+jet	3800 \pm 1900 (tot)	530 \pm 106 \pm 11	500 \pm 100 \pm 10	345 \pm 69 \pm 7	229 \pm 46 \pm 6	182 \pm 37 \pm 5	130 \pm 26 \pm 5
$t\bar{t}$	1210 \pm 120 \pm 8	272 \pm 27 \pm 4	314 \pm 31 \pm 4	234 \pm 23 \pm 3	171 \pm 17 \pm 3	121 \pm 12 \pm 2	92 \pm 9 \pm 2
Diboson	1822 \pm 91 \pm 7	95 \pm 5 \pm 2	99 \pm 5 \pm 2	72 \pm 4 \pm 2	53 \pm 3 \pm 1	39 \pm 2 \pm 1	29 \pm 2 \pm 1
N_{sig}	1246300	8320	5720	2957	1707	1147	667
\pm data stat.	\pm 1120	\pm 96	\pm 81	\pm 60	\pm 47	\pm 39	\pm 30
\pm tot syst.	\pm 1920	\pm 110	\pm 110	\pm 73	\pm 49	\pm 39	\pm 28
DY signal PYTHIA	1199040 \pm 760	8261 \pm 46	5556 \pm 31	2820 \pm 22	1670 \pm 17	1057 \pm 13	710 \pm 11
DY signal MC@NLO	1235200 \pm 1300	8514 \pm 70	5529 \pm 40	2742 \pm 29	1591 \pm 22	1027 \pm 17	651 \pm 14

	m_{ee} [GeV]						
	230-250	250-300	300-400	400-500	500-700	700-1000	1000-1500
Data	675	1011	757	217	125	29	6
multi-jet + W+jet	92 \pm 18 \pm 4	147 \pm 29 \pm 4	113 \pm 23 \pm 3	32 \pm 6 \pm 2	15 \pm 3 \pm 1	4.7 \pm 0.94 \pm 0.89	0.8 \pm 0.2 \pm 0.4
$t\bar{t}$	64 \pm 6 \pm 2	94 \pm 9 \pm 2	66 \pm 7 \pm 2	17 \pm 2 \pm 1	6 \pm 1 \pm 1	0.4 \pm <0.1 \pm 0.2	0.1 \pm <0.1 \pm 0.1
Diboson	23 \pm 1 \pm 1	36 \pm 2 \pm 1	29 \pm 2 \pm 1	10 \pm 1 \pm 1	6 \pm <1 \pm <1	1.5 \pm <0.1 \pm 0.2	0.2 \pm <0.1 \pm 0.1
N_{sig}	496	734	549	158	98	22.3	4.9
\pm data stat.	\pm 26	\pm 32	\pm 28	\pm 15	\pm 11	\pm 5.4	\pm 2.4
\pm tot syst.	\pm 20	\pm 31	\pm 24	\pm 7	\pm 4	\pm 1.3	\pm 0.4
DY signal PYTHIA	475.5 \pm 8.4	685.6 \pm 4.6	500.5 \pm 3.7	158.0 \pm 1.3	84.4 \pm 0.5	20.8 \pm 0.1	3.73 \pm 0.01
DY signal MC@NLO	461 \pm 11	674 \pm 10	482 \pm 9.1	158.4 \pm 3.4	86.3 \pm 2.0	22.4 \pm 1.2	3.93 \pm 0.03

Table 4.4: Number of candidate events in data passing the selection of Section 4.3 in bins of m_{ee} . The number of background events from multi-jet and W+jets, $t\bar{t}$ and diboson processes are also shown with their systematic and statistical uncertainties, respectively. The multi-jet and W+jets component is estimated from the data and its statistical uncertainty comes from the size of the normalisation sample. The $t\bar{t}$ and diboson components are estimated from MC simulation and their statistical uncertainty originates from the finite MC statistics. The subtraction of these backgrounds gives the number of signal events N_{sig} in each bin which is reported with its total systematic uncertainty (sum in quadrature of total statistical and systematic uncertainties on background estimate) and the statistical uncertainty of the data. Comparisons are made to the MC predictions with statistical uncertainties. All MC corrections are applied, which includes K-factors on the signal predictions.



(a)



(b)

Figure 4.8: (a) Distribution of m_{ee} in data and MC in binning constant in $\log(m_{ee})$ and the ratio of the data to the total expectation. The total expectation comes from MC with statistical uncertainties except for the multi-jet and W+jets component which comes from the Fake Rate (Jet Stream) method with its total uncertainty. The dotted lines indicate the region of the cross section measurement. (b) The m_{ee} distribution in the measurement bins.

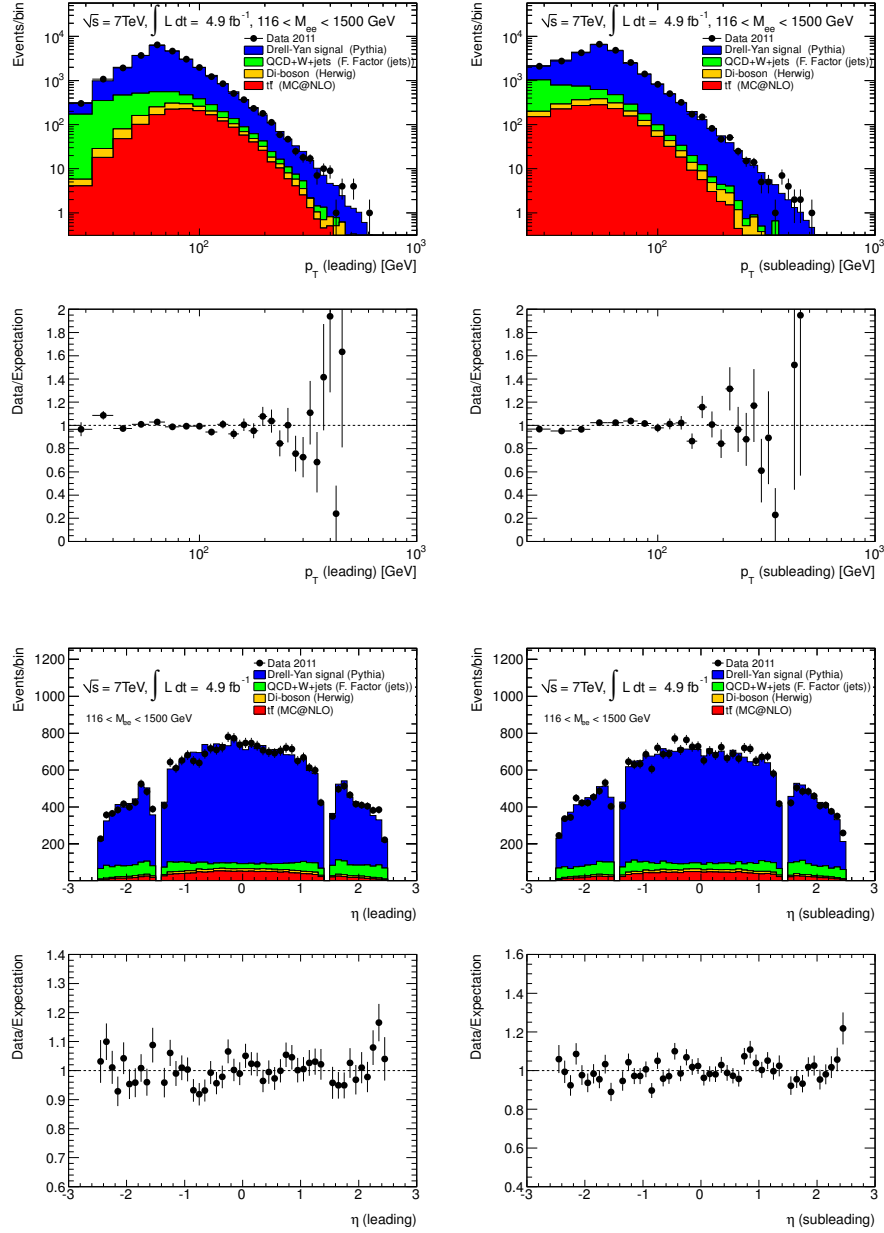


Figure 4.9: Distributions of E_T and η of the leading and subleading electron candidates in the m_{ee} region of the cross section measurement in data and MC. In the corresponding ratio plots, the total expectation comes from MC with statistical uncertainties except for the QCD + W+jets component which comes from the QCD fake rate method with its total uncertainty.

4.5 Electron Identification Efficiency Measurement

The electron reconstruction and identification (ID) algorithms used in ATLAS are designed to achieve both a large background rejection and a high and uniform efficiency over the full acceptance of the detector. Isolated electrons need to be separated from hadrons in jets, from background electrons (originating mostly from photon conversions in the tracker material), and from non-isolated electrons from heavy flavour decays. The identification efficiency, which is an important ingredient in any physics analysis, is in reality not uniform over all the coverage in solid angle of the detector. It is a function of the pseudorapidity η , mainly as a consequence of the non-uniform material distribution in the detector. Furthermore the identification efficiency depends also on the transverse energy (E_T) of the electron, as the interaction with the detector material (the shower shapes in the EM calorimeter or the probability of bremsstrahlung) is energy-dependent. Before this study, measurements of this dependence on data were only available up to an E_T of 50 GeV and the anticipated behaviour of the identification efficiency at high transverse energy needed to be investigated/confirmed as the high E_T region becomes more accessible in physics analyses such as the Drell-Yan cross section measurement as well as, for instance, searches for heavy gauge bosons in dielectron resonances at high invariant mass.

4.5.1 Methodology

A measured electron spectrum needs to be corrected for efficiencies related to the electron selection in order to derive cross sections of observed physics processes or limits on new physics. This correction factor is defined as the product of different efficiency terms, and in the DY cross section measurement the decomposition of the correction factor C_{DY} reads as

$$C_{DY} = \epsilon_{\text{event}} \cdot (\epsilon_{\text{reco}})^2 \cdot (\epsilon_{\text{ID}})^2 \cdot \epsilon_{\text{isol}} \cdot (\epsilon_{\text{trig}})^2 \cdot \Gamma \quad (4.2)$$

where ϵ_{event} accounts for the efficiency of the selection cuts applied on event level, ϵ_{reco} for the reconstruction efficiency, ϵ_{ID} for the identification (ID) efficiency, ϵ_{isol} for the isolation efficiency and ϵ_{trig} for the trigger efficiency for a single electron. Finally, Γ is a bin migration factor, see Section 4.6 for more details.

Electron efficiencies are typically measured by Tag-and-Probe methods at the LHC. In general, a Tag-and-Probe method aims to select a clean and unbiased sample of electrons, called *probe* electrons, using selection cuts, called *tag* requirements, primarily on other objects in the event. The efficiency of any selection cut can then be measured by applying it to the probe sample. In the case of this electron identification efficiency measurement, events of interest contain two electrons in the final state, one which is used to tag the event, and the other forming the probe sample. In the case of an electron ID efficiency measurement, the probe sample corresponds approximately to all reconstructed electrons. A typical such event with two reconstructed electrons corresponding to

a Z boson candidate can be illustrated in Fig. 4.10.

The above decomposition (Eq. 4.2) is particularly useful when the Monte Carlo predicted quantities for e.g. ϵ_{reco} , ϵ_{ID} , ϵ_{trig} and ϵ_{isol} can or have to be replaced by data-driven measurements. The replacement of MC predicted efficiencies by data-driven measurements can be done for any physics process based for example on Tag-and-Probe analyses, provided that the kinematic ranges of the efficiency measurement and the physics analysis in question overlap well enough. This replacement is done by multiplicative scale factors (SF) (Eq. 4.3) applied to the MC prediction. Scale factors are defined as the ratio of the data to MC efficiencies in a specific bin:

$$\text{scale factor (SF)} = \frac{\epsilon^{\text{data}}}{\epsilon^{\text{MC}}} \quad (4.3)$$

The range of validity of such scale factors depends on the kinematic parameters of the electrons used in the respective physics analysis itself, but may also depend significantly on more implicit observables such as the amount of jet activity in the events considered in the analysis with respect to that observed in the Tag-and-Probe samples.

The identification (ID) efficiency of an electron in data is defined as the number of observed probe electrons minus the estimated background passing the respective ID cuts divided by the number of base level electrons:

$$\epsilon_{\text{ID}}^{\text{data}} = \frac{N_{\text{ID}}^{\text{signal}}}{N_{\text{base}}^{\text{signal}}} \quad (4.4)$$

where $N_{\text{ID}}^{\text{signal}} = (N_{\text{observed}} - N_{\text{background}})_{\text{ID}}$ and accordingly $N_{\text{base}}^{\text{signal}} = (N_{\text{observed}} - N_{\text{background}})_{\text{base}}$. In general, there are various methods to estimate the contribution of the background, this measurement using templates taken directly from data, the details of which are given in Section 4.5.3. “Base” level refers to simple track quality cuts in this measurement, i.e. a minimum number of hits in the Pixel and SCT detector on top of the reconstruction. “ID” level is then the identification level of choice, which for this measurement is *Medium*.

The decomposition of the correction factor C_{DY} in Equation 4.2 hides for simplicity the dependence of the individual components on the pseudorapidity η and transverse energy E_{T} . In reality this dependence needs to be corrected for, especially if the kinematical distributions in the MC simulation differ from the real ones. With increasing statistics, the accuracy of the efficiency measurements based on data should match the statistical accuracy and bin sizes required by the physics measurements. The kinematical phase space has therefore been divided into bins defined in the probe electron phase space in pseudorapidity η and the transverse kinetic energy E_{T} , the resulting efficiencies and scale factors being potentially different from bin to bin.

The statistics with the full 2011 dataset available in the highest E_{T} bin ($E_{\text{T}} > 50 \text{ GeV}$) were not sufficient to measure the critical efficiency components in two dimensions. In Fig. 4.11 it can be seen that even for wide bins in η , the highest E_{T} bin contains only a few 100 events in certain

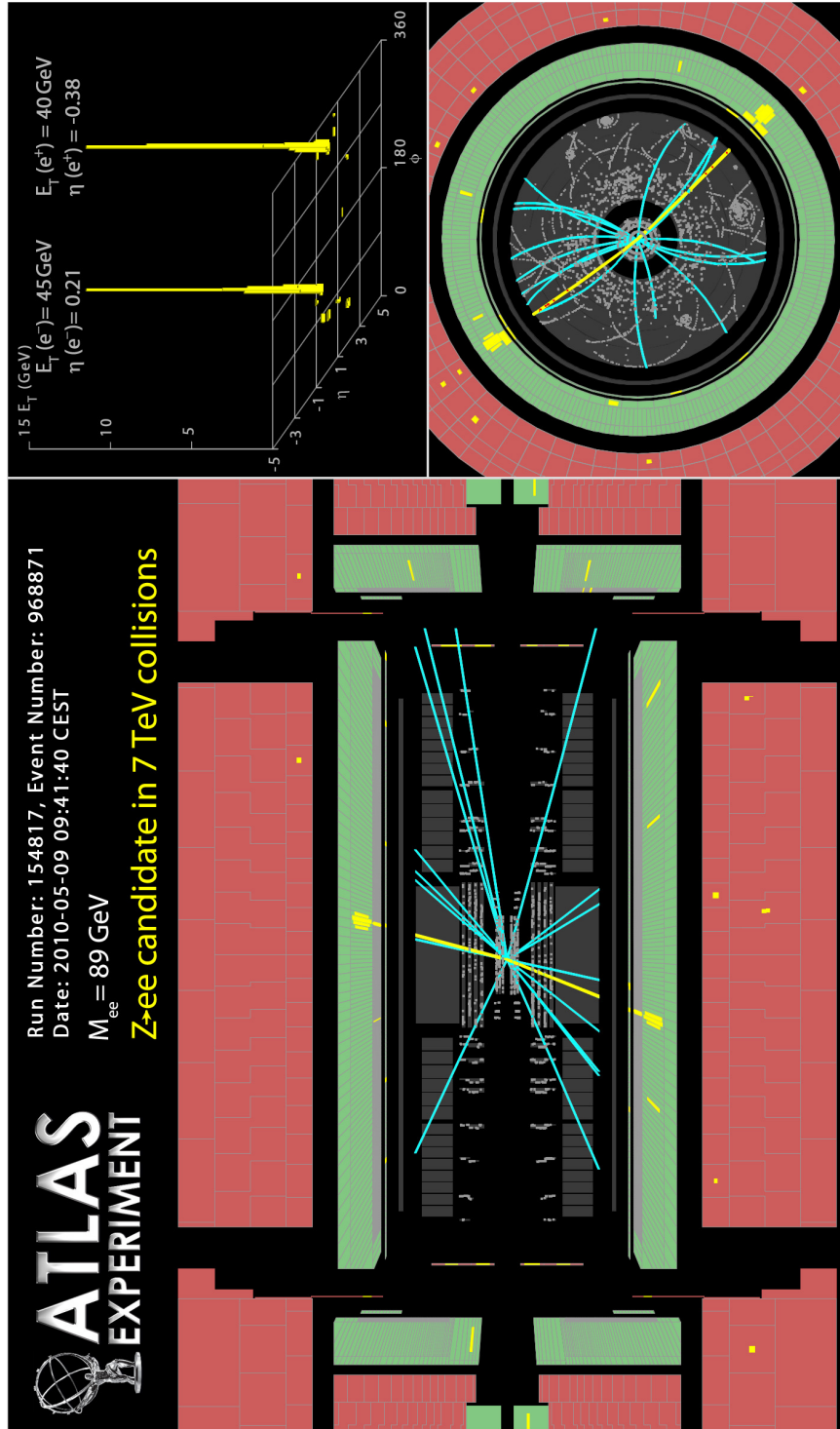


Figure 4.10: *Event Display for $Z \rightarrow ee$ from May 9th, 2010: two reconstructed electron candidates back-to-back with an invariant mass of $m_{ee} = 89 \text{ GeV}$.*

regions, while for a good measurement, a number of about 1000 probes per bin is required. Thus the corresponding scale factors were evaluated separately in bins of η and E_T as given in Table 4.5.

η	-2.47, -2.01, -1.52, -1.37, -0.80, -0.10, 0.10, 0.80, 1.37, 1.52, 2.01, 2.47
E_T	20, 25, 30, 35, 40, 45, 50, 80, 150, 500 (GeV)

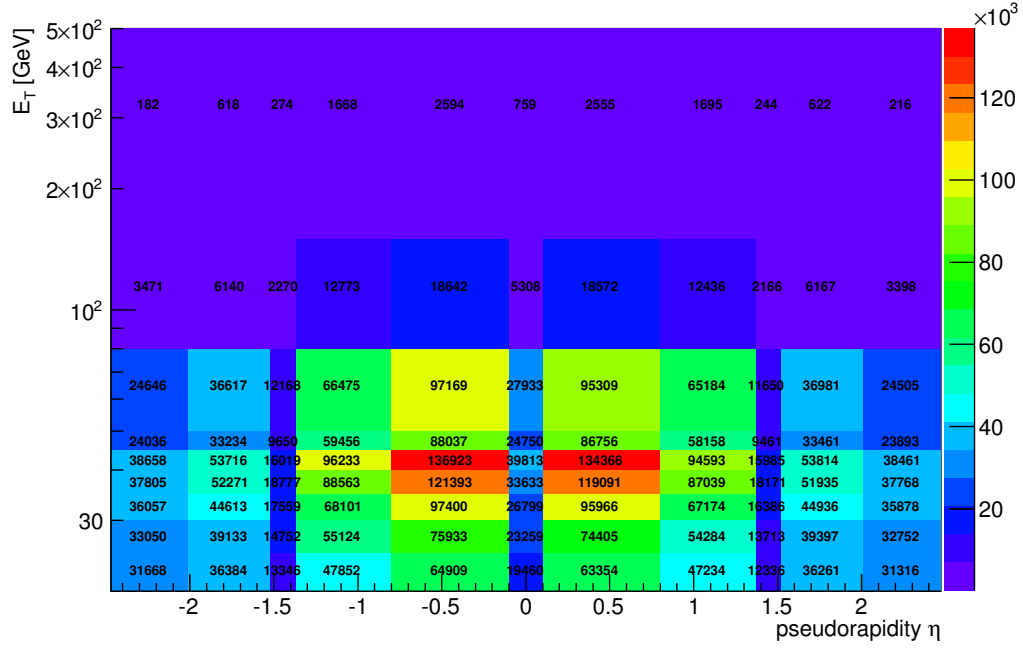
Table 4.5: *Bin boundaries in electron η and E_T used for the efficiency and scale factor measurement. The binning in η follows the changes in detector geometry. The E_T bins follow the binning of the cut optimization for $E_T < 50$ GeV, at higher E_T they are adjusted to contain sufficient statistics.*

4.5.2 Data and Monte Carlo Samples, Trigger and Event Selection

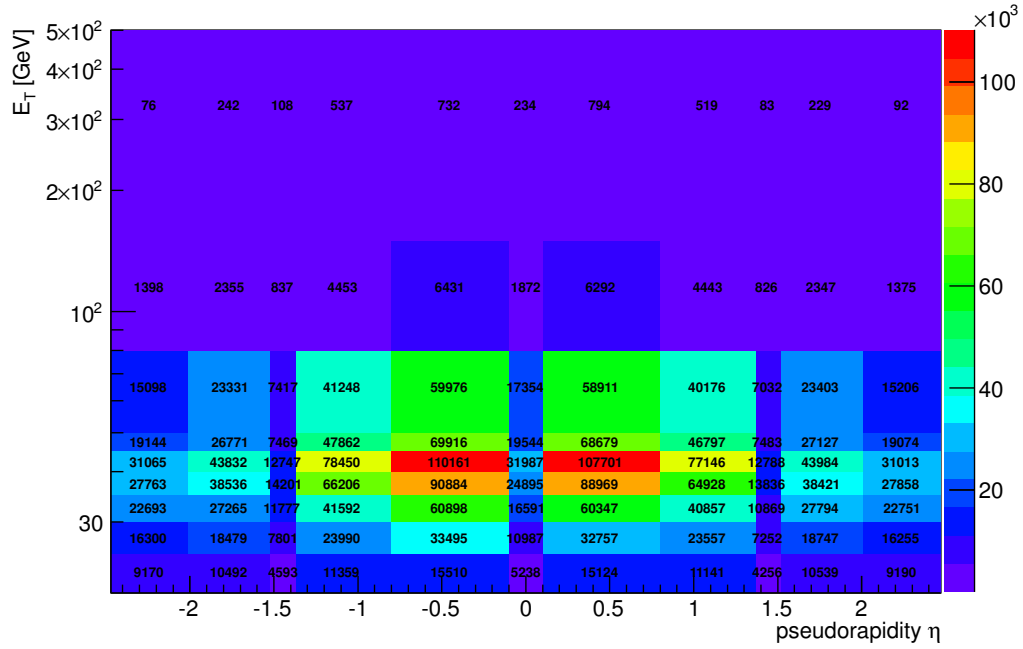
For this ID efficiency measurement, the same data was used as for the Drell-Yan cross section measurement: all of the data collected in 2011 (data taking periods B-M, see the table in appendix A.1). The same energy scale corrections were applied to the data as described in Section 4.2. Also the PYTHIA and the MC@NLO samples for the signal are the same as the ones used for the signal in the Drell-Yan cross section measurement, with the same corrections for pile-up.

Unlike for the Drell-Yan cross section measurement, a single electron trigger was used for this measurement, requiring at least one well-identified *Medium* electron with a transverse energy above 20 GeV (“e20_medium”) in data taking periods B-J and above 22 GeV (“e22_medium”) in period K. In the last periods L and M, a combination of two triggers was used, one with a threshold of 22 GeV (“e22vh_medium1”) and one with a threshold of 45 GeV (“e45_medium1”). For details on the data taking periods, see appendix A.1. The lower threshold “vh” trigger requires the hadronic leakage core isolation to be less than 1 GeV at LVL1. This is similar to the hadronic leakage selection in electron identification but as it uses a fixed upper energy cut it causes an inefficiency at very high transverse energy ($E_T > 300$ GeV). Therefore e45_medium1 is used in an OR combination to recover losses of very high E_T electrons. The different choice of trigger is due to the requirement of the probe sample to be unbiased, as for the “2g20_loose” trigger the probe would also need to pass the *Loose* identification. For MC, the trigger in use corresponds to the the trigger conditions in the represented data taking periods.

Only events collected by these single electron triggers and passing data-quality criteria, in particular concerning the Inner Detector and the calorimeters, were considered. At least one reconstructed primary vertex with at least three tracks should be present in the event. Additional cuts were applied to remove electron candidates pointing to problematic regions of the calorimeter readout. On event level, the selection is the same as for the Drell-Yan analysis.



(a)



(b)

Figure 4.11: Available probe statistics with the full 2011 dataset on (a) base level ("track quality") and (b) Medium ID level in bins of η and E_T as defined in Table 4.5.

Probe Selection

For the probe selection on reconstructed electron level, the following criteria had to be met. The pseudorapidity of the probe electron candidate should be within the acceptance of the EM calorimeter ($|\eta| < 2.47$) and its transverse energy should be > 20 GeV. Calorimeter Object Quality requirements should be met and possible LAr noise bursts should be vetoed. Furthermore, the probe electron candidate should have at least one hit in the pixel detector and at least 7 hits total in the pixel and SCT system (“track quality” criteria). The probe electron candidate should also be away from jet activity, i.e. there should be no jet with $E_T > 20$ GeV within $\Delta R < 0.4$ of the probe electron candidate in the same event.

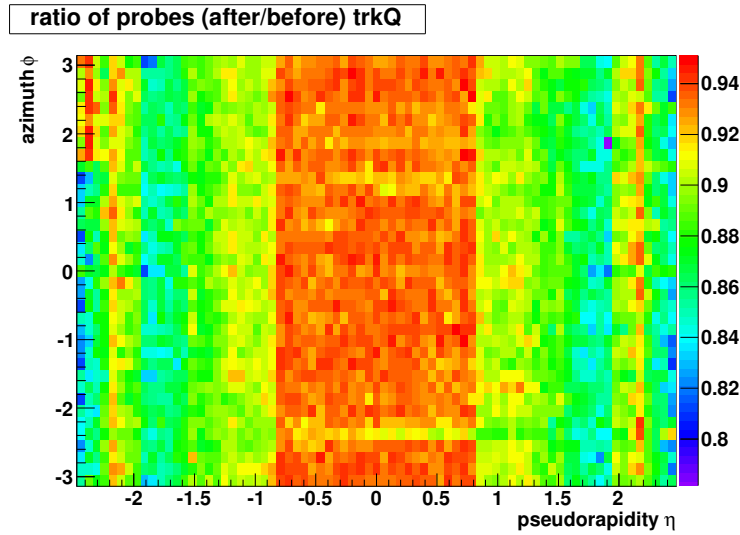


Figure 4.12: The efficiency of the “track quality” cut as the ratio of (probes after track quality)/ (probes before track quality).

Track quality cuts are required by an alternative ID efficiency measurement using $W \rightarrow e\nu$ decays. In that analysis, beam-halo background muons producing high-energy bremsstrahlung clusters in the EM calorimeter can be selected as electron probes and then be wrongly matched to a collision track in the TRT. For a better compatibility of the ID efficiency measurements, the same track quality requirement is applied also in this measurement. The efficiency of this track quality cut is illustrated in Fig. 4.12. While the difference in the amount of probes before and after the cut is very small ($\sim 3\%$) at low pseudorapidity $|\eta|$, it amounts up to $\sim 14\%$ at $\eta > 1.52$. The efficiency of this cut in data is measured in a dedicated analysis.

Tag Selection

In addition to the probe selection requirements, the tag electron candidate should be from outside of the EM Calorimeter barrel - end-cap transition region: $|\eta| < 1.37$ or $1.52 < |\eta| < 2.47$ and have an $E_T > 25$ GeV. The tag must also pass the *Tight* selection. The selected tag must match the event filter trigger object (i.e. the object that set off the trigger in the event) within a cone of $\Delta R < 0.15$ to avoid any trigger bias on the probe electron sample.

After the above selection, all possible tag and probe combinations are considered. The kinematic distributions are shown in Fig. 4.13 for *Medium* identification level. The visible difference in all distributions between data points and DY signal Monte Carlo is due to the presence of background events (hadronic jets faking electrons or electrons from heavy flavour decays or from photon conversions) in data.

4.5.3 Background Estimation

A discriminating variable is required to estimate the signal and background contributions in each E_T or η bin. At the track quality (base) level, the fraction of incorrectly identified electron candidates is relatively high. The misidentified electron candidates at this level originate mostly from hadronic jets, a small fraction comes from heavy flavour decays or photon conversions from bremsstrahlung of another electron in the event.

Hadronic jets faking electrons are estimated from data directly using the EM calorimeter isolation E_T^{cone} (as described in Section 3.3.2) as a discriminating variable. The method is based on the characteristic that real electrons such as from the DY process are well isolated, and their E_T^{cone} distribution peaks at values close to zero, with a width determined by the combination of electronic noise, shower leakage, underlying event and pile-up contributions. For the background from jets the same isolation distribution is much wider.

The signal region is defined by requiring the calorimeter isolation to be below a certain threshold. The background subtraction is then based on a template obtained directly from data and normalized to the number of selected electron probes in the background region at high E_T^{cone} values. Then the normalized template is subtracted from the probe isolation distribution at the chosen threshold.

The background template was obtained by inverting cuts of the electron identification (see Table 3.3 in Section 3.3.2) and/or cutting on the calorimeter shower shape variable $f_{\text{side}} > 0.55$ and on the energy ratio $R_\phi < 0.9$, according to their discriminating potential as discussed in Section 3.3.2. Five different background templates are formed, starting from the base level probe electron selection:

- **fside:** Probe with $f_{\text{side}} > 0.55$.
- **fside + !rTRT:** Probe with $f_{\text{side}} > 0.55$ and failing the f_{HT} electron identification cut for probe electrons with $|\eta| < 2.01$; for probes with $|\eta| > 2.01$, $R_\phi < 0.9$ is required instead.

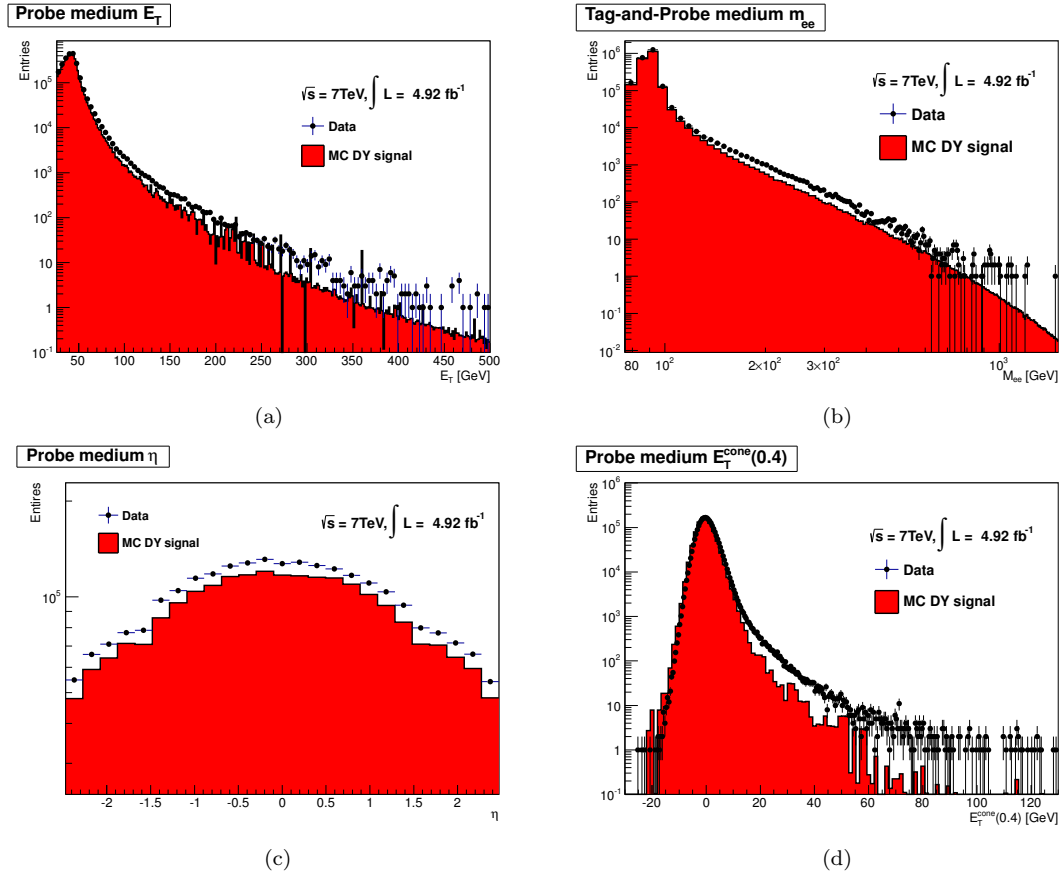


Figure 4.13: Control distributions on Medium Level for (a) electron E_T , (b) dielectron invariant mass, (c) electron pseudorapidity η and (d) isolation $E_T^{\text{cone}(0.4)}$. The data points and DY signal MC prediction do not match exactly as no background subtraction was performed on data. Thus the data contain backgrounds (jets faking electrons or electrons from heavy flavour decays or photon conversions) which leads to an increased number of events with respect to MC. The invariant mass of the Tag-and-Probe pair is required to be $m_{ee} > 76 \text{ GeV}$.

- **SS + !loose**: Probe with the same sign charge as the tag and failing the *Loose* electron identification requirement described in Table 3.3.
- **!Trackmatch**: Probe failing the $\Delta\eta$ electron identification cut.
- **!wstot + !rTRT + rphi**: Probe failing both the w_{stot} and f_{HT} electron identification cuts and having $R_\phi < 0.9$; for probe electrons with $|\eta| > 2.01$, only failing w_{stot} and $R_\phi < 0.9$ is required.

In addition, a template is defined using events collected by the jet trigger:

- **jet template**: Probe $f_{\text{side}} > 0.55$. For technical reasons, this template is not available in the transverse energy bin $E_T = 20 - 25 \text{ GeV}$ and in bins of pseudorapidity η .

The background template selections are the same for base level and *Medium* ID level, however for ID level, the electron probes need to pass the hadronic leakage cut (see Table 3.3) on top of the above definitions. Examples of these templates on base level are given in Fig. 4.14 and on *Medium* ID level in Fig. 4.15 for Tag-and-Probe pairs satisfying $76 < m_{ee} < 116 \text{ GeV}$. In addition to the selections discussed above, the measurement was divided into three regions of interest in terms of invariant mass of the Tag-and-Probe electron pair, the details are discussed in Section 4.5.6. See Appendix A.3 for all templates.

The “quality” of the background templates was evaluated such that the shape of the template matches well the tail of the probe isolation distribution and no significant signal contamination is present. A direct comparison of all available templates at base as well as ID level is shown in an example η bin in the EM calorimeter end-cap in Fig. 4.16 and the calorimeter barrel region in Fig. 4.17. In E_T bins, the same comparison is shown in Fig. 4.18 for the bin $E_T = 50\text{-}80 \text{ GeV}$. and in Fig. 4.19 for $E_T = 80\text{-}150 \text{ GeV}$.

The SS+!loose background template yields the best results both in bins of pseudorapidity η and transverse energy E_T , as it exhibits no signal contamination in the background template distribution. It also yields the most stable efficiencies and signal-to-background ratios for all m_{ee} selections. A similar behaviour is observed in an alternative measurement (Section 3.2 of Ref [63]), where background subtraction is performed using a sideband method with the invariant mass of the Tag-and-Probe pair as the discriminating variable. The shape of the background is then taken from same-sign-charge Tag-and-Probe pairs.

In the case of pseudorapidity η bins, not all templates were used as some of them showed significant signal contamination, most prominently the fside template. Thus only the SS+!loose and the !wstot+!rTRT+rphi templates were finally considered for the efficiency measurement in η bins, the latter to estimate the systematic uncertainty coming from the template choice.

In bins of transverse energy E_T , some templates were restricted to a certain region in E_T . All details concerning the templates and their validity range in this measurement are given in Table 4.6.

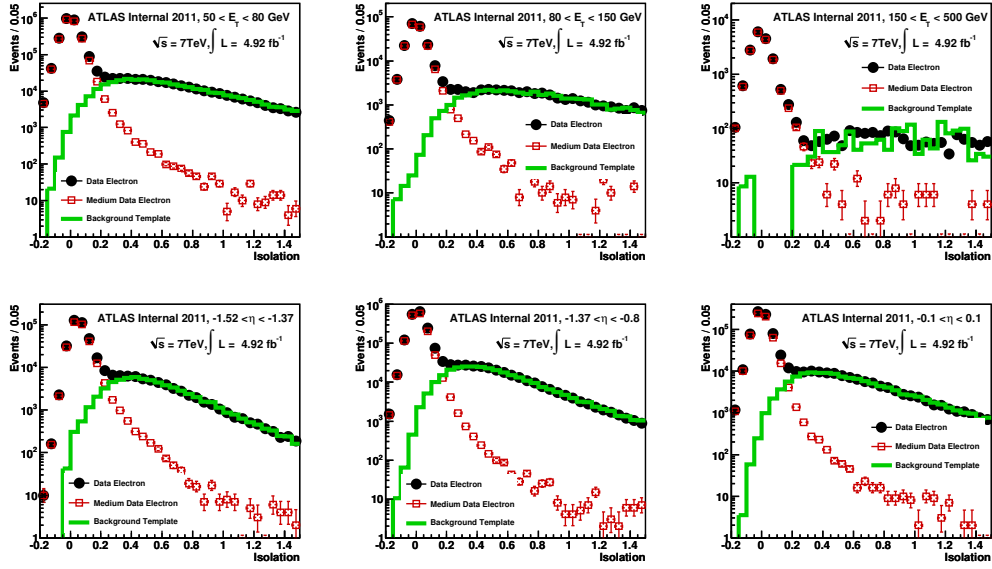


Figure 4.14: Isolation distribution using the $E_T^{\text{cone}}(0.4)/50 \text{ GeV}$ variable for all probes at base level passing track quality requirements (black dots), for all Medium probes (red squares) and the background template using the $SS+!loose$ selection (green line). Depicted are the last three bins in E_T (50 - 80, 80 - 150, 150 - 500 GeV) and three bins in η : $[-1.52, -1.37]$, $[-1.37, -0.8]$, $[-0.1, 0.1]$ for an invariant mass of the Tag-and-Probe pair with $76 < m_{ee} < 116 \text{ GeV}$. For all templates, please see appendix A.3.

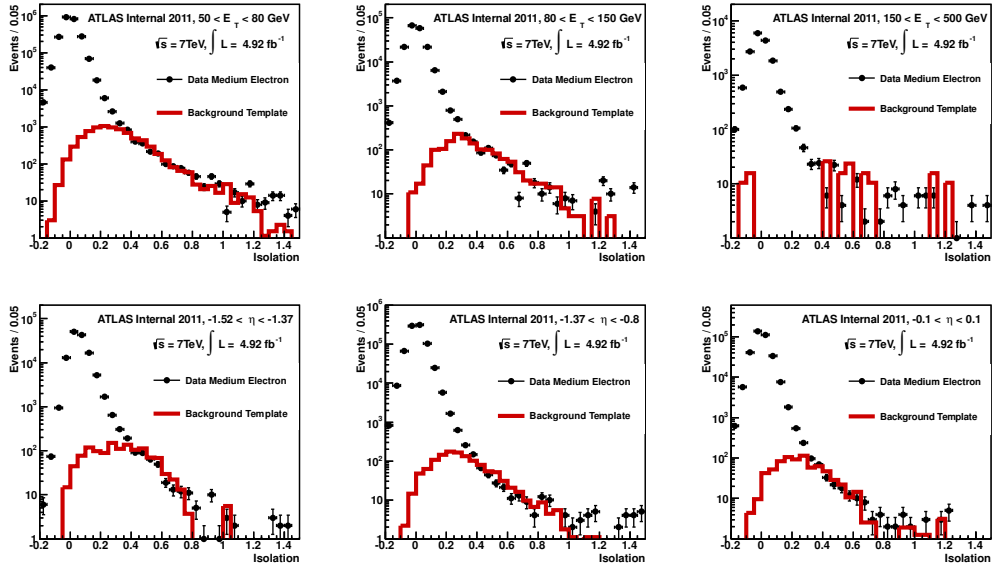


Figure 4.15: Isolation distribution using the $E_T^{\text{cone}}(0.4)/50 \text{ GeV}$ variable for all Medium probes (black dots) and the background template using the $SS+!loose$ selection (red line). Depicted are the last three bins in E_T (50 - 80, 80 - 150, 150 - 500 GeV) and three bins in η : $[-1.52, -1.37]$, $[-1.37, -0.8]$, $[-0.1, 0.1]$ for an invariant mass of the Tag-and-Probe pair with $76 < m_{ee} < 116 \text{ GeV}$. For all templates, please see appendix A.3.

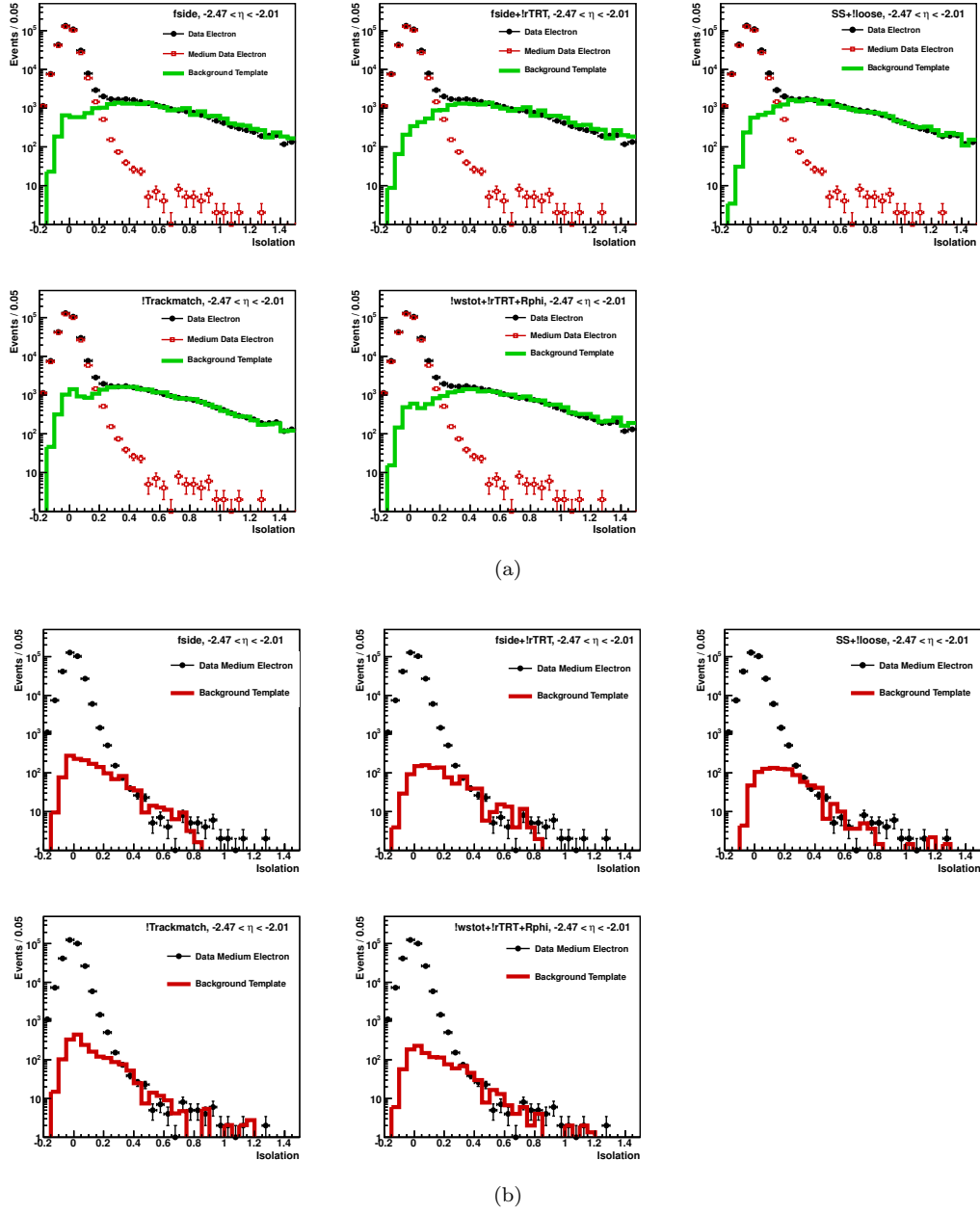


Figure 4.16: Isolation distribution using the $E_T^{\text{cone}}(0.4)/50$ variable in the pseudorapidity bin $[-2.47, -2.01]$ in the calorimeter end-cap region for (a) all probes at base level passing track quality requirements (black dots), for all Medium probes (red squares) and the background templates (green line) and (b) for all Medium probes (black dots) and the background template (red line). Depicted are all templates for an invariant mass of the Tag-and-Probe pair with $76 < m_{ee} < 116$ GeV.

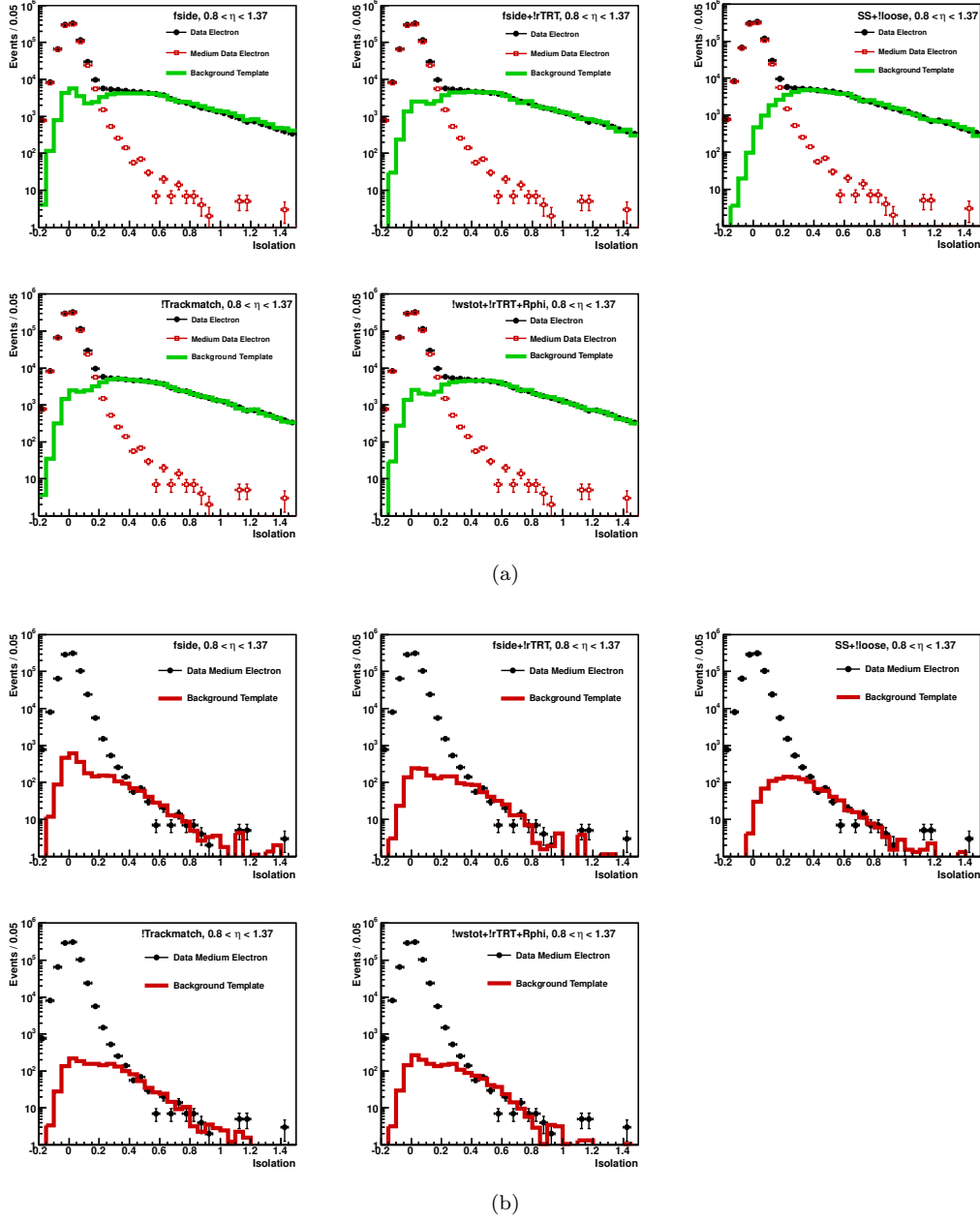


Figure 4.17: Isolation distribution using the $E_T^{\text{cone}}(0.4)/50$ variable in the pseudorapidity bin $[0.8, 1.37]$ in the calorimeter barrel region for (a) all probes at base level passing track quality requirements (black dots), for all Medium probes (red squares) and the background templates (green line) and (b) for all Medium probes (black dots) and the background template (red line). Depicted are all templates for an invariant mass of the Tag-and-Probe pair with $76 < m_{ee} < 116 \text{ GeV}$.

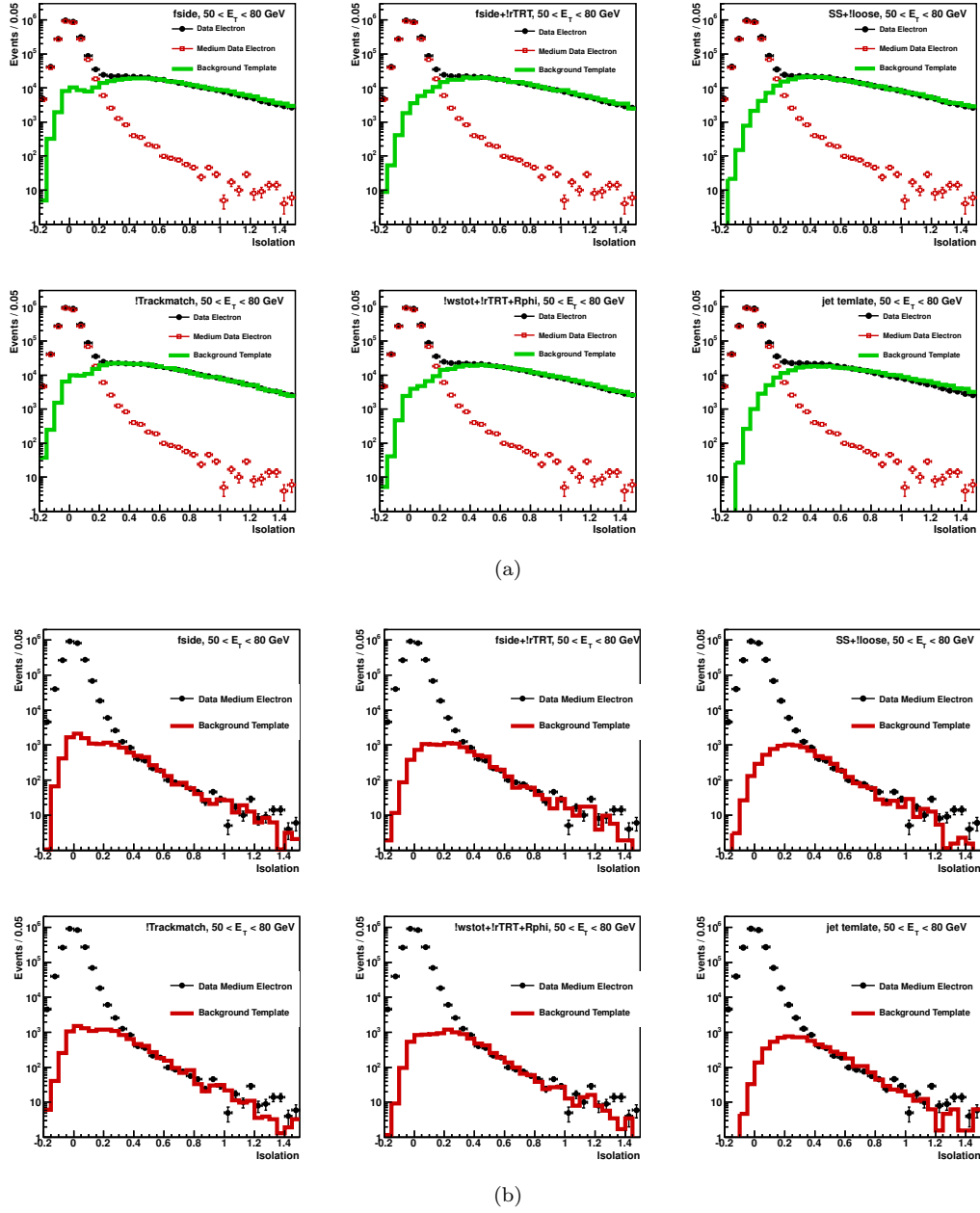


Figure 4.18: Isolation distribution using the $E_T^{\text{cone}}(0.4)/50$ variable in the transverse energy bin 50-80 GeV for (a) all probes at base level passing track quality requirements (black dots), for all Medium probes (red squares) and the background templates (green line) and (b) for all Medium probes (black dots) and the background template (red line). Depicted are all templates for an invariant mass of the Tag-and-Probe pair with $76 < m_{ee} < 116$ GeV.

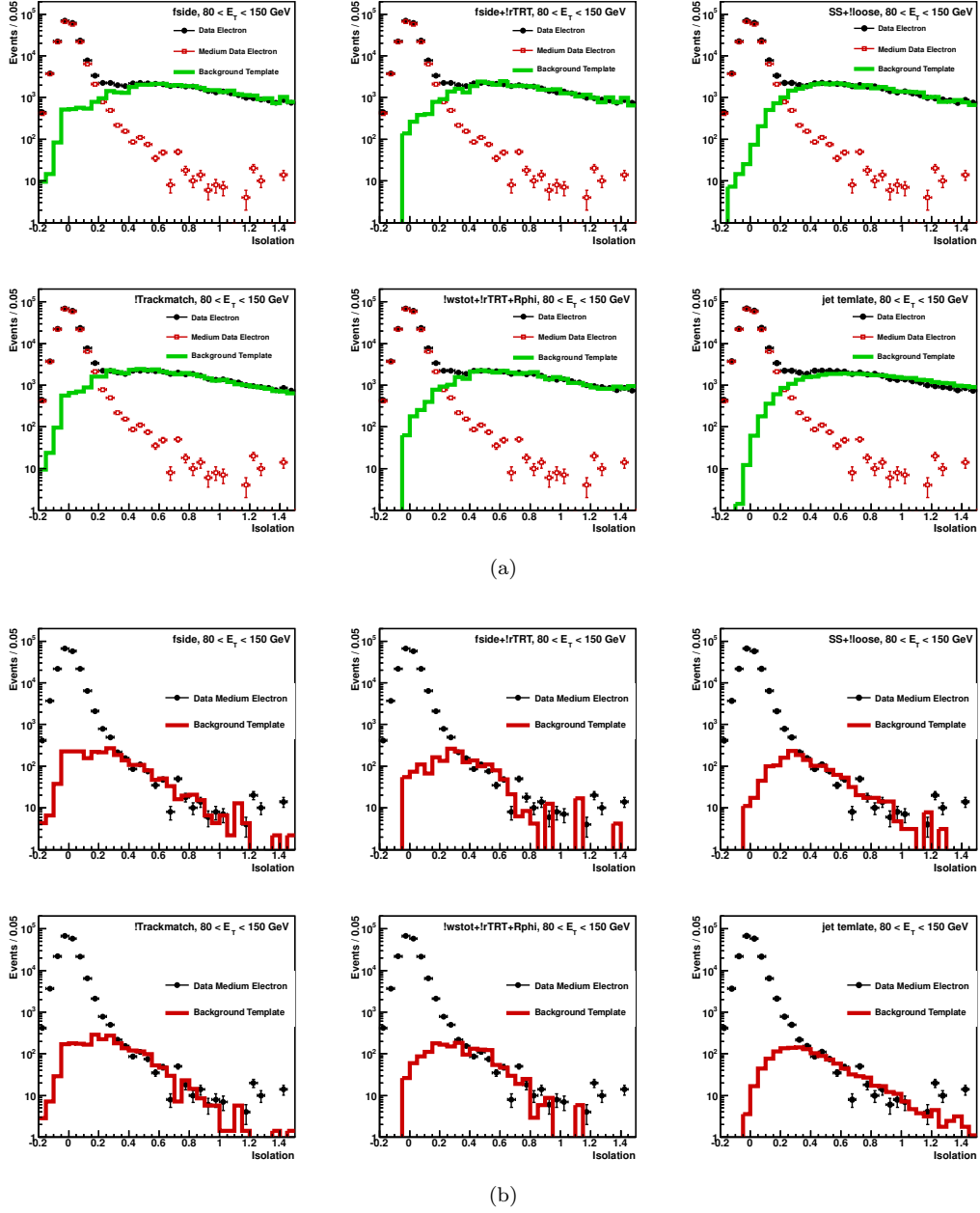


Figure 4.19: Isolation distribution using the $E_T^{\text{cone}}(0.4)/50$ variable in the transverse energy bin 80-150 GeV for (a) all probes at base level passing track quality requirements (black dots), for all Medium probes (red squares) and the background templates (green line) and (b) for all Medium probes (black dots) and the background template (red line). Depicted are all templates for an invariant mass of the Tag-and-Probe pair with $76 < m_{ee} < 116$ GeV.

4.5.4 Statistical and Systematic Uncertainties

Because of the presence of background, the simple binomial formula for the calculation of the statistical uncertainty on an efficiency measurement does not apply. The following variance applies for the error on the measured efficiencies when background needs to be subtracted following Ref. [107]:

$$(\Delta\epsilon_{\text{ID}}^{\text{stat}})^2 = \frac{(1 - 2\epsilon_{\text{ID}}) \cdot (\Delta N_{\text{ID}}^{\text{signal}})^2 + \epsilon_{\text{ID}}^2 \cdot (\Delta N_{\text{base}}^{\text{signal}})^2}{(N_{\text{base}}^{\text{signal}})^2} \quad (4.5)$$

where $\Delta N_{\text{base}}^{\text{signal}}$ and $\Delta N_{\text{ID}}^{\text{signal}}$ are the propagated statistical errors from N_{observed} and $N_{\text{background}}$ at base and ID level, respectively, as defined according to Eq. 4.4.

The dominant systematic uncertainties on the efficiency measurement are linked to the background subtraction from the probe samples, especially before applying the electron identification cuts. The background level under the signal was therefore varied substantially to verify the stability of the background subtraction procedure, mostly by varying the cuts applied to the tag component of the event. Furthermore, the background subtraction method itself was also varied by changing the discriminating variable and the isolation threshold. The following sources of systematic uncertainties were considered:

- **Background level:**

- The *tag* requirements were varied to induce variations of the background level under the signal. The electron candidate was selected with or without and *isolation* requirement for the tag, $E_{\text{T}}^{\text{cone}}(0.4) < 5 \text{ GeV}$.
- The *probe* was required to have *opposite sign charge* as the tag or there was no charge constraint at all.

- **Discriminating variable used in the background estimation:**

- The *isolation variable* was either $E_{\text{T}}^{\text{cone}}(0.4)$ or $E_{\text{T}}^{\text{cone}}(0.3)$. The latter was not used for the background template derived from the jet trigger stream.
- Three different values of the *isolation threshold* were chosen to test the signal contamination and the identification dependence on the isolation $E_{\text{T}}^{\text{cone}}/50 = 15, 17.5, 20 \text{ GeV}$.

- **Background subtraction:** six background templates as described in Section 4.5.3 were considered to assess the possible bias of the efficiency extraction method due to the template shape and possible signal contamination in the template.

This leads to a total of 2 (tag isolation) $\times 2$ (charge requirement) $\times 2$ (isolation variable) $\times 3$ (isolation threshold) $\times 6$ (background template) = 144 possible combinations. However, some configurations were excluded from the final combined results as the efficiencies were found to be unstable either because of limited statistics for certain templates in a given bin or due to the poor quality of

some background templates which showed significant signal contamination, i.e. contained isolated electrons. In bins of electron pseudorapidity η , the total number of combinations considered for the final results of the measurement is 24. In bins of transverse energy E_T the total number of combinations is ~ 100 . See Table 4.6 for a summary of the configurations considered for the evaluation of the systematic uncertainties on the ID efficiency in bins of η and E_T .

Template	η bins	E_T bins [GeV]			$E_T^{\text{cone}}(0.3)$	$E_T^{\text{cone}}(0.4)$
		20-25	25-50	50-500		
fside	×	✓	✓	×	✓	✓
fside + !rTRT/rphi	×	✓	✓	✓	✓	✓
SS+!loose	✓	✓	✓	✓	✓	✓
!Trackmatch	×	✓	✓	×	✓	✓
!wstot + !rTRT + rphi	✓	×	×	✓	✓	✓
jet template	×	×	✓	✓	×	✓

Table 4.6: *Templates as used in bins of pseudorapidity η and E_T for background subtraction in this measurement.*

Calculation of final efficiency results

The central value of the measured efficiency and scale factor was defined as the mean of the distribution of all the efficiency and scale factor values obtained through the variations discussed above. The root mean squared (RMS) of the measured uncertainties of the template variations was assigned as the systematic error. The statistical error is the mean of the statistical errors of all measurements corresponding to these configurations.

4.5.5 Efficiencies from Monte Carlo Simulation

To assess the ID efficiency in Monte Carlo (MC), there is no need for template-based background subtraction, but a so-called loose truth matching procedure is performed. As previous studies have shown, truth matching for electrons has an impact on the efficiencies expected for the identification cuts [108]. This is due to the possibility to match the EM calorimeter cluster not to the primary electron but another particle track after interactions of the electron with the material of the Inner Detector. A typical case is the so-called trident configuration in which the electron undergoes an early hard bremsstrahlung and the bremsstrahlung photon converts in the first silicon layers producing two additional tracks, one of which has charge opposite to that of the primary electron. In the cases where this latter track is chosen as a best match to the EM calorimeter cluster, the reconstructed electron object undergoes charge mis-measurement and has a much lower probability to pass the chosen identification cuts [63].

In MC simulation, information is kept for hits in the Inner Detector about which generated tracks

created them. A majority logic chooses the best matched generated track for any reconstructed track in an event. From this information, one can classify the reconstructed electron tracks in simulation into electrons directly matched to a true primary electron, into electrons indirectly matched to a true primary electron via tracks generated by bremsstrahlung photons or final-state-radiation photons from the process itself, and finally into electron tracks which correspond to charged hadrons or photon conversions, for example, from π^0 decays in hadronic jets.

Applying loose truth matching means accepting all reconstructed electrons matched to a true electron identified as coming from Z/γ^* decays or to one coming from final state radiation (FSR) or bremsstrahlung photons connected to the original Z . In other words not only the electron tracks created directly by the primary electron are considered as truth matched, but also those from photon conversions, both for photons produced through bremsstrahlung in the Inner Detector material and for FSR photons emitted in the process. For more details on MC truth matching, see also appendix 10.1.1 of Ref. [63].

4.5.6 Results and Comparison to Previous Measurements

As the the ID efficiency results for all dielectron invariant masses with $m_{ee} > 76 \text{ GeV}$ showed an unstable behaviour, two regions of interest in terms of the invariant mass m_{ee} of the Tag-and-Probe pair were defined. The ID efficiency results were evaluated separately and are discussed below for the choices:

- $76 < m_{ee} < 116 \text{ GeV}$
- $m_{ee} > 116 \text{ GeV}$

The Tag-and-Probe pairs with invariant masses above 76 GeV represent the sum of the above selection. While the results based on the full m_{ee} range are not discussed here in detail, the corresponding plots for measured ID efficiency and signal-over-background ratio (S/B) at ID and base level can be found in the appendix (A.4).

The predicted MC efficiencies are shown separately from MC@NLO and PYTHIA DY MC samples for a dielectron invariant mass of $76 < m_{ee} < 116 \text{ GeV}$ in Fig. 4.20 and for $m_{ee} > 116 \text{ GeV}$ in Fig. 4.21. There is no significant difference in ID efficiency between the two dielectron invariant mass ranges. The dependence of the ID efficiency on the isolation cut is small, at most 2%, typically less than 1%.

The results of all the relevant systematic variations for the ID efficiency in data and the S/B after *Medium* identification and for base level (TrkQ) are shown in Figs. 4.22 and 4.23 for $76 < m_{ee} < 116 \text{ GeV}$ and Figs. 4.24 and 4.25 for $m_{ee} > 116 \text{ GeV}$ in bins of electron pseudorapidity η and E_T separately. As can be seen from those plots, events with an invariant mass $m_{ee} > 116 \text{ GeV}$ “contaminate” the measurement by introducing strong fluctuations depending mostly on the choice

of the background template. As discussed in Section 4.5.3, the quality of certain templates is poor as they exhibit visible signal contamination which introduces a bias to the background subtraction, as shown in Figs. 4.16 - 4.19. This effect is more significant for a low S/B as it is the case when going beyond an invariant mass of Tag-and-Probe pairs $m_{ee} > 116 \text{ GeV}$. In case of Tag-and-Probe pairs with $m_{ee} > 116 \text{ GeV}$, the S/B is a factor ~ 25 lower at base level and a factor 10 lower at ID level with respect to the $76 < m_{ee} < 116 \text{ GeV}$. The spread of the S/B of the different variations indicates the systematic uncertainty on the background estimate. The systematic uncertainty on the background at the base level has a larger impact on the efficiency than at the ID level as the S/B is smaller for the former.

To minimize the bias coming from the choice of the background template by preserving a good signal-to-background ratio, only events with an invariant mass in the region $76 < m_{ee} < 116 \text{ GeV}$ were considered for the evaluation of the final results and for comparison to other measurements in bins of η and E_T .

The results of the ID efficiency measurement for *Medium* identification for $76 < m_{ee} < 116 \text{ GeV}$ are summarized in Fig. 4.26 which shows the efficiency averaged over the selected systematic variations in bins of η and E_T . Overall, there is good agreement between the measured efficiency in data and MC for both PYTHIA and MC@NLO in bins of E_T , except for the lowest $E_T = 20 - 25 \text{ GeV}$ bin for both generators, where the difference is about 3%. The efficiencies in data and MC disagree most in the central region of $|\eta| = 0.1 - 0.8$, in the calorimeter transition region and the highest $|\eta|$ bin by $\sim 1\%$. The exact values with statistical and systematic uncertainties separately are also listed in Tables 4.7 and 4.8.

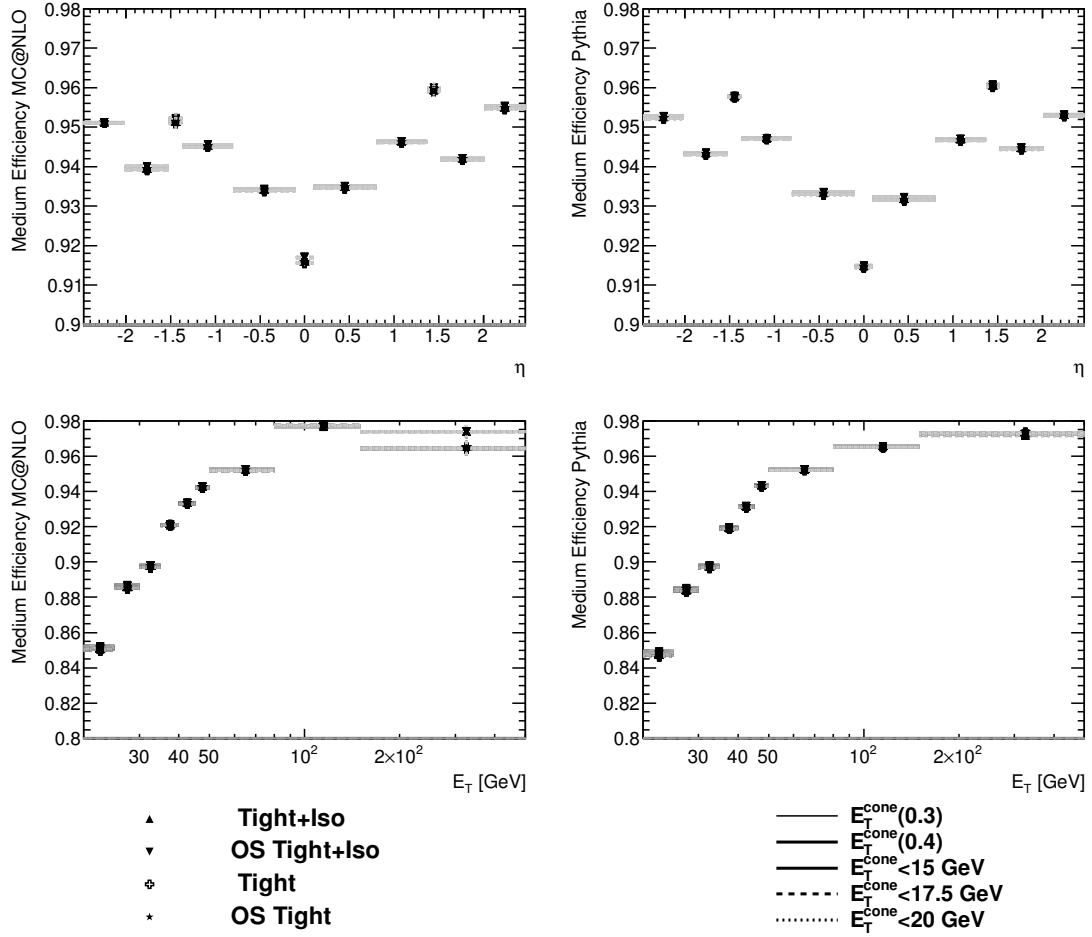


Figure 4.20: *Expected Medium identification efficiency from MC@NLO and PYTHIA Drell-Yan MC samples using loose truth matching, in bins of electron pseudorapidity η and transverse energy E_T , for dielectron invariant mass $76 < m_{ee} < 116$ GeV. Variations of the discriminating variable, the integration threshold, the charge sign requirement and the tag isolation are shown.*

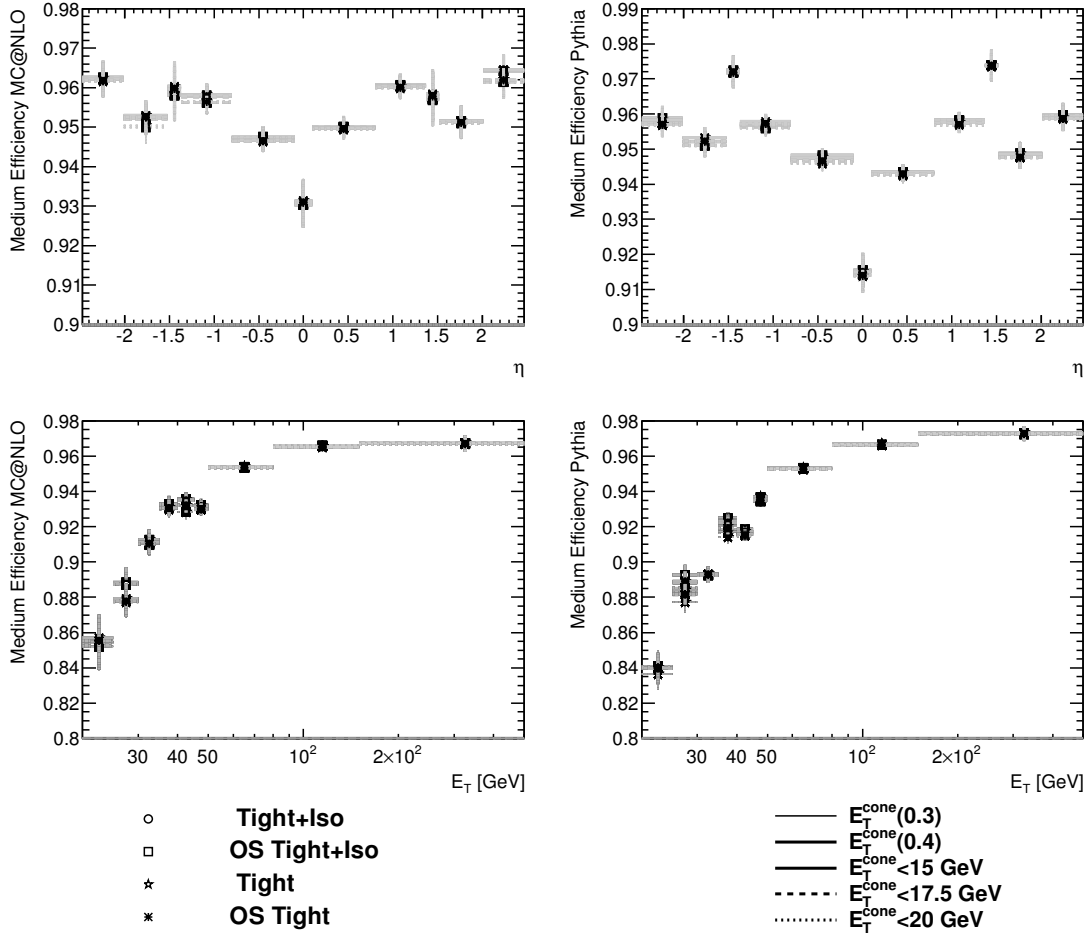


Figure 4.21: *Expected Medium Identification Efficiency from MC@NLO and PYTHIA Drell-Yan MC samples using loose truth matching, in bins of electron pseudorapidity and transverse energy, selection $m_{ee} > 116 \text{ GeV}$. Variations of the discriminating variable, the integration threshold, the charge sign requirement and the tag isolation are shown.*

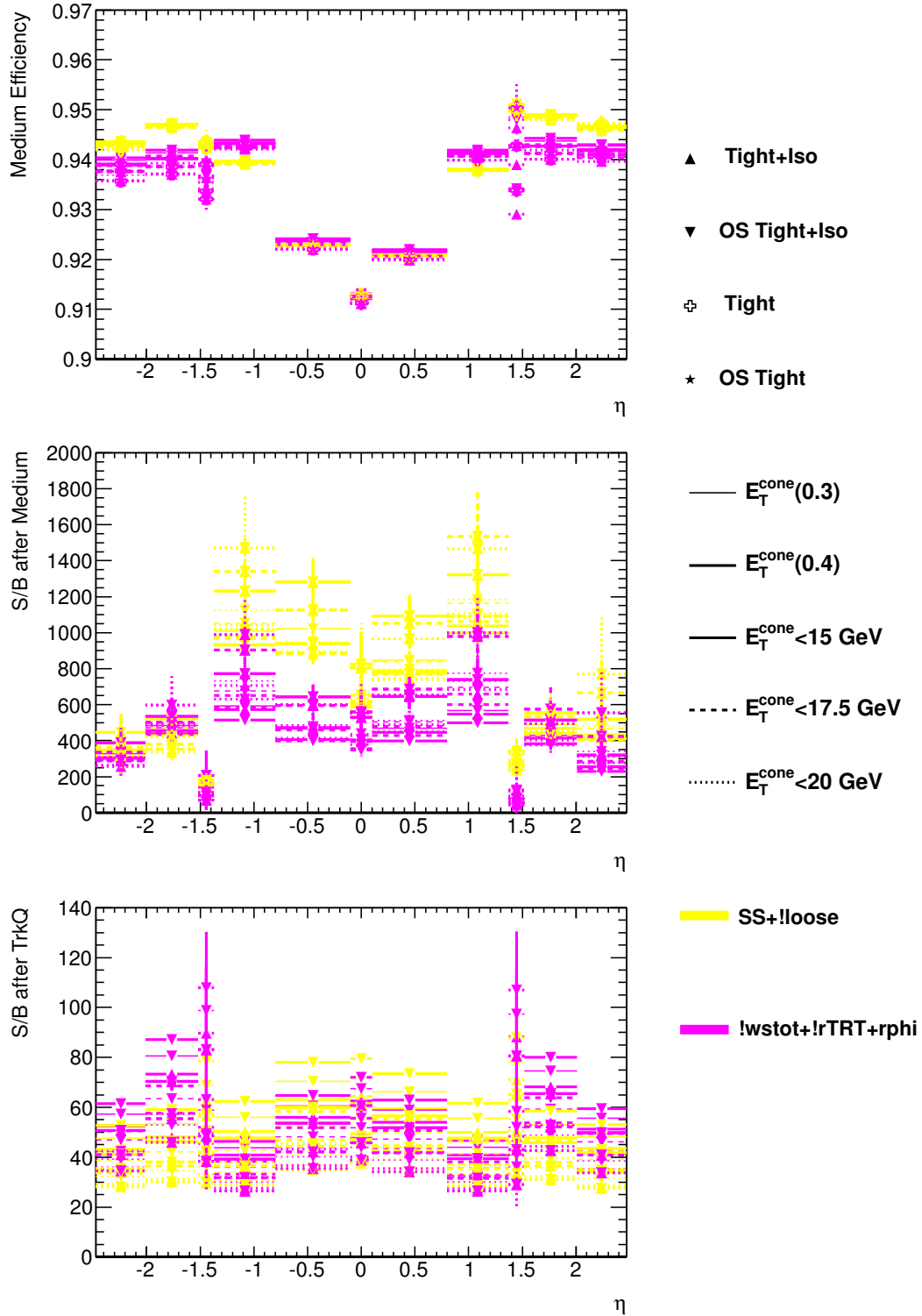


Figure 4.22: Measured Medium identification efficiency in data, signal over background ratio after Medium ID and for base level (TrkQ), in bins of electron pseudorapidity, for dielectron invariant mass $76 < m_{ee} < 116 \text{ GeV}$. For this measurement only the SS+!loose and !wstot + !rTRT + rphi templates were used.

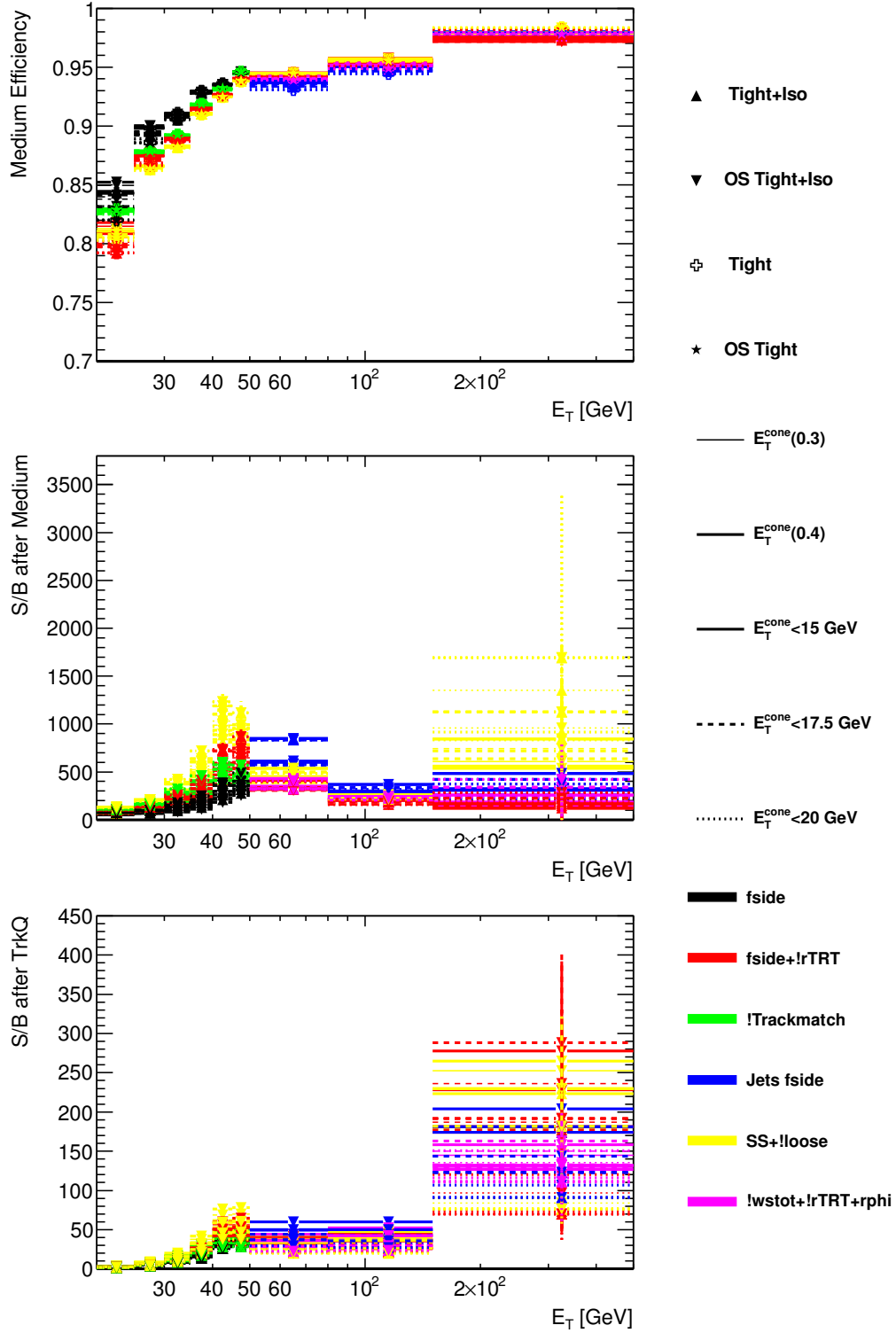


Figure 4.23: Measured Medium identification efficiency in data, signal over background ratio after Medium ID and for base level (TrkQ), in bins of electron transverse energy, for dielectron invariant mass $76 < m_{ee} < 116$ GeV, for all considered variations. Probes from within the EM calorimeter transition region ($1.37 < \eta < 1.52$) were omitted.

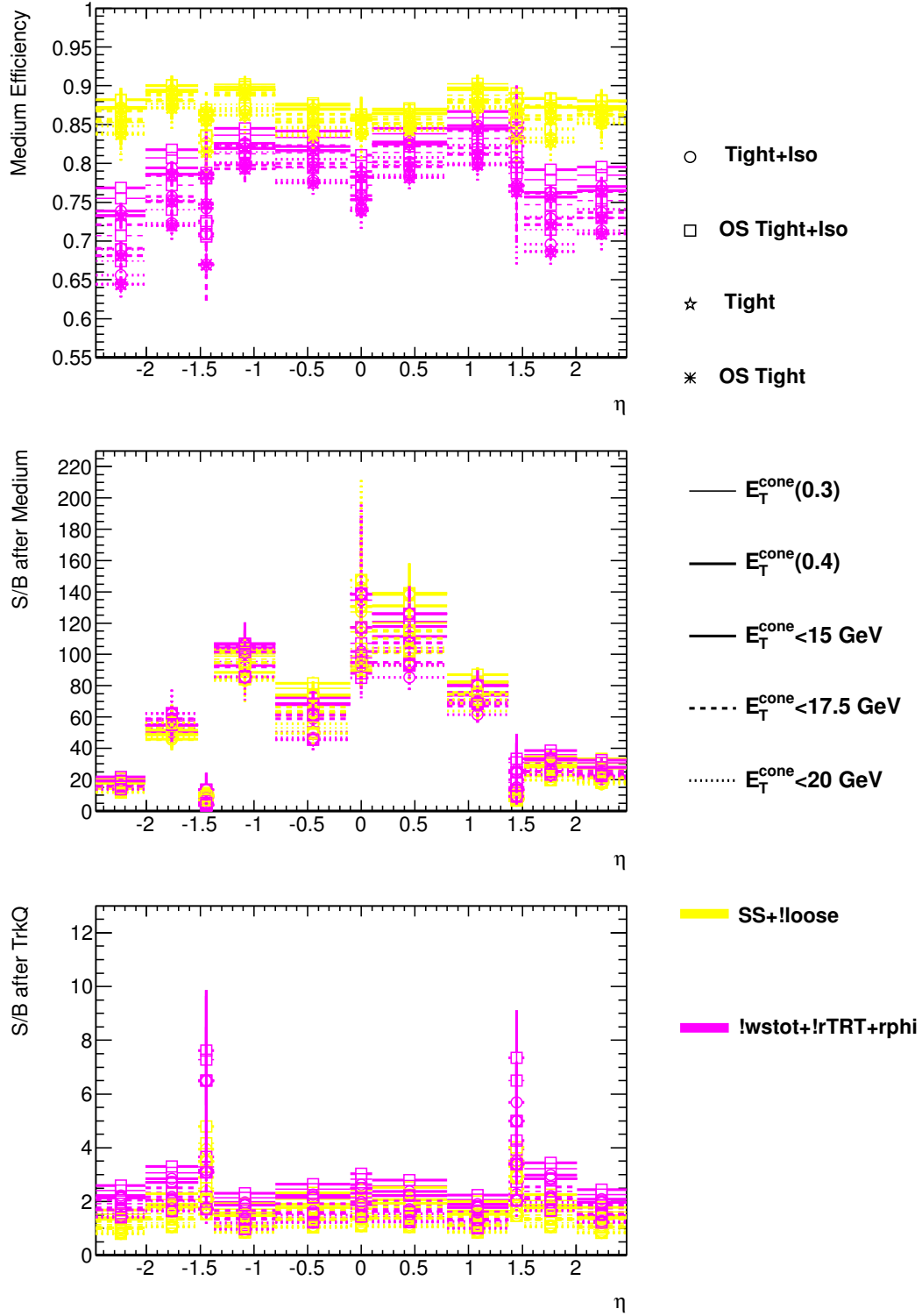


Figure 4.24: Measured Medium Identification efficiency in data, signal over background ratio after Medium ID and for base level (TrkQ) in bins of electron pseudorapidity, for dielectron invariant mass $m_{ee} > 116 \text{ GeV}$. For this measurement only the SS+!loose and !wstot + !rTRT + rphi templates were used.

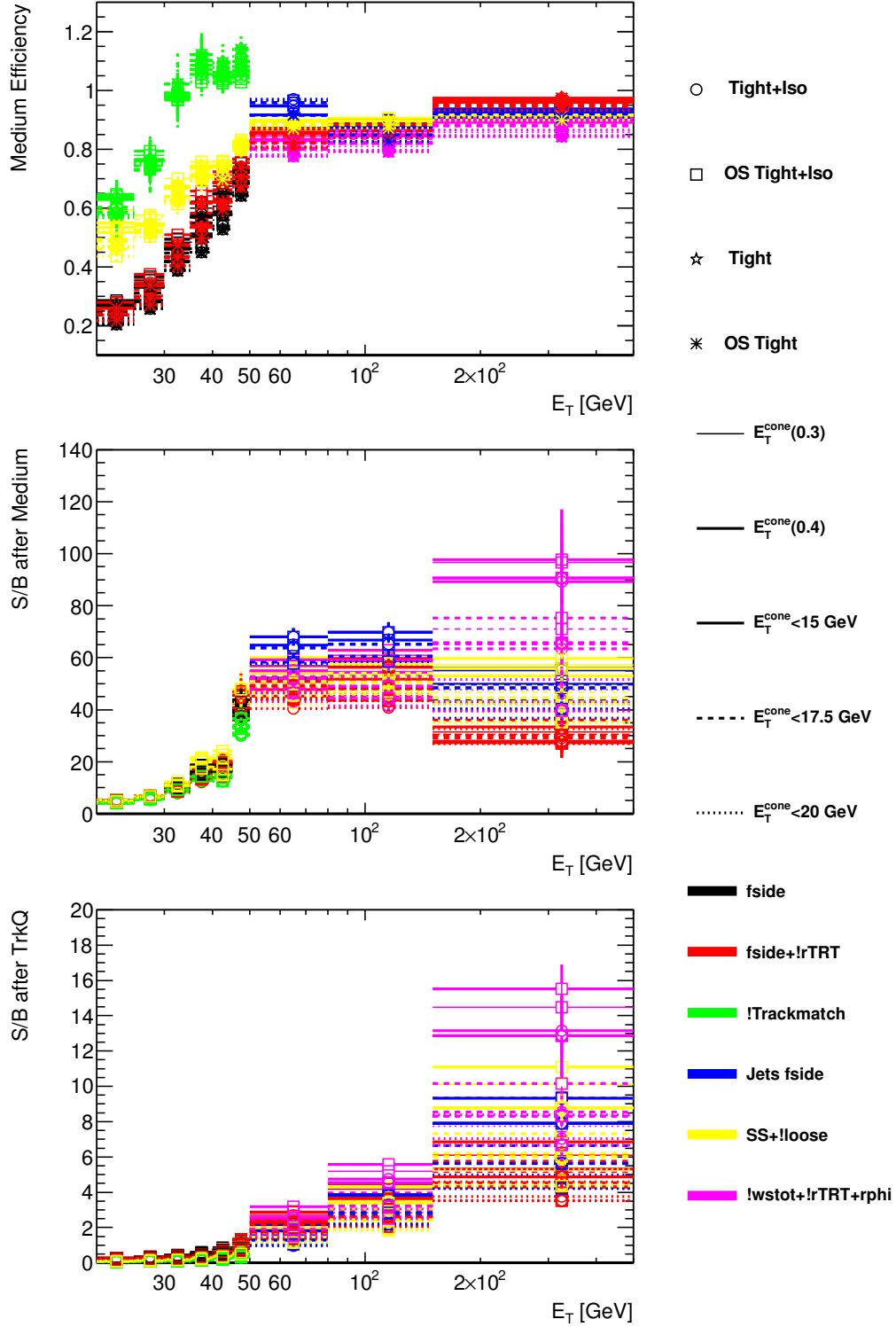


Figure 4.25: Measured Medium Identification efficiency in data, signal over background ratio after Medium ID and for base level (TrkQ), in bins of electron transverse energy, for dielectron invariant mass $m_{ee} > 116$ GeV, for all considered variations. Probes from within the EM calorimeter transition region ($1.37 < \eta < 1.52$) were omitted.

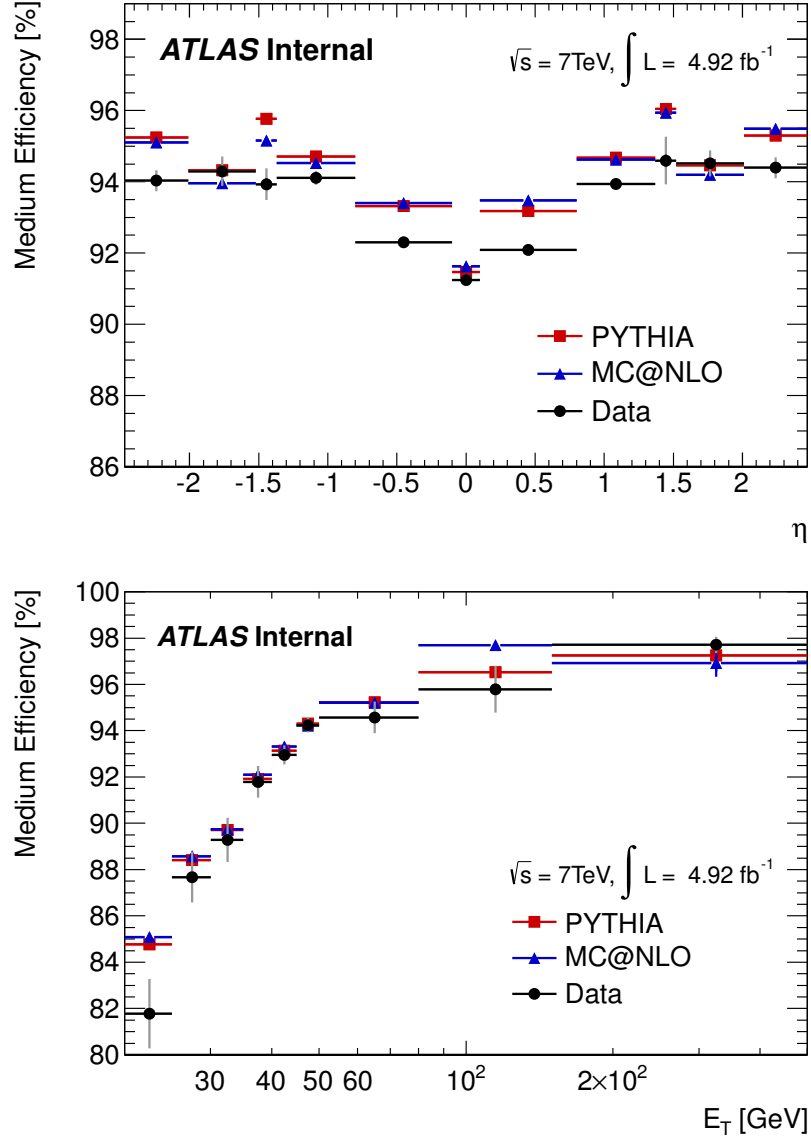


Figure 4.26: Average measured efficiency for data (black dots) and expectation from PYTHIA (red squares) and MC@NLO (blue triangles) DY MC simulation for Medium identification level in bins of electron pseudorapidity and transverse energy, for dielectron invariant mass $76 < m_{ee} < 116 \text{ GeV}$. The quoted uncertainties are combined statistical and systematic (gray error bars on data).

Calculating the ratio of the efficiency in data and in Monte Carlo yields the scale factors, evaluated separately for MC@NLO and PYTHIA, in bins of η and E_T (Fig. 4.27). The exact values for the measured scale factors with their statistical and systematic uncertainties are listed also in Tables 4.9 and 4.10. The total uncertainty in this “DY T&P” measurement is at most 1.8% in the lowest E_T bin and 0.8% in the highest E_T bin. In the lowest E_T bin, the uncertainty is dominated by systematics, in the highest E_T bin the contribution of the statistical error to the total uncertainty is larger. In Fig. 4.27 the scale factors of this measurement (“DY T&P”) are compared to previous measurements performed by the ATLAS e/γ working group, referred to as “ e/γ combined”, which were derived as a combination of two alternative Tag-and-Probe measurements: one using $W \rightarrow e\nu$ events and isolation templates for background subtraction, the other using $Z \rightarrow ee$ and the invariant of the Tag-and-Probe pair as the discriminating variable. The SF values from the latter are also separately shown as “ e/γ Z T&P”. The values of this measurement agree within total uncertainties in all the common E_T bins with “Z T&P” and in η bins with either “ e/γ combined” or “Z T&P” in all bins for PYTHIA. The precision of the measurement is limited by the systematic uncertainty in bins of η .

η	Data	PYTHIA	MC@NLO
[-2.47, -2.01]	$94.03 \pm 0.10 \pm 0.19$	$95.24 \pm 0.03 \pm 0.01$	$95.11 \pm 0.09 \pm 0.00$
[-2.01, -1.52]	$94.29 \pm 0.09 \pm 0.33$	$94.33 \pm 0.03 \pm 0.01$	$93.96 \pm 0.08 \pm 0.01$
[-1.52, -1.37]	$93.93 \pm 0.17 \pm 0.28$	$95.77 \pm 0.04 \pm 0.00$	$95.15 \pm 0.13 \pm 0.01$
[-1.37, -0.8]	$94.11 \pm 0.08 \pm 0.12$	$94.71 \pm 0.02 \pm 0.00$	$94.53 \pm 0.06 \pm 0.01$
[-0.8, -0.1]	$92.30 \pm 0.06 \pm 0.02$	$93.32 \pm 0.02 \pm 0.01$	$93.40 \pm 0.05 \pm 0.00$
[-0.1, 0.1]	$91.25 \pm 0.11 \pm 0.01$	$91.46 \pm 0.04 \pm 0.01$	$91.63 \pm 0.11 \pm 0.02$
[0.1, 0.8]	$92.08 \pm 0.06 \pm 0.02$	$93.18 \pm 0.02 \pm 0.02$	$93.48 \pm 0.05 \pm 0.01$
[0.8, 1.37]	$93.94 \pm 0.08 \pm 0.09$	$94.68 \pm 0.02 \pm 0.01$	$94.62 \pm 0.06 \pm 0.00$
[1.37, 1.52]	$94.60 \pm 0.16 \pm 0.50$	$96.04 \pm 0.04 \pm 0.01$	$95.94 \pm 0.12 \pm 0.01$
[1.52, 2.01]	$94.52 \pm 0.09 \pm 0.28$	$94.46 \pm 0.03 \pm 0.01$	$94.19 \pm 0.08 \pm 0.00$
[2.01, 2.47]	$94.40 \pm 0.11 \pm 0.19$	$95.30 \pm 0.03 \pm 0.00$	$95.49 \pm 0.08 \pm 0.01$

Table 4.7: Measured Medium ID efficiency in data compared to the prediction of PYTHIA and MC@NLO in % in bins of electron pseudorapidity η . The first error is statistical, the second systematic.

The “DY T&P” scale factor results for *Medium* identification in bins of E_T and η are normalized to the integral of the η efficiency measurement by a factor of 0.9913 for PYTHIA and 0.9909 for MC@NLO to compare directly with the “ e/γ combined” scale factors in the common E_T bins, shown in Fig. 4.28. These e/γ scale factors are also normalized to the integral of the η efficiency and available in bins of pseudorapidity η and transverse energy up to $E_T = 50$ GeV, in both cases in the same choice of bins as used in this ID efficiency measurement. The value from the last bin in electron transverse energy was recommended for analyses measuring electrons with E_T above 50 GeV.

As the statistical uncertainty is smaller for the PYTHIA MC samples than for MC@NLO, the scale factors for PYTHIA from this measurement were chosen as the basis for comparison with the e/γ scale

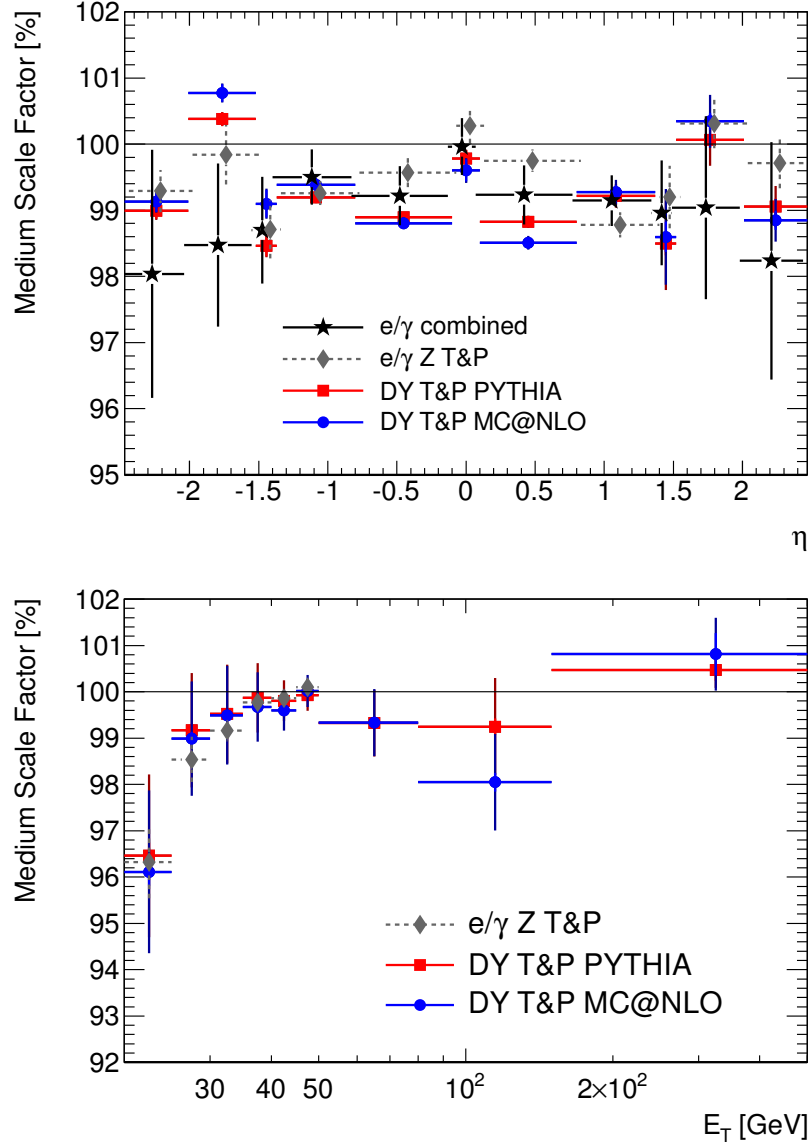


Figure 4.27: Measured Scale factors (“DY T&P”) for Medium identification for dielectron invariant mass $76 < m_{ee} < 116$ GeV for PYTHIA (red squares) and MC@NLO (blue dots). (a) In bins of electron pseudorapidity compared to SFs obtained by other measurements using $Z \rightarrow ee$ events and m_{ee} as the discriminating variable (“ e/γ Z T&P”, gray diamonds) and a combination of two measurements, “ e/γ Z T&P” and another one using $W \rightarrow e\nu$ events and isolation templates for background estimation (“ e/γ combined”, black stars). For clarity, the DY T&P and the e/γ values are slightly displaced horizontally in opposite direction with respect to each other. (b) In bins of electron transverse energy E_T the SF of this measurement are compared to SFs “ e/γ Z T&P” (gray diamonds). Very good agreement is seen in the common bins. The quoted uncertainties are statistical and systematic (darker hue).

E_T [GeV]	Data	PYTHIA	MC@NLO
[20, 25]	$81.78 \pm 0.23 \pm 1.27$	$84.78 \pm 0.03 \pm 0.06$	$85.09 \pm 0.08 \pm 0.02$
[25, 30]	$87.68 \pm 0.12 \pm 0.97$	$88.41 \pm 0.02 \pm 0.05$	$88.57 \pm 0.05 \pm 0.04$
[30, 35]	$89.29 \pm 0.07 \pm 0.89$	$89.72 \pm 0.01 \pm 0.03$	$89.74 \pm 0.04 \pm 0.02$
[35, 40]	$91.79 \pm 0.04 \pm 0.64$	$91.91 \pm 0.01 \pm 0.02$	$92.09 \pm 0.03 \pm 0.01$
[40, 45]	$92.95 \pm 0.03 \pm 0.38$	$93.13 \pm 0.01 \pm 0.02$	$93.32 \pm 0.02 \pm 0.01$
[45, 50]	$94.24 \pm 0.04 \pm 0.28$	$94.31 \pm 0.01 \pm 0.02$	$94.22 \pm 0.03 \pm 0.01$
[50, 80]	$94.58 \pm 0.05 \pm 0.64$	$95.22 \pm 0.01 \pm 0.01$	$95.21 \pm 0.03 \pm 0.02$
[80, 150]	$95.79 \pm 0.17 \pm 0.84$	$96.52 \pm 0.03 \pm 0.01$	$97.70 \pm 0.09 \pm 0.01$
[150, 500]	$97.71 \pm 0.19 \pm 0.16$	$97.25 \pm 0.10 \pm 0.02$	$96.92 \pm 0.38 \pm 0.22$

Table 4.8: Measured Medium ID efficiency in data compared to the prediction of PYTHIA and MC@NLO in % in bins of electron transverse energy E_T . The first error is statistical, the second systematic.

E_T [GeV]	PYTHIA	MC@NLO
[-2.47, -2.01]	$98.73 \pm 0.11 \pm 0.19$	$98.87 \pm 0.15 \pm 0.18$
[-2.01, -1.52]	$99.96 \pm 0.10 \pm 0.34$	$100.36 \pm 0.13 \pm 0.32$
[-1.52, -1.37]	$98.08 \pm 0.19 \pm 0.28$	$98.72 \pm 0.24 \pm 0.26$
[-1.37, -0.8]	$99.37 \pm 0.08 \pm 0.12$	$99.56 \pm 0.10 \pm 0.11$
[-0.8, -0.1]	$98.91 \pm 0.07 \pm 0.02$	$98.82 \pm 0.09 \pm 0.02$
[-0.1, 0.1]	$99.76 \pm 0.13 \pm 0.01$	$99.58 \pm 0.17 \pm 0.03$
[0.1, 0.8]	$98.82 \pm 0.07 \pm 0.02$	$98.51 \pm 0.09 \pm 0.02$
[0.8, 1.37]	$99.22 \pm 0.09 \pm 0.09$	$99.27 \pm 0.10 \pm 0.08$
[1.37, 1.52]	$98.49 \pm 0.18 \pm 0.52$	$98.60 \pm 0.23 \pm 0.50$
[1.52, 2.01]	$100.06 \pm 0.10 \pm 0.29$	$100.34 \pm 0.13 \pm 0.27$
[2.01, 2.47]	$99.06 \pm 0.12 \pm 0.19$	$98.85 \pm 0.15 \pm 0.18$

Table 4.9: Medium ID scale factors for PYTHIA and MC@NLO in % in bins of electron pseudorapidity η . The first error is statistical, the second systematic.

E_T [GeV]	PYTHIA	MC@NLO
[20, 25]	$96.46 \pm 0.29 \pm 1.47$	$96.11 \pm 0.30 \pm 1.45$
[25, 30]	$99.17 \pm 0.14 \pm 1.09$	$98.99 \pm 0.15 \pm 1.08$
[30, 35]	$99.52 \pm 0.08 \pm 0.99$	$99.49 \pm 0.09 \pm 0.98$
[35, 40]	$99.87 \pm 0.05 \pm 0.70$	$99.67 \pm 0.06 \pm 0.69$
[40, 45]	$99.81 \pm 0.04 \pm 0.40$	$99.60 \pm 0.04 \pm 0.40$
[45, 50]	$99.93 \pm 0.04 \pm 0.30$	$100.02 \pm 0.05 \pm 0.29$
[50, 80]	$99.32 \pm 0.05 \pm 0.39$	$99.33 \pm 0.06 \pm 0.38$
[80, 150]	$99.25 \pm 0.18 \pm 0.36$	$98.05 \pm 0.20 \pm 0.35$
[150, 500]	$100.47 \pm 0.23 \pm 0.15$	$100.81 \pm 0.46 \pm 0.29$

Table 4.10: Medium ID scale factors for PYTHIA and MC@NLO in % in bins of electron transverse energy E_T . The first error is statistical, the second systematic.

factors, which are also computed with respect to PYTHIA predictions. Table 4.11 compares the scale factors for PYTHIA (DY T&P) directly bin-by-bin and after fitting over three different ranges with the scale factors of the last available bin in E_T for e/γ ($E_T = 45 - 50$ GeV). The results are also illustrated in Fig. 4.28. The values from this measurement agree within uncertainties (statistical + systematic) with the e/γ recommendations.

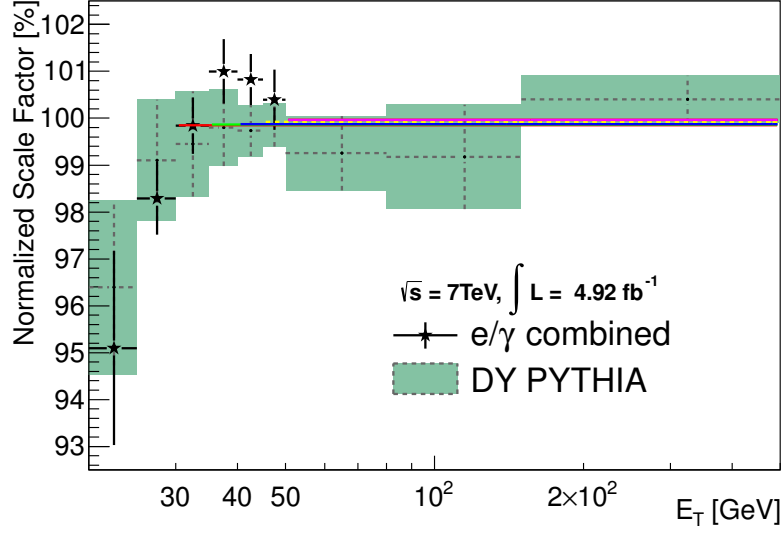


Figure 4.28: Normalized scale factor in bins of E_T for PYTHIA. The results for this measurement as well as constant fits in various fit ranges (in various colours) are compared to the official e/γ recommendations (“ e/γ combined”). All values agree within uncertainties, see also Table 4.11 for a direct bin-by-bin comparison.

E_T [GeV]	e/γ combined SF [%]	DY T&P SF [%]
20 - 25	95.10 ± 2.07	96.39 ± 1.86
25 - 30	98.29 ± 0.78	99.10 ± 1.29
30 - 35	99.84 ± 0.60	99.45 ± 1.13
35 - 40	101.00 ± 0.69	99.80 ± 0.82
40 - 45	100.83 ± 0.54	99.74 ± 0.55
45 - 50	100.39 ± 0.65	99.86 ± 0.47
50 - 80		99.26 ± 0.80
80 - 150		99.18 ± 1.11
150 - 500		100.40 ± 0.50

E_T range [GeV]	Scale Factor [%]
fit 30 - 500	99.85 ± 0.25
fit 35 - 500	99.87 ± 0.25
fit 40 - 500	99.88 ± 0.27
fit 45 - 500	99.92 ± 0.30
fit 50 - 500	99.96 ± 0.40

Table 4.11: Comparison of normalized DY T&P SF values and fit results for PYTHIA with the e/γ combined results: The DY T&P results agree within uncertainties with the e/γ recommendations when comparing bin-by-bin in the common bins of electron E_T (top). The values of this measurement obtained from fit results over various ranges of electron E_T (bottom) agree within uncertainties with the value in the last bin of the e/γ recommendations (“ e/γ combined”).

4.5.7 B-Layer Hit Efficiency Measurement

As in the high mass Drell-Yan analysis a hit in the B-Layer is required (if it is expected), the ID efficiency for *Medium+B-Layer* requirement as well as scale factors were also measured. The results of the efficiency measurement for *Medium+B-Layer* identification with respect to base level (“track quality”) are shown in Fig. 4.29, the scale factors are shown in Fig. 4.30. Precise values for both efficiencies and scale factors are given in Tables 4.12, 4.13, 4.14 and 4.15.

To compare the above values to other measurement and thus to validate the results, the efficiency of the the B-Layer hit with respect to electron candidates passing the *Medium* selection was measured as well. The efficiency of the B-Layer hit is then defined as:

$$\epsilon_{\text{B-Layer}} = \frac{\epsilon_{\text{Medium+B-Layer}}}{\epsilon_{\text{Medium}}} \quad (4.6)$$

The results of this B-Layer hit efficiency measurement are plotted in Fig. 4.31. The scale factor for B-Layer hit over *Medium* identification is then the ratio of the above B-Layer hit efficiency in data over the MC prediction:

$$SF_{\text{B-Layer}} = \frac{\epsilon_{\text{B-Layer}}^{\text{data}}}{\epsilon_{\text{B-Layer}}^{\text{MC}}} \quad (4.7)$$

These scale factors for *B-Layer* hit were also evaluated in the 2011 Z' dielectron resonance search in bins of pseudorapidity η and transverse energy up to $E_T = 250$ GeV. The results of this measurement (“DY T&P”) are compared to the “B-Layer SF Z' ” in Fig. 4.32. The exact Z' B-Layer scale factors are given in Tables 4.16 and 4.17. The binning in this measurement and that of the 2011 Z' B-Layer SF is not exactly the same, thus no direct bin-by-bin comparison can be made. However, very good agreement is observed within uncertainties in the common bins as well as the overlapping bins in both η and E_T . The 2011 Z' SF values were eventually used for the Drell-Yan analysis for full compatibility with the published results of exotic dielectron resonance searches in ATLAS.

4.5.8 Summary

The efficiencies in data and MC for *Medium* identification cuts were measured and scale factors were evaluated in bins of electron pseudorapidity η and transverse energy. This work extended the available measurement range of electron identification to the $E_T = 50\text{-}500$ GeV region in ATLAS with a precision of $\sim 2\%$ in the lowest E_T bin and $\sim 1\%$ in the high E_T bins. Good agreement was found with other measurements. Moreover, the B-Layer hit efficiency was measured, scale factors were evaluated and compared to the results of a similar measurement up to $E_T = 250$ GeV. Again, good agreement was found between the values from this and those from the other measurement whose scale factors were finally used for the Drell-Yan differential cross section measurement for reasons of full compatibility with other ATLAS analyses.

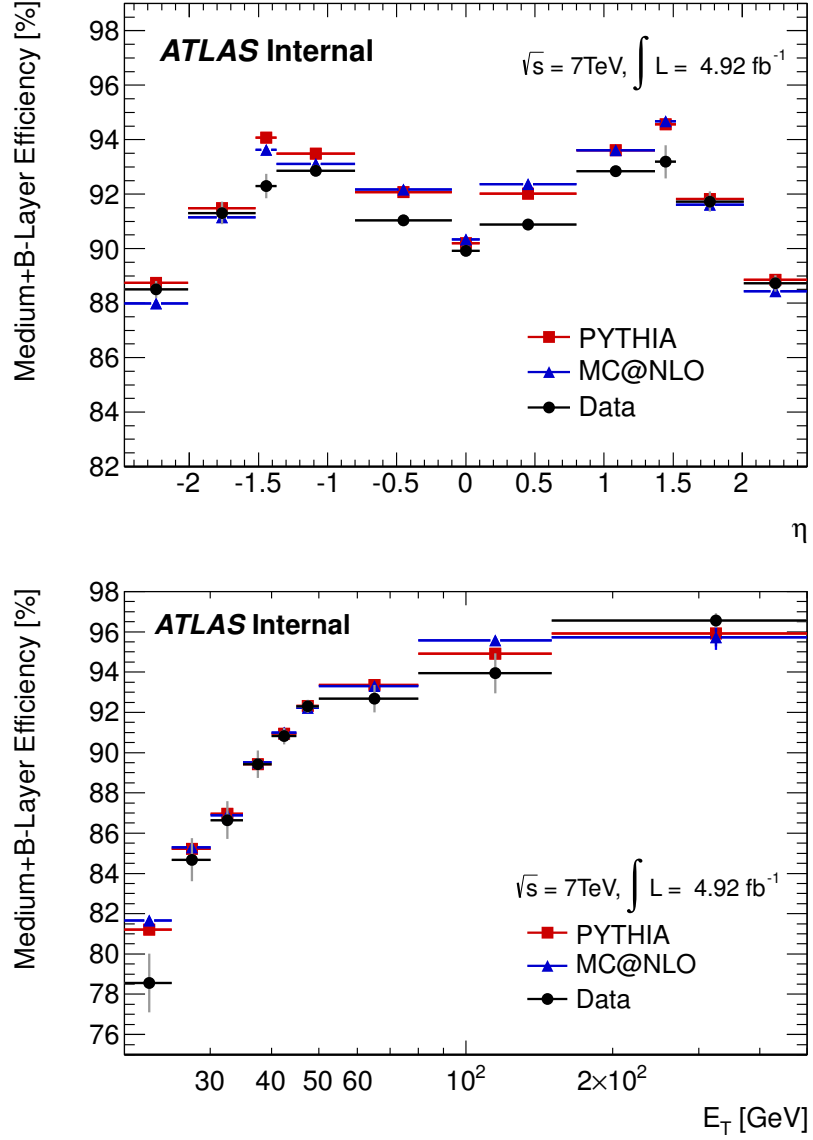


Figure 4.29: Average measured efficiency for Medium+B-Layer identification wrt. base level in data (black dots), and expectation from PYTHIA (red squares) and MC@NLO DY MC simulation (blue triangles) in bins of electron pseudorapidity and transverse energy. The quoted uncertainties are combined statistical and systematic (gray error bars on data).

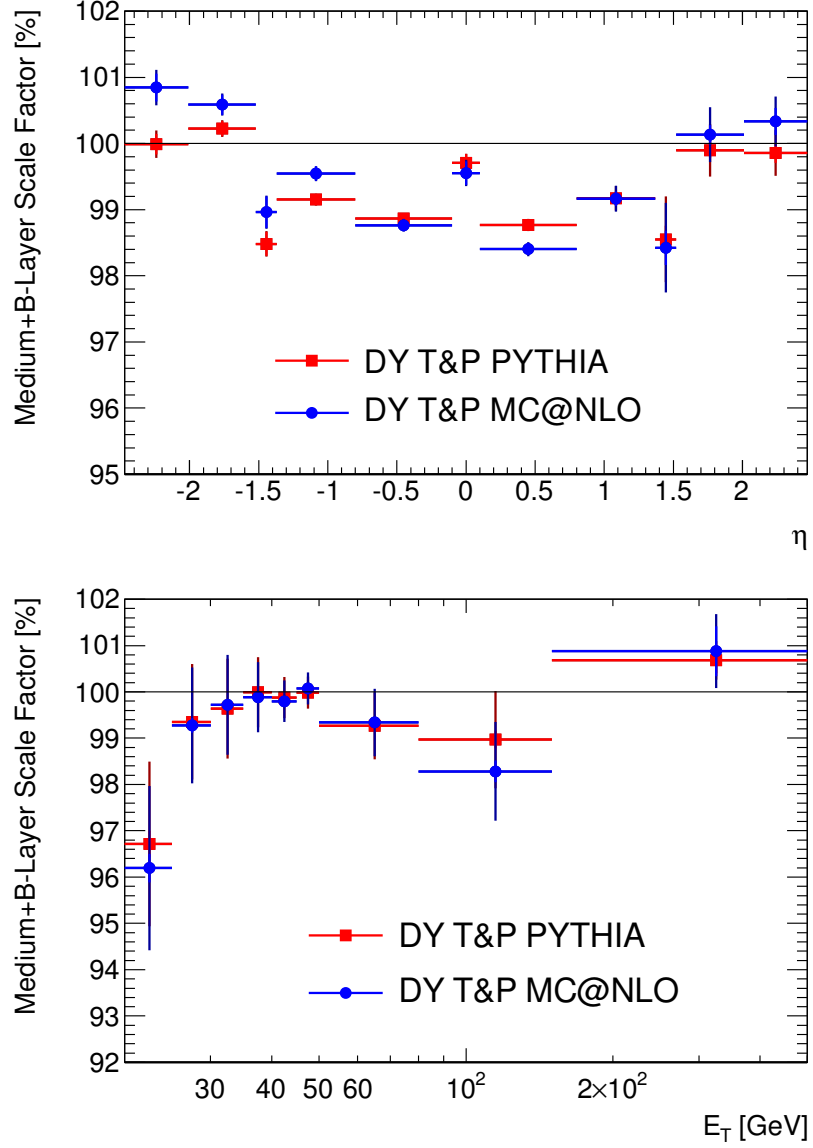


Figure 4.30: Scale factors for Medium+B-Layer identification wrt. base level for PYTHIA (red squares) and MC@NLO (blue dots) in bins of electron pseudorapidity η and transverse energy E_T . The quoted uncertainties are statistical and systematic.

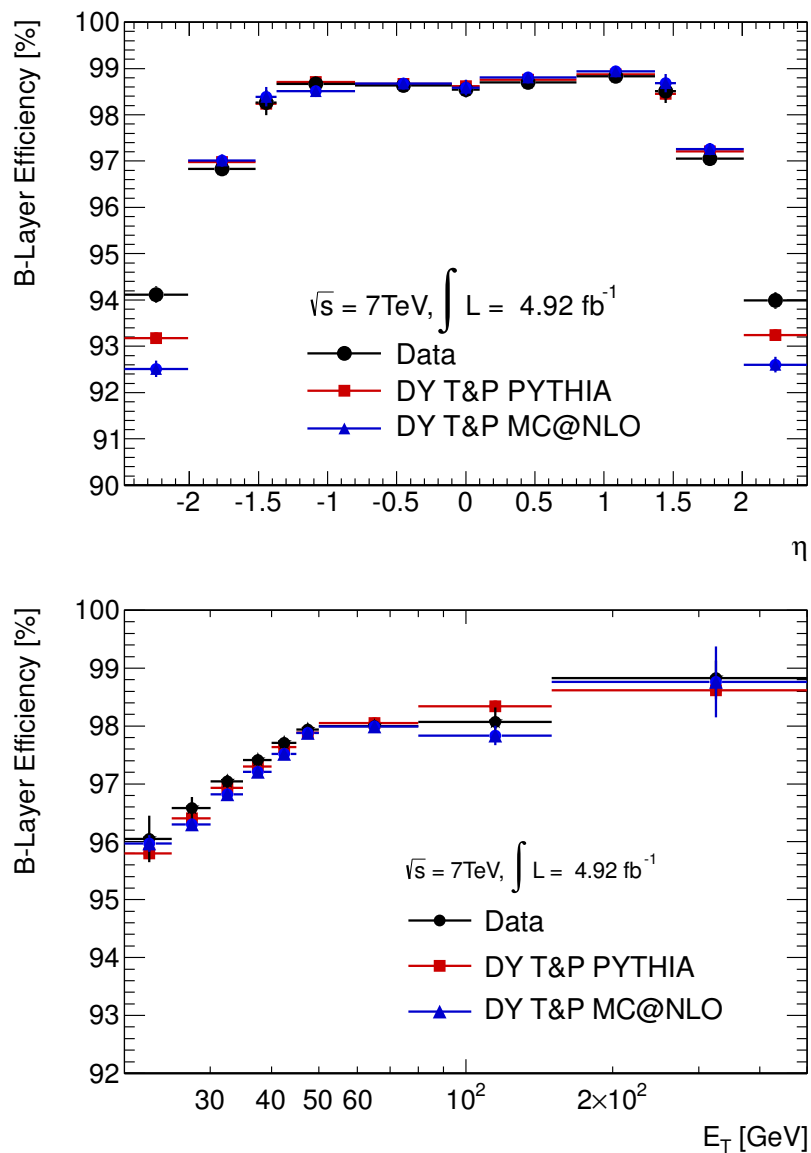


Figure 4.31: Measured efficiency for B -Layer hit in data (black dots), and expectation from PYTHIA (red squares) and MC@NLO DY MC simulation (blue triangles) in bins of electron pseudorapidity and transverse energy.

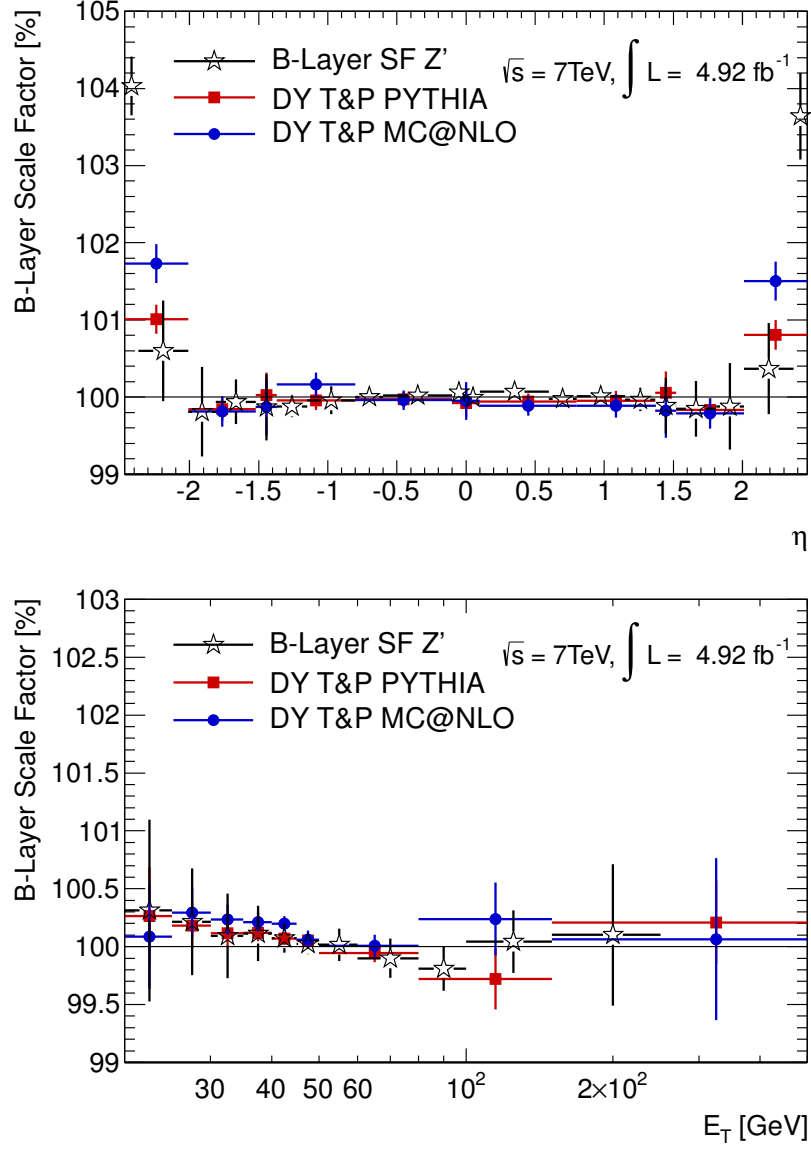


Figure 4.32: *SF for Medium+B-Layer hit over Medium identification in bins of electron pseudo rapidity η and transverse energy E_T . The results from this measurement (DY T&P) for PYTHIA (red squares) and MC@NLO (blue dots) are compared to those evaluated for the 2011 Z' analysis (black stars). Due to a slightly different choice of binning, no direct bin-by-bin comparison is possible. However, good agreement is seen.*

η	Data	PYTHIA	MC@NLO
[-2.47, -2.01]	$88.50 \pm 0.12 \pm 0.19$	$88.74 \pm 0.04 \pm 0.01$	$87.99 \pm 0.13 \pm 0.00$
[-2.01, -1.52]	$91.31 \pm 0.10 \pm 0.32$	$91.48 \pm 0.03 \pm 0.0$	$91.15 \pm 0.09 \pm 0.02$
[-1.52, -1.37]	$92.30 \pm 0.19 \pm 0.26$	$94.08 \pm 0.05 \pm 0.00$	$93.62 \pm 0.15 \pm 0.01$
[-1.37, -0.8]	$92.86 \pm 0.08 \pm 0.11$	$93.48 \pm 0.02 \pm 0.00$	$93.12 \pm 0.06 \pm 0.00$
[-0.8, -0.1]	$91.04 \pm 0.06 \pm 0.02$	$92.07 \pm 0.02 \pm 0.01$	$92.17 \pm 0.05 \pm 0.01$
[-0.1, 0.1]	$89.91 \pm 0.11 \pm 0.01$	$90.20 \pm 0.04 \pm 0.01$	$90.34 \pm 0.11 \pm 0.03$
[0.1, 0.8]	$90.89 \pm 0.06 \pm 0.02$	$92.02 \pm 0.02 \pm 0.02$	$92.36 \pm 0.05 \pm 0.01$
[0.8, 1.37]	$92.84 \pm 0.08 \pm 0.09$	$93.61 \pm 0.02 \pm 0.01$	$93.62 \pm 0.06 \pm 0.00$
[1.37, 1.52]	$93.19 \pm 0.18 \pm 0.42$	$94.56 \pm 0.05 \pm 0.00$	$94.68 \pm 0.14 \pm 0.01$
[1.52, 2.01]	$91.73 \pm 0.10 \pm 0.27$	$91.82 \pm 0.03 \pm 0.01$	$91.61 \pm 0.09 \pm 0.00$
[2.01, 2.47]	$88.73 \pm 0.12 \pm 0.18$	$88.85 \pm 0.04 \pm 0.00$	$88.43 \pm 0.13 \pm 0.00$

Table 4.12: Measured Medium+B-Layer ID efficiency in data compared to the prediction of PYTHIA and MC@NLO in % in bins of electron pseudorapidity η . The first error is statistical, the second systematic.

E_T [GeV]	Data	PYTHIA	MC@NLO
[20, 25]	$78.55 \pm 0.22 \pm 1.23$	$81.22 \pm 0.03 \pm 0.05$	$81.66 \pm 0.09 \pm 0.02$
[25, 30]	$84.68 \pm 0.12 \pm 0.95$	$85.23 \pm 0.02 \pm 0.05$	$85.30 \pm 0.06 \pm 0.04$
[30, 35]	$86.65 \pm 0.07 \pm 0.87$	$86.96 \pm 0.01 \pm 0.03$	$86.89 \pm 0.04 \pm 0.02$
[35, 40]	$89.42 \pm 0.04 \pm 0.63$	$89.43 \pm 0.01 \pm 0.02$	$89.52 \pm 0.03 \pm 0.00$
[40, 45]	$90.82 \pm 0.03 \pm 0.37$	$90.93 \pm 0.01 \pm 0.02$	$91.00 \pm 0.03 \pm 0.01$
[45, 50]	$92.3 \pm 0.04 \pm 0.28$	$92.31 \pm 0.01 \pm 0.02$	$92.23 \pm 0.03 \pm 0.01$
[50, 80]	$92.68 \pm 0.05 \pm 0.63$	$93.37 \pm 0.01 \pm 0.01$	$93.30 \pm 0.04 \pm 0.01$
[80, 150]	$93.94 \pm 0.17 \pm 0.82$	$94.92 \pm 0.04 \pm 0.01$	$95.58 \pm 0.13 \pm 0.04$
[150, 500]	$96.56 \pm 0.22 \pm 0.15$	$95.91 \pm 0.12 \pm 0.03$	$95.72 \pm 0.45 \pm 0.16$

Table 4.13: Measured Medium+B-Layer ID efficiency in data compared to the prediction of PYTHIA and MC@NLO in % in bins of electron transverse energy E_T . The first error is statistical, the second systematic.

E_T [GeV]	PYTHIA	MC@NLO
[-2.47, -2.01]	$99.73 \pm 0.15 \pm 0.20$	$100.58 \pm 0.21 \pm 0.19$
[-2.01, -1.52]	$99.81 \pm 0.11 \pm 0.34$	$100.17 \pm 0.15 \pm 0.31$
[-1.52, -1.37]	$98.11 \pm 0.22 \pm 0.27$	$98.59 \pm 0.27 \pm 0.23$
[-1.37, -0.8]	$99.33 \pm 0.09 \pm 0.12$	$99.73 \pm 0.11 \pm 0.11$
[-0.8, -0.1]	$98.88 \pm 0.07 \pm 0.02$	$98.78 \pm 0.09 \pm 0.02$
[-0.1, 0.1]	$99.69 \pm 0.13 \pm 0.01$	$99.53 \pm 0.18 \pm 0.03$
[0.1, 0.8]	$98.77 \pm 0.07 \pm 0.02$	$98.40 \pm 0.09 \pm 0.02$
[0.8, 1.37]	$99.17 \pm 0.09 \pm 0.09$	$99.16 \pm 0.11 \pm 0.08$
[1.37, 1.52]	$98.55 \pm 0.21 \pm 0.44$	$98.42 \pm 0.26 \pm 0.42$
[1.52, 2.01]	$99.9 \pm 0.11 \pm 0.29$	$100.13 \pm 0.15 \pm 0.27$
[2.01, 2.47]	$99.86 \pm 0.15 \pm 0.2$	$100.33 \pm 0.20 \pm 0.17$

Table 4.14: Medium + B-Layer *ID scale factors for PYTHIA and MC@NLO in % in bins of electron pseudorapidity η . The first error is statistical, the second systematic.*

E_T [GeV]	PYTHIA	MC@NLO
[20, 25]	$96.72 \pm 0.29 \pm 1.49$	$96.20 \pm 0.31 \pm 1.47$
[25, 30]	$99.35 \pm 0.14 \pm 1.10$	$99.28 \pm 0.16 \pm 1.09$
[30, 35]	$99.64 \pm 0.08 \pm 0.99$	$99.72 \pm 0.09 \pm 0.98$
[35, 40]	$99.99 \pm 0.05 \pm 0.71$	$99.88 \pm 0.06 \pm 0.69$
[40, 45]	$99.88 \pm 0.04 \pm 0.41$	$99.80 \pm 0.05 \pm 0.40$
[45, 50]	$99.98 \pm 0.05 \pm 0.3$	$100.08 \pm 0.06 \pm 0.29$
[50, 80]	$99.27 \pm 0.06 \pm 0.4$	$99.34 \pm 0.07 \pm 0.38$
[80, 150]	$98.97 \pm 0.19 \pm 0.36$	$98.28 \pm 0.23 \pm 0.36$
[150, 500]	$100.68 \pm 0.28 \pm 0.14$	$100.88 \pm 0.54 \pm 0.23$

Table 4.15: Medium + B-Layer *ID scale factors for PYTHIA and MC@NLO in % in bins of electron transverse energy E_T . The first error is statistical, the second systematic.*

η	B-Layer SF [%]
-2.47,-2.37	104.03 \pm 0.38
-2.37,-2.01	100.60 \pm 0.65
-2.01,-1.81	99.81 \pm 0.58
-1.81,-1.52	99.94 \pm 0.29
-1.52,-1.37	99.87 \pm 0.43
-1.37,-1.15	99.88 \pm 0.14
-1.15,-0.8	99.96 \pm 0.18
-0.8,-0.6	100.00 \pm 0.10
-0.6,-0.1	100.02 \pm 0.10
-0.1,0	100.06 \pm 0.12
0,0.1	99.99 \pm 0.08
0.1,0.6	100.07 \pm 0.11
0.6,0.8	99.98 \pm 0.06
0.8,1.15	100.01 \pm 0.13
1.15,1.37	99.97 \pm 0.15
1.37,1.52	99.89 \pm 0.36
1.52,1.81	99.85 \pm 0.36
1.81,2.01	99.88 \pm 0.56
2.01,2.37	100.37 \pm 0.59
2.37,2.47	103.64 \pm 0.56

Table 4.16: Scale factors for bins of η in % for the B-Layer hit (subleading electron) requirement (with respect to Medium identification), as derived for the Z' dielectron resonance search. The quoted uncertainties include both systematic and statistical.

E_T [GeV]	B-Layer SF [%]
20-25	100.31 \pm 0.79
25-30	100.22 \pm 0.46
30-35	100.09 \pm 0.37
35-40	100.11 \pm 0.24
40-45	100.07 \pm 0.13
45-50	100.02 \pm 0.09
50-60	100.02 \pm 0.14
60-80	99.90 \pm 0.17
80-100	99.81 \pm 0.19
100-150	100.05 \pm 0.27
150-250	100.10 \pm 0.61

Table 4.17: Scale factors in % for bins of E_T for the B-Layer hit (subleading electron) requirement (with respect to Medium identification) as derived for the Z' dielectron resonance search. The quoted uncertainties include both systematic and statistical.

4.6 Efficiency and Migration Corrections

The central values of the correction factor C_{DY} defined in Eq 4.2 at *Born* and *dressed* levels have been obtained from the PYTHIA and MC@NLO DY signal samples.

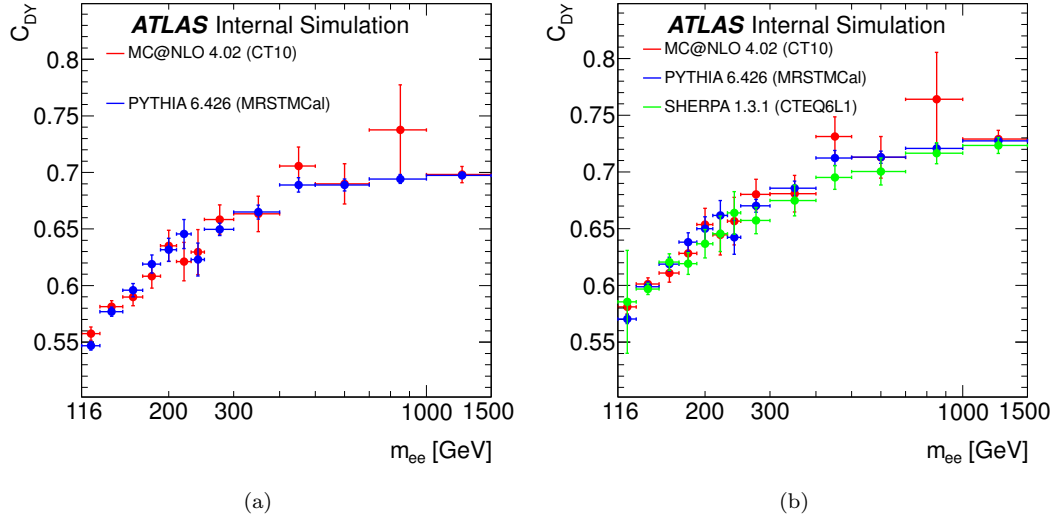


Figure 4.33: Central values for C_{DY} (see Eq. 4.2) from PYTHIA and MC@NLO at *Born* level (a) and PYTHIA, MC@NLO and SHERPA at *dressed* level (b) with statistical uncertainties. The statistical uncertainties are assumed to be Gaussian and therefore conservative. Due to the migration effects the uncertainties are not binomial.

For the central value of C_{DY} the PYTHIA curve is used, as this MC has the smallest statistical uncertainties. The values of C_{DY} vary from 0.63 to 0.78 depending on m_{ee} and agree within the statistical uncertainties with the values for the other generators as can be seen in Fig 4.33(a). For further comparison C_{DY} at *dressed* level was also calculated on a SHERPA DY signal sample, as shown in Fig. 4.33(b). It shows a good agreement with PYTHIA. The difference of the Born with respect to the dressed values of C_{DY} is shown in Fig 4.34(a).

Fig. 4.34(b) illustrates quantitatively the so-called bin-migration effect. Bin migration arises due to the limited measurement resolution which is quantified in the MC by the migration of events across bins between the true and reconstructed distributions. There are several possible physical causes for bin migration which act unevenly in different bins of the measured distribution. For instance, a final state radiation photon can be emitted at a large angle from the Drell-Yan electron, altering the rapidity of the reconstructed Z boson. Other scenarios include detector effects, such as the emission of bremsstrahlung photons, energy loss in the tracker, limitations in the detector energy resolution (finite resolution) or errors in the tracker position measurement [109, 110]. As a consequence, reconstructed quantities do not match real quantities, i.e. the reconstructed invariant mass of the electron pair might not fall into the same bin in m_{ee} as the true mass. Fig. 4.34(b) shows

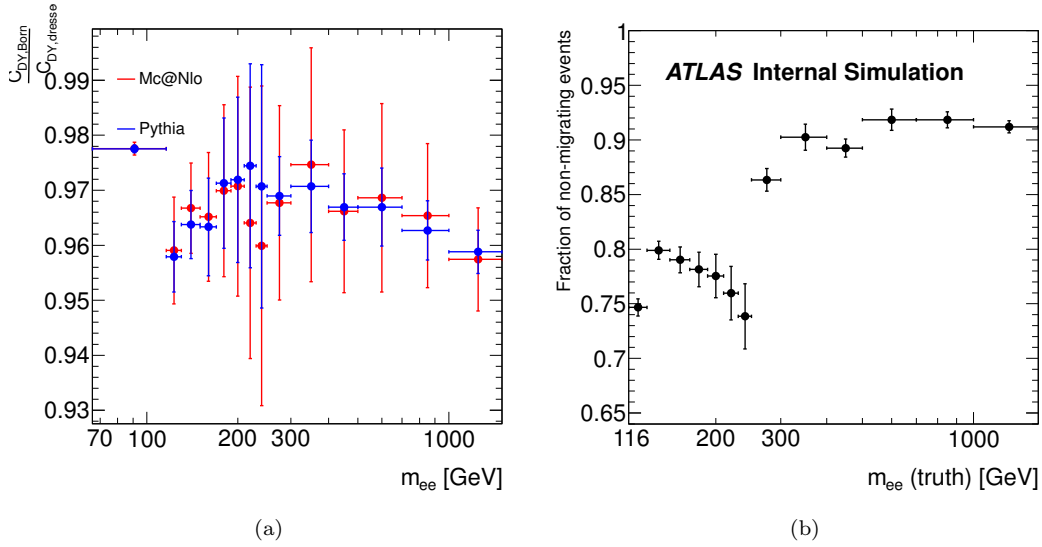


Figure 4.34: Born over dressed ratio of C_{DY} from MC@NLO and PYTHIA (a). Fraction of events for which the reconstructed mass and the true mass (Born level) fall in the same bin in the PYTHIA signal sample (b).

the fraction of events per bin where the the invariant mass was actually reconstructed in the bin of the true mass. The plot was obtained by taking the diagonal bin in the 2-dimensional histogram of true and reconstructed mass, and dividing their content by the entries of the true m_{ee} distribution. The visible step at 250 GeV is due to the change from a bin width of 20 GeV to a bin width of 50 GeV. Naturally the purity is higher when the bins are larger.

As discussed earlier, the MC samples are reweighed to match the pile-up distribution in data and smeared to reproduce the energy resolution. Moreover, the trigger, reconstruction, *Medium* identification, B-Layer and isolation efficiencies obtained from MC need to be corrected to the measured performance in data by applying E_T and η dependent *scale factors*. The measurement of the *Medium* identification and B-Layer hit efficiencies was discussed in detail in Section 4.5.

Trigger scale factor

Scale factors to account for the difference in data and MC of the EM signal trigger efficiency were obtained by comparing the efficiency in MC to that measured on data using a Tag-and-Probe method. $Z \rightarrow ee$ events were tagged by selecting events passing an alternative single-electron trigger, thus providing one electron probe free of trigger bias to test against the signal trigger requirements. The efficiency of the 2g20_loose trigger to select two electrons passing the medium plus B-Layer identification requirements has been determined as part of the 2011 Z' analysis [111]. In that work, possible inefficiencies at high energies (due to e.g. trigger signal saturation) were investigated and

no such losses were found. The scale factors which correct the efficiencies in MC to those measured in data are very close to unity and are given in Tables 4.18 and 4.19 for reference.

E_T [GeV]	Scale Factor [%]
20,25	100.06 ± 0.80
25,30	99.34 ± 0.15
30,35	99.52 ± 0.08
35,40	99.65 ± 0.05
40,45	99.73 ± 0.02
45,50	99.78 ± 0.03
50,60	99.80 ± 0.02
60,80	99.81 ± 0.03
80,100	99.85 ± 0.05

Table 4.18: *2g20_loose trigger efficiency scale factors per electron as a function of E_T with respect to Medium+B-Layer offline selection. For the uncertainties, statistical and systematic values are taken in to account.*

η	Scale Factor [%]
-2.47,-2.37	100.85 ± 2.12
-2.37,-2.01	99.97 ± 0.04
-2.01,-1.81	99.94 ± 0.05
-1.81,-1.52	100.09 ± 0.36
-1.52,-1.37	102.81 ± 2.79
-1.37,-1.15	99.71 ± 0.14
-1.15,-0.8	98.87 ± 0.06
-0.8,-0.6	99.86 ± 0.06
-0.6,-0.1	99.79 ± 0.03
-0.1,0.0	99.78 ± 0.05
0.0,0.1	99.25 ± 0.11
0.1,0.6	99.81 ± 0.03
0.6,0.8	99.73 ± 0.06
0.8,1.15	99.21 ± 0.09
1.15,1.37	99.81 ± 0.10
1.37,1.52	102.78 ± 1.79
1.52,1.81	99.84 ± 0.27
1.81,2.01	100.00 ± 0.09
2.01,2.37	99.90 ± 0.04
2.37,2.47	102.01 ± 1.47

Table 4.19: *2g20_loose trigger efficiency scale factors as a function of η with respect to Medium+B-Layer offline selection. For the uncertainties, statistical and systematic values are taken into account.*

B-Layer + Isolation scale factors

In addition to the *Medium* identification + B-Layer hit for the subleading electron, the signal selection requires the leading electron in the event to be isolated. The efficiencies and scale factors of these additional cuts have been derived using the Tag-and-Probe method for use in the 2011 Z' analysis. The values are given in Tables 4.20 and 4.21 for reference. They are multiplicative with the official *EGamma Medium* and reconstruction scale factors (and the trigger scale factor), i.e. each electron will be given a weight according to the product of all scale factors in the corresponding p_T and η bin.

η	B-Layer + Isolation [%]
-2.47,-2.37	103.98 ± 0.43
-2.37,-2.01	100.59 ± 0.74
-2.01,-1.81	99.83 ± 0.66
-1.81,-1.52	99.96 ± 0.40
-1.52,-1.37	99.65 ± 0.79
-1.37,-1.15	99.87 ± 0.32
-1.15,-0.8	99.97 ± 0.31
-0.8,-0.6	99.98 ± 0.25
-0.6,-0.1	100.00 ± 0.23
-0.1,0	100.06 ± 0.27
0,0.1	100.00 ± 0.14
0.1,0.6	100.06 ± 0.23
0.6,0.8	99.94 ± 0.17
0.8,1.15	100.02 ± 0.26
1.15,1.37	99.97 ± 0.36
1.37,1.52	99.65 ± 0.73
1.52,1.81	99.89 ± 0.49
1.81,2.01	99.84 ± 0.77
2.01,2.37	100.35 ± 0.71
2.37,2.47	103.58 ± 0.60

Table 4.20: Additional scale factors for bins of η in % for the B-Layer hit (subleading electron) + Isolation (leading electron) requirement (with respect to Medium identification). The quoted uncertainties include both systematic and statistical.

E_T [GeV]	B-Layer + Isolation [%]
20-25	100.18 ± 1.13
25-30	100.11 ± 0.84
30-35	100.03 ± 0.73
35-40	100.06 ± 0.54
40-45	100.01 ± 0.43
45-50	99.96 ± 0.40
50-60	99.95 ± 0.44
60-80	99.79 ± 0.44
80-100	99.58 ± 0.47
100-150	99.81 ± 0.57
150-250	100.27 ± 0.93

Table 4.21: Additional scale factors in % for bins of E_T for the B-Layer hit (subleading electron) + Isolation (leading electron) requirement (with respect to Medium identification). The quoted uncertainties include both systematic and statistical.

4.7 Systematic Uncertainties

The main contributions to the systematic uncertainties on the DY cross section measurement are described below.

4.7.1 Background estimation

In the estimate of the dominant di-jet and W +jets background, a total systematic uncertainty of 20 % is assigned. The overall resulting uncertainty on the cross section varies between 1.3 and 7.9 %, depending on m_{ee} .

Uncertainties on the diboson and $t\bar{t}$ backgrounds are dominated by the theoretical uncertainties on the calculated cross sections to which the simulated samples are rescaled, taken as 5 % and 10 %, respectively, and the limited MC statistics at high m_{ee} . The resulting uncertainty on the cross section is small compared to the data-driven di-jet and W +jets contributions, ranging from less than 0.5 % at low m_{ee} to 2.0 % in the highest m_{ee} bin.

4.7.2 Uncertainties on Corrections

The systematic uncertainties on C_{DY} in bins of m_{ee} are given in Table 4.22. These values are obtained using the PYTHIA predictions at Born level. Almost identical results are obtained from MC@NLO and at the dressed level.

Electron identification and reconstruction The reconstruction and identification efficiencies of electrons have been determined previously from data for electrons with E_T up to 50 GeV, using Tag-and-Probe methods following the prescription of Ref. [95]. As described in Section 4.5, the

$m_{e\bar{e}}^{min}$	$m_{e\bar{e}}^{max}$	C_{DY}	stat.	Trig. Eff.	Rec. Eff.	ID Eff.	E-scale	E-res	pileup	Z_{pt}	z_{vertex}	K-factor	Unfolding	total sys
116	130	0.628	0.7	0.8	1.6	2.3	2.1	0.3	0.1	0.0	0.1	0.1	1.5	3.9
130	150	0.661	0.7	0.8	1.6	2.3	1.7	0.2	0.1	0.0	0.5	0.1	1.5	3.8
150	170	0.683	1.0	0.8	1.6	2.3	1.6	0.4	0.1	0.1	0.0	0.0	1.5	3.7
170	190	0.710	1.3	0.8	1.6	2.3	1.0	0.0	0.1	0.1	0.2	0.0	1.5	3.5
190	210	0.721	1.7	0.9	1.6	2.4	1.5	0.1	0.1	0.2	0.2	0.0	1.5	3.7
210	230	0.740	2.0	0.8	1.6	2.4	2.0	0.2	0.2	0.1	0.8	0.0	1.5	4.0
230	250	0.714	2.4	0.9	1.6	2.4	1.1	0.5	0.2	0.1	0.0	0.0	1.5	3.6
250	300	0.745	0.9	0.8	1.6	2.4	1.7	0.2	0.1	0.1	0.0	0.1	1.5	3.8
300	400	0.761	1.0	0.8	1.6	2.5	1.7	0.1	0.1	0.1	0.3	0.1	1.5	3.9
400	500	0.785	0.9	0.8	1.6	2.6	2.3	0.1	0.0	0.2	0.5	0.1	1.5	4.2
500	700	0.781	0.8	0.8	1.6	2.6	2.4	0.1	0.1	0.0	0.2	0.1	1.5	4.3
700	1000	0.780	0.6	0.8	1.7	2.6	2.8	0.2	0.1	0.0	0.2	0.1	1.5	4.5
1000	1500	0.775	0.4	0.8	1.7	2.5	3.4	0.0	0.1	0.0	0.3	0.1	1.5	4.9

Table 4.22: The correction factor C_{DY} and its statistical (from MC statistics) and systematic uncertainties with respect to Born level, calculated with PYTHIA. The values are given in percent. The sources of the systematic uncertainty are trigger efficiency, reconstruction efficiency, identification (ID) efficiency (which combines the Medium, B-Layer and isolation (for leading electron) requirements), energy scale, energy resolution, pile-up, description of Z transverse momentum distribution (Z_{pt}) influence of z_{vertex} reweighting and the influence of extrapolation to NNLO theory (K-factor) . In addition the central value of C_{DY} with the statistical uncertainty is given for comparison.

measurement was extended to an E_T of up to 500 GeV and the efficiency results are found to be consistent with those obtained by the method of Ref. [95] in the common measurement range, with a stable behaviour at high electron E_T . Varying the scale factors up and down within their systematic uncertainties results in a change in the cross section of about $\pm 3\%$.

Energy scale and resolution Both the scale and resolution corrections, estimated from $Z/\gamma^* \rightarrow e^+e^-$ events, are varied in the simulation within their uncertainties. The overall effect on the cross section is between 1.0 and 3.3 %.

Bin migration The results obtained from the bin-by-bin correction have been cross-checked using an iterative Bayesian approach and found to be in good agreement. In addition, a closure test is performed by correcting the MC@NLO signal sample using the PYTHIA-derived C_{DY} factor. Due to the slightly different shapes of the m_{ee} distribution between the two generators, considered to represent the possible shape difference between data and PYTHIA, a non-closure of around 1.5 % is found, as shown in Fig 4.35(a). Fig. 4.35(b) illustrates the difference in the shape of the m_{ee} distribution between the MC@NLO MC and the PYTHIA MC and between the data (N_{sig}) and the PYTHIA MC. This 1.5 % is added as a systematic uncertainty on the cross section in all m_{ee} bins.

Trigger efficiency Varying the trigger efficiency scale factors up and down within their systematic uncertainties has an effect of approximately $\pm 1\%$ on the cross section.

MC modelling and statistics Systematic uncertainties are associated to the reweighting of the PYTHIA signal MC events in order to better match the data in terms of the transverse momentum distribution of the Z bosons, the mean number of interactions per bunch crossing, and also to the use of K-factors. These uncertainties enter into the calculation of C_{DY} and result in an overall uncertainty on the cross section of less than 1 %.

Theoretical uncertainties Several theoretical uncertainties apply to the extrapolation of the cross section in $|\eta|$ from the measured region to the fiducial region and thus form an additional uncertainty on C_{DY} . To evaluate the effect of the choice of PDF, the calculation of C_{DY} using PYTHIA with its default PDF (MRSTMCa1) is compared to that obtained after reweighting to CT10 and HERAPDF1.5 [112, 113]. The largest difference between the reweighted results and the default is taken as the systematic uncertainty, which amounts to at most 0.2 %. A further systematic uncertainty is calculated using the MC@NLO sample reweighted to the 52 CT10 eigenvector error sets, the result being 0.5 % at most. Finally, comparisons are made between PYTHIA reweighted to the CT10 PDF and MC@NLO (which uses as default CT10) and cross-checked using FEWZ 2.1 at NLO using the CT10 PDF. The effect is at most 0.3 %. These systematic uncertainties, which each have a

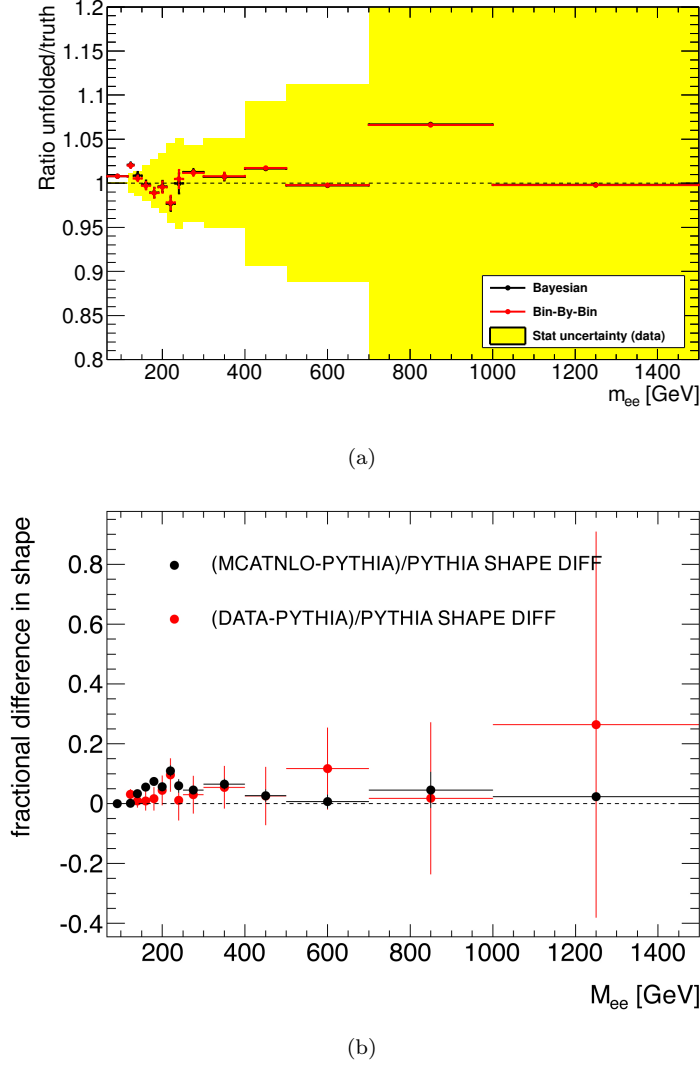


Figure 4.35: (a) Ratio of the MC@NLO unfolded cross section to its true cross section in bins of m_{ee} . The unfolding is performed using PYTHIA MC with the bin by bin and Bayesian methods. Only the statistical uncertainties from the PYTHIA MC enter the error bars. The RMS of the ratio from the bin by bin method is 1.5 %. The statistical uncertainty on the data is overlaid for illustration. (b) Difference in the shape of the m_{ee} distribution between the MC@NLO MC and the PYTHIA MC and between the data (N_{sig}) and the PYTHIA MC. The relative differences are calculated as indicated in the legend after first normalizing the distributions. The uncertainties from the PYTHIA MC do not enter the error bars.

different dependence on m_{ee} , are added in quadrature and together give a 0.3 - 0.4% uncertainty on the cross section.

Luminosity The uncertainty on the luminosity is 1.8%.

The contributions from the above sources of systematic uncertainty to the uncertainty on the measured cross section are summarised in Table 4.23 for the lowest and highest bin in the m_{ee} range considered. The overall systematic uncertainty, excluding that on the luminosity, increases with m_{ee} from 4.2% at low m_{ee} to 9.8% in the highest m_{ee} bin. This should be compared to the statistical uncertainty of 1% in the first bin of m_{ee} up to 50% in the highest m_{ee} bin.

Source of uncertainty	Uncertainty [%] in m_{ee} bin	
	116-130 GeV	1000-1500 GeV
Total background estimate	1.3	8.2
Electron reconstruction & identification	2.8	3.0
Electron energy scale & resolution	2.1	3.3
Bin migration	1.5	1.5
Trigger efficiency	0.8	0.8
MC modelling	0.2	0.3
MC statistics	0.7	0.4
Theoretical uncertainty	0.3	0.4
Total systematic uncertainty	4.2	9.8
Luminosity uncertainty	1.8	1.8
Data statistical uncertainty	1.1	50

Table 4.23: Summary of systematic uncertainties on the cross section measurement, shown for the lowest and highest bin in m_{ee} . The statistical uncertainties are also given for comparison.

4.8 Results and Comparison to Theory

The cross-sections obtained at the *Born* and *dressed* levels in the fiducial region (electron $E_T > 25$ GeV and $|\eta| < 2.5$) are given in Table 4.24. The difference between the two results is at most 4%. The precision of the measurement is limited by the statistics of the data sample for $m_{ee} > 400$ GeV. Figure 4.36 shows the results at the dressed level, where they are compared to the predictions of the PYTHIA, MC@NLO and SHERPA MC generators. No m_{ee} dependent K -factors are applied to the generator level predictions; instead, the prediction of each generator has been scaled globally to match the total number of events observed in data. The resulting scale factors are 1.23 for PYTHIA, 1.08 for MC@NLO and 1.41 for SHERPA; as expected, the only prediction at NLO in pQCD, i.e., the one from the MC@NLO generator using the CT10 NLO PDF, yields the smallest scale factor. The overall shape of the m_{ee} distribution from all three generators is in agreement with the data.

m_{ee} [GeV]	$\frac{d\sigma}{dm_{ee}}$ (Born)	$\frac{d\sigma}{dm_{ee}}$ (dressed)	Stat. err. [%]	Syst. err. [%]
116-130	2.24×10^{-1}	2.15×10^{-1}	1.1	4.2
130-150	1.02×10^{-1}	9.84×10^{-2}	1.4	4.3
150-170	5.12×10^{-2}	4.93×10^{-2}	2.0	4.6
170-190	2.84×10^{-2}	2.76×10^{-2}	2.7	4.7
190-210	1.87×10^{-2}	1.82×10^{-2}	3.0	5.3
210-230	1.07×10^{-2}	1.04×10^{-2}	4.4	6.1
230-250	8.23×10^{-3}	7.98×10^{-3}	5.2	5.9
250-300	4.66×10^{-3}	4.52×10^{-3}	4.3	5.8
300-400	1.70×10^{-3}	1.65×10^{-3}	5.1	5.9
400-500	4.74×10^{-4}	4.58×10^{-4}	9.4	6.3
500-800	1.46×10^{-4}	1.41×10^{-4}	11	5.7
800-1000	2.21×10^{-5}	2.13×10^{-5}	24	7.5
1000-1500	2.88×10^{-6}	2.76×10^{-6}	50	9.8

Table 4.24: Measured differential cross-sections $\frac{d\sigma}{dm_{ee}}$ (in pb/GeV) at Born and dressed levels for DY production of electron pairs in the fiducial region (electron $|\eta| < 2.5$ and $E_T > 25$ GeV) with statistical (stat.) and overall systematic (syst.) uncertainties in %. The overall 1.8 % luminosity uncertainty is not included.

Figure 4.37 shows the differential cross-section at the Born level compared to calculations in the FEWZ 3.1 framework. This framework allows the (N)NLO QCD corrections to lepton pair production to be combined with the NLO electroweak corrections. It was verified at NLO that the choice of electroweak scheme, G_μ or $\alpha(M_Z)$ as introduced in Ref. [114], is at most 0.4 % after applying NLO electroweak corrections. The electroweak-corrected NNLO QCD predictions shown in the plot are calculated using the G_μ electroweak scheme and five PDF sets at NNLO: MSTW2008 [115], ABM11 [116], CT10 [98, 117], HERAPDF1.5 [113, 118] and NNPDF2.3 [119, 120]. The electroweak corrections include a positive contribution from the irreducible, non-resonant photon-induced background, i.e., $\gamma\gamma \rightarrow e^+e^-$. This contribution has been estimated at leading order using the MRST2004qed PDF, currently the only set available that contains a description of the QED part of the proton, by taking an average of the predictions obtained under the current and constituent quark mass schemes. The symmetric difference to either scheme is assigned as the corresponding uncertainty on this additive correction, being approximately 50 % and representing a 3 % uncertainty on the cross-section prediction in the highest m_{ee} bin. An additional small correction arises from single or di-boson production in which the final state charged lepton radiates a real W or Z [121]. This has been estimated using MADGRAPH 5 [122] to be at most 2 %, in the highest m_{ee} bin.

Except for the prediction from the ABM11 PDF set at low m_{ee} , the deviations between the different PDF central values of MSTW2008 and CT10, HERAPDF1.5, ABM11 and NNPDF2.3 are covered by the total uncertainty on the MSTW2008 prediction. This uncertainty band includes the uncertainty on the

photon-induced contribution as well as the renormalisation and factorization scale variations and the 68 % C.L. envelope based on the PDF and α_s uncertainties. The latter dominate the uncertainty band (2-4 %) with the scale uncertainties contributing up to 1 % only in the highest m_{ee} bin, having been evaluated by varying both scales up or down together by a factor of two, using VRAP [123].

The size of the photon-induced contribution is similar to the sum of the PDF, α_s and scale uncertainties as can be seen in the lower panel of Fig. 4.37 (top), where the nominal calculation using the MSTW2008 PDF set is compared to the case where this contribution is not taken into account. The data are largely consistent with the nominal calculations for all PDF sets: taking into account the bin-to-bin correlations between uncertainties, the comparison between data and the different FEWZ predictions yields chi-squared values of 13.9 for MSTW2008, 18.9 for CT10, 13.5 for HERAPDF1.5, 14.7 for ABM11, 14.8 for NNPDF2.3 for the 13 data points.

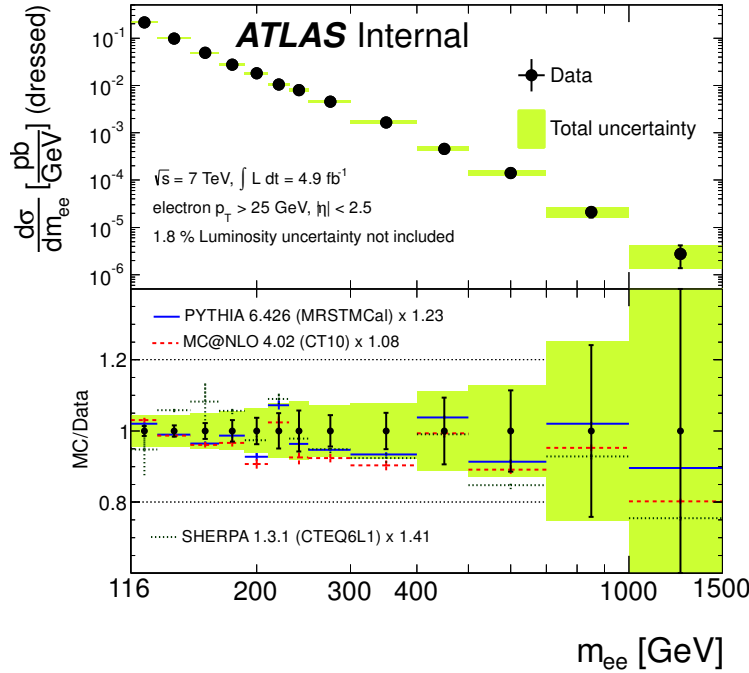


Figure 4.36: Measured differential cross-section at the dressed level within the fiducial region (electron $E_T > 25 \text{ GeV}$ and $|\eta| < 2.5$) with statistical and combined statistical and systematic uncertainties, excluding the 1.8% uncertainty on the luminosity. In the lower panel the measurement is compared to the prediction of the PYTHIA, MC@NLO and SHERPA MC generators including their statistical uncertainties. The cross-section predictions of each generator have been scaled by a global factor of 1.23 for PYTHIA 1.08 for MC@NLO and 1.41 for SHERPA to match the total number of events observed in data.

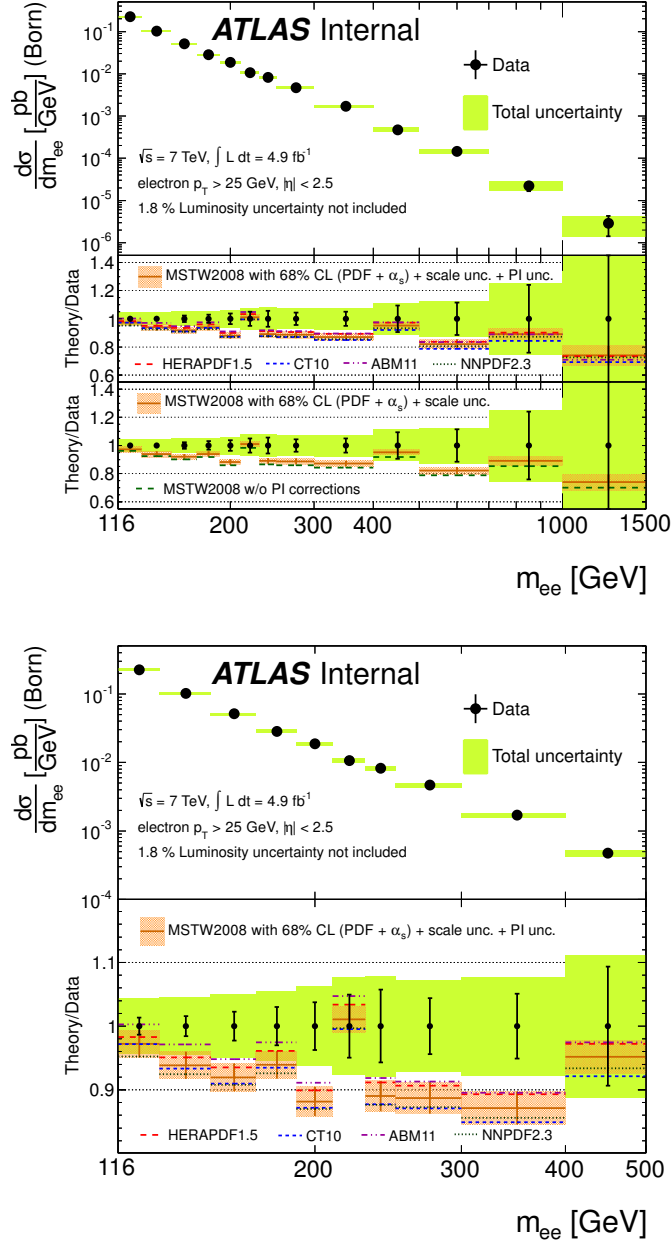


Figure 4.37: Measured differential cross-section at the Born level within the fiducial region (electron $E_T > 25$ GeV and $|\eta| < 2.5$) with statistical and combined statistical and systematic uncertainties, excluding the 1.8% uncertainty on the luminosity. The measurement is compared to FEWZ 3.1 calculations at NNLO in pQCD using the G_μ electroweak parameter scheme and including electroweak corrections. (top) In the upper ratio plot, the photon-induced (PI) corrections have been added to the predictions of the MSTW2008, HERAPDF1.5, CT10, ABM11 and NNPDF2.3 NNLO PDFs, and for the MSTW2008 prediction the total uncertainty band arising from the PDF, α_s , renormalisation and factorisation scale, and photon-induced uncertainties is drawn. The lower ratio plot shows the influence of the photon-induced corrections on the MSTW2008 prediction, the uncertainty band including only the PDF, α_s and scale uncertainties. (bottom) The results are shown for a restricted range of m_{ee} .

4.9 Summary

Using 4.9 fb^{-1} of LHC pp collision data collected by ATLAS in 2011, the invariant mass distribution of electron pairs from Drell-Yan production has been measured in the range $116 < m_{ee} < 1500 \text{ GeV}$ for electrons with $E_T > 25 \text{ GeV}$ and $|\eta| < 2.5$.

To support this cross section measurement, the identification efficiency for electrons for *Medium* and B-Layer hit requirement has been evaluated up to $E_T < 500 \text{ GeV}$ via a dedicated Tag-and-Probe method. Comparisons have been made to the predictions of the **PYTHIA**, **MC@NLO** and **SHERPA** MC generators, after scaling them globally to match the total number of events observed in data. The MC predictions show good agreement with the shape of the measured m_{ee} distribution. The predictions of the **FEWZ 3.1** framework, combining calculations at NNLO QCD with NLO electroweak corrections in the G_μ electroweak scheme, with the addition of LO photon-induced corrections, have also been studied, using five PDF sets at NNLO. The resulting predictions are largely consistent with the measured differential cross-section for all PDFs.

The results of this work are largely presented in the ATLAS Conference Note ATL-CONF-2012-159 [124] and are currently in preparation for publication in a physics journal.

Chapter 5

Summary and Conclusion

This thesis reported stability and upgrade studies of the ATLAS beam pipe and a high mass Drell-Yan differential cross section measurement. In the scope of the ATLAS beam pipe studies, the position stability has been evaluated for the period from April 2010 until June 2012 using secondary hadronic vertex distributions of particle tracks interacting with the beam pipe and the detector material. Fits of the vertex distributions for different data points (per period of a few days up to a few weeks) in the x , y and z directions were used to estimate the position of the beam pipe as a function of time. The values in x and y indicate the position of the centre of the beam pipe at the interaction point, while the vertical displacement of the beam pipe was computed at a position 3.7 m away from the interaction point from an extrapolation of a fit along the z axis. No movement of the centre of the beam pipe in x , y nor a vertical displacement at the extrapolated position along the z -axis could be observed. The secondary vertex fit values were compared to data collected in 2010 by a hydrostatic levelling sensor system installed in the ATLAS cavern to monitor movements of the floor. There is good agreement between the two methods: the HLS data show a heave of the centre of the ATLAS cavern floor, as predicted by civil engineering simulations, but no tilt in the horizontal plane of the ATLAS beam pipe could be observed. The results of this study showed that the supports of the current beam pipe set-up yield sufficiently good stability and no changes need to be made for the new beam pipe.

As ATLAS plans to exchange all parts of the beam pipe during the technical stop starting in 2013, a simulation study was done to evaluate the gain in units of radiation length traversed by the particles when moving from stainless steel to aluminium. The beam pipe part under consideration in this study is situated inside the LAr calorimeter end-cap. Furthermore, three options for the positioning of a new flange were considered. Using aluminium instead of stainless steel yields a reduction in radiation length of 27.1 %, while no significant difference between the three flange configurations could be observed. This information has been used by the engineering team for the design of the new beam pipe in the ATLAS experiment, for which the aluminium alloy AA2219 was

chosen as the new material.

The data collected in 2011 by ATLAS were used for the measurement of the high mass Drell-Yan differential cross section measurement in the di-electron final state. The invariant mass distribution of electron pairs was measured in the range $116 < m_{ee} < 1500$ GeV for electrons with $E_T > 25$ GeV and $|\eta| < 2.5$. Background subtraction has been performed by measuring the “QCD fake rate”, the probability of a jet being misidentified as an electron. Up to a $m_{ee} \approx 400$ GeV, the accuracy of the measurement is dominated by systematic errors, above that the main source of uncertainty is the statistical error on the data of up to 50 % in the highest invariant mass bin. The highest precision of 5.3 % total uncertainty is reached in the lowest invariant mass bin of $m_{ee} = 116$ -130 GeV.

As the identification efficiencies for electrons at high electron transverse energy were not yet validated on data, for the high mass Drell-Yan cross section measurement, they were measured via a data-driven Tag-and-Probe method up to $E_T = 500$ GeV. The measured efficiencies were compared with previous results in the transverse energy region $E_T < 50$ GeV. The method used the calorimetric isolation as a discriminating variable against the jet background. Background subtraction was performed via inversion of cuts on the identification variables. Identification efficiencies were obtained separately in bins of E_T and pseudorapidity η . The systematic uncertainty was evaluated as a function of various input parameters to the background estimation. Restricting the invariant mass of the Tag-and-Probe pairs to $m_{ee} = 76$ - 116 GeV improved the precision of the measurement by significantly increasing the signal-to-background ratio and therefore decreasing the possible bias introduced by the background template.

The results from data and MC were combined into scale factors which were compared to previous measurements with different background subtraction methods. Both in bins of pseudorapidity η and transverse energy E_T , the values show good agreement. In the common E_T bins of 20 - 50 GeV, the total uncertainty on the measured scale factors is at most 1.8 %, in the highest E_T region, $50 < E_T < 500$ GeV the precision reaches approximately 0.8 %. Scale factors for the B-Layer hit requirement were also evaluated and compared to an alternative measurement up to $E_T = 250$ GeV and found to be in good agreement.

Comparisons of the Drell-Yan differential cross section were made to the predictions of the PYTHIA and MC@NLO and SHERPA MC generators, which show good agreement with the shape of the observed distribution. The predictions of the FEWZ 3.1 framework, combining calculations at NNLO QCD with NLO electroweak corrections in the G_μ electroweak scheme have also been studied using the MSTW2008, HERAPDF1.5, CT10, ABM11 and NNPDF2.3 NNLO PDFs, with the addition of LO photon-induced corrections as well as a small correction for real W or Z radiation from di-boson production. The resulting predictions are consistent with the measured differential cross-section in the fiducial region for all PDFs. As photon-induced di-lepton production processes are not part of the MC simulation, no further extrapolation for the fiducial region of electron E_T and $|\eta| < 2.5$ to a total cross section was done.

Appendix A

Electron Identification Efficiency

A.1 Data Taking Periods

A.2 ATLAS Monte Carlo Production for 2011

MC11c is the final production campaign for 2011 ATLAS data analyses and was used in this work. The AtlasProduction releases used are 16.6.6.3 - 16.6.7.X for event generation, using Generators/MC11JobOptions and 15.6.6.3 - 16.6.7.X for the GEANT4 (G4) simulation. The G4 simulation uses two beam spot settings: the first approx. 100 million events were produced using a wide beam spot (90 mm in z) and the subsequent production uses a narrow(er) beam spot (75 mm in z). The narrow beam spot production uses frozen showers for the Forward Calorimeter (FCal) simulation. The ATLAS geometry used is the ATLAS-GEO-18-01-00 and ATLAS-GEO-18-01-03, the default physics list is `QGSP_BERT` (as described in [126]). The GEANT4 simulation conditions are OFLCOND-SDR-BS7T-05-12 for narrow beam spot indicating a beam spot length of 75 mm and improved B-tagging calibration.

The relevant tags for the samples used in this analysis are s1310 indicating frozen showers, GEO-18-01-03 and by default narrow beam spot, s1300 for G4 HITS merging (GEO-18-01-00, narrow beam spot), r3043 for tight trigger and r2993 for the AOD merging.

Period & Date	Conditions	Run Range
B Mar 21 - 24	Data taken just before 2.76 TeV running. Toroid field partly off	177986 - 178109
D Apr 14 - 29	50 ns bunch spacing	179710 - 189481
E Apr 30 - May 03	LAr Front End Board problem in EMBA	180614 - 180776
F May 15 - 25	50 ns bunch spacing. Tier0 Reco improved conditions to correct for EMEC sagging and for tilt of ID w.r.t. solenoid field	182013 - 182519
G May 27 - Jun 14	new trigger cache using pile-up noise suppression EMEC sagging correction	182726 - 183462
H Jun 16 - 28	update to L1 muon firmware to fix misconfiguration affecting A-side	183544 - 184169
I Jul 13-29	4 LAr Front End Boards in Layer 2 recovered	185353 - 186493
J Jul 30 - Aug 04	adiabatically increasing beam currents thus changes to primary high p_T triggers in trigger menu	186516 - 186755
K Aug 04 - 22	new trigger menu	186873 - 187815
L Sep 07 - Oct 05	change in trigger menu	188902-190343
M Oct 06 - 30	-	190503 - 191933

Table A.1: ATLAS data taking periods in 2011. Some details on the conditions are given, for more complete information, see Ref. [125].

Run	Data Period	Data Fraction	LAr Conditions	Dead Tile Modules	Pixel Conditions
180164	B-D	3.2% (160 pb^{-1})	all Front End Boards (FEBs) ok	5	54/7
183003	E-H	17.4% (872 pb^{-1})	6 missing FEBs (EMB: 4 in layer 2, 2 in layer 3)	6	56/7
186169	I-K	25.8% (1291 pb^{-1})	2 missing FEBs (EMB layer 3)	7	62/10
189751	L-M	53.5% (2677 pb^{-1})	2 missing FEBs (EMB layer 3)	9	63/10

Table A.2: Conditions in MC11c, Pixel conditions indicate the ratio of dead pixel modules to dead B-layer modules. The Run number corresponds to the data taking period.

A.3 Electron Isolation Distributions

A.3.1 Bins of Transverse Energy

Base Level (“track quality, TrkQ”) Identification

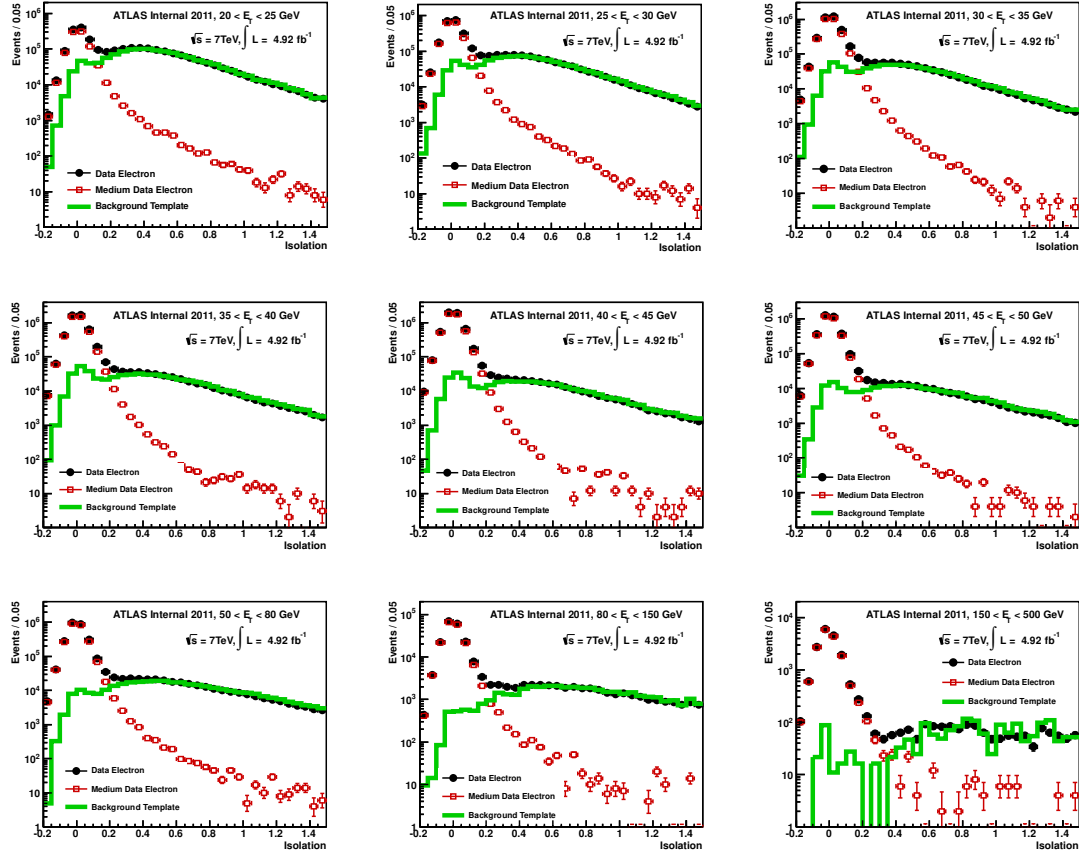


Figure A.1: fside template for base level identification and opposite sign charge Tag-and-Probe pair with an invariant mass of $76 < M_{ee} < 116$ GeV in bins of electron E_T .

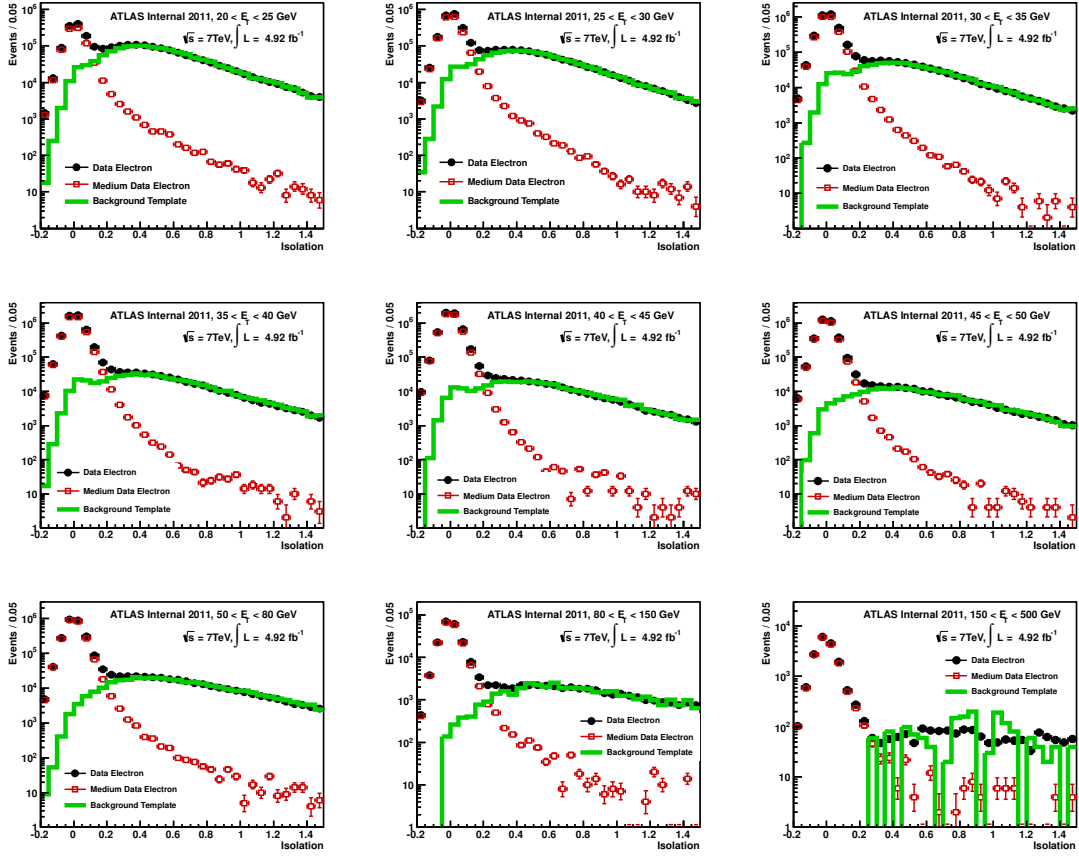


Figure A.2: $f_{\text{side}} + \ln \text{TRT}/r_{\text{phi}}$ template for base level identification and opposite sign charge Tag-and-Probe pair with an invariant mass of $76 < M_{\text{ee}} < 116$ GeV in bins of electron E_T .

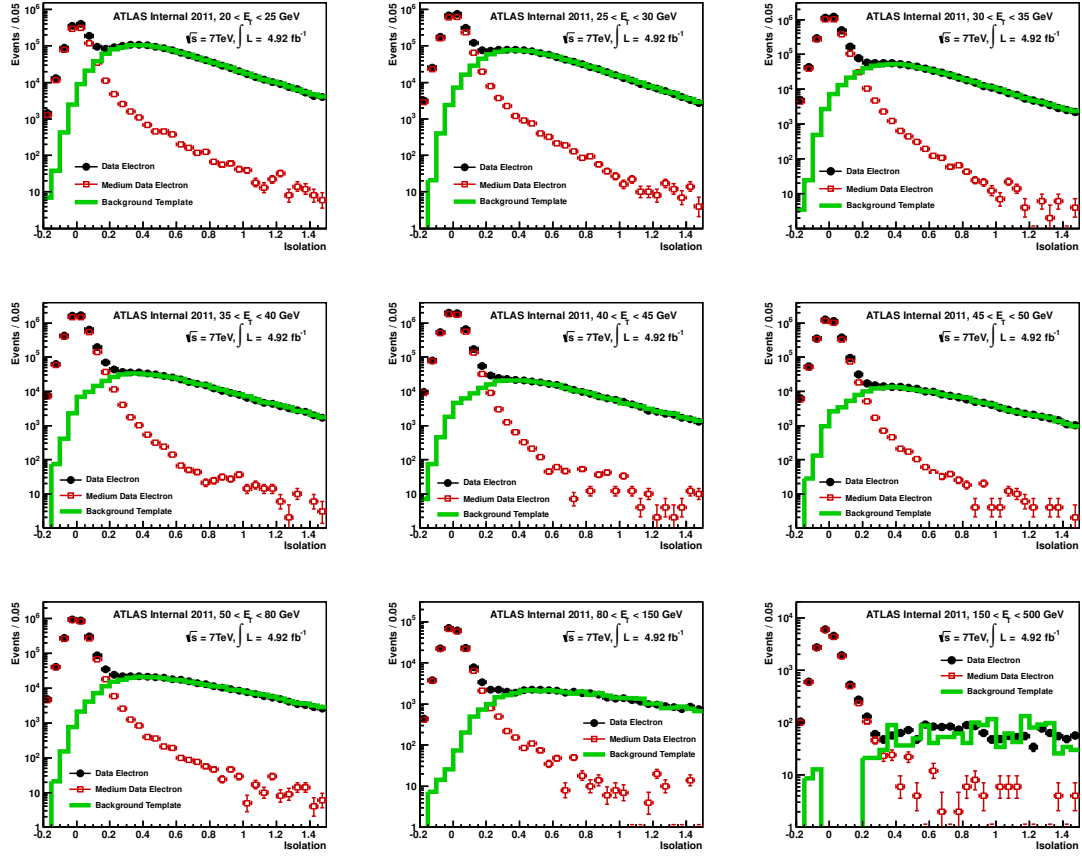


Figure A.3: SS+!loose template for base level identification and opposite sign charge Tag-and-Probe pair with an invariant mass of $76 < M_{ee} < 116$ GeV in bins of electron E_T .

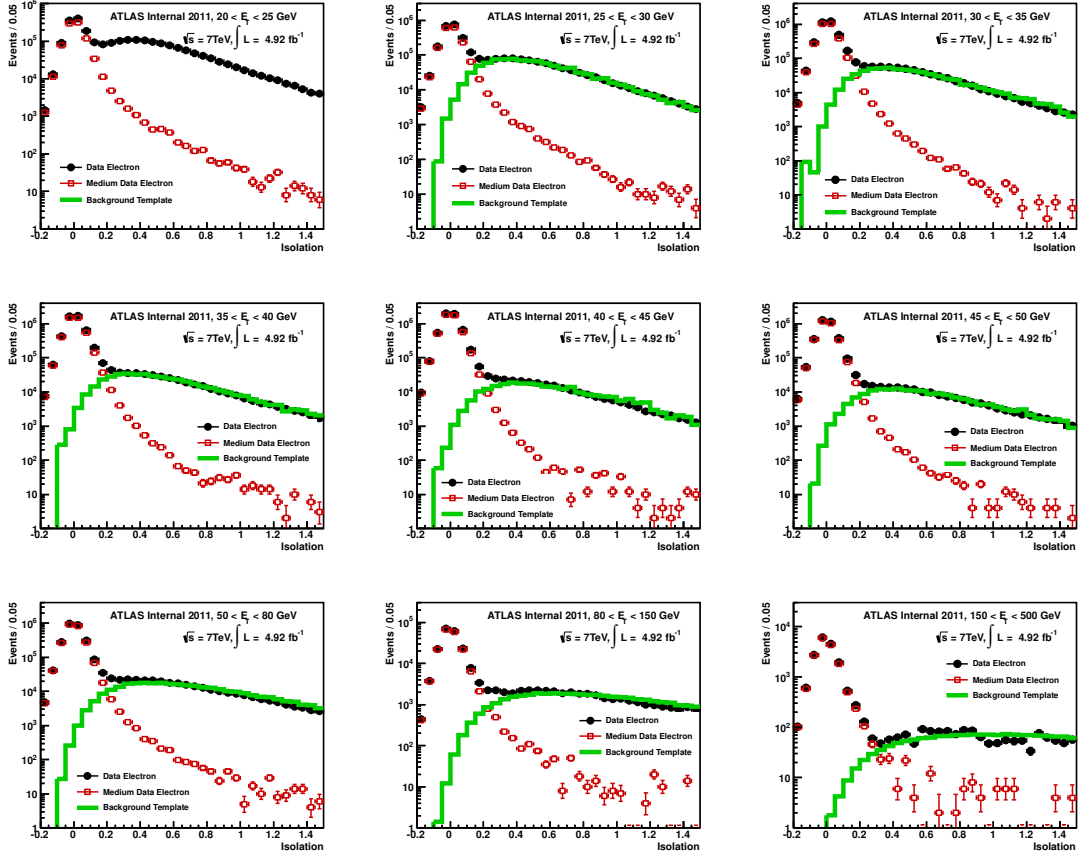


Figure A.4: Jet template for base level identification and opposite sign charge Tag-and-Probe pair with an invariant mass of $76 < M_{ee} < 116$ GeV in bins of electron E_T .

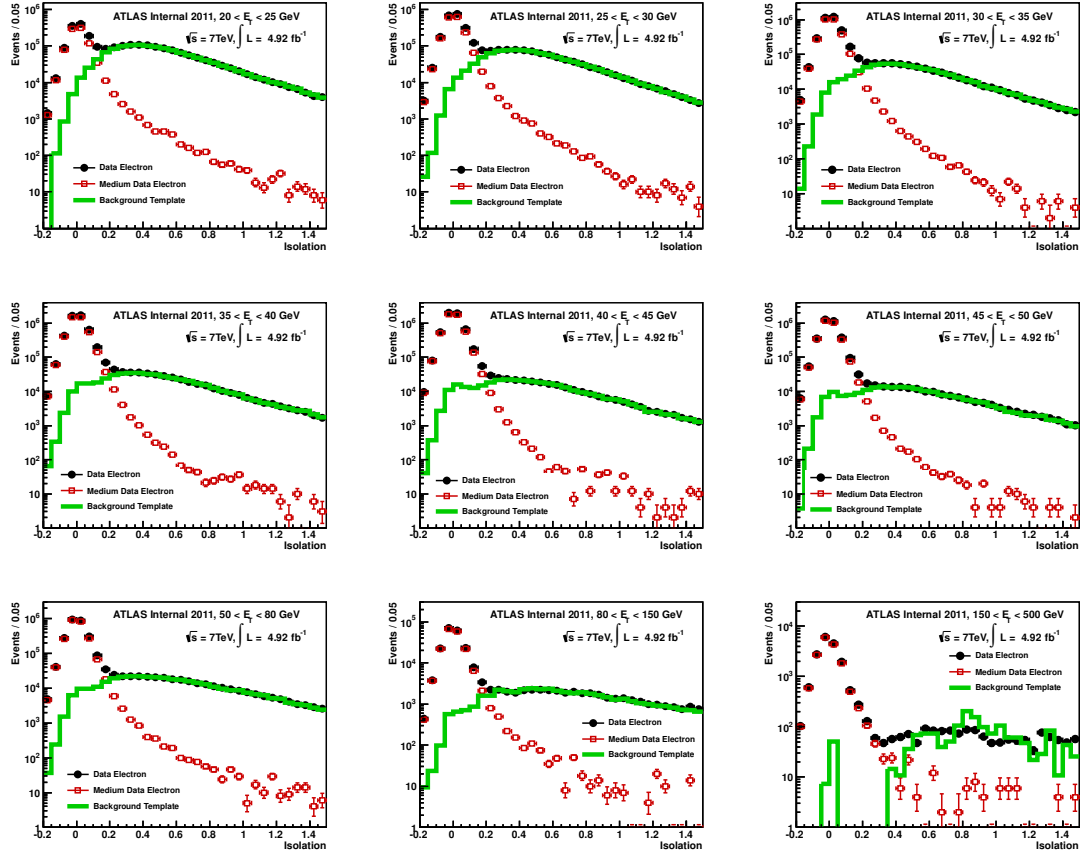


Figure A.5: !TrackMatch template for base level identification and opposite sign charge Tag-and-Probe pair with an invariant mass of $76 < M_{ee} < 116$ GeV in bins of electron E_T .

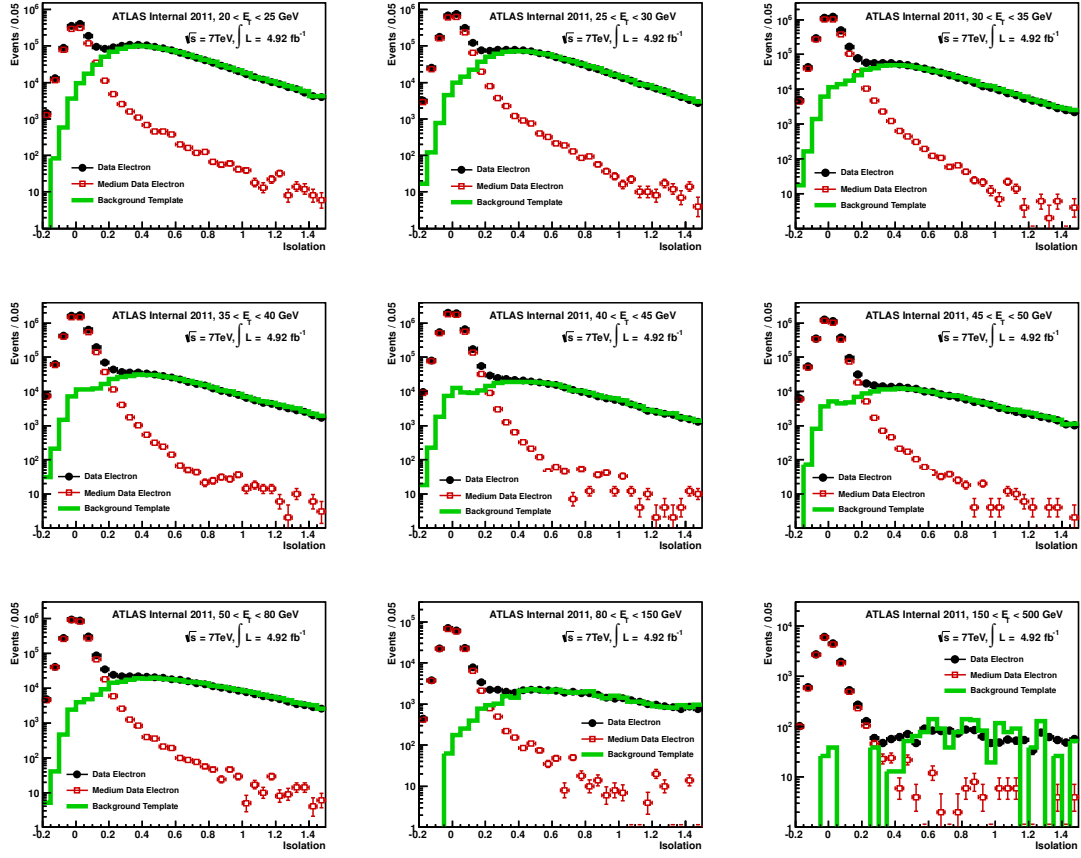


Figure A.6: $\Delta\text{wstot} + \Delta\text{TRT} + \text{rphi}$ template for base level identification and opposite sign charge Tag-and-Probe pair with an invariant mass of $76 < M_{ee} < 116 \text{ GeV}$ in bins of electron E_T .

Medium Identification (ID) Level

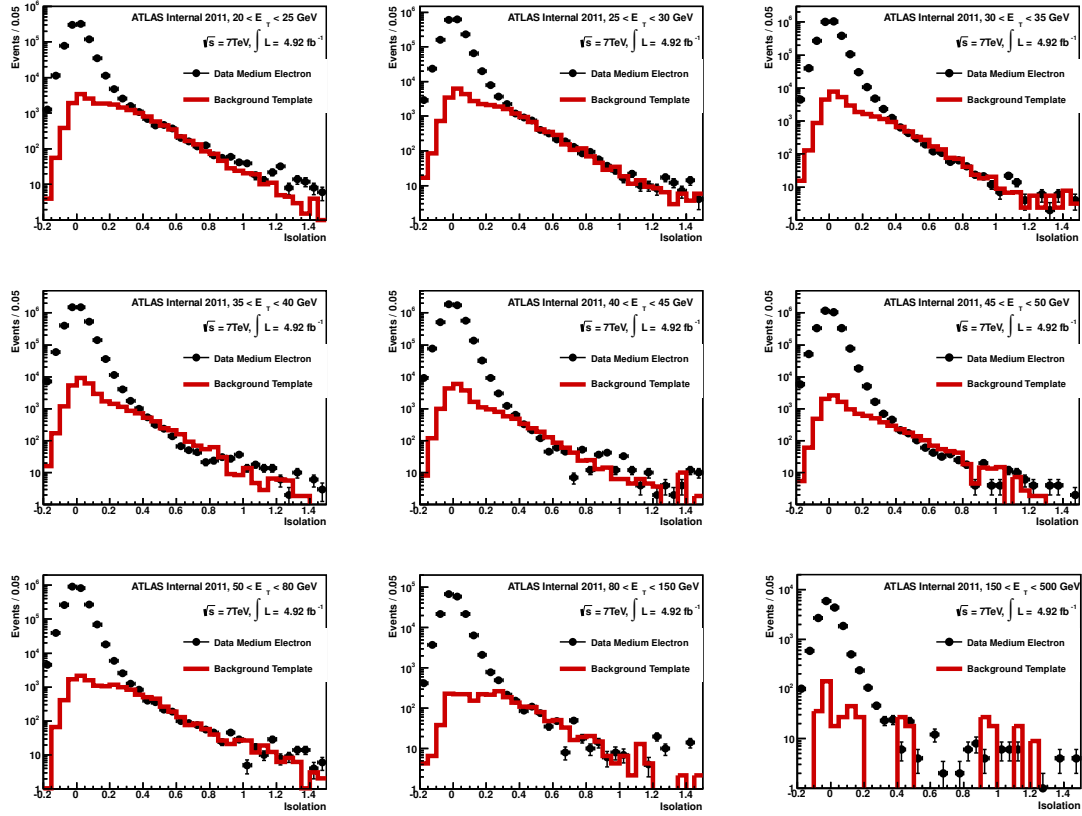


Figure A.7: fside template for *Medium* ID level and opposite sign charge Tag-and-Probe pair with an invariant mass of $76 < M_{ee} < 116$ GeV in bins of electron E_T .

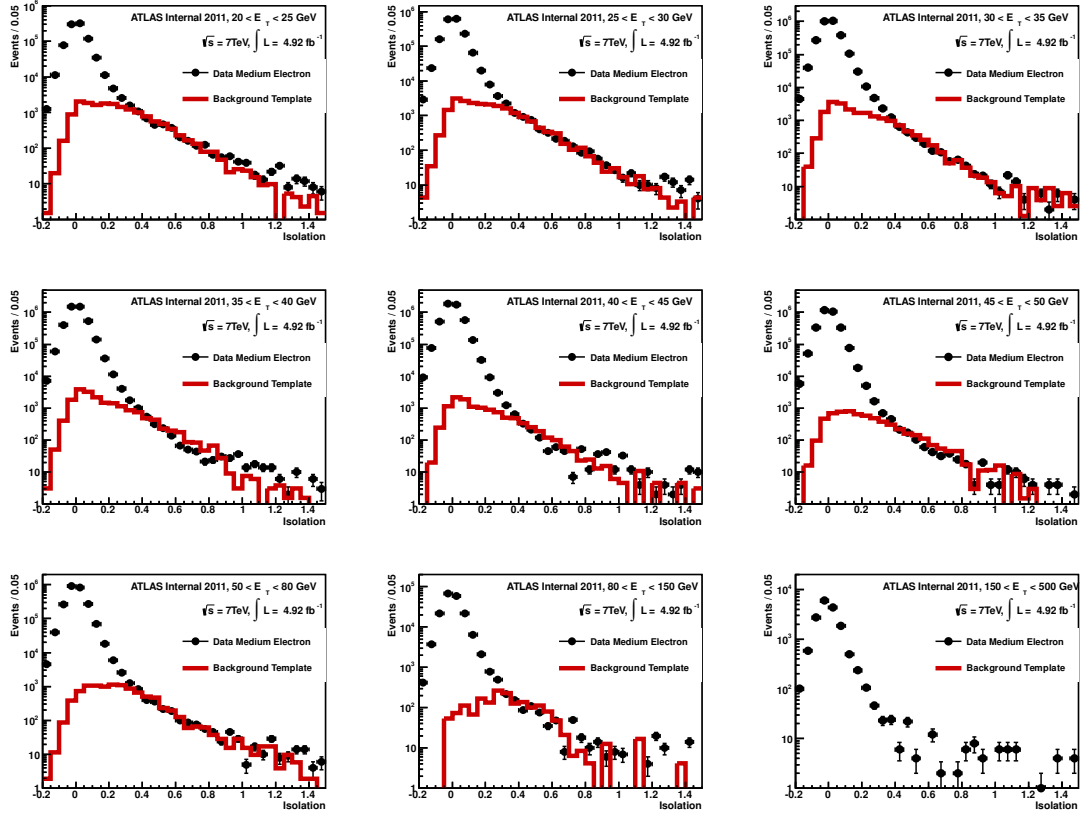


Figure A.8: $f_{\text{side}} + \text{!rTRT/rphi}$ template for *Medium* ID level and opposite sign charge Tag-and-Probe pair with an invariant mass of $76 < M_{ee} < 116 \text{ GeV}$ in bins of electron E_T .

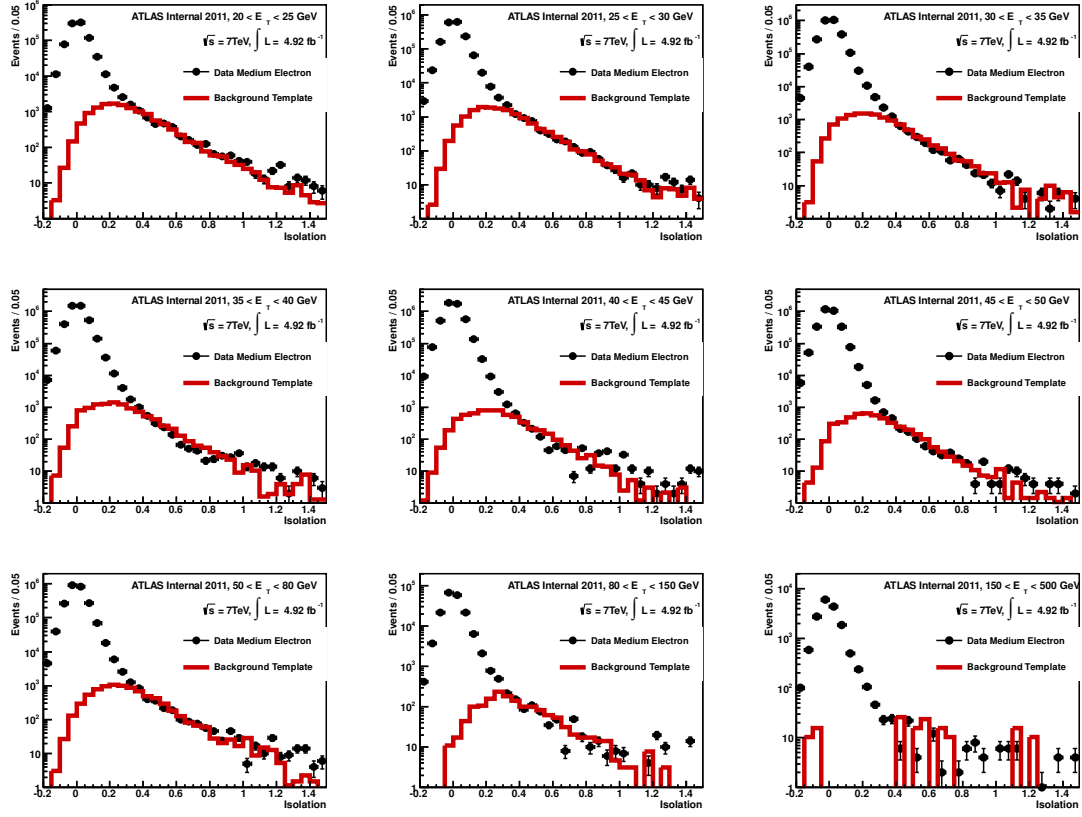


Figure A.9: SS+!loose template for *Medium* ID level and opposite sign charge Tag-and-Probe pair with an invariant mass of $76 < M_{ee} < 116$ GeV in bins of electron E_T .

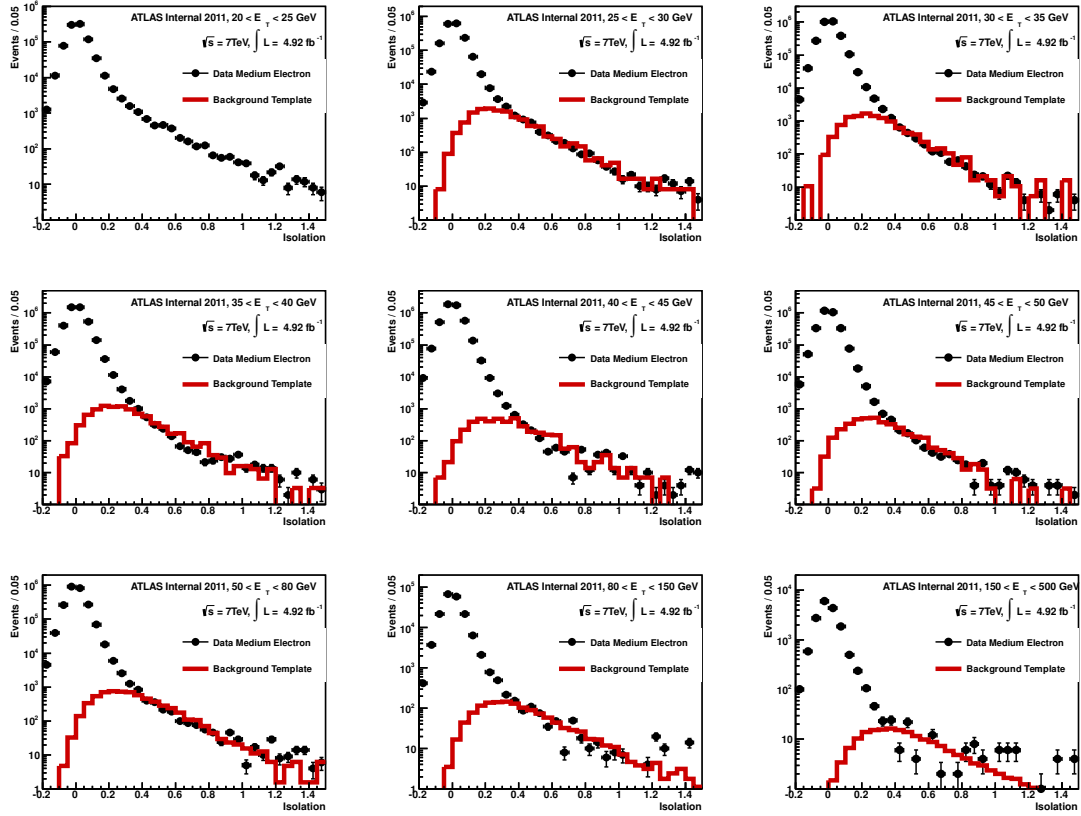


Figure A.10: Jet template for *Medium* ID level and opposite sign charge Tag-and-Probe pair with an invariant mass of $76 < M_{ee} < 116$ GeV in bins of electron E_T .

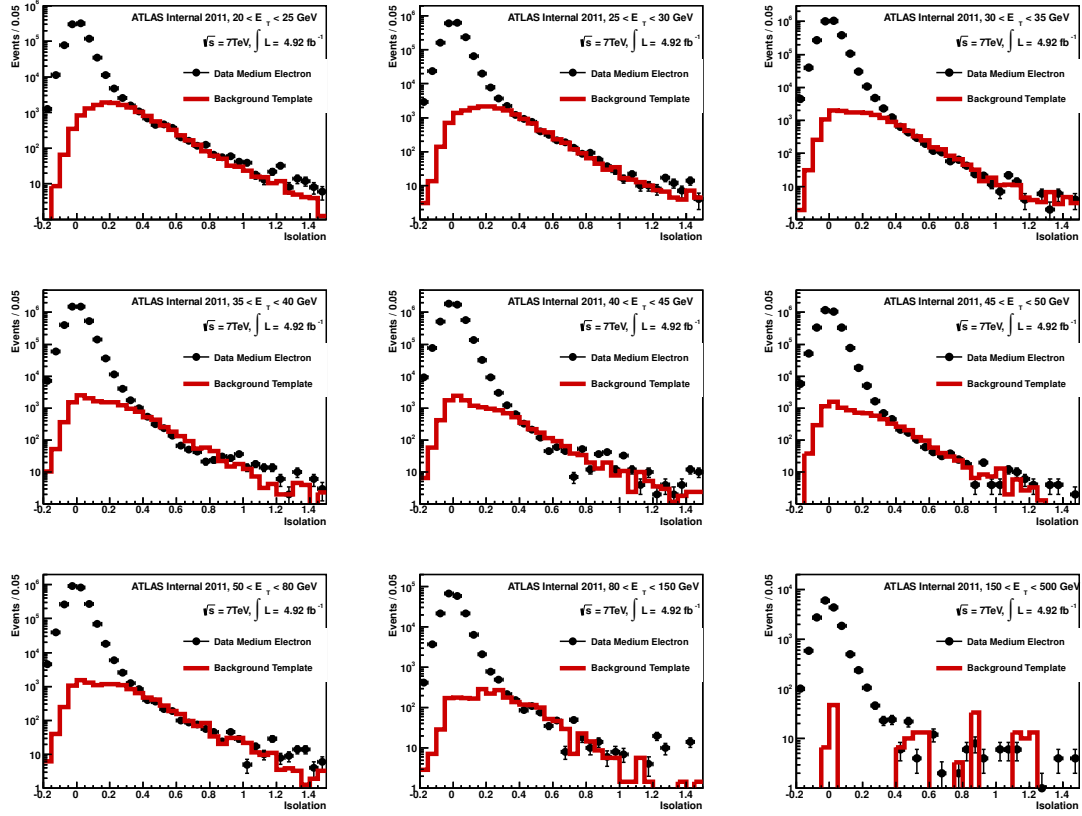


Figure A.11: !TrackMatch template for *Medium* ID level and opposite sign charge Tag-and-Probe pair with an invariant mass of $76 < M_{ee} < 116$ GeV in bins of electron E_T .

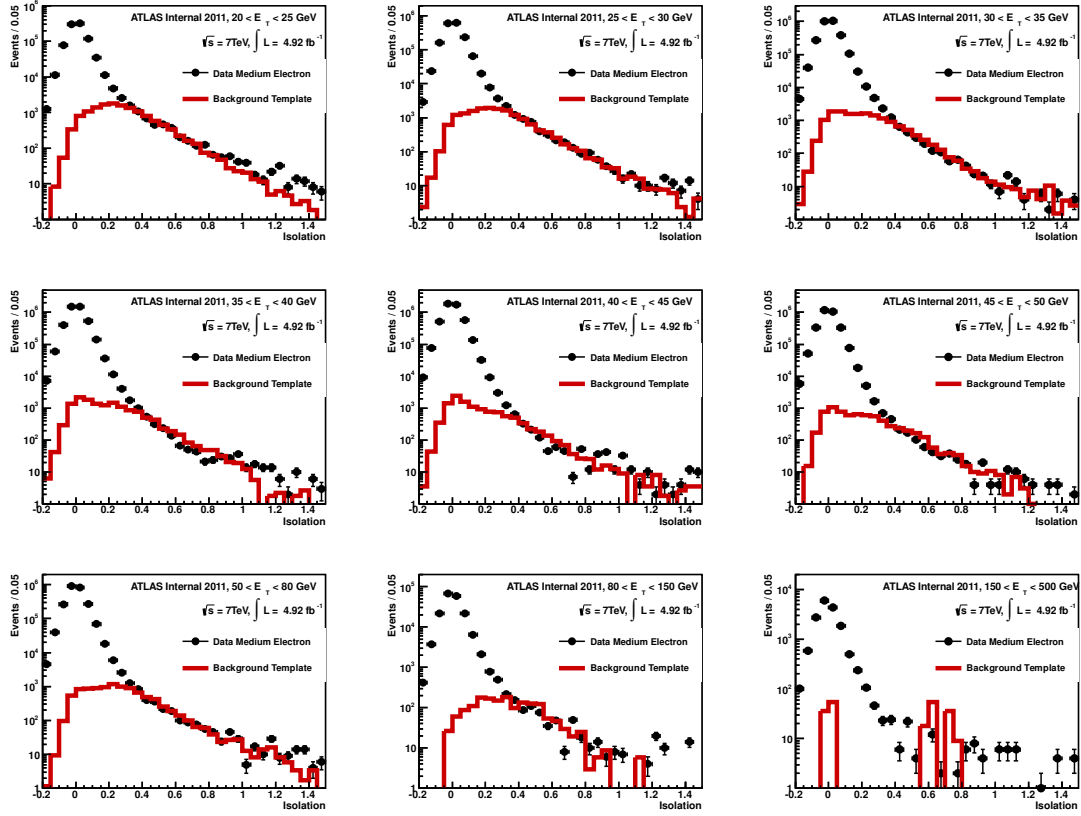


Figure A.12: $!w_{tot} + !r_{TRT} + r_{phi}$ template for *Medium* ID level and opposite sign charge Tag-and-Probe pair with an invariant mass of $76 < M_{ee} < 116$ GeV in bins of electron E_T .

A.3.2 Bins of Pseudorapidity

Base Level (“track quality, trkQ”) Identification

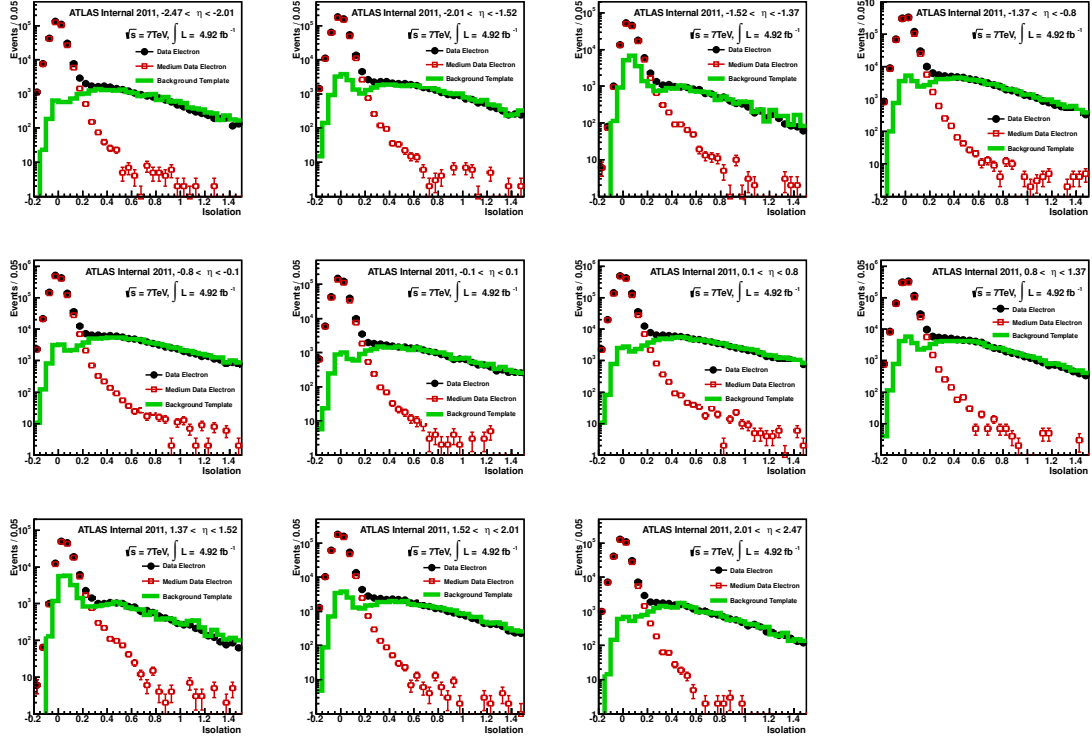


Figure A.13: fside template for base level identification and opposite sign charge Tag-and-Probe pair with an invariant mass of $76 < M_{ee} < 116$ GeV in bins of electron η .

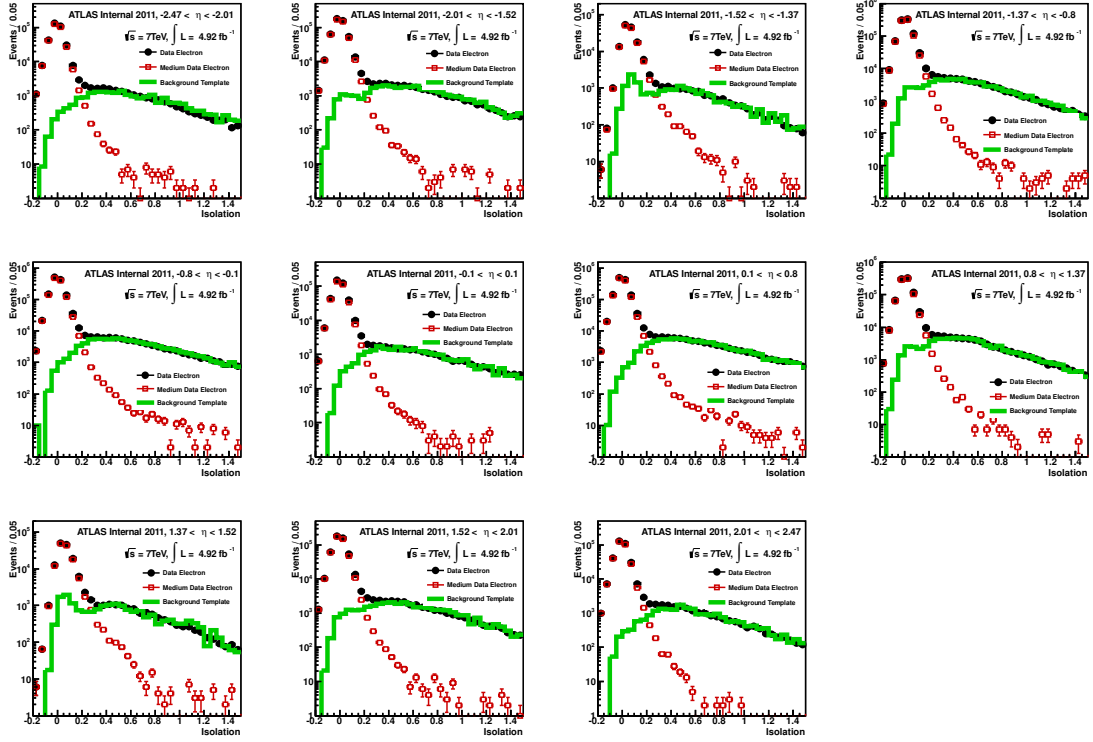


Figure A.14: $\sqrt{s} + \text{!rTRT/rphi}$ template for base level identification and opposite sign charge Tag-and-Probe pair with an invariant mass of $76 < M_{ee} < 116$ GeV in bins of electron η .

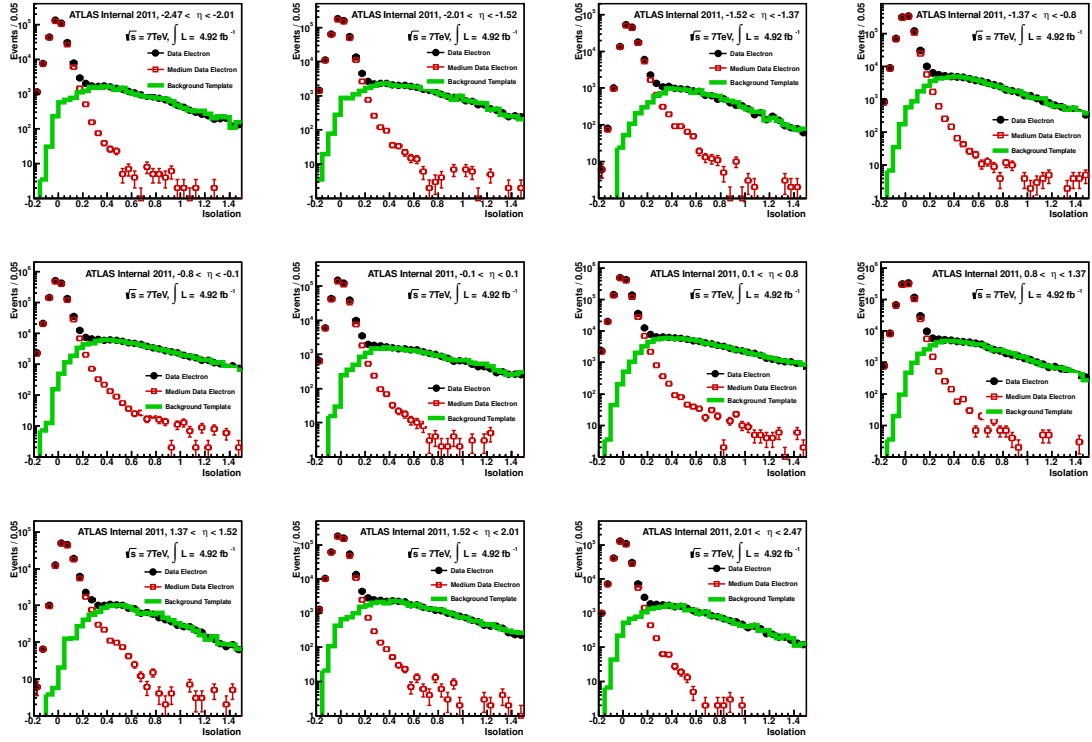


Figure A.15: SS+ll loose template for base level identification and opposite sign charge Tag-and-Probe pair with an invariant mass of $76 < M_{ee} < 116$ GeV in bins of electron η .

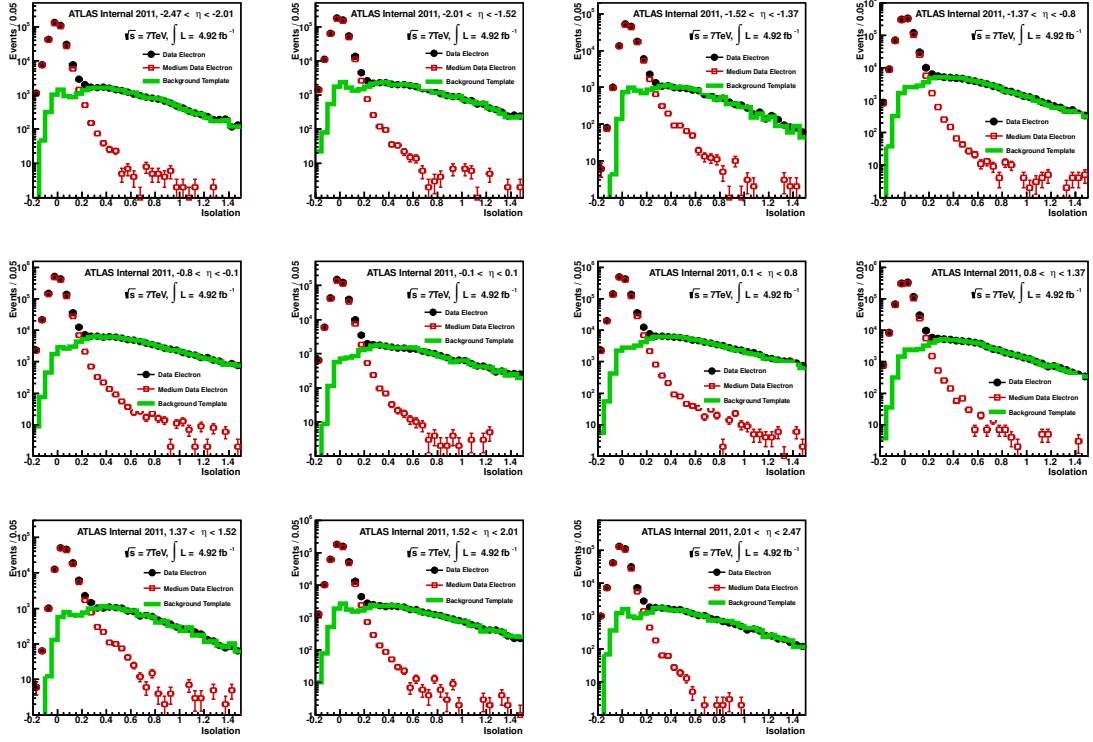


Figure A.16: !TrackMatch template for base level identification and opposite sign charge Tag-and-Probe pair with an invariant mass of $76 < M_{ee} < 116$ GeV in bins of electron η .

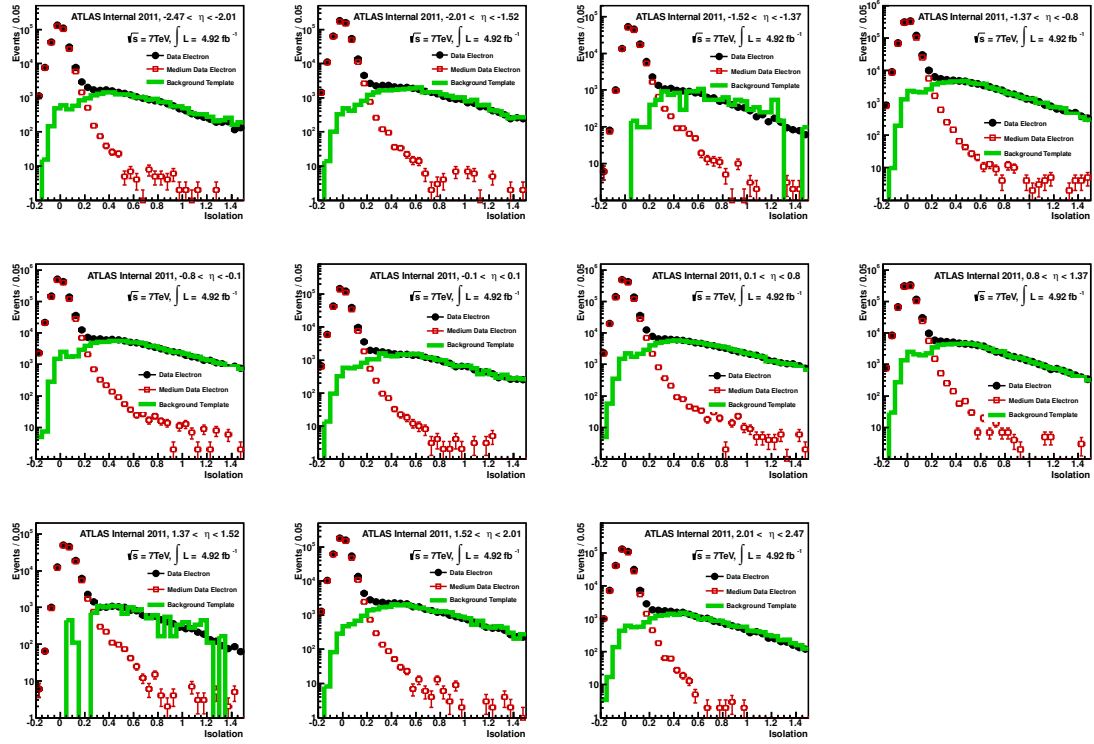


Figure A.17: $lwstot + lrTRT + rphi$ template for base level identification and opposite sign charge Tag-and-Probe pair with an invariant mass of $76 < M_{ee} < 116$ GeV in bins of electron η .

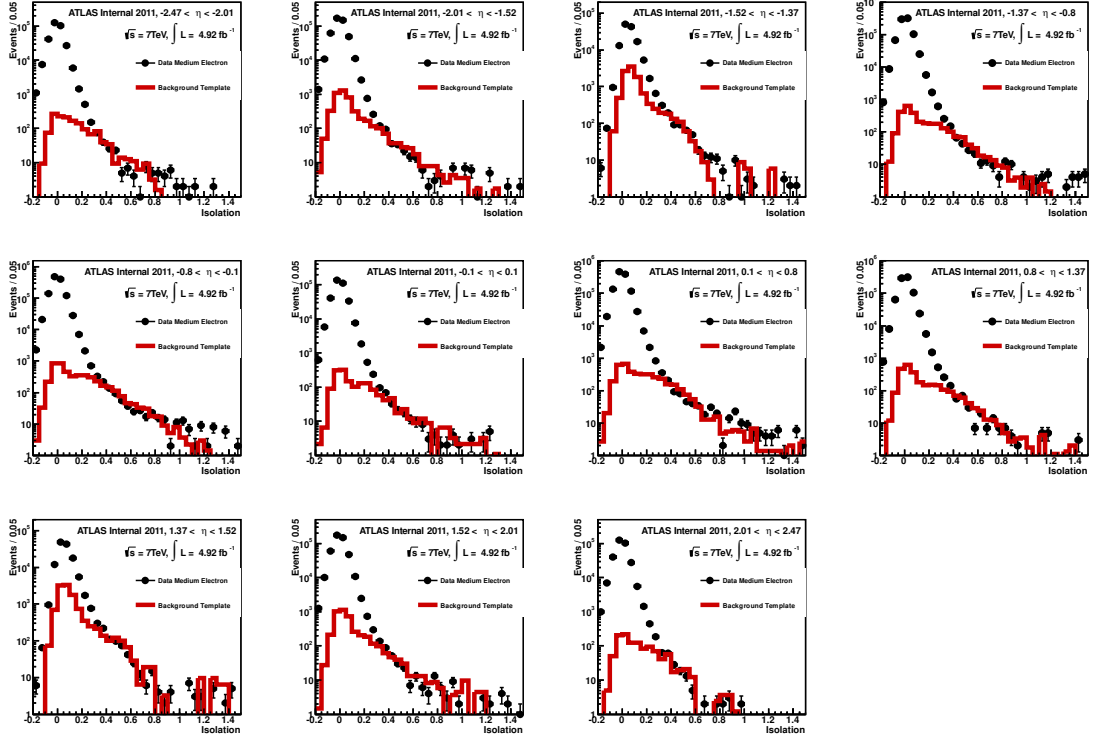
Medium Identification (ID) Level

Figure A.18: f_{side} template for *Medium* ID level and opposite sign charge Tag-and-Probe pair with an invariant mass of $76 < M_{ee} < 116$ GeV in bins of electron η .

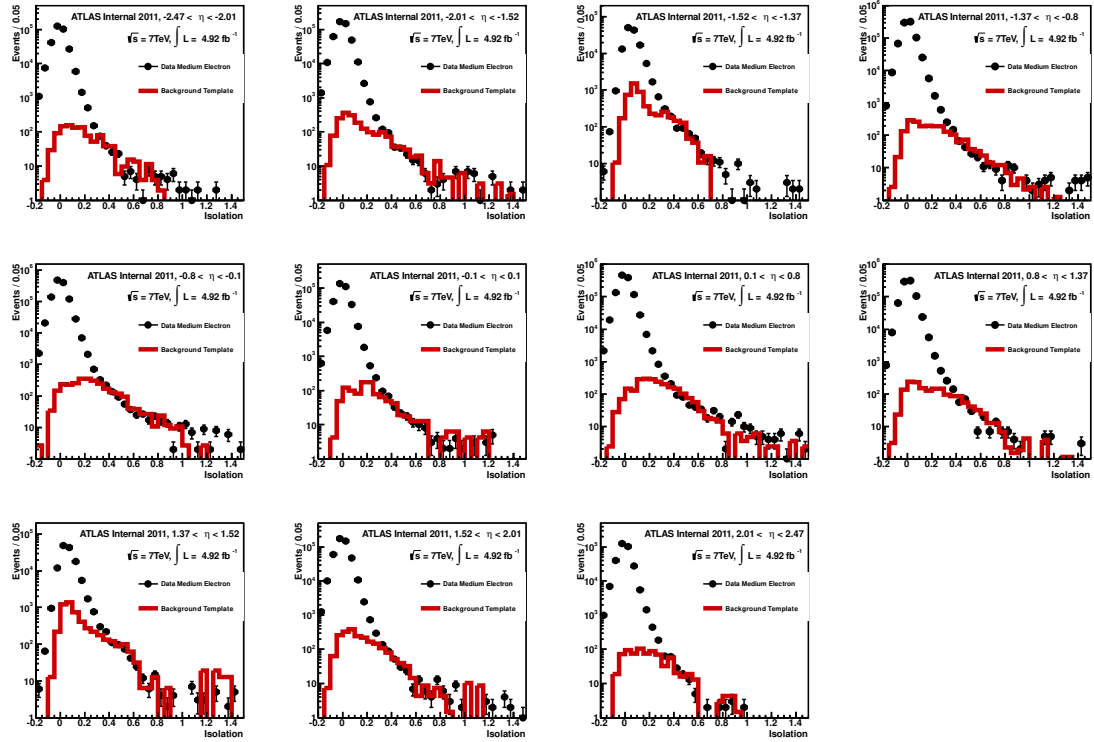


Figure A.19: $f_{\text{side}} + l_{\text{rTRT}}/r_{\text{phi}}$ template for *Medium* ID level and opposite sign charge Tag-and-Probe pair with an invariant mass of $76 < M_{ee} < 116$ GeV in bins of electron η .

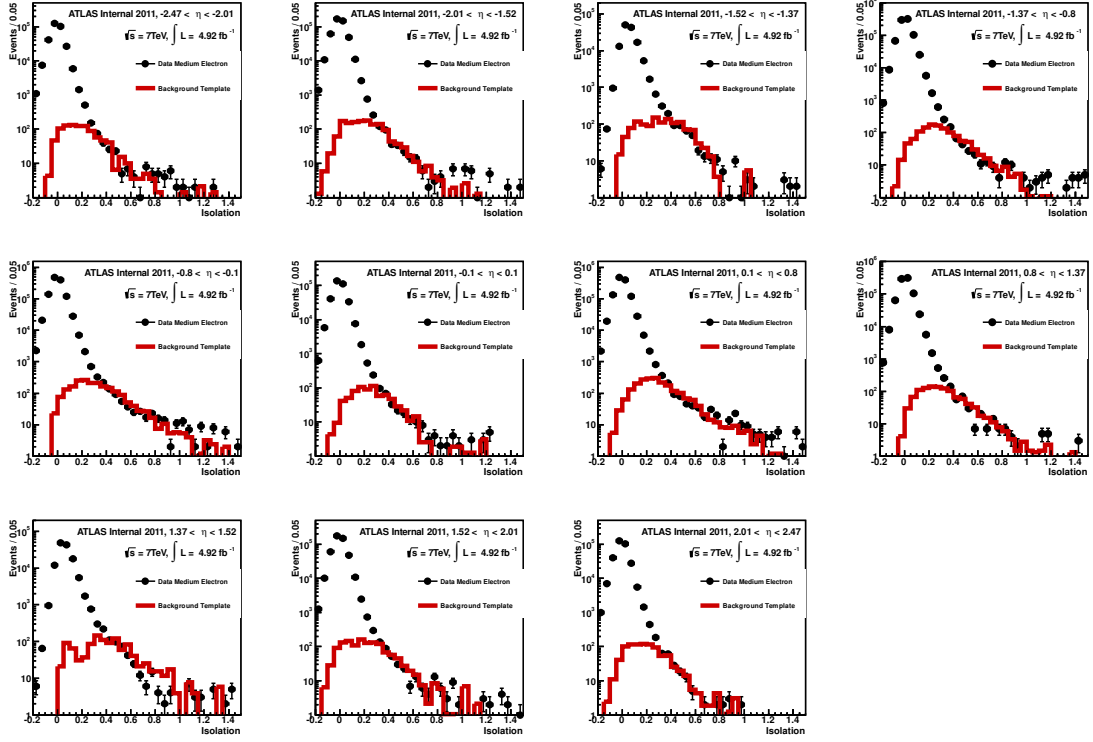


Figure A.20: \sqrt{s} +!loose template for *Medium* ID level and opposite sign charge Tag-and-Probe pair with an invariant mass of $76 < M_{ee} < 116$ GeV in bins of electron η .

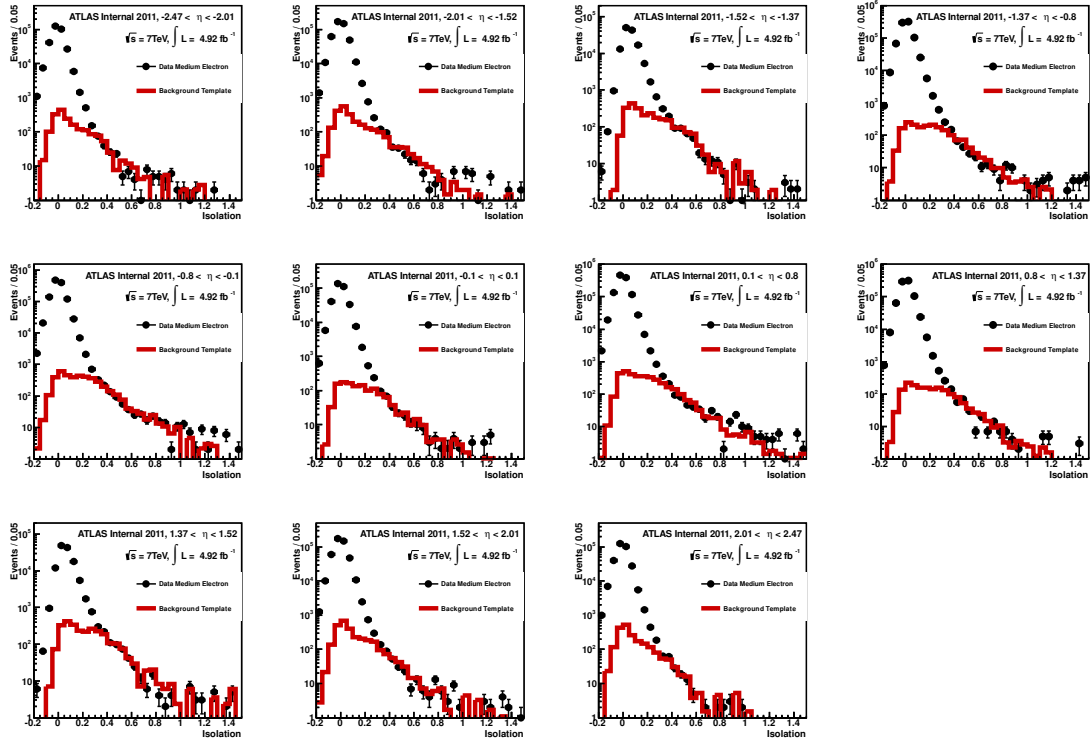


Figure A.21: $!TrackMatch$ template for *Medium* ID level and opposite sign charge Tag-and-Probe pair with an invariant mass of $76 < M_{ee} < 116$ GeV in bins of electron η .

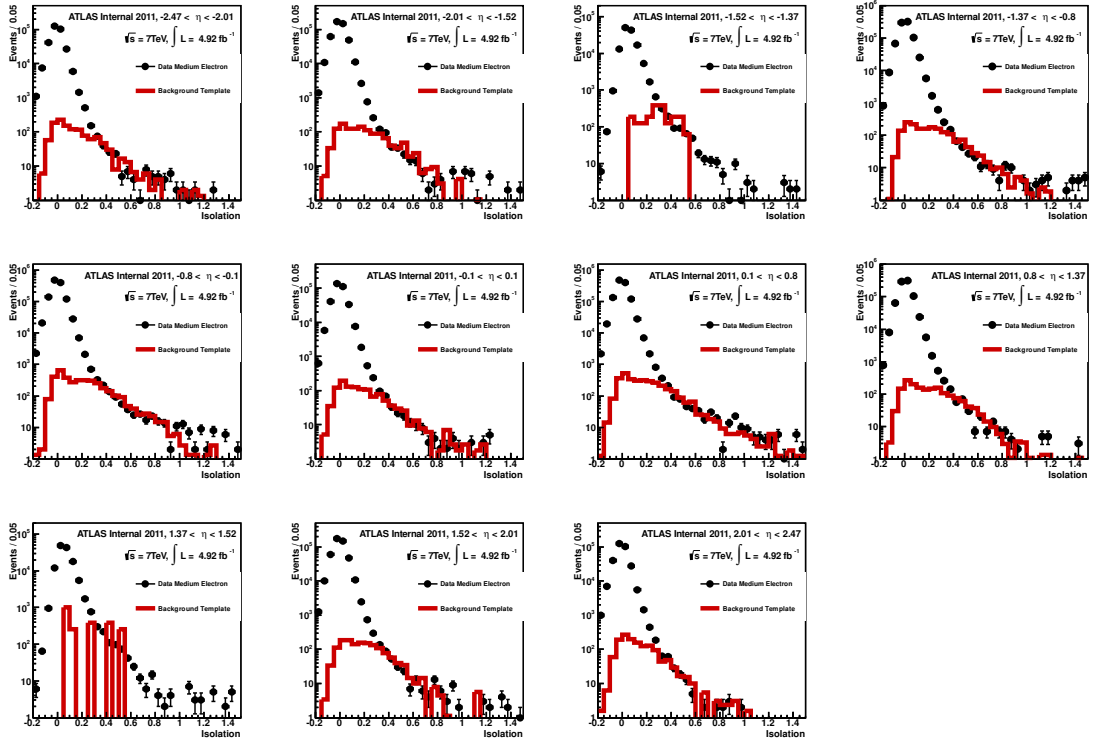


Figure A.22: $!w_{\text{tot}} + !r_{\text{TRT}} + \text{rphi}$ template for *Medium* ID level and opposite sign charge Tag-and-Probe pair with an invariant mass of $76 < M_{\text{ee}} < 116$ GeV in bins of electron η .

A.4 Efficiency Measurement for $m_{ee} > 76 \text{ GeV}$

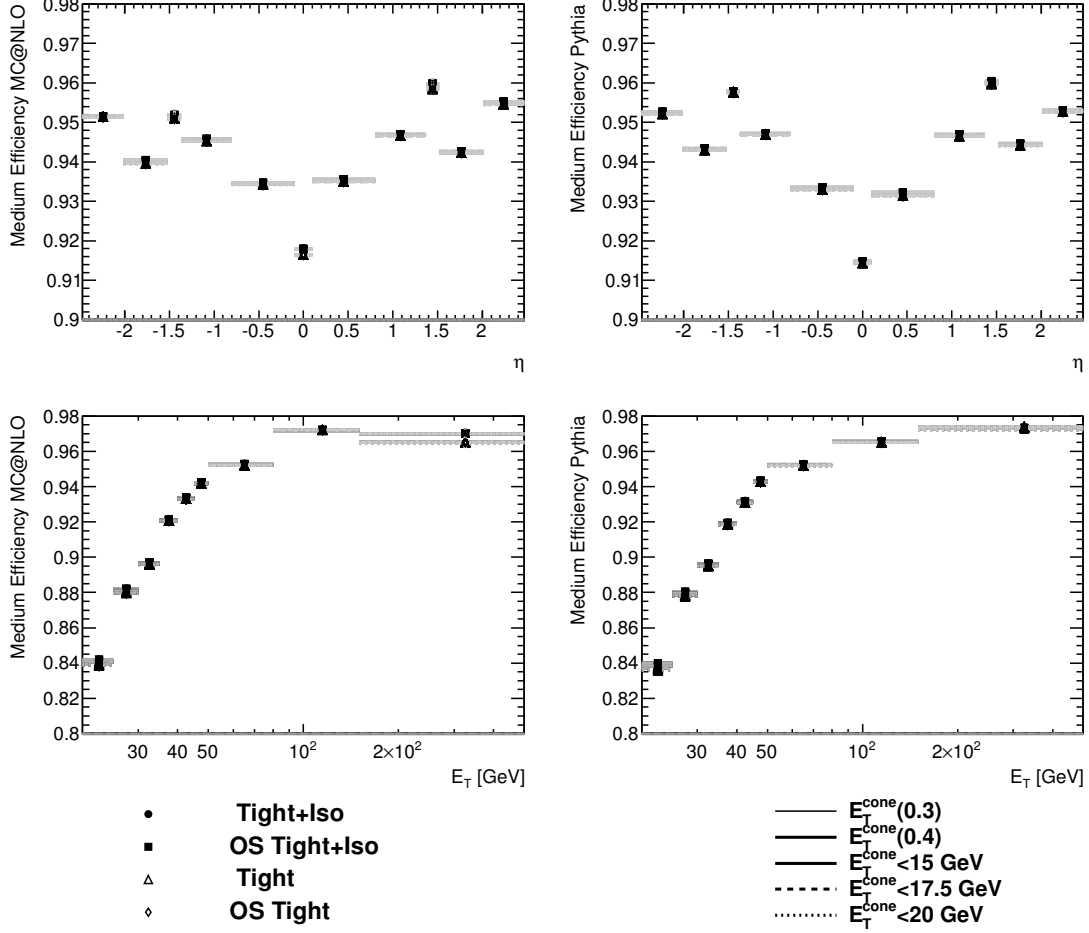


Figure A.23: Expected Medium identification efficiency from MC@NLO and PYTHIA Drell-Yan samples using loose truth matching, in bins of electron η and E_T , di-electron invariant mass $m_{ee} > 76 \text{ GeV}$. Variations of the discriminating variable, the integration threshold the charge sign requirement and the tag isolation are shown.

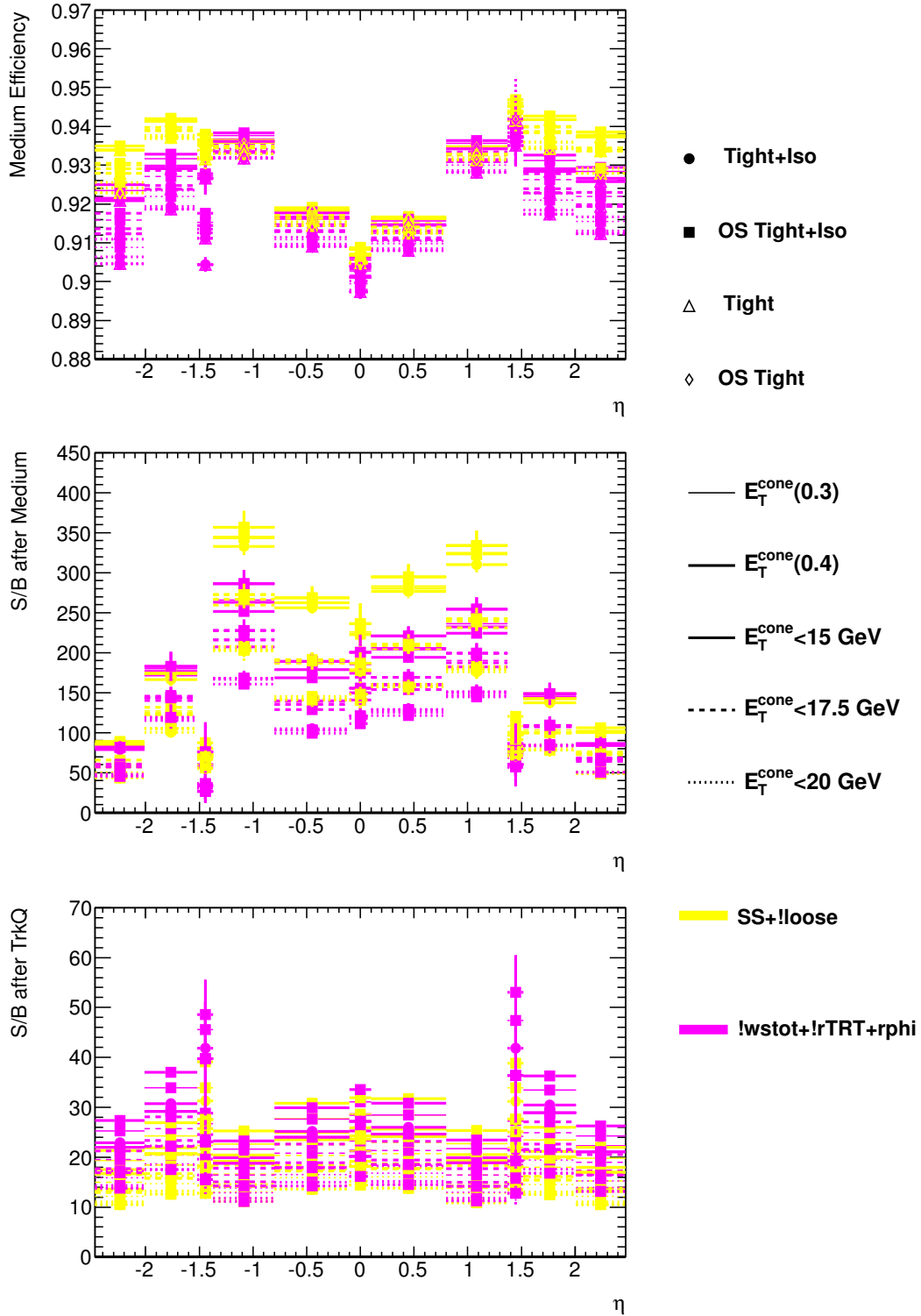


Figure A.24: Measured Medium identification efficiency in data and signal-over-background ratio after Medium ID and for base level (TrkQ), for Tag-and-Probe pairs with an invariant mass of $m_{ee} > 76 \text{ GeV}$ in bins of electron pseudorapidity η . For this measurement only the SS+!loose and !wstot + !rTRT + rphi templates were used.

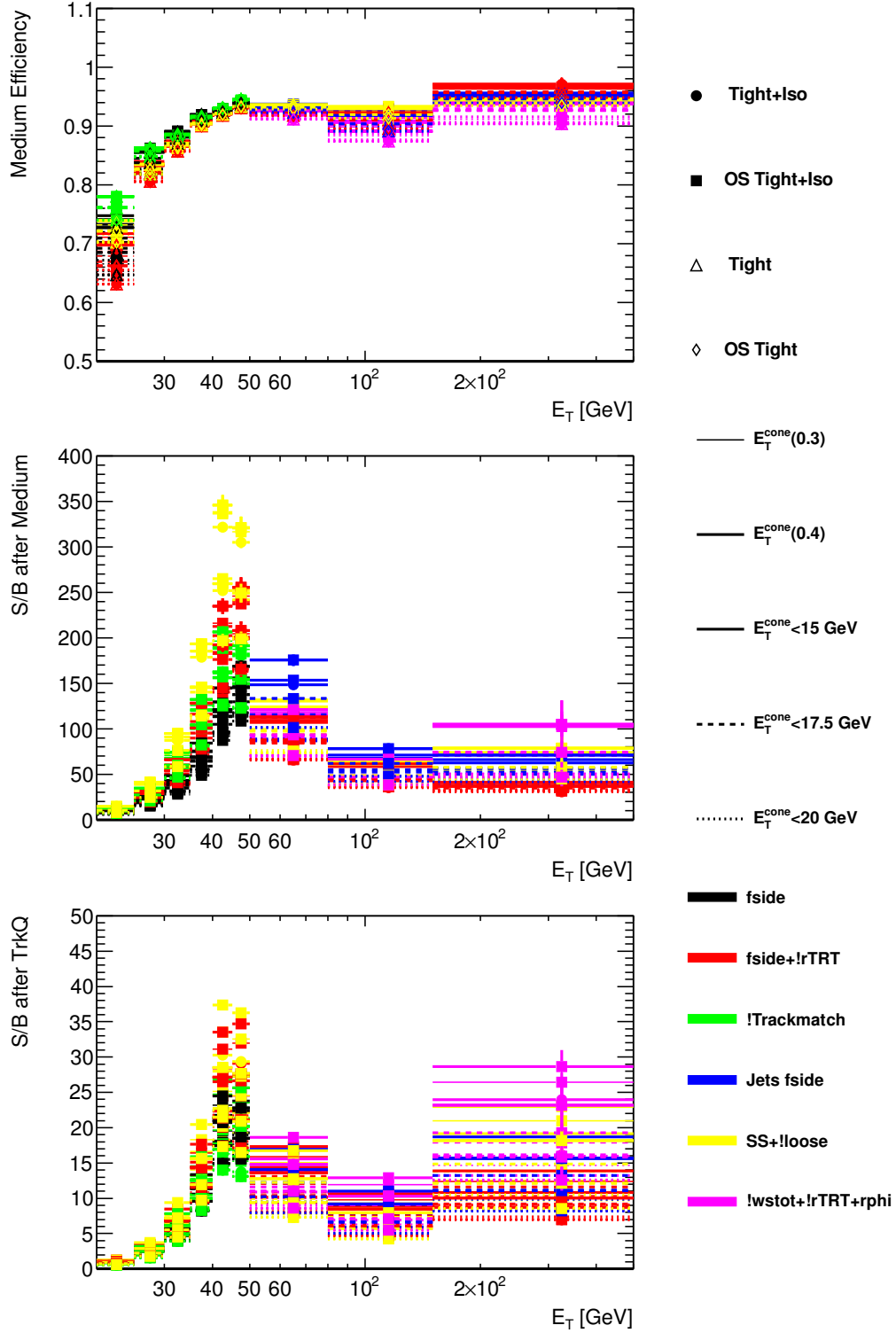


Figure A.25: Measured Medium identification efficiency in data and signal-over-background ratio after Medium ID and for base level (TrkQ), for Tag-and-Probe pairs with an invariant mass of $m_{ee} > 76$ GeV in bins of electron transverse energy E_T .

Appendix B

Acknowledgments

Most of all I want to thank my thesis advisor Marzio Nessi for having taken me as his student, for the liberty he left me and the support he gave me in the moments when I needed it. I also want to thank Gabriella Pásztor for all her efforts to support me and the encouragement when I was on the verge of despair. Many thanks also to Paul Bell for his guidance and helpful comments.

Andrea dell’Acqua deserves a considerable amount of my gratitude too, for his help with the beam pipe simulations and for being the laid-back and unpretentious person he is. Many thanks to Vivek Jain as well who was always ready to help with questions regarding the secondary hadronic interaction study. In addition, I would like to thank Aleandro Nisati and Guiseppe Iacobucci for carefully reading my thesis and asking curious questions about my work. I want to thank these people not only for their help with the actual work but also for their inspiration and motivation to learn and improve myself.

In the course of my PhD, many other people contributed in their own ways: Xin Wu, my (part time) office mates William Bell, Killian Rosbach, Francesco Guescini and Spyros Argyropoulos. Furthermore Moritz Backes, Snezana Nektarijevic, Valerio Dao, Eleonora Benhar Noccioli and Attilio Picazio, my colleagues and fellow sufferers in university lectures and/or physics schools. At this point I should also mention Nuno Oliveira and his training sessions for the SLIMOS shifts, a truly unforgettable experience.

Many thanks also to Martine Desynder-Ivesdal, Fabiola Gianotti, Dave Charlton, Andy Lankford, Markus Nordberg and Peter Jenni for the warm welcome on the 4th floor in building 40 at CERN, my “home” for most of the past 3 years. I feel very privileged having had the opportunity to work in an such an inspiring and special environment.

Finally, merci Mathieu, for having stood by me in many bad moments - and despite the abundance of my geeky jokes -, for having taught me a lot about physics, ATLAS and many other interesting things. Je suis très contente de t’avoir dans ma vie, toé.

Bibliography

- [1] YAO, W.-M. ET AL., *Journal of Physics G* **33** (2006).
- [2] W. GREINER, S. SCHRAMM, and E. STEIN, *Quantum Chromodynamics*, Springer, third edition.
- [3] RYDER, LEWIS H., *Quantum Field Theory*, Cambridge, second edition.
- [4] THE ATLAS COLLABORATION, *Physics Letters B* **716**, 1 (2012).
- [5] THE CMS COLLABORATION, *Physics Letters B* **716**, 30 (2012).
- [6] FERMLAB, OFFICE OF SCIENCE, Inquiring minds: The science of matter, space and time.
- [7] F. TANEDO, Quantum Diaries: Helicity, Chirality, Mass, and the Higgs.
- [8] E. LECTURES, Electroweak Interactions.
- [9] A. SALAM, *Nobel Symposium 8, Aspenasgarden* (1969).
- [10] S. GLASHOW, *Nucl.Phys.* **22**, 579 (1961).
- [11] S. L. GLASHOW, J. ILIOPOULOS, and L. MAIANI, *Phys. Rev. D* **2**, 1285 (1970).
- [12] S. WEINBERG, *Phys.Rev.Lett.* **19**, 1264 (1967).
- [13] HASERT, F.J., *Phys. Lett.* **46B** (1973).
- [14] THE UA1 COLLABORATION, *Physics Letters B* **122**, 103 (1983).
- [15] THE UA2 COLLABORATION, *Phys.Lett.* **B122**, 476 (1983).
- [16] J. SCHWINGER, *Annals of Physics* **2**, 407 (1957).
- [17] S. BLUDMAN, *Il Nuovo Cimento Series 10* **9**, 433 (1958).
- [18] J. LEITE LOPES, *Nuclear Physics* **8**, 234 (1958).

- [19] J. GOLDSTONE, *Il Nuovo Cimento (1955-1965)* **19**, 154 (1961), 10.1007/BF02812722.
- [20] P. W. HIGGS, *Phys. Rev. Lett.* **13**, 508 (1964).
- [21] G. S. GURALNIK, C. R. HAGEN, and T. W. B. KIBBLE, *Phys. Rev. Lett.* **13**, 585 (1964).
- [22] F. ENGLERT and R. BROUT, *Phys. Rev. Letters* **13** (1964).
- [23] S. NOVAES, *Standard model: An Introduction*, 1999.
- [24] M. S. CARENA and H. E. HABER, *Prog.Part.Nucl.Phys.* **50**, 63 (2003).
- [25] A. DJOUADI, *Physics Reports* **457**, 1 (2008).
- [26] BERINGER J ET AL. (PDG), *PR D86* **010001** (2012).
- [27] THE PARTICLE DATA GROUP, PDG Live - Particle Properties.
- [28] R. MCALLISTER and R. HOFSTADTER, *Phys.Rev.* **102**, 851 (1956).
- [29] ELLIS, R.K., *Quantum Chromodynamics*, 2005.
- [30] W.A. BARDEEN ET AL., *Phys. Rev. D* **18** (1978).
- [31] J. SCHIECK, (2011).
- [32] O. GREENBERG, *ArXiv e-prints* , 255 (2008).
- [33] J. D. BJORKEN, *Phys. Rev.* **179**, 1547 (1969).
- [34] M. PESKIN and D. SCHROEDER, *An Introduction to Quantum Field Theory*, Westview ABP, 1995.
- [35] A. MARTIN, W. STIRLING, R. THORNE, and G. WATT, *The European Physical Journal C - Particles and Fields* **63**, 189 (2009), 10.1140/epjc/s10052-009-1072-5.
- [36] V. GRIBOV and L. LIPATOV, *Sov. J. Nucl. Phys.* **15** (1972).
- [37] G. ALTARELLI and G. PARISI, *Nucl. Phys. B* **126** (1977).
- [38] Y. DOKSHITZER, *Sov. Phys. JETP* **46** (1977).
- [39] S. D. DRELL and T.-M. YAN, *Phys. Rev. Lett.* **25**, 316 (1970).
- [40] J. H. CHRISTENSON, G. S. HICKS, L. M. LEDERMAN, P. J. LIMON, B. G. POPE, and E. ZAVATTINI, *Phys. Rev. Lett.* **25**, 1523 (1970).
- [41] W. VAN NEERVEN and E. ZIJLSTRA, *Nuclear Physics B* **382**, 11 (1992).

- [42] T. SJÖSTRAND, S. MRENN, and P. SKANDS, *JHEP* **05**, 026 (2006).
- [43] É. KURAEV, L. LIPATOV, and V. FADIN, *Soviet Journal of Experimental and Theoretical Physics* **45**, 199 (1977).
- [44] T. SJÖSTRAND, *Nuclear Physics B* **248**, 469 (1984).
- [45] Y. KOVCHegov, *Phys. Rev. D* **60** (1999).
- [46] T. SJÖSTRAND, Monte Carlo Generators, in *The 2006 European School of High-Energy Physics Aronsborg, Sweden*, 2006.
- [47] S. HOECHE, F. KRAUSS, N. LAVESSON, L. LONNBLAD, M. MANGANO, et al., (2006).
- [48] P. GOLONKA and Z. WAS, *Eur.Phys.J.* **C45**, 97 (2006).
- [49] G. CORCELLA, I. KNOWLES, G. MARCHESINI, S. MORETTI, K. ODAGIRI, P. RICHARDSON, M. SEYMOUR, and B. WEBBER, *JHEP* **0101**, 010 (2001).
- [50] J. BUTTERWORTH, J. FORSHAW, and M. SEYMOUR, *Z. Phys.* **C72**, 637 (1996).
- [51] M. L. MANGANO, M. MORETTI, F. PICCININI, R. PITTAU, and A. D. POLOSA, *JHEP* **0307**, 001 (2003).
- [52] S. FRIXIONE and B. WEBBER, *arXiv:hep-ph/0204244v2*, *JHEP* **0206**, 029 (2002).
- [53] T. GLEISBERG, S. HOECHE, F. KRAUSS, M. SCHONHERR, S. SCHUMANN, et al., *JHEP* **0902**, 007 (2009).
- [54] LHC MACHINE OUTREACH FOR WEB CERN, Collisions.
- [55] ATLAS TWIKI, Public Results: Luminosity.
- [56] X. CID VIDAL and R. CID, Taking a closer look at the LHC.
- [57] THE ATLAS COLLABORATION, *ATLAS detector and physics performance: Technical Design Report, 1*, Technical Design Report ATLAS, CERN, Geneva, 1999, Electronic version not available.
- [58] V. GALLO, *Proceedings of LHC on the March, Protvino, Russia* (2011).
- [59] ATLAS TWIKI, *Overview of the ATLAS trigger system*.
- [60] S. ARMSTRONG ET AL., *Nuclear Instruments and Methods in Physics Research Section A: Accelerators, Spectrometers, Detectors and Associated Equipment* **518**, 537 (2004), Frontier Detectors for Frontier Physics: Proceedings.

- [61] M. NESSI, Private Communication.
- [62] THE ATLAS COLLABORATION, *The European Physical Journal C - Particles and Fields* **72**, 1 (2012), 10.1140/epjc/s10052-012-1909-1.
- [63] O. ARNAEZ, D. FROIDEVAUX, M. AHARROUCHE, J. ALISON, E. BERGLUND, R. BERNHARD, A. BOCCI, V. DAO, F. ELLINGHAUS, F. DERUE, M. FIASCARIS, S. HEIM, F. HUBAUT, L. ICONOMIDOU-FAYARD, N. KERSCHEN, J. KRETZSCHMAR, Z. LIANG, D. LIU, K. LOHWASSER, J. MAURER, G. PASZTOR, R. POTTGEN, E. RICHTER-WAS, A. ROBICHAUD-VERONNEAU, T. THEVENEUX-PELZER, R. SCHAFFER, E. SCHMIDT, M. TEINTURIER, and H. ZHU, Electron efficiency measurements using ATLAS 2010 data at $\sqrt{s} = 7$ TeV: Supporting note for the 2010 egamma paper, Technical Report ATL-COM-PHYS-2011-322, CERN, Geneva, 2011.
- [64] M. AGUSTONI, M. AHARROUCHE, A. AHMAD, N. BESSON, M. BOONEKAMP, L. CARMINATI, J. DE VIVIE, H. DE LA TORRE, J. DEL PESO, J. FARLEY, V. GALLO, S. GLAZOV, C. HANDEL, S. HAUG, M. KARNEVSKIY, I. KOLETSSOU, N. LORENZO MARTINEZ, N. MAKOVEC, L. MANDELLI, Y. NAKAHAMA, R. TURRA, and G. UNAL, Electromagnetic energy scale in-situ calibration and performance: Supporting document for the egamma performance paper, Technical Report ATL-COM-PHYS-2011-263, CERN, Geneva, 2011.
- [65] THE ATLAS COLLABORATION, *Eur. Phys. J. C* **72** (2012) 1909 (2011).
- [66] THE ATLAS COLLABORATION, *Expected performance of the ATLAS experiment: detector, trigger and physics*, CERN, Geneva, 2009.
- [67] M. CAPEANS, G. DARBO, K. EINSWEILLER, M. ELSING, T. FLICK, M. GARCIA-SCIVERES, C. GEMME, H. PERNEGGER, O. ROHNE, and R. VUILLERMET, ATLAS Insertable B-Layer Technical Design Report, Technical Report CERN-LHCC-2010-013. ATLAS-TDR-19, CERN, Geneva, 2010.
- [68] J.-C. GAYDE, A. HERTY, H. MAINAUD DURAND, and C. LASSEUR, Combined Levelling Systems for the Vertical Monitoring of a Large Physics Experiment, Technical report, CERN, Geneva, 2006.
- [69] THE ATLAS COLLABORATION, *Journal of Instrumentation* **3**, S08003 (2008).
- [70] J.-C. GAYDE, ATLAS - HLS BEDPLATES - VARIATION OF DIFFERENCES IN HEIGHT OF HLS SENSORS FROM 01 JAN 2010 TO 08 DEC 2010, Technical report.
- [71] V. KHOZE, F. KRAUSS, A. MARTIN, M. RYSKIN, and K. ZAPP, *Eur.Phys.J.* **C69**, 85 (2010).
- [72] THE ATLAS COLLABORATION, *Journal of Instrumentation* **7**, P01013 (2012).

- [73] THE ATLAS COLLABORATION, *JINST* **3**, S08003 (2008).
- [74] D. MERGELKUHLE and A. WIART, ATLAS Beam Pipe - Measurement of VI A- and C-End in UX15, Technical report, 2007.
- [75] S. BARANOV, M. BOSMAN, I. DAWSON, V. HEDBERG, A. NISATI, and M. SHUPE, Estimation of Radiation Background, Impact on Detectors, Activation and Shielding Optimization in ATLAS, Technical Report ATL-GEN-2005-001. ATL-COM-GEN-2005-001. CERN-ATL-GEN-2005-001, CERN, Geneva, 2005.
- [76] E. SEGRÉ, *Nuclei and Particles*, W.A. Benjamin Inc., 1965.
- [77] Y. TSAI, *Review of Modern Physics* **46**, 815 (1974).
- [78] EIDELMAN, S. ET AL, *Physics Letters B* **592** (2004).
- [79] M. VIRCHAUX, ATLAS Muon Spectrometer: Persint; TWiki.
- [80] M. RAYMOND, Private Communication.
- [81] A. ABULENCIA et al., *Phys.Rev.Lett.* **96**, 211801 (2006).
- [82] C. T. HILL and E. H. SIMMONS, *Physics Reports* **381**, 235 (2003).
- [83] L. RANDALL and R. SUNDRUM, *Phys.Rev.Lett.* **83**, 3370 (1999).
- [84] T. KALUZA, *Sitzungsber. Preuss. Akad. Wiss. Berlin. (Math. Phys.)* **96**, 6972.
- [85] O. KLEIN, *Zeitschrift fur Physik* **37**, 895 (1926).
- [86] THE ATLAS COLLABORATION, *Phys. Rev. D* **85**, 072004 (2010).
- [87] THE CMS COLLABORATION, *J. High Energy Phys* **10**, 132 (2011).
- [88] THE CDF COLLABORATION, *J. Phys G* **34**, 2457 (2007).
- [89] THE D0 COLLABORATION, *Phys. Rev. D* **61**, 072001 (2000).
- [90] THE CMS COLLABORATION, *JHEP* **10**, 007 (2011).
- [91] THE ATLAS COLLABORATION, *Phys. Rev. Lett* **107**, 272002 (2011).
- [92] THE ATLAS COLLABORATION, *JHEP* **1211**, 138 (2012).
- [93] THE CMS COLLABORATION, *Phys.Lett.* **B714**, 158 (2012).
- [94] THE CMS COLLABORATION, (2012).
- [95] THE ATLAS COLLABORATION, *Eur. Phys. J. C* **72**, 1909 (2011).

- [96] A. SHERSTNEV and R. S. THORNE, *Eur. Phys. J.* **C55**, 553 ff. (2008).
- [97] J. PUMPLIN, D. STUMP, J. HUSTON, H. LAI, P. NADOLSKY, and W. TUNG, *JHEP* **0207**, 012 (2002).
- [98] M. GUZZI, P. NADOLSKY, E. BERGER, H.-L. LAI, and F. E. A. OLNES, *ArXiv e-prints* (2011).
- [99] YENNIE, D. R. AND FRAUTSCHI, S. C. AND SUURA, H., *Annals Phys.* **13**, 379 (1961).
- [100] ATLAS COLLABORATION, *ATL-PHYS-PUB-2011-009*, cdsweb.cern.ch/record/1363300 (2011).
- [101] WZ PHYSICS GROUP, WZ Electroweak Common Topics 2011.
- [102] L. APERIO-BELLA, P. BELL, F. ELLINGHAUS, S. GADOMSKI, C. GOERINGER, M. GOULETTE, U. KLEIN, K. NIKOLICS, G. PASZTOR, Y.-J. SCHNELLBACH, S. WOLLSTADT, and X. WU, Measurement of the high-mass Drell-Yan differential cross-section in the di-electron nal state: Supporting Document, Technical Report ATL-COM-PHYS-2012-519, CERN, Geneva, 2012.
- [103] R. HAMBERG, W. VAN NEERVEN, and T. MATSUURA, *Nucl. Phys.* **B359**, 343 (1991).
- [104] T. NUNNEMANN, Private Communication.
- [105] C. CARLONI CALAME, G. MONTAGNA, O. NICROSINI, and A. VICINI, *arXiv:0710.1722 [hep-ph]*. *JHEP* **10**, 109 (2007).
- [106] L. ASQUITH, B. BRELIER, J. M. BUTTERWORTH, M. CAMPANELLI, T. CARLI, G. CHOUDALAKIS, P. A. DELSART, S. DE CECCO, P. O. DEVIVEIROS, M. D'ONOFRIO, S. ECKWEILER, E. FENG, P. FRANCAVILLA, S. GRINSTEIN, I. LA PLANTE, J. HUSTON, N. GHODBANE, D. LOPEZ MATEOS, B. MARTIN, N. MAKOVEC, S. MAJEWSKY, M. MARTINEZ, D. W. MILLER, J. MONK, K. PEREZ, C. RODA, J. ROBINSON, A. SCHWARTZMANN, F. SPANO, K. TERASHI, F. VIVES, P. WEBER, and S. ZENZ, Performance of Jet Algorithms in the ATLAS Detector, Technical Report ATL-PHYS-INT-2010-129, CERN, Geneva, 2010.
- [107] C. BLOCKER, Treatment of errors in efficiency calculations, Technical report, 2004.
- [108] P. VIDAL, Monte Carlo Truth Charged Track Association Studies, Technical report.
- [109] MIRMAN, NATHAN, Study of Bin Migration in the Z Boson Rapidity Measurement at CMS, 2010.
- [110] BLOBEL, VOLKER, An Unfolding method for high-energy physics experiments, Technical report, 2002.

- [111] T. ADDY et al., *ATL-COM-PHYS-2012-111*, 2012.
- [112] THE H1 AND ZEUS COLLABORATIONS, F.D. AARON ET AL., *arXiv:0911.0884 [hep-ex]*, *JHEP* **1001**, 109 (2010).
- [113] www.hepforge.org/archive/lhapdf/pdfsets/current/HERAPDF15NNLO.EIG.LHgrid.
- [114] S. DITTMAIER and M. HUBER, *JHEP* **1001**, 060 (2010).
- [115] A.D. MARTIN, W.J. STIRLING, R.S. THORNE AND G. WATT, *arXiv:0901.0002v3 [hep-ph]*, *Eur.Phys.J.* **C63**, 189 (2009).
- [116] S. ALEKHIN, J. BLUMLEIN, and S. MOCH, *Phys.Rev.* **D86**, 054009 (2012).
- [117] WWW.HEPFORGE.ORG/ARCHIVE/LHAPDF/PDFSETS/CURRENT/CT10NNLO.LHGRID.
- [118] THE H1 AND ZEUS COLLABORATIONS, F.D. AARON ET AL., *arXiv:0911.0884 [hep-ex]*, *JHEP* **1001**, 109 (2010).
- [119] BALL, R.D. AND BERTONE, V. AND CARRAZZA, S. AND DEANS, C. S. AND DEL DEBBIO, L. AND FORTE, S. AND GUFFANTI, A. AND HARTLAND, N. P. ET AL., *Nucl. Phys.* **B867**, 244 (2012).
- [120] www.hepforge.org/archive/lhapdf/pdfsets/current/NNPDF23_nnlo_as0118.LHgrid.
- [121] U. BAUR, *Phys. Rev.* **D75**, 013005 (2007).
- [122] ALWALL, J. AND HERQUET, M. AND MALTONI, F. AND MATTELAER O. AND STELZER, T., *JHEP* **1106**, 128 (2011).
- [123] C. ANASTASIOU, L. J. DIXON, K. MELNIKOV, AND F. PETRIELLO, *arXiv:hep-ph/0312266v2*, *Phys. Rev.* **D69**, 094008 (2004).
- [124] Measurement of the high-mass Drell-Yan differential cross-section in pp collisions at $\sqrt{s}=7$ TeV with the ATLAS detector, Technical Report ATLAS-CONF-2012-159, CERN, Geneva, 2012.
- [125] ATLAS TAG SERVICES, COMA Period Description Report.
- [126] THE GEANT4 COLLABORATION, Summary of Hadronic Processes, Models and Cross Sections for Physics List QGSP_BERT.